EXPLORING IMBALANCED FERMI GASES WITH STOCHASTIC QUANTIZATION

Dem Fachbereich Physik der Technischen Universität Darmstadt zur Erlangung des Grades eines Doktors der Naturwissenschaften (Dr. rer. nat.) vorgelegte Dissertation von

Dipl. Ing. Lukas Rammelmüller

aus Linz.

Darmstadt 2019 - D 17

EN: Exploring imbalanced Fermi gases with stochastic quantization
DE: Untersuchungen asymmetrischer Fermigase mit stochastischer Quantisierung

Dem Fachbereich Physik der Technischen Universität Darmstadt zur Erlangung des Grades eines Doktors der Naturwissenschaften (Dr. rer. nat.) vorgelegte Dissertation von Dipl. Ing. Lukas Rammelmüller geboren in Linz.

1. Gutachten: Prof. Dr. Jens Braun
2. Gutachten: Prof. Dr. Hans-Werner Hammer

Tag der Einreichung: 20. November 2019
Tag der Prüfung: 16. Dezember 2019
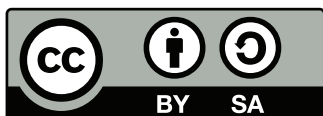
Darmstadt 2019 - D 17

Abstract

Strongly coupled quantum matter displays a rich phenomenology including phase transitions and often unexpected collective behavior. Remarkable advances in experiments with ultracold Fermi gases allow us to gain deep insight into these intriguing systems. Their theoretical description, however, is often challenging as exact analytic solutions are available only in a few special cases, and approximate techniques such as mean-field or perturbation theory are of limited use. Numerical treatment with Monte Carlo (MC) methods has led to profound success in this regard. Unfortunately, for many systems - and especially for asymmetric quantum gases - the infamous sign problem slows progress due to an exponentially scaling of the computational effort with inceasing system size.

In this thesis, we set out to explore the rich physics of two-component Fermi gases in the presence of finite spin polarization and/or mass imbalance. To surmount an arising sign problem, we learn from methodological advances made in the field of quantum chromodynamics and further develop these lattice approaches in the context of nonrelativistic Fermi gases. An extensive overview of the numerical methods is presented, including several toy problems to detail the capabilities and shortcomings of the developed approaches.

With these tools in hand, we perform extensive benchmarks of the hybrid Monte Carlo method with imaginary asymmetries (iHMC) and the complex Langevin (CL) method, which is based on a complex version of stochastic quantization. Both approaches are shown to yield excellent results for the ground-state energy equation of state of mass-imbalanced Fermi gases in one spatial dimension. Due to its great versatility, the CL method is subsequently employed to study pairing in one-dimensional Fermi gases, for which suitable two-body correlations are computed, revealing unexpected pairing patterns for spin- and mass-imbalanced systems.

Another major system of interest in this thesis is the paradigmatic unitary Fermi gas which is investigated at finite temperature and spin polarization. A precise determination of the density equation of state in the normal phase enables us to explore a broad range of thermodynamic properties. We infer valuable information on the finite-temperature phase diagram, such as a flat phase boundary of the normal-to-superfluid transition near the balanced limit and indications for the absence of an extensive pseudogap phase above this transition. The presented results provide experimentally testable *ab initio* predictions for a range of previously inaccessible thermodynamic quantities.

Kurzfassung

Stark wechselwirkende Quantenmaterie besitzt eine facettenreiche Phänomenologie, welche unter anderem Phasenübergänge und kollektives Verhalten umfasst. Experimente mit ultrakalten Fermigasen erlauben tiefe Einblicke in diese spannenden Systeme. Ihre theoretische Beschreibung ist jedoch schwierig, da es nur in einigen Spezialfällen möglich ist analytische Lösungen zu erhalten und Näherungsverfahren, wie zum Beispiel die sogenannte Molekularfeldnäherung oder die Störungsrechnung, oft nur bedingt hilfreich sind. Numerische Rechnungen mittels Monte-Carlo Methoden haben dagegen zu großen Erfolgen geführt. Im Fall von asymmetrischen Quantengasen werden diese jedoch durch das sogenannte Vorzeichenproblem erschwert, welches einen exponetiellen Anstieg der notwendigen Ressourcen mit wachsenden Systemgrößen verursacht.

Die vorliegende Dissertation behandelt die vielfältige Physik von zweikomponentigen Fermigasen mit Spin- und/oder Massenpolarisierung. Um das Vorzeichenproblem zu umgehen werden methodische Fortschritte im Bereich der Quantenchromodynamik genutzt und die dort gängigen Gittermethoden auf nichtrelativistische Fermigase erweitert. Die Diskussion beinhaltet einen ausführlichen Überblick über die entwickelten numerischen Methoden, deren Stärken und Schwächen mitunter anhand von verschiedenen simplen Testfällen diskutiert werden.

Anschließend werden umfangreiche Benchmark-Tests der sogenannten Hybrid-Monte-Carlo-Methode mit imaginären Massen und der Complex-Langevin-Methode durchgeführt, wobei letztere auf einer komplexen Version der stochastischen Quantisierung beruht. Es zeigt sich, dass beide Algorithmen hervorragende Resultate für die Zustandsgleichung der Grundzustandsenergie eindimensionaler Fermigase mit asymmetrischen Massen liefern. Darüberhinaus wird die Complex-Langevin-Methode dazu verwendet die Paarbildung in eindimensionalen Fermigasen mit unterschiedlichen Spinbesetzungen zu untersuchen. Hierfür werden entsprechende Zweiteilchen-Korrelationsfunktionen berechnet, welche ein unerwartetes Paarungsmuster zum Vorschein bringen.

Schließlich wird das unitäre Fermigas bei endlicher Temperatur und Spinpolarisierung behandelt. Ausgehend von einer präzisen Bestimmung der Dichte-Zustandsgleichung in der normalen Phase, wird eine Vielzahl an thermodynamischen Größen berechnet. Daraus kann wertvolle Information über das Phasendiagramm bei endlicher Temperatur abgeleitet werden, wie zum Beispiel eine flache Phasengrenze, welche den normalen in den suprafluiden Zustand trennt, in der Nähe des Spin-symmetrischen Gases sowie die Abwesenheit einer ausgedehnten Pseudogap-Phase überhalb dieses Phasenübergangs. Die präsentierten Resultate liefern experimentell verifizierbare *ab initio* Vorhersagen für eine Reihe von bis dato unzugänglicher thermodynamischen Größen.

Acknowledgements

Writing these lines lets me realize that my days in Darmstadt are coming to an end. I guess time flies, if you're having fun - and I most certainly did. I was extremely fortunate to spend my time with an exceptional group of people. These words can only be a tiny token of my appreciation, which goes well beyond what a few lines of text can express.

First and foremost, I want to extend my deepest gratitude to my advisor Jens Braun. The visits next door have made many of my days, may it be for a discussion of physics, to catch up on some recent sports event (seriously: how do you keep up with all that?) or just you telling me that there is actually a dash or a comma missing in my writing. I love that you always make time for a "kurze Frage", even if you know exactly that these mostly end up being extended discussions. I want to thank you for somehow directing my unpredictably meandering physical and computational interests, for the opportunity to visit countless conferences and colleagues, for giving me the chance to teach and supervise students and most importantly for your trust that all of these things might actually work out. But I also have to warn you: One of these days I will actually set up the bad-joke jar, and we all know where this is going! In all seriousness though: Thank you for all you have done for me. You go out of your way to make the life for people in your group just a tiny bit better. It is a true privilege to be part of your team.

I want to genuinely acknowledge the collaboration with the quantum matter group over at Chapel Hill. Joaquìn, you are the reason why I came to Darmstadt in the first place for which I cannot thank you enough. I cherish the times we had in Chapel Hill and the many Skype calls we had mostly because of countless questions of mine that you are still not weary to answer (sometime we will remember that there is a 5h time shift for two weeks of the year). Also, working with you on countless projects and hanging out with you on three different continents is hard to beat! I am happy to call you a colleague and a friend.

I also want to thank Josh for a fun Summer in Chapel Hill, for our somewhat weekly physics discussions, and for jumping on the lattice project with me that turned out to be more challenging than initially thought. Thanks also to Casey for hanging in there with me and for the fun times during the mad review-paper project. Working with you guys means a lot to me.

Of the many people I have enjoyed discussions with during the last few years, Artem deserves a special mention here. You have been my number one address for 1D related questions, to discuss cold atoms in general and much more. Your patience in enduring my requests for actual numbers is amazing. I apologize for dragging my foot on the latest project we've been working on - one day we'll manage! Thank you for always taking the time, for your excellent advice and watching out for me! The IKP was not the same after you left.

Aside from collaborating with a set of outstanding individuals, I had the pleasure to enjoy my time in Darmstadt in great company. First of all, I want to thank Christian, my brother in

crime, for the amazing time we had as flat mates. You somehow guilt-tripped me into going to crossfit (roughly) once a week, which I never would have deemed possible. I will dearly miss the countless epic matches of Fifa, Darts, "lost" nights at Cafe Hess and our amazing ability for just-in-time-furnishing. Thanks for always having my back!

To Marius and Marc, who have been the real "Office's Delight", I can only say: Matt auf! I would not have thought possible half of the silly things that went down in the legendary room 108, but I wouldn't want to miss a single one of them. A special shoutout in this regard goes to Albino, with whom we enjoyed one of the more interesting "scientific" discussions. I also want to thank Laura, whose frequent appearances in our office brightened up many afternoons. Ich verabschiede mich aufs Herzlichste - see you at Snow2020!

I also want to thank the Braunbären group for countless (often delayed) enjoyable lunch breaks and discussions on physics and far beyond. A special shoutout goes to Martin and Marc, who have been my "classmates" from day one. It was an honor to figure out this PhD thing together with you two. It's hard to believe that the era is over - at least we'll always have Bad Honnef. Martin, I will wait for that beer in Munich! I also want to thank Fabian, Felix and Flo, whose projects I had the privilege to co-supervise. Your questions challenged me to be on top of my physics game. A special shoutout goes also to Flo, who ultimately was responsible for pushing gMacs to completion. Go Team CL! Andreas, Benedikt, Daniel, Juliane, Sebastian, and Timon: I'm looking forward to our next semi-annual LAN party - let's keep this tradition alive!

Besides the IKP, I owe special thanks to several people for making Darmstadt a fun place to live. I want to especially thank Philipp, Sabrina and Patrick for starting this endeavor with a proper Bockbieranstich when I was unaware of the holiday. Lukas and Mimi for warmly welcoming me in Darmstadt and for letting me a part of their gang. Patrick for pushing me to actually going to crossfit and for being the best Ski-Trip organizer for all of us - eight or nothing! Kevin, amongst many things, for finally defeating our old nemesis, the Botanist. And finally the Coffe-Crew, Sabrina, Philipp, Marc, Martin, Rodric, Christian and Thorsten for enjoying countless Milchreis and Coffees with me. Fridays have definitely been the most enjoyable Mensa-Days thanks to you guys!

As for the completion of this thesis, I want to thank my tireless proofreaders Josh, Casey, Kathi, Christian, Marc, Marius, Flo, Kevin, Joaquìn and Rodric. Without you this thesis would not have made sense. In this regard, I also want to thank Tilman Enss, Bernhard Frank, Martin Zwierlein, Scott Jensen, Hersh Singh and David Huber for sharing their data with me.

Besides many new friends I have made during my time in Darmstadt, this experience would not have been the same without frequent visits from my close friends from home. I want to thank Alex, Thomas, Philipp, Ritschi, Schmerzi, Tom, Hias, Geri, Lidi, Sietziboy, Kiki, Chri, Mats, Alex, Mani, Theresa, Stefan and Sulzi for taking the time and showing up repeatedly. These Sauna weekends have been legendary!

Zu guter Letzt möchte ich mich bei meiner Familie bedanken. Obwohl ich mir sicher bin, dass ihr euch anfangs gefragt habt ob Physik das Richtige für mich ist, habt ihr mich ohne zu zögern unterstützt und wart immer für mich zur Stelle. Vielen Dank dafür! Kathi, du weißt, dass ohne dich hier nichts gegangen wäre. Danke für die Motivation, die bei Zeiten nötig war, und für deine Art mich in der Balance zu halten.

Although I will never understand the combination of "Grüne Soße" with a breaded Schnitzel, I will always remember my time in Darmstadt with a bright smile on my face. So long, and thanks for all the fish!

Contents

1 | Introduction

When we try to understand phenomena occurring in nature, we often observe a system influenced by the interplay of a large number of constituents. A view on the exact underlying principles might then be obstructed by the competition of several physical effects such that it may be hard to tell the signal from the noise. The full theoretical understanding of all the mechanisms at work requires a precise solution of the equations of motions under consideration of all microscopic details. Within our most accurate description of nature at the moment, quantum mechanics, this amounts to solving the quantum many-body problem. In this regard, already 90 years ago Dirac famously remarked that "the difficulty is only that the exact application of these laws leads to equations much too complicated to be soluble" and that we should look for more practical descriptions "which can lead to an explanation of the main features of complex atomic systems without too much computation" [1]. This statement already hints at an extremely successful strategy to cope with this complexity of nature, namely the construction of effective theories. These contain just enough features to capture the physics of interest at a given scale, but cut out subleading effects such that our understanding is not obscured by unimportant side effects.

Unfortunately, even these idealized models are not guaranteed to be easily solvable. Take for instance the famous Hubbard model, which was proposed to describe the behavior of electrons in the periodic potential of certain transition metals. The electronic orbitals are assumed to be sufficiently localized near the lattice ions such that electrons reside in their close proximity. The movement of the charge carriers through the crystal is described by electrons tunneling to nearby orbitals and interaction only takes place if two electrons are present in the same orbital. This is a tremendous idealization of the real world but nevertheless provides a good description of many materials and is even thought to contain the physics of such exotic effects as high-T_c superconductivity. Despite the simplest possible structure, however, it is hopeless to solve this model with pen and paper.

It is the strong correlation between the particles that prohibits the analytic treatment of the above model and many others in essentially all areas of physics. While approximate approaches, such as mean-field calculations, provide us with qualitative insights, a quantitative description of these systems is only possible via sophisticated numerical treatment. Computationally, the challenge to overcome is the exponential growth of the underlying Hilbert space. It implies that straightforward diagonalization of the Hamiltonian in some basis is limited to a small number of degrees of freedom beyond which even the most powerful supercomputers quickly meet their limitations. To circumvent this unfavorable scaling, a large number of many-body methods have

been developed over the years, each of which is suitable to treat a certain class of problems and comes with its own strengths and weaknesses.

One of the most successful strategies to obtain reliable results is based on the stochastic evaluation of the partition sum, referred to as Monte Carlo (MC) sampling. If applicable, such a treatment only exhibits polynomial scaling with the number of degrees of freedom in the system, rather than an exponential one. This drastic reduction of computational effort allows us to explore large enough systems to accurately approximate nature and has helped to fundamentally shape our understanding of physics of strongly correlated systems. In many cases, though, even these powerful methods face a major roadblock, namely the notorious sign problem [2]. It clouds the signal with an enormous amount of statistical noise such that the computational effort again increases exponentially with the system size. This limitation, which especially slows progress in systems containing fermions, is a major unresolved issue in theoretical physics and is the subject of intensive investigation.

1.1 Cold atoms to the rescue

Instead of looking at a system exactly as nature provides it, we may just build a simpler model in the lab to understand its key features. Loosely speaking, in theory "building a simpler model" means neglecting or altering certain terms in the Hamiltonian. In an experimental context, on the other hand, the procedure is much less clear. The solution was found in the preparation of ultracold atomic gases, which enables us to systematically study the physics of strongly correlated matter.

The central challenge in the preparation of these systems lies in reaching the quantum degenerate regime in a controlled fashion. This is best achieved in gaseous matter cooled to low temperatures to switch of thermal fluctuations. Below a certain point though, most substances liquefy or turn solid, which stands in the way of a controlled study of quantum effects. The issue is prevented by working at ultralow densities such that the scattering rates for three-body inelastic processes are sufficiently suppressed and the gas exists in a long-lived metastable state. This requirement, however, comes at the price of significantly reduced degeneracy temperatures: With typical densities of the order of $10^{14}/\mathrm{cm}^{-3}$ the temperatures drop to the microkelvin regime. Reaching these is far from trivial and was only achieved through remarkable experimental finesse and progress based on techniques such as laser cooling and evaporative cooling.

This procedure, which to some extent follows Feynman's proposal to simulate quantum theories with actual quantum devices [3], allows to put long-standing theoretical predictions to a practical test. Undoubtedly, the defining milestone for the field was achieved when the prediction of Bose-Einstein condensation was confirmed by its observation in a cold gas of sodium atoms [4, 5]. This heralded the start of the now flourishing field of ultracold atom physics which led to an enormous amount of physical insights into quantum many-body systems.

From a theorist's perspective, these experimental advances allow us to play a sort of "quantum lego" with pieces of Hamiltonians that may actually be realized in experiment. The topic of this thesis is inspired by the virtually endless possibilities and explores the rich physics of spin-$\frac{1}{2}$ Fermi gases. These have been the center of numerous experimental efforts, where the two spin states are typically realized as two different hyperfine states of some fermionic atom species. Early Fermi gases have been realized with the alkali metals ^{6}Li or ^{40}K because of their favorable scattering properties [6]. Although these atom species are still the predominant choice, more

exotic fermion species such as ^{53}Cr, ^{87}Sr, ^{161}Dy, ^{167}Er and ^{171}Yb are being brought to degeneracy these days.

The present work focuses on systems with different amounts of spin-up and -down particles and/or different masses of the two species. The tuning of these properties allows for a detailed study of so-called imbalanced Fermi mixtures which are expected to exhibit fundamentally altered pairing behavior and novel phases of matter. Theoretically, their study via stochastic numerical methods is hindered by the sign problem which calls for the development of suitable numerical techniques. This dissertation builds on several existing numerical approaches, originally employed in high-energy physics, and extends them to the realm of ultracold Fermi gases. These new tools prove to be a valuable resource in this context and are able to deliver results from first principles in previously inaccessible physical regimes.

1.2   Engineering the interaction: the BCS-BEC crossover

As a consequence of the low density and temperatures in these dilute vapors, scattering between the particles predominantly happens in the s-wave channel. This is due to the fact that the colliding particles have a thermal wavelength larger than the range of the interatomic potential and therefore are unable to resolve its exact shape. Consequently, the van-der-Waals potential may be safely approximated with a contact potential

$$V(\vec{x}, \vec{y}) = g\,\delta^{(d)}(\vec{x} - \vec{y}) \tag{1.2.1}$$

with the strength set by the bare coupling constant g. Since the Pauli principle forbids two fermions of the same spin to be present at the same position, interaction only happens between up and down particles but not between alike spins.

1.2.1   Two types of pairing

For attractive interactions, which corresponds to negative values of g in Eq. (1.2.1), spin-up and -down particles tend to form pairs. The exact nature of this process is dimension-dependent: While the two-body Schrödinger equation has a bound-state solution for infinitesimally small couplings in one and two spatial dimensions, the three-dimensional potential has to surpass a certain threshold in order to support two-body pairing. Far above that threshold, the up and down particles therefore clump together to form a molecule which will be a tightly bound state, effectively acting as a composite boson. Consequently, a gas of spin-up and -down fermions in this regime behaves like a weakly repulsive gas of composite bosons which, at low temperatures, populate the lowest energy state, i.e., forms a Bose-Einstein condensate (BEC).[1] Hence, the regime is referred to as BEC limit.

Below the bound-state threshold, the situation is slightly more delicate. Although pairing is not supported on the two-body level, the situation drastically changes in the presence of many weakly interacting fermions at low temperatures. Specifically, it was shown that in the presence of a Fermi surface the existence of a shallow two-body bound state is favored even for infinitesimal attraction [7]. The pairs are protected by a gap in the single-particle energy spectrum such

---

[1]The effective Hamiltonian for the bosonic system can only be bounded from below if the interaction is repulsive. For attractive interaction it is impossible to form a stable gas and the system collapses.
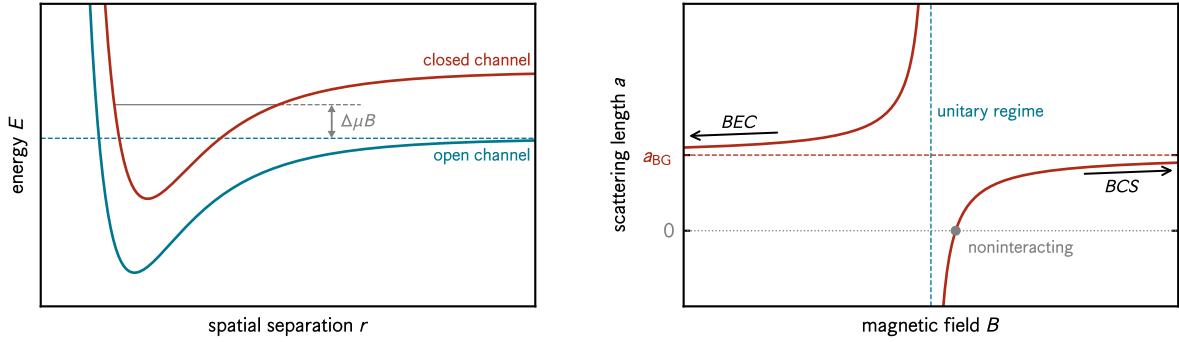
Figure 1.1: Sketch of a Feshbach resonance. (Left) Interatomic potential as a function of separation r of the closed and open channels. The gray solid line represents the energy of the bound state in the closed channel. (Right) Scattering length as a function of the magnetic field. The resonance occurs at the vertical dashed blue line and the gray point reflects the noninteracting point.

that the ground state is stable against fluctuations. Opposed to the strong interaction case, this type of pairing is localized in momentum space which implies that the size of such a $\uparrow\downarrow$-pair is much larger than the average particle spacing. The mechanism was in fact introduced in order to explain the behavior of electrons in superconductors, which are subject to a slight attractive interaction through Coloumb screening and phonon exchange [8]. These large pairs are nothing but the well-known Cooper pairs and the regime is consequently called Bardeen-Cooper-Schrieffer (BCS) limit.

Thus, there are two seemingly different worlds on the two ends of the possible interaction strengths: Tight two-body paring on the strongly attractive BEC end and many-body pairing in the weakly attractive BCS regime. Naturally, theorists asked the question what would happen if the scattering properties would be changed continuously to interpolate between these limits [9–11]. Indeed, it was found that the above limits are two sides of the same coin which are connected through a smooth evolution from the BCS side to the BEC limit, referred to as the BCS-BEC crossover [12, 13].

1.2.2 Feshbach resonances

One of the most striking features of ultracold atoms experiments is that these theoretical considerations can actually be probed through the ability to tune the interaction between the particles. Opposed to the situation in, e.g., nuclear physics, where the potential between the nucleons is complicated and we have to live with whatever nature gives us, this ability allows us to systematically study the influence of the coupling on the behavior of the particles. This is achieved via the usage of so-called magnetic Feshbach resonances, allowing us to tune the interaction via an external magnetic field [14–16].

The mechanism is best understood by considering a two-channel model as sketched in the left panel of Fig. 1.1. A channel merely describes the particle configuration and is denoted as (A, B). For two-body collisions in spin-$\frac{1}{2}$ systems, possible channels include $(\uparrow, \uparrow)$ or $(\uparrow, \downarrow)$ which correspond to different hyperfine levels, as remarked above. At large interatomic distance r, the interaction potential is negligible and the total energy of the state is given by the sum of the single-particle energies $E = E_A + E_B$. If E of the incoming particle configuration is below the

energy E' of some other channel (at large separation), the latter is said to be closed since energy conservation forbids it as the final scattering state. Conversely, energetically allowed channels are said to be open.

The particles in the model with one open and one closed channel scatter elastically, which means the scattering process will not change the particle configuration. While momentum transfer still takes place, the scattering is then of the form $(A, B) \to (A, B)$. Since the two potentials are coupled via the hyperfine interaction, however, the presence of the closed channel can have a dramatic impact on the scattering cross-section. This is the case if a bound state with binding energy ε_{B} is supported in the closed but not in the open channel. If the energy of the incoming particles is in the vicinity of the bound-state energy, a resonance occurs, where the particles could briefly flip the hyperfine state, form a virtual bound state (which may be achieved within the energy uncertainty), and then again separate to conserve the energy at large separations. The strength of this phenomenon is governed by the energy difference $\varepsilon_{\mathrm{B}} - E$, which in turn depends on the external magnetic field B, because the different hyperfine levels react differently to the external field. By changing B, the scattering properties may therefore be altered which is described via the relation

$$a(B) = a_{\mathrm{BG}} \left(1 - \frac{\Delta}{B_0 - B} \right), \tag{1.2.2}$$

where a_{BG} denotes the background scattering length, B_0 the position of the resonance and Δ is a shape parameter. The qualitative dependence is shown in the right panel of Fig. 1.1. Although, the scenario is more complicated in real atomic systems the physics is captured by these simple considerations. For more details it is referred to the extensive review [17] and to [18] for an educational example.

For the low-energy processes relevant in cold Fermi gases, the s-wave scattering length fully characterizes the bare coupling between the particles such that the interaction essentially can be tuned at will.[2] Large negative values of a correspond to the BCS limit and large positive values to the molecular BEC regime. This remarkable possibility has been exploited in several cold atoms experiments and the BCS-BEC crossover was beautifully confirmed in a series of experiments (see [12, 13, 20] for reviews).

1.2.3 The unitary regime

Right "in the middle" of the crossover, i.e., at the resonance, is a special point of interest which corresponds to the threshold of two-body bound-state formation. The scattering cross section in this regime is at the maximum allowed by the unitary property of the scattering matrix and it is therefore referred to as the unitary regime. In this region, the scattering length dominates all other length scales in the system. For dilute gases, where the interparticle distance $n^{-1/3}$ is much larger than the effective interaction range r_0, this implies a separation of scales:

$$a \gg n^{-1/3} \gg r_0. \tag{1.2.3}$$

---

[2]The exact relation can, e.g., be obtained via solving the Lippmann-Schwinger equation and is generally dependent on the spatial dimension (see, e.g, [19]).

At this point, a effectively drops out of all physical quantities as it is much larger than all other length scales in the system. Hence, all information on the shape of the interaction potential is lost and the density, along with the temperature, is the only dimensionful scale left to determine the physics. As a consequence, the scattering and thermodynamic properties of the unitary Fermi gas (UFG) are universal and valid for all other systems with sufficiently short-ranged interaction potentials and large scattering length.

The universal nature of the UFG reaches far beyond cold quantum gases and renders the system relevant for such disparate energy scales as those of atomic and astrophysics and has, moreover, been shown to reflect a nonrelativistic type of conformal invariance [21–24]. Interesting connections exist to the inner crust of neutron stars, where dilute neutron matter exhibits a dominating s-wave scattering length [13, 25–27]. Other examples include the nature of pairing above the critical temperature for superfluidity, often termed the pseudogap regime [28], which might share common features with the cuprates. Combined with the unusually high critical temperature for superfluidity of the UFG, this suggests intriguing connections to high-T_c superconductors. Because of such relevance of the UFG for various fields, the past two decades have witnessed uncounted studies exploring its unpolarized limit both theoretically and experimentally [20].

From a theoretical perspective, the UFG is challenging to access due to the absence of a small parameter which renders the regime intrinsically nonperturbative. While the case of balanced spin-up and -down populations may be treated with conventional MC approaches, the situation changes drastically for the imbalanced scenario which will be discussed in the following. A goal of this thesis is to arrive at a quantitative treatment of this regime based on stochastic methods beyond the fermionic sign problem.

1.3 Imbalanced Fermi gases

A natural question to ask is what happens if not every up particle has a down partner, i.e., what happens in the presence of finite spin polarization? In this case, the Fermi surfaces of the species differ and BCS-type pairing will be "disturbed" in some way. The spin imbalance is quantified by the relative polarization

$$p \equiv \frac{N_\uparrow - N_\downarrow}{N_\uparrow + N_\downarrow} = \frac{M}{N}, \tag{1.3.1}$$

where N_σ denotes the number of particles in the spin state σ. In the balanced limit at $p = 0$, the gas is well known to be a superfluid at sufficiently low temperatures [12]. At $p = 1$, on the other hand, only up particles are present which corresponds to a noninteracting system due to the Pauli exclusion principle. Since pair formation is impossible in this case, no superfluidity is suppressed and the system will be in the normal phase. Regardless of the interaction strength, this implies the existence of at least one phase transition at some critical polarization p_c, above which the excess fermions destroy the superfluid behavior.
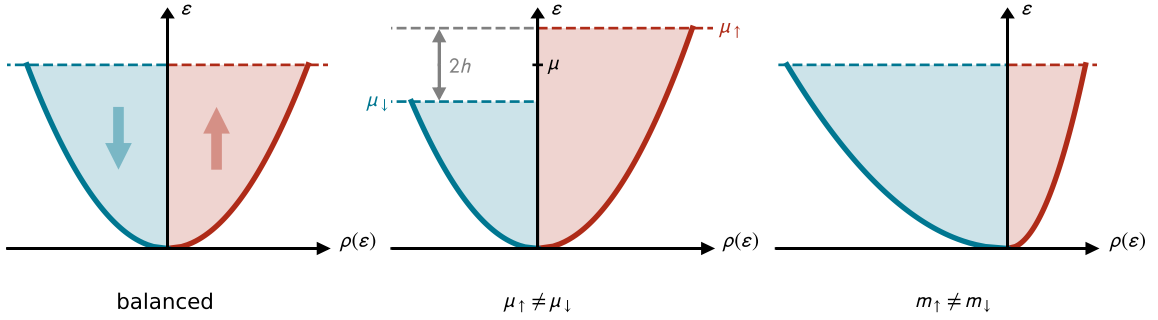
Figure 1.2: Sketch of the density of states in three spatial dimensions for spin-up (red) and down (blue) particles. From left to right: balanced system, spin imbalance, mass imbalance.

1.3.1 Chandrasekhar-Clogston limit

To better understand the physics associated with the critical polarization, the finite spin asymmetry may be viewed as the consequence of an effective magnetic field.[3] It couples to the magnetic moment of the spins and causes an energy contribution depending on its orientation such that spins gain free energy by aligning. This tendency competes with the pair formation in the superfluid phase, which yields an energy gain of Δ per particle. If the Zeemann energy $h = \mu_{\mathrm{B}} B$ for flipping the spin of a particle is larger than the gap, superfluidity is destroyed because the normal phase has a lower free energy.

The actual limit, however, is even lower than this naive estimate due to a shift of the Fermi surfaces in the normal phase. This is depicted in the central panel of Fig. 1.2, where the density of states (DOS) for both spin species of a noninteracting gas is shown. The DOS quantifies the number of states per volume and energy interval as a function of the energy ε and in three dimensions is given by

$$\rho(\varepsilon) = \frac{1}{4\pi^2} (2m)^{\frac{3}{2}} \sqrt{\varepsilon}. \tag{1.3.2}$$

At zero temperature, the total number of atoms for a given spin species is obtained by integrating $\rho(\varepsilon)$ up to the associated Fermi energy μ_σ. Evidently, the separation of Fermi surfaces leads to a different number of spin-up and -down particles in the gas, which is proportional to the shaded areas under the respective curves.

The free energy for two unequal Fermi surfaces is given by

$$E_{\mathrm{N}}(\mu_\uparrow, \mu_\downarrow) = \int_0^{\mu_\uparrow} \mathrm{d}\varepsilon \, \varepsilon \rho(\varepsilon) + \int_0^{\mu_\downarrow} \mathrm{d}\varepsilon \, \varepsilon \rho(\varepsilon) - \mu_\uparrow N_\uparrow - \mu_\downarrow N_\downarrow, \tag{1.3.3}$$

which may be rewritten as a function of the effective magnetic field through the substitution $\mu_{\uparrow/\downarrow} = \mu \pm h$:

$$E_{\mathrm{N}}(\mu, h) = -\frac{4V}{15} \rho(\mu) \mu^2 \left[\left(1 + \frac{h}{\mu}\right)^{\frac{5}{2}} + \left(1 - \frac{h}{\mu}\right)^{\frac{5}{2}} \right]. \tag{1.3.4}$$

---

[3]Note that this "magnetic field" should only be understood as the origin of the Zeemann splitting of the energy levels and has nothing to do with the Feshbach mechanism discussed above.

An expansion in h yields

$$E_N(\mu, h) = E_N(\mu, 0) - V\rho(\mu)h^2 + \mathcal{O}(h^4), \tag{1.3.5}$$

which quantifies the energy gain by adjusting the Fermi surfaces in the presence of a magnetic field. At the critical field strength h_c, this energy gain must be equal to the free energy difference between the normal and superfluid phases. At mean-field level, the latter is given by

$$E_N(\mu, 0) = E_S(\mu) + \Delta^2 \frac{V\rho(\mu)}{2}, \tag{1.3.6}$$

where $\frac{V}{2}\rho(\mu)\Delta$ is the number of pairs at the Fermi surface in the energy interval of the gap Δ. Comparing this expression to Eq. (1.3.5) yields the critical field strength

$$h_c = \frac{\Delta}{\sqrt{2}}. \tag{1.3.7}$$

This is known as the Chandrasekhar-Clogston (CC) or Pauli limit [29, 30]. For magnetic fields above this value, the pairing gap is surmounted by flipping spins such that the normal state has a lower free energy than the superfluid.[4]

The above expression is valid in the weakly attractive BCS regime. There, the gap is related to the coupling via $\Delta \sim e^{-const./g}$ such that even a small magnetic field will destroy the superfluid. Under the assumption that a similar mechanism is at work in the UFG, despite the strong interaction, the superfluid is expected to be stable against some external magnetic disturbance because of the large gap of $\Delta \approx 0.5\,\varepsilon_F$, where ε_F denotes the Fermi energy. Although this comparison is qualitative at best, experimental studies in the strongly interacting regime indeed found superfluidity in the presence of finite spin imbalance [31–36].

In the strongly interacting regime, a precise theoretical characterization of this transition beyond this simple mean-field picture requires sophisticated many-body methods. Progress in this regard was achieved based on functional methods [37, 38] or MC studies in the zero-temperature limit [39]. A full characterization of the transition at arbitrary temperatures based on *ab initio* methods, however, remains to be explored.

1.3.2 The Fermi polaron

At large imbalances, near the limit of full polarization, the gas may be envisioned to consist of a single impurity moving in a sea of majority fermions. It turns out that this simple picture, called the Fermi polaron, is a surprisingly good description of even strongly correlated Fermi gases in the normal phase.

Along the BCS-BEC crossover, the impurity undergoes a change from an essentially free particle at weak interaction to a strongly bound ↑↓-molecule in the presence of a majority background. When the interaction is not strong enough to form a bound state, collisions limit the free propagation of the impurity. This configuration may be described by a variational ansatz due to Chevy [40] which introduces a single minority atom dressed by a cloud of particle-hole excitations.

---

[4]Note that the derivation of the CC limit neglects the existence of the Meissner effect such that a magnetic field may enter the superfluid. This is only justified for neutral particles. For superconductivity, which necessarily involves charged particles, the critical field is far below the CC limit due to the induced current to keep the magnetic field from permeating the superconductor.
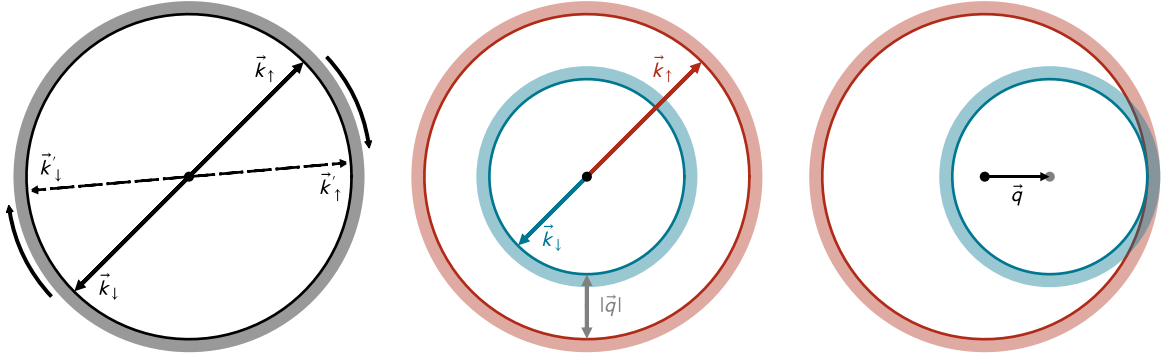
Figure 1.3: Schematic pairing of spin-up and -down particles. Solid lines represent Fermi surfaces (FS) and shaded areas indicate kinematically possible scattering states near the FS. (Left) Balanced case, with scattering $(\vec{k}_\uparrow, \vec{k}_\downarrow) \to (\vec{k'}_\uparrow, \vec{k'}_\downarrow)$. (Center) Spin imbalanced case, $|\vec{q}| = |\vec{k}_{F\uparrow} - \vec{k}_{F\downarrow}|$. (Right) Minority FS is shifted by $\vec{q}$. The overlap of the shaded areas shows favorable pairing states with finite center-mass-momentum $\vec{q}$.

At polarizations below the single impurity limit, multiple Fermi polarons are present in the gas. For low impurity densities, or equivalently, large spacing between the polarons, the impurities form a weakly interacting gas of fermionic quasiparticles in a background of majority atoms. Hence, the new degrees of freedom comprise a Fermi liquid with rescaled physical properties such as an effective mass larger than the bare particle mass.

At unitarity, this mechanism has indeed been observed to describe experiments accurately not only at large temperatures [41] but even at large polarizations in the ground state [42–44]. Furthermore, the picture is consistent with Diffusion Monte Carlo (DMC) simulations at $T = 0$ in the normal phase [39] where the quasiparticle properties are determined and has furthermore been used to study various other quantities [45]. Increasing the minority density further leads to an effective interaction between the quasiparticles, as the spacing between the Fermi polarons reaches the size of the surrounding majority cloud. By adding an effective interaction term to a variational ansatz, the quasiparticle picture may still be applied up to intermediate values of minority concentrations [36, 46].

1.3.3 Polarized superfluids?

The nature of superfluidity in spin-imbalanced Fermi gases turns out to be a much more subtle question. The original formulation of the BCS theory requires equal densities for both spin species and it is unclear how exactly excess majority fermions would interfere with the formation of a condensate. Possible scenarios include a total breakdown of superfluid behavior or a phase separation into a balanced BCS-type superfluid region and an either fully or partially polarized normal fluid [47]. Alternatively, exotic types of pairing could occur, featuring a coexistence region where the superfluid exists despite the spin imbalance.

Several mechanisms have been proposed to accommodate a polarized superfluid, where not every majority particle has a partner to form a pair. Proposals include the deformation of Fermi surfaces [48], breached pairing inside the majority Fermi surface [49, 50] and p-wave pairing of spin alike particles as a consequence of a mediated interaction through the minority species [51].

A particularly interesting possibility is pairing at opposite, but incommensurate momenta, as depicted in Fig. 1.3. This is similar in spirit to the BCS theory, but in this scenario the Cooper pairs form at a finite center-of-mass momentum proportional to the mismatch of the Fermi momenta

$$|\vec{q}| \propto |\vec{k}_{\mathrm{F},\uparrow} - \vec{k}_{\mathrm{F},\downarrow}|. \tag{1.3.8}$$

This is expected to have profound effects on the order parameter $\Delta(\vec{r})$, which is given by the expectation value of the pairing field

$$\Delta(\vec{r}) \propto \langle \psi_\uparrow(\vec{r})\psi_\downarrow(\vec{r}) \rangle. \tag{1.3.9}$$

While in standard BCS theory the order parameter is translationally invariant, i.e. $\Delta(\vec{r}) = \Delta$, the finite momentum of the Cooper pairs suggests a nontrivial spatial dependence. Two mechanisms have been proposed to accommodate this behavior: The Fulde-Ferrell (FF) ansatz includes a single mode with momentum $\vec{q}$ such that the order parameter becomes $\Delta(\vec{r}) = \Delta e^{i\vec{q}\cdot\vec{k}}$ [52]. Alternatively, the Larkin-Ovchinnikov (LO) mechanism requires at least two modes at $\pm\vec{q}$ and obtains $\Delta(\vec{r}) = \Delta\cos(\vec{q}\cdot\vec{k})$ for the order parameter [53]. Both scenarios are similar and are typically referred to as FFLO pairing.[5]

At zero temperature in the BCS regime, the critical field strength above which the FFLO phase vanishes was found to be $h_c = 0.754\Delta$, which is slightly above the CC limit. Beyond the ground state, it was suggested that such a state is stable, if at all, only at very low temperatures. The state is expected to be particularly feeble in continuous systems and it has been argued that lattice geometries are more likely to favor such an exotic pairing mechanism through a better Fermi surface nesting. Additionally, reduced dimensionality could help to stabilize an inhomogeneous pairing state. Regardless of the interaction strength and geometry, the phase has so far eluded experimental measurements. This is in part a consequence of the necessity of a trap which renders the chemical potential, and with it the phase structure, position dependent. Recent advances regarding flat traps could improve this shortcoming [55]. A recent extensive review on FFLO physics can be found in [54].

The full phase-diagram for the BCS-BEC crossover, including the possibility of polarized superfluids, was discussed qualitatively within an effective field theoretical approach in [56]. Several mean-field studies have investigated the weakly-interacting regime (see [57–59] for reviews) and functional methods have been used to study the phase diagram at unitarity [37, 38]. The exact nature of the phase diagram, in particular at strong interaction, remains an open question.

1.3.4 Mass imbalance

A mismatch of Fermi surfaces may not only be induced via different chemical potentials but can also be achieved via a mass asymmetry between the species. The latter enhances the number of available energy states in a given interval, as depicted in the right panel of Fig. 1.2 for a mass ratio of $m_\downarrow/m_\uparrow = 2$. Populating two mass-imbalanced species up to the same energy level, therefore, results in a finite spin-imbalance with similar consequences for the pairing as discussed

---

[5]The FFLO state is still associated with spontaneous breaking of the $U(1)$ symmetry of the ground state. For the FF state, an additional breaking of time-reversal symmetry occurs, whereas the LO state is associated with breaking of translational invariance. See, e.g., [54] for further details.

above. A difference to the mass-balanced case, however, is the reduced energy cost to excite the heavier particles into a higher state, as the density of states is enhanced. The larger the mass asymmetry, the more likely it is to excite the heavier species. Furthermore, the bound-state energy of the two-body problem depends on the reduced mass, such that the onset of two-body pairing, i.e., the unitary regime in three-dimensional systems, is shifted to larger bare couplings. While theoretically the mass parameter may be tuned at will, only certain values are accessible in experiment due to the limited number of fermionic atom species suitable for experiments. As a further complication, not only the single-species scattering properties are relevant but also so-called heteronuclear Feshbach resonances need to be present. Promising systems currently probed in experiments include mixtures of $^6\mathrm{Li}^{40}\mathrm{K}$, $^{40}\mathrm{K}^{161}\mathrm{Dy}$ and $^6\mathrm{Li}^{53}\mathrm{Cr}$ with mass-ratios of $\kappa = m_\downarrow/m_\uparrow = 6.67, 4.02$ and 8.83, respectively. While other mixtures are in principle possible, their mass ratios are either too close to unity to observe a noticeable effect or above the threshold of $\kappa \approx 13.6$ beyond which three-body losses prevent long-lived experiments. An alternative to different particle masses can be realized with optical lattices, where the hopping parameter may be made spin-selective [60]. While this emulates a mass-imbalanced system, the procedure is intrinsically limited to lattice geometries.

Generally, the theoretical study of mass-imbalanced systems in three spatial dimensions is surprisingly scarce in the literature. Beyond mean-field considerations, which for instance suggest a stabilized FFLO phase at large enough imbalances [61], renormalization group studies [62] and MC calculations in the ground-state based on lattice approaches with imaginary asymmetries [63] as well as DMC [64–66] seem to be the notable exceptions to the otherwise dire situation because of the sign problem.

1.4   Reduced dimensionality

One way to address the challenging many-body problem, at least in theory, is to consider an at least seemingly simpler version of it by reducing the spatial dimension. Indeed, in one dimension (1D), several many-body models such as the Gaudin-Yang model [67, 68] and the Hubbard model [69] may be solved exactly via the Bethe Ansatz (BA) [70, 71].

Besides providing a first test ground for numerical methods, as will be explored in the second part of this thesis, the 1D world is in fact the stage of vastly different physics compared to our natural three-dimensional (3D) habitat [72, 73]. This originates from the special influence of interactions in 1D: when a particle moves along the line, it necessarily has to impact its neighbors since there is nowhere else to go. Therefore, all movement in a 1D geometry is collective. This has profound consequences and leads to the breakdown of Fermi liquid theory. Instead, the low-energy properties of 1D systems are described by what is known as a Luttinger liquid [74, 75].[6]

As an example of the somewhat counterintuitive situation, let us consider the density of states for a single fermion species:

$$\rho^{(1D)}(\varepsilon) = \frac{1}{\pi}\sqrt{\frac{2m}{\varepsilon}}. \tag{1.4.1}$$

This is in contrast to the 3D version in Eq. (1.3.2), which grows with $\sqrt{\varepsilon}$. As a consequence, the ratio of the interaction energy to kinetic energy scales as $\propto n^{-1}$ which implies that the system is actually less interacting at higher densities. Loosely speaking, this may be compared to a traffic

jam: The reduced dimensionality forbids the particles to move past each other such that at large densities not much movement is possible at all.

These days, the simplified world of 1D is not only of theoretical interest as experiments with ultracold atoms actually provide a way to prepare such setups [71]. One way to effectively reduce the dimensionality is achieved via highly anisotropic trapping potentials which take the generic form

$$V_{\text{trap}} = \frac{m}{2} \left(\omega_x^2 x^2 + \omega_y^2 y^2 + \omega_z^2 z^2 \right). \tag{1.4.2}$$

By choosing the frequencies such that $\omega_x \ll \omega_y, \omega_z$ the trap is very steep in the transverse y- and z-directions compared to the longitudinal x-direction and the system effectively turns into a 1D tube. Through the large energy spacing of the harmonic oscillator levels in the transverse directions, the particles will be in the lowest energy state $(n_y, n_z) = (0, 0)$ if the aspect ratio is large enough. As the associated wavefunction is strongly peaked in the center of the transverse directions, this effectively confines the movement of particles to the x-direction whereas the y and z coordinates are "frozen" to the zero-point motion. Other options of preparing low-dimensional quantum gases include optical lattices with strongly anisotropic hopping [76] and atom chips [77].

1.5 Outline

This thesis is structured in two main parts: a technical discussion of the many-body framework and the presentation of numerical results for strongly interacting Fermi gases.

The first part introduces, the applied numerical approach in detail, starting from the Hamiltonian and its treatment on the lattice. In Chapter 2, a suitable path-integral representation based on an auxiliary-field decomposition, which is amenable to stochastic sampling, is developed. Subsequently, elements of Monte Carlo simulations are presented in Chapter 3, with some emphasis on the treatment of Markov chains. Chapter 4 constitutes the central piece of our many-body discussion and contains an in-depth derivation of the two global update algorithms applied in this work, namely the hybrid Monte Carlo and complex Langevin methods. The former is based on the Metropolis algorithm and consequently suffers from a sign problem for imbalanced systems. It is shown that the issue may be mitigated for mass-imbalanced systems by introducing an imaginary asymmetry. The second approach is an extension of the concept of stochastic quantization to complex fields which potentially allows us to circumvent unfavorable scaling due to the sign problem. The possible shortcomings arising with such a treatment are discussed in detail, along with practical remarks relevant for a stable implementation.

The second part builds on these advances and presents results for imbalanced Fermi gases. In Chapter 5, a detailed study of one-dimensional Fermi gases is shown ranging from balanced few-body systems to spin- and mass-imbalanced many-body systems. The numerical behavior of the developed methods in the presence of imbalances is analyzed and results are compared to benchmark data wherever available.

Finally, an extensive study of the thermodynamics of the spin-polarized UFG is presented in Chapter 6. The investigation involves a treatment of numerical artifacts as well as an exhaustive benchmark for the balanced UFG, for which numerous calculations exist in the literature. General conclusions are presented in Chapter 7 along with an outlook regarding technical improvements as well as interesting physical systems that could be attacked with the presented developments.

Details of derivations in the main text are presented only where necessary and additional steps are summarized in Apppendix A. Moreover, a practical overview on error estimation is given in Apppendix B and useful relations for noninteracting Fermi gases, the virial expansion and the derivation of some thermodynamic relations are summarized in the Appendices C to E, respectively. Finally, a hands-on example introducing the Python package `gMacs` which was developed as a part of this thesis, is presented in Apppendix F.

The compilation of this thesis was done solely by the author. Most results have been published or are available as preprints under the following references:

[78]   *Evolution from few- to many-body physics in one-dimensional Fermi systems: One- and two-body density matrices and particle-partition entanglement*
Lukas Rammelmüller, William J. Porter, Jens Braun, and Joaquín E. Drut
Published in Phys. Rev. A **96**, 033635 (2017)

[79]   *Surmounting the sign problem in nonrelativistic calculations: A case study with mass-imbalanced fermions*
Lukas Rammelmüller, William J. Porter, Joaquín E. Drut and Jens Braun
Published in Phys. Rev. D **96**, 094506 (2017)

[80]   *A complex Langevin approach to ultracold fermions*
Lukas Rammelmüller, Joaquín E. Drut, and Jens Braun
Published in J. Phys. Conf. Ser. **1041**, 012006 (2018)

[81]   *Finite-Temperature Equation of State of Polarized Fermions at Unitarity*
Lukas Rammelmüller, Andrew C. Loheac, Joaquín E. Drut, and Jens Braun
Published in Phys. Rev. Lett. **121**, 173001 (2018)

[82]   *Complex Langevin and other approaches to the sign problem in quantum many-body physics*
Casey E. Berger, Lukas Rammelmüller, Andrew C. Loheac, Florian Ehmann, Jens Braun, and Joaquín E. Drut
Preprint in arXiv:1907.10183 (2019)

Parts of the text which are taken from these articles are not marked explicitly but mainly incorporated as follows: The discussion of the methodological framework in Sections 4.4 and 4.5 is based on the review article [82]. The discussion of balanced few-body systems in Section 5.2 is in large parts taken from [78]. The subsequent presentation of mass-imbalanced 1D Fermi gases in Section 5.3 originates from [79] and [80]. Finally, results and parts of the text of [81] have been used in the discussion of the UFG in Chapter 6.

Part I

From statistical mechanics to complex Langevin

2 | Nonrelativistic fermions, the lattice & auxiliary fields

Having introduced the phenomenology of the physics concerning this work, we now lay out the framework which allows us to study strongly interacting Fermi gases. The goal of this chapter is to arrive at a representation amenable to a numerical treatment, starting from the Hamiltonian of our system of interest. Along the way, we introduce the field-theoretical tools and subsequently present a lattice formulation of the problem. While the spatial lattice occurs naturally in a condensed-matter setting, in this work we primarily consider it a mathematical tool to represent the underlying field theory. This strategy was originally proposed by Wilson to study the confinement problem in quantum chromodynamics (QCD) [83] and is at the heart of so-called lattice gauge theories [84]. The tremendous success of lattice methods to address nonperturbative effects in high-energy physics has motivated applications in the context of nonrelativistic systems such as effective theories for nuclear physics [85] and ultracold quantum gases [86].

Another central part of our numerical methods are so-called auxiliary-field transformations, which reduce two-body operators to one-body terms coupled to an auxiliary field. Eventually this procedure leads to a path-integral representation of the partition sum, allowing us to numerically investigate thermodynamics of our desired system. The main benefit of such an approach is its versatility, as it can be formulated for a broad range of Hamiltonians. Moreover, these methods may be employed not only at finite temperature but can be adapted to zero-temperature via a projection to the ground state, as shown below.

2.1 From the Hamiltonian to the path integral

The system we consider in this work is the two-component Fermi gas with short-ranged interaction between the species. From the discussion in the previous section it is evident that the interaction may be modeled by a δ-potential, such that the corresponding Hamiltonian in arbitrary dimension d reads

$$\hat{H} = \int_{\mathbb{R}^d} \mathrm{d}^d x \left\{ \sum_\sigma \hat{\psi}_\sigma^\dagger(\vec{x}) \left(-\frac{\hbar^2}{2m_\sigma} \vec{\nabla}^2 \right) \hat{\psi}_\sigma(\vec{x}) + g\, \hat{\psi}_\uparrow^\dagger(\vec{x}) \hat{\psi}_\downarrow^\dagger(\vec{x}) \hat{\psi}_\downarrow(\vec{x}) \hat{\psi}_\uparrow(\vec{x}) \right\} \equiv \hat{H}_0 + \hat{H}_{\text{int}}. \quad (2.1.1)$$

Here, g is the bare interaction parameter related to the s-wave scattering length as discussed previously.[1] The sum in the kinetic term runs over all species and the operators $\hat{\psi}_\sigma^\dagger(\vec{x})$ and $\hat{\psi}_\sigma(\vec{x})$ create and annihilate fermions of type σ at position $\vec{x}$. These operators fulfill the standard anticommutation rules

$$\{\hat{\psi}_\sigma^\dagger(\vec{x}), \hat{\psi}_{\sigma'}^\dagger(\vec{x}')\} = \{\hat{\psi}_\sigma(\vec{x}), \hat{\psi}_{\sigma'}(\vec{x}')\} = 0, \tag{2.1.2a}$$

$$\{\hat{\psi}_\sigma^\dagger(\vec{x}), \hat{\psi}_{\sigma'}(\vec{x}')\} = \delta_{\sigma\sigma'}\, \delta^{(d)}(\vec{x} - \vec{x}'). \tag{2.1.2b}$$

From these relations it is obvious that the second term in Eq. (2.1.1) represents the δ-potential. From now on, the units are fixed to $\hbar = c = k_B = 1$ along with a dimensionless mass-parameter, leaving length-scales as our only unit of reference. Accordingly, energies and temperatures carry the units of L^{-2} and momenta are given in L^{-1}.

To study the thermodynamics, the central object of interest is the partition function which generically is written as

$$\mathcal{Z}(\beta) = \mathrm{Tr}\left[e^{-\beta\hat{H}}\right], \tag{2.1.3}$$

where $\beta = \frac{1}{T}$. For a noninteracting system, i.e. the ideal gas, the computation of this quantity amounts to evaluating Gaussian integrals and can be done analytically. In the case of interacting theories, however, the study of nonperturbative physics beyond the mean-field level poses a formidable challenge and advanced concepts, such as the numerical methods developed in this work, have to be employed.

The standard procedure to connect Eq. (2.1.3) to a field-theoretic description involves chopping β into small slices $\Delta\tau = \frac{\beta}{N_\beta}$ and inserting suitable factors of $\mathbb{1}$ in terms of fermionic coherent states (see, e.g., [87]). After formally performing the limit $N_\beta \to \infty$ we arrive at the fermionic path-integral

$$\mathcal{Z}(\beta) = \int [\mathcal{D}\bar{\eta}\mathcal{D}\eta]\, e^{-S_F[\eta,\bar{\eta}]}, \tag{2.1.4}$$

where $\eta^T = (\eta_\uparrow, \eta_\downarrow)$ represents a Grassmann field for two spin species and the action is given by

$$S_F[\eta, \bar{\eta}] = \int_0^\beta d\tau \int_{\mathbb{R}^d} d^d x\, \eta^\dagger \partial_\tau \eta + H(\eta, \eta^\dagger) \tag{2.1.5a}$$

$$= \int_0^\beta d\tau \int_{\mathbb{R}^d} d^d x\, \eta^\dagger \left(\partial_\tau - \frac{\nabla^2}{2m}\right)\eta + g\bar{\eta}_\uparrow \eta_\uparrow \bar{\eta}_\downarrow \eta_\downarrow \tag{2.1.5b}$$

with a normal-ordered Hamiltonian H expressed with the Grassmann fields η and $\eta^\dagger$. The integration over τ must satisfy antiperiodic boundary conditions $\eta(\vec{x}, 0) = -\eta(\vec{x}, \beta)$ which follows from the Pauli principle. Through this procedure, the path integral in Eq. (2.1.4) naturally arises in the Euclidean formulation, where we can interpret the inverse temperature β as the imaginary-time axis of a $d + 1$ dimensional Euclidean field theory.

The partition function holds all information, once we know it as a function of a given parameter.

---

[1]Note that the exact relation between the scattering length and g as well as its dimension is highly dependent on the spatial dimension. In two-dimensional problems, for instance, g is dimensionless leading to a scale anomaly that does not occur in one- or three-dimensional systems.

$$\hat{T}(\tau, \tau - 1) \qquad\qquad \prod_{\tau=\theta}^{\theta'} \hat{T}(\tau, \tau - 1) = \hat{T}(\theta', \theta)$$

$$\beta \qquad\qquad \rightarrow \Delta\tau \leftarrow \qquad\qquad 0$$
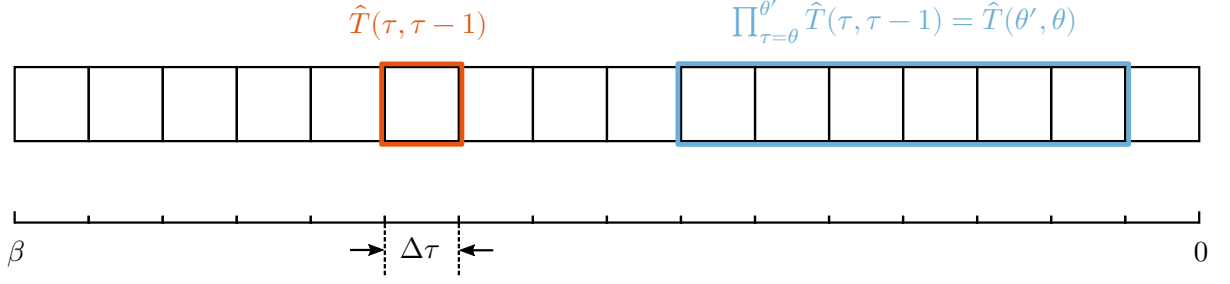
Figure 2.1: Visualization of the imaginary-time discretization. Single blocks represent the transfer matrix $\hat{T}$ which can be viewed as the propagator for a single time step. Products of N blocks, according to Eq. (2.2.1) represent imaginary-time evolutions from θ to $\theta' = \theta + N\Delta\tau$.

To learn about specific observables, we need to compute expressions of the form

$$\langle \hat{O} \rangle = \frac{\text{Tr}\left[\hat{O}e^{-\beta\hat{H}}\right]}{\text{Tr}\left[e^{-\beta\hat{H}}\right]}. \tag{2.1.6}$$

Within the framework of quantum field theory, this is typically achieved by introducing source terms into the partition sum

$$\mathcal{Z}(\beta, J, \bar{J}) \equiv \int [\mathcal{D}\bar{\eta}\mathcal{D}\eta] \ e^{-S_{\text{F}}[\eta,\bar{\eta}] + \int d^d x \ \bar{J}(\vec{x})\eta(\vec{x}) + \bar{\eta}(\vec{x})J(\vec{x})} \tag{2.1.7}$$

so that we end up with the generating functional $\mathcal{Z}(\beta, J, \bar{J})$. We may take corresponding derivatives of arbitrary order

$$\langle \eta(\vec{x}_1) \dots \eta(\vec{x}_n) \rangle = \frac{1}{\mathcal{Z}} \frac{\delta^n \mathcal{Z}(\beta, J, \bar{J})}{\delta \bar{J}(\vec{x}_1) \dots \delta \bar{J}(\vec{x}_n)} \bigg|_{J=\bar{J}=0} = \frac{\int [\mathcal{D}\bar{\eta}\mathcal{D}\eta] \ \eta(\vec{x}_1) \dots \eta(\vec{x}_n) \ e^{-S_{\text{F}}[\eta,\bar{\eta}]}}{\int [\mathcal{D}\bar{\eta}\mathcal{D}\eta] \ e^{-S_{\text{F}}[\eta,\bar{\eta}]}} \tag{2.1.8}$$

allowing us, to obtain n-point functions of any desired order.

2.2 Transfer matrix & time discretization

Although it is natural to describe fermionic theories in terms of the Grassmann path integral, this description is not ideal in the context of numerical calculations. Loosely speaking, this is due to the simple fact that we cannot just take statistical averages of products of Grassmann numbers as they lack actual numerical values. For practical purposes, it is thus more convenient to reformulate Eq. (2.1.3) in terms of transfer matrices in the Hamiltonian picture. We keep the time discretization introduced above and write

$$\mathcal{Z} = \text{Tr}\left[\prod_{\tau=1}^{N_\beta} e^{-\Delta\tau\hat{H}}\right] \equiv \text{Tr}\left[\hat{T}^{N_\beta}\right], \tag{2.2.1}$$

where we call $\hat{T}$ the normal-ordered transfer matrix for a single time slice. A product of transfer matrices is itself a propagator over multiple time slices, as visualized in Fig. 2.1.

In the limit of $\Delta\tau \to 0$ we then recover Eq. (2.1.3). Furthermore, it is straightforward to implement an arbitrary number of Lagrange multipliers such as the chemical potential for the grand canonical ensemble:

$$\hat{T}(\mu_\uparrow, \mu_\downarrow) = \hat{T} \, e^{-\beta(\mu_\uparrow \hat{N}_\uparrow + \mu_\downarrow \hat{N}_\downarrow)}. \tag{2.2.2}$$

For the further (formal) development of the method it does not matter whether we explicitly write down these terms since they can be absorbed into the one-body part of the Hamiltonian.

From a computational standpoint we have not profited as of yet - we still need to diagonalize an interacting Hamiltonian which is a very costly task. The small time step $\Delta\tau$, however, allows for a controlled approximation that splits the exponentials of the generally noncommuting parts $\hat{H}_0$ and $\hat{H}_{\mathrm{int}}$ at the expense of a discretization error:

$$e^{-\Delta\tau(\hat{H}_0 + \hat{H}_{\mathrm{int}})} = e^{-\frac{\Delta\tau}{2}\hat{H}_0} e^{-\Delta\tau \hat{H}_{\mathrm{int}}} e^{-\frac{\Delta\tau}{2}\hat{H}_0} + \mathcal{O}(\Delta\tau^3). \tag{2.2.3}$$

This procedure is called the Trotter-Suzuki decomposition [88]. It is worth noting that there exist several versions of such a discretization, also including formulations taking into account higher-order terms in the time step. The symmetric third-order decomposition in Eq. (2.2.3) reflects the standard-choice for auxiliary-field methods due to the positive coefficients which implies an absence of a sign problem.

2.3   The lattice

Before treating the transfer matrix introduced in the previous section, we introduce a central piece of the numerical methods of this work: the spatial lattice. We start by again considering Eq. (2.1.4) which defines a field theory with an infinite number of degrees of freedom labeled by the continuous variables $\vec{x}$ and β. The procedure to obtain this expression involves chopping the temporal direction into small segments and then performing the limit to infinitesimally small discretization. In order to obtain a finite number of degrees of freedom, we refrain from taking this limit, which corresponds to a discrete temporal direction.[2] A similar step can be done for the spatial coordinate, where the fields $\psi(\vec{x})$ are defined to live only on integer multiples of the lattice spacing a. This allows us to write the model in discretized form:

$$\hat{H} = \sum_i \left\{ \sum_\sigma \sum_j \hat{\psi}^\dagger_{\sigma i} \left(-\frac{\Delta_{ij}}{2m_\sigma} \right) \hat{\psi}_{\sigma j} + g \hat{\psi}^\dagger_{\uparrow i} \hat{\psi}^\dagger_{\downarrow i} \hat{\psi}_{\downarrow i} \hat{\psi}_{\uparrow i} \right\}, \tag{2.3.1}$$

where the index i denotes the lattice coordinates $(x_1 = n_1 \vec{1}, \ldots, x_d = n_d \vec{d})$ and Δ_{ij} is the second order difference matrix summed over all spatial directions:

$$\Delta_{ij} = \frac{1}{a^2} \sum_{k=1}^{d} \left\{ \delta_{i+\vec{k},j} + \delta_{i-\vec{k},j} - 2\delta_{i,j} \right\}. \tag{2.3.2}$$

---

[2]In fact, the continuous formulation for Grassmann fields is purely symbolic as there is no numerical value associated with then and hence no notion of $\frac{\psi(x+\Delta\tau)-\psi(x)}{\Delta\tau}$ being a small quantity for arbitrarily small $\Delta\tau$.

The discretization of space is not unique and variants such as the honeycomb lattice or the Kagome lattice are frequently used in condensed-matter studies[3] and even random lattices have been used in the context of lattice-QCD. For this work we stick to equally spaced lattices in d dimensions leading to the spacetime volume of $N_x^d \times N_\beta$ lattice sites and a coordination number of $2d$. Furthermore, we fix the lattice spacing to $a = 1$ so that the temporal step $\Delta\tau$ sets the lattice units.

Naturally this procedure is very convenient for numerical investigations as it would be impossible to treat an infinite number of degrees of freedom on a (classical) computer. However, the discretization of space has subtle consequences and, strictly speaking, means that we are dealing with a different theory. In order to obtain the properties of the continuum theory it is important to relate the couplings of the continuum field theory to the lattice version. For low-energy scattering properties this can be done by using Lüscher's formula [89, 90] which relates the interaction parameter g with the s-wave scattering length. The central question then is whether a sequence of lattice theories with increasingly finer lattice spacing a and properly renormalized physical couplings approaches the correct continuum limit.

2.3.1 Momentum space cutoffs

The effect of a spatial lattice can be made clear by considering the Fourier transform of a function f defined on the lattice sites na, with n being integer:

$$f(na) = \int_{-\infty}^{\infty} \mathrm{d}k \; \tilde{f}(k)\mathrm{e}^{ikna} = \int_{-\frac{\pi}{a}}^{\frac{\pi}{a}} \mathrm{d}k \; \tilde{f}_a(k)\mathrm{e}^{ikna}. \tag{2.3.3}$$

Thus, the consequence of a discretized spatial coordinate is a periodic (but continuous) momentum space commonly referred to as the first Brillouin zone (BZ). Effectively this introduces an ultraviolet (UV) cutoff associated with the minimal length scale a and therefore makes the lattice theory UV-finite. Going through a sequence of lattice spacings then corresponds to studying the cutoff dependence of the regularized theory.

In practical applications, the number of lattice sites needs to be restricted to a finite number, i.e. we have to consider finite system sizes. Consequently, the momentum space will not only be periodic but also discrete, leading to a dual lattice related through a discrete Fourier transform (DFT).[4] This so-called infrared (IR) cutoff leads to a minimally accessible momentum scale and thus to potential issues once we are interested in low-energy physics. These problems become especially severe near phase transitions, as critical phenomena cause long correlation lengths and ultimately are challenging to resolve because of the finite system size.

It should be mentioned that the choice of the lattice model that eventually leads to the correct continuum version is not unique. This opens the possibility to devise so-called improved actions with the objective to optimizing the numerical methods for faster convergence towards the continuum limit [91–95]. However, improved actions are not considered in this work.

---

[3]The usage of specialized lattice geometries is motivated by the crystalline structure of certain alloys and minerals or synthetic materials such as graphene.

[4]The discretized momentum space can also be understood by simply reversing the above argument: through a discrete real space we obtain a bounded momentum space. Here, we obtain a discrete momentum space through a bounded spatial extent.

2.3.2 Dispersion relations on the lattice

Along the lines of improved actions (but by far not as sophisticated), we may choose from a set of available dispersion relations to reduce the systematic effect of the discretization. The form in Eq. (2.3.2) leads to a tight-binding dispersion relation

$$\hat{H}_0 = \sum_\sigma \sum_k \hat{\psi}_{\sigma k}^\dagger \hat{\psi}_{\sigma k}(1 - 2t_\sigma \cos k), \tag{2.3.4}$$

which corresponds to the hopping term in the Hubbard model with hopping parameter $t_\sigma \sim m_\sigma^{-1}$ and is the standard choice for condensed-matter studies. Alternatively, we may choose an "exact" dispersion relation in momentum space that reproduces the correct continuum energy spectrum up to arbitrary momenta

$$\hat{H}_0 = \sum_\sigma \sum_k \hat{\psi}_{\sigma k}^\dagger \hat{\psi}_{\sigma k} \frac{k^2}{2m_\sigma} \tag{2.3.5a}$$

$$\equiv \sum_\sigma \sum_k \hat{\psi}_{\sigma k}^\dagger \hat{\psi}_{\sigma k} \varepsilon_{\sigma k}. \tag{2.3.5b}$$

Here, $\varepsilon_{\sigma k}$ denotes the single-particle energy. This expression is as close as possible to the thermodynamic limit and thus introduces the least amount of systematic errors. As we are interested in continuum physics we shall use this form for our further investigations.

2.3.3 Discretization effects for Fermi gases

As it was mentioned above, the IR cutoff becomes problematic for low-energy physics, i.e. at low temperatures or near phase transitions. For Fermi gases, the behavior can be explained by considering the occupation probabilities in terms of the Fermi-Dirac distribution. Since the mean energy is proportional to the temperature, higher energy states are more likely to be occupied in the high temperature regime. This is where a lot of states are available on the lattice due to the (quasi-)degeneracy of different directions[5] and the vanishing separation between energy states. At low temperatures, on the other hand, the probability of low-lying states to be occupied is strongly enhanced. Since these low-momentum states are distributed much more sparsely we face resolution issues as the temperature decreases, i.e. we cannot resolve Fermi surface physics such as Cooper pairing sufficiently well if the spatial system size is too small. To illustrate this behavior, the Fermi-Dirac distributions on a 3D lattice are shown in Fig. 2.2 for various (β, N_x) configurations. As β increases (i.e. the temperature decreases), the Fermi surface becomes more pronounced and larger lattices are required to resolve it.

2.4 Auxiliary-field transformations

Having introduced a finite set of degrees of freedom, we are now in a position to address the transfer matrix defined in Eq. (2.2.1). The Trotter decomposition separates the kinetic and the interaction parts of our Hamiltonian, and while the former are straightforward to treat we have to apply more effort to deal with the latter. The strategy is to decouple the interaction so that we end up with a linear occurrence of one-body operators coupled to some external

---

[5]For instance, the $(k_x, k_y, k_z) = (1, 0, 0)$ and $(0, 1, 0)$ in a 3D lattice are energetically equivalent.
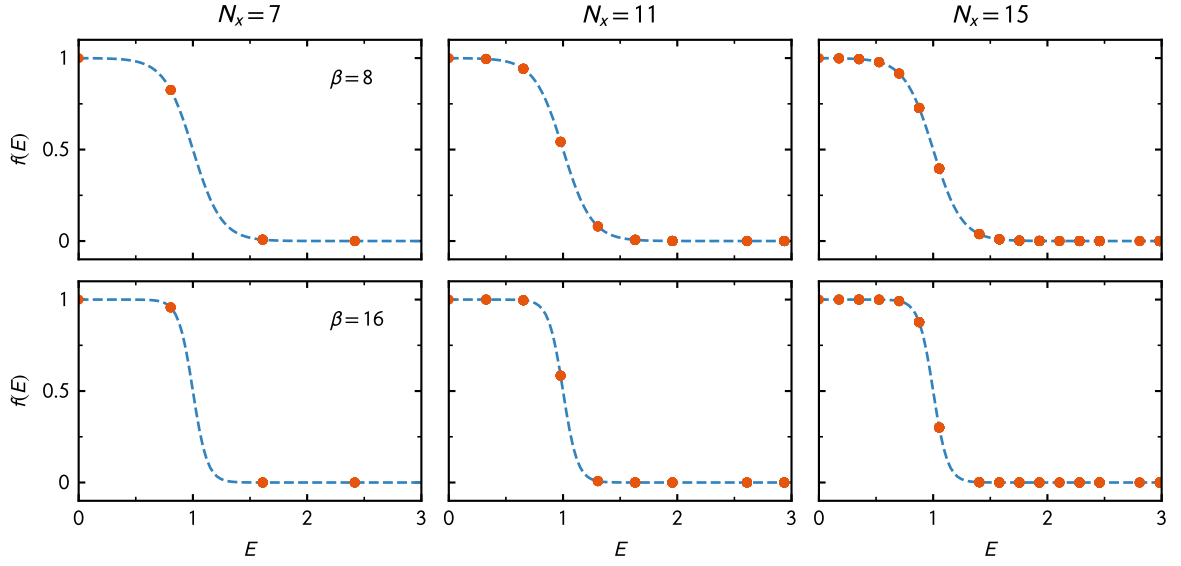
Figure 2.2: Sketch of the available energy states (red dots) for various spatial lattice sizes N_x and inverse temperatures β. The corresponding Fermi function $f(E)$ in the continuum is shown as dashed blue line and the chemical potential is set to $\mu = 1$ (in arbitrary units).

field, rather than a quadratic occurrence. This is achieved via a so-called auxiliary-field or Hubbard-Stratonovich (HS) transformation which originally was proposed by inserting a suitable factor of $\mathbb{1}$ and subsequently performing a Gaussian integral through an appropriate coordinate shift [96, 97]. For a single spacetime lattice point the standard form reads

$$e^{-a\hat{\rho}^2} = \sqrt{\frac{1}{\pi a}} \int_{-\infty}^{\infty} d\phi \; e^{-\frac{1}{4a}\phi^2 - i\hat{\rho}\phi}. \tag{2.4.1}$$

Here, $\hat{\rho}$ represents a fermionic density operator and ϕ is the bosonic auxiliary field. For practical purposes the form in Eq. (2.4.1) is not well suited. Conveniently, due to the anticommuting nature of the fermionic operators, there are many different auxiliary-field transformations available, suitable for different physical systems and/or algorithms (see, e.g., [86, 98]). For condensed-matter lattice systems, for example, discrete decompositions are often the variant of choice [99]. For the purpose of this work, however, it is necessary to use a continuous decomposition, since only then can we exploit the numerical methods introduced in the later chapters of this thesis. Additionally, it is convenient to use a bounded version of the auxiliary-field transformation [98], since then we do not necessarily have to deal with stabilization issues stemming from a separation of scales (see, e.g., [100, 101]).[6] The form we will use may be written as

$$e^{-g\Delta\tau\hat{\rho}_\uparrow\hat{\rho}_\downarrow} = \int_{-\pi}^{\pi} \frac{d\phi}{2\pi} \; [1 + \hat{\rho}_\uparrow A\sin\phi] \; [1 + \hat{\rho}_\downarrow A\sin\phi] \tag{2.4.2a}$$

$$\equiv \int_{-\pi}^{\pi} \frac{d\phi}{2\pi} \; \hat{V}_\uparrow(\phi)\hat{V}_\downarrow(\phi), \tag{2.4.2b}$$

---

[6]For large values of β, the scale separation might still be problematic. A careful investigation could increase the range of accessible β values.

where $\hat{\rho}_\sigma = \hat{\psi}_\sigma^\dagger \hat{\psi}_\sigma$ denotes the fermionic density operator and $A = \sqrt{2(\mathrm{e}^{-g\Delta\tau} - 1)}$. Details of the derivation of Eq. (2.4.2a) can be found in Apppendix A.1. For our further discussion of the auxiliary-field method, the exact form of the transformation is not essential, as suggested by the second line that defines the single-body operators $\hat{V}_\sigma(\phi)$.

We may now perform such a decoupling of the interaction at every point of our spacetime lattice. Note that since the decomposition is independent for every spacetime coordinate, the auxiliary field has a degree of freedom per spacetime lattice site which we denote by the index $\phi_{i\tau}$. Therefore, we have to change Eq. (2.2.1) such that it reads

$$\mathcal{Z} = \mathrm{Tr}\left[\prod_{\tau=1}^{N_\beta} \hat{T}(\tau, \tau - 1)\right], \tag{2.4.3}$$

where we have introduced the τ-dependent transfer matrix:

$$\hat{T}(\tau, \tau - 1) = \mathrm{e}^{-\frac{\Delta\tau}{2}\sum_\sigma \sum_k \hat{\rho}_{\sigma k}\varepsilon_{\sigma k}}\left[\prod_i \int_{-\pi}^{\pi} \frac{\mathrm{d}\phi_{i\tau}}{2\pi}\, \hat{V}_\uparrow(\phi_{i\tau})\hat{V}_\downarrow(\phi_{i\tau})\right]\mathrm{e}^{-\frac{\Delta\tau}{2}\sum_\sigma \sum_k \hat{\rho}_{\sigma k}\varepsilon_{\sigma k}} \tag{2.4.4a}$$

$$= \int_{-\pi}^{\pi} \prod_i \frac{\mathrm{d}\phi_{i\tau}}{2\pi} \bigotimes_\sigma \left\{ \mathrm{e}^{-\frac{\Delta\tau}{2}\sum_k \hat{\rho}_{\sigma k}\varepsilon_{\sigma k}}\left[\prod_i \hat{V}_\sigma(\phi_{i\tau})\right]\mathrm{e}^{-\frac{\Delta\tau}{2}\sum_k \hat{\rho}_{\sigma k}\varepsilon_{\sigma k}}\right\} \tag{2.4.4b}$$

$$\equiv \int_{-\pi}^{\pi} \prod_i \frac{\mathrm{d}\phi_{i\tau}}{2\pi} \bigotimes_\sigma \hat{B}_\sigma \hat{V}_\sigma(\phi_\tau)\hat{B}_\sigma\,. \tag{2.4.4c}$$

The tensor product over the spin-species arises through the decoupling of the interaction which causes the operators to act on different sub-spaces (one per spin-species). Furthermore, in the last line we have implicitly defined the operator $\hat{B}$ as a shorthand notation. Inserting the above expression into Eq. (2.4.3) yields

$$\mathcal{Z} = \int \mathcal{D}\phi\, \mathrm{Tr}\left[\prod_{\tau=1}^{N_\beta} \bigotimes_\sigma \hat{B}_\sigma \hat{V}_\sigma(\phi_\tau)\hat{B}_\sigma\right] \tag{2.4.5a}$$

$$\equiv \int \mathcal{D}\phi\, \mathrm{Tr}\left[\hat{T}_\phi(\beta, 0)\right], \tag{2.4.5b}$$

where the last equality defines the field-dependent propagator T_ϕ as the product of single step transfer matrices and we have introduced the path-integral measure

$$\mathcal{D}\phi \equiv \prod_{\tau=1}^{N_\beta} \prod_i \frac{\mathrm{d}\phi_{i\tau}}{2\pi}\,. \tag{2.4.6}$$

Since the product over all time slices is nothing but a string of one-body operators, we may perform the trace over the Fock space:

$$\mathrm{Tr}\left[\prod_{\tau=1}^{N_\beta} \bigotimes_\sigma \hat{B}_\sigma \hat{V}_\sigma(\phi_\tau)\hat{B}_\sigma\right] = \det\left[\mathbb{1} + \prod_{\tau=1}^{N_\beta} \bigotimes_\sigma B_\sigma V_\sigma(\phi_\tau)B_\sigma\right] \tag{2.4.7a}$$

$$= \prod_\sigma \det\left[\mathbb{1} + \prod_{\tau=1}^{N_\beta} B_\sigma V_\sigma(\phi_\tau)B_\sigma\right] \tag{2.4.7b}$$

$$\equiv \prod_\sigma \det M_\phi^\sigma, \tag{2.4.7c}$$

where the last line of the above expression defines the so-called Fermi matrix M_ϕ^σ. Note that while the trace on the left-hand side still contains field operators (as indicated by the hats) the determinant on the right-hand side is taken over some matrix representation of these operators.[7] A derivation of the first equality is given in Apppendix A.2. Finally, we arrive at the expression for the path integral

$$\mathcal{Z} = \int \mathcal{D}\phi \prod_\sigma \det M_\phi^\sigma \tag{2.4.8a}$$

$$\equiv \int \mathcal{D}\phi \; e^{-S[\phi]}. \tag{2.4.8b}$$

The action is given by

$$S[\phi] = -\sum_\sigma \ln \det M_\phi^\sigma. \tag{2.4.9}$$

We have achieved the goal set out for this section: to write down a path-integral representation of the partition sum that reflects our model of interest. Is is worth noting that an equivalent expression in terms of bosonic variables could as well have been derived in the Lagrangian picture starting from a discrete version of Eq. (2.1.4). In fact, such an approach is regularly employed (see, e.g., [102] and references therein) and ultimately the choice between the representations is a matter of convenience.

Such a bosonization procedure is very common in high-energy and condensed-matter physics and bears an analogy concerning the interaction: since the two species are decoupled, the auxiliary field ϕ mediates the interaction between the two fermion species and thus plays the role of an exchange boson in our lattice theory. Only the integration over all possible values of ϕ restores the original interaction between the fermions. Analogously, we may interpret this procedure as trading a highly complicated interacting problem for an infinite sum of noninteracting problems in a background field.

The final expression in Eq. (2.4.8) does not look particularly friendly at first glance - after all we would have to deal with a $N_x^d N_\beta$-dimensional integral over a continuous field ϕ. However, under certain conditions, these integrals are amenable to stochastic evaluation by means of Monte Carlo methods. We shall see this in the following chapter, where we introduce the basic concepts of stochastic integration as well as possible issues that arise with such a treatment.

The above derivation constitutes the basis of the so-called determinantal MC approach [103] and although we have derived the formalism with the specific Hamiltonian of Eq. (2.1.1) in mind, we could have done so for a large class of models. In fact, the approach is extremely versatile and routinely applied in such diverse areas as quantum chemistry, polymer physics, condensed-matter physics, high-energy physics and beyond.

Finally, it should be noted that the decoupling does not necessarily have to happen in the density channel but could also be done in the pairing channel. Although this leads to larger matrices, and thus to increased numerical effort, such an approach could lead to more stable results for

---

[7]This step is often referred to as "integrating out the fermions" since all that is left are bosonic degrees of freedom.

attractive systems, particularly in the vicinity of a superfluid phase transition. Moreover, the interaction does not necessarily have to be between two particles - for instance, auxiliary-field transformations for three-body contact interactions have been studied recently [104, 105].

2.5 Projective formulation

So far, the method has been implicitly assumed to describe systems at finite temperature as the imaginary-time direction naturally arises as the inverse temperature. Conveniently, the approach can be extended to study systems at zero temperature, i.e. in the ground state, by defining the partition function as the overlap of the ground-state (GS) wavefunction

$$\mathcal{Z} = \langle \psi_{\mathrm{GS}} | \psi_{\mathrm{GS}} \rangle. \tag{2.5.1}$$

The task is now to find $| \psi_{\mathrm{GS}} \rangle$ which can be achieved by a projective approach. We define our partition function as a function of the projection time β:

$$\mathcal{Z}(\beta) \equiv \langle \psi_{\mathrm{T}} | \hat{U}(\beta) | \psi_{\mathrm{T}} \rangle, \tag{2.5.2}$$

where $\hat{U}(\beta)$ is the imaginary-time evolution operator and $| \psi_{\mathrm{T}} \rangle$ represents a trial wavefunction that must have a nonzero overlap with the true ground state. In this case, it can be shown that

$$\lim_{\beta \to \infty} \mathcal{Z}(\beta) = \lim_{\beta \to \infty} \langle \psi_{\mathrm{T}} | \hat{U}(\beta) | \psi_{\mathrm{T}} \rangle = \langle \psi_{GS} | \psi_{GS} \rangle \tag{2.5.3}$$

and the rate of convergence will in general depend on the gap between the GS and excited states.[8] Now we can follow essentially the same procedure as above: discretize the imaginary-time direction and perform an auxiliary-field transformation in order to end up with a path-integral representation of the partition function in analogy to Eq. (2.4.8).

To find the transfer matrix for a given imaginary-time slice, we first introduce some single-particle basis consisting of the states labeled by the quantum number k_j:

$$| k \rangle = \hat{\psi}_{\uparrow k}^{\dagger} | 0 \rangle. \tag{2.5.4}$$

The standard choice for $| \psi_{\mathrm{T}} \rangle$ in Fermi systems is a Slater determinant (SD) composed of these single-particle states

$$| \psi_{\mathrm{T}} \rangle = \prod_{j=1}^{N_{\uparrow}} \hat{\psi}_{\uparrow k_j}^{\dagger} | 0 \rangle \; \otimes \; \prod_{j=1}^{N_{\downarrow}} \hat{\psi}_{\downarrow k_j}^{\dagger} | 0 \rangle \tag{2.5.5a}$$

$$= \prod_{j=1}^{N_{\uparrow}} \left[\hat{\psi}_{\uparrow}^{\dagger} S_{\uparrow} \right]_j | 0 \rangle \otimes \prod_{j=1}^{N_{\downarrow}} \left[\hat{\psi}_{\downarrow}^{\dagger} S_{\downarrow} \right]_j | 0 \rangle, \tag{2.5.5b}$$

where we have assumed a system with a fixed amount of particles N_{σ} per spin state, i.e. the canonical ensemble. The matrices S_{σ} uniquely represent the SDs in a given basis and are of the

---

[8]Of course, there will always be a nonzero gap in finite lattice systems. Nevertheless, for Hamiltonians that are gapless in the continuum (spin frustrated systems for example) the projection to the ground state is a challenging task since the gap imposed by the lattice will necessarily go to zero as the continuum limit is approached.

shape $N \times N_\sigma$. Here, N denotes the number of states in the basis (in our case the number of lattice sites). These SDs have a set of advantageous properties: if we act on an arbitrary SD with the exponential of a single-particle operator, we again obtain a SD (Thouless theorem [106]). Another nice property is the fact that the overlap between two SDs is just the determinant of the representing matrix product

$$\langle \psi' | \psi \rangle = \det [S'S] , \qquad (2.5.6)$$

where $| \psi' \rangle$ and $| \psi \rangle$ are two different SDs represented by S' and S, respectively [100].

We can immediately connect these properties to Eq. (2.4.5), which is just a long string of exponentiated single-particle operators. This allows us to write the time-propagation operator $\hat{U}_\phi^\sigma(\beta)$ at a given auxiliary-field configuration as the overlap of two SDs:

$$\langle \psi_\mathrm{T} | \hat{U}_\phi^\sigma(\beta) | \psi_\mathrm{T} \rangle = \det \left[M_\phi^\sigma(\beta) \right] \qquad (2.5.7)$$

where the matrix elements of the Fermi matrix are given by

$$\left[M_\phi^\sigma(\beta) \right]_{ab} = \langle b | \hat{U}_\phi^\sigma(\beta) | a \rangle . \qquad (2.5.8)$$

Finally, we again arrive at the path-integral representation of the ground-state partition function

$$\mathcal{Z} = \int \mathcal{D}\phi \, \prod_\sigma \det M_\phi^\sigma . \qquad (2.5.9)$$

Generally, we are free to choose any single-particle basis to represent the SD. The most convenient choice for the calculation of ground-state properties are momentum eigenstates. In this case the energetically lowest states will be filled up to the Fermi level (per spin species). Such a state will be a reasonably good guess at least in the weakly interacting regime as the SD is the ground state for the noninteracting Fermi gas. For strong interactions, the guess is still valid, however, more sophisticated wavefunctions may drastically improve the convergence properties as they might lie closer to the true ground state of the interacting system. An example that has been investigated is the choice of a BCS-type wavefunction as a trial state which was shown to be effective for strongly attractive systems [107–109].

2.6 Calculation of observables

The final part of this chapter is devoted to the computation of observables within the auxiliary-field framework. As a consequence of the decoupled interaction, the problem reduces to a large number of noninteracting one-body problems in a background field. This leads to the applicability of Wick's theorem and constitutes one of the major advantages of auxiliary-field methods: the possibility to construct arbitrary observables from the knowledge of the one-body density matrix at a given field ϕ. Technically, this means that all we have to do is find an expression for the quantity

$$\rho_{ij}^\sigma(\phi) = \langle \hat{\psi}_{\sigma i}^\dagger \hat{\psi}_{\sigma j} \rangle_\phi \qquad (2.6.1)$$

where the subscript ϕ denotes the evaluation at a given auxiliary field. Through contractions of the one-body correlation function it is now possible, in principle, to obtain correlation functions to arbitrary order. In practice, however, the maximum obtainable order will be limited by numerical constraints and essentially becomes a matter of statistics.

In order to obtain an expression for generic observables (including the one-body density matrix) we again introduce a source term coupled to the desired operator similar to Eq. (2.1.7). The source-dependent partition sum then reads

$$\mathcal{Z}[J] = \int \mathcal{D}\phi \int \mathcal{D}\phi \ \mathrm{Tr}\left[\hat{T}_\phi(\beta, \theta)\,\mathrm{e}^{J\hat{O}}\,\hat{T}_\phi(\theta, 0)\right], \tag{2.6.2}$$

where we have used the freedom to choose at which time slice we introduce the source term. Even an extension to time-dependent observables is possible and merely requires the introduction of multiple sources at different time slices. In this work, we will only consider equal-time observables and, without loss of generality, we set $\theta = 0$ unless noted otherwise.

For the evaluation of expectation values, we take the derivative with respect to J and evaluate it at vanishing source term:

$$\langle \hat{O} \rangle = \frac{1}{\mathcal{Z}} \frac{\partial \mathcal{Z}[J]}{\partial J}\bigg|_{J=0} \tag{2.6.3a}$$

$$= \frac{1}{\mathcal{Z}} \int \mathcal{D}\phi \ \det M_\phi \ \mathrm{Tr}\left[\hat{T}_\phi(\theta, 0)\,M_\phi^{-1}\hat{T}_\phi(\beta, \theta)\,O\right] \tag{2.6.3b}$$

$$\equiv \int \mathcal{D}\phi \ P[\phi]\,O[\phi]. \tag{2.6.3c}$$

A detailed derivation of this expression can be found in Apppendix A.3. The expression Eq. (2.6.3c) motivates a probabilistic interpretation with the normalized probability density

$$P[\phi] = \frac{1}{\mathcal{Z}} \det M_\phi \tag{2.6.4}$$

and thus we have expressed expectation values as a weighted integral over auxiliary-field configurations. This interpretation will be the central part in the subsequent chapters where we aim to evaluate these path integrals via stochastic methods.

3 | Stochastic sampling & the sign problem

> *"If you don't believe in random sampling, the next time you have a blood test, tell the doctor to take it all."*
>
> Arthur C. Nielsen

The purpose of this chapter is to briefly introduce the basics of stochastic integration, more commonly referred to as Monte Carlo (MC) methods. At the heart of these methods is the astonishing fact that it is possible to address physical questions by appropriately accumulating random numbers. The anecdotal origin dates back into the late 1940's when Stan Ulam, then working at Los Alamos National Lab, was recovering from surgery [110]. While playing cards, he was wondering what the chances would be to lay out a successful Canfield solitaire game consisting of 52 cards. After abandoning the idea to come up with a combinatorial answer, he resorted to the more practical idea to play a hundred games and estimate the probability by the percentage of successful games. It turns out, that the approach can be extended to a whole variety of problems. In fact the importance of MC related methods can hardly be overstated. Applications reach far beyond an academic setting and are commonly found in such diverse areas as engineering, economics and even life sciences.

In the following, we formalize these considerations and highlight key ingredients needed for efficient sampling strategies. Undisputedly, the most fundamental building block of modern Monte Carlo algorithms is the concept of Markov chains, which essentially describes a time-ordered sequence of random samples. A large class of methods are based on this strategy and are generically referred to as Markov Chain Monte Carlo (MCMC). While we leave the specific algorithms to construct such Markov chains for the subsequent chapter, we address some technical details as well as possible shortcomings that arise with such a treatment. Finally the so-called sign problem is discussed, particularly for the case of fermionic theories, along with a selection of methods to avoid this nagging issue.

3.1 Sampling path integrals

To connect Stan Ulam's card game to our problem at hand, we consider the path-integral representation of the partition function derived in the previous chapter. Typical spacetime lattice sizes of interest in this thesis are on the order of $d = 10^6$ sites. By using an integration grid of n points per degree of freedom, we would end up with a sum of n^{10^6} terms. Computing this sum is not only not feasible, but straight up impossible to achieve with any present or future digital
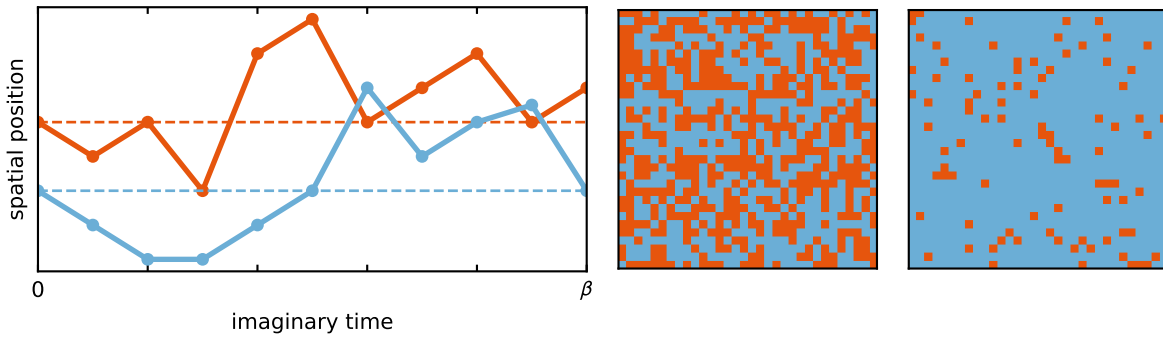
Figure 3.1: Examples for representations of configurations. (Left) Worldlines of a particle (in imaginary time) represented by a vector of N_τ entries for the positions at a given time. (Right) Snapshots of the 2D Ising model at high and low temperatures.

computer.[1] In fact, stochastic algorithms are already superior to deterministic methods at much lower dimensionality. As we shall see below, the error associated with these algorithms scales with $N^{-1/2}$ where N is the number of drawn random samples. Deterministic approaches, on the other hand, produce an error that behaves like $n^{-c/d}$, where c encodes the efficiency of a given algorithm. This fact, often called the curse of dimensionality, clearly shows that stochastic treatment will outperform deterministic methods already at relatively low dimensionality, regardless of the specific algorithm. It is therefore save to say that without random sampling techniques the numerical study of ultracold Fermi gases in *ab initio* fashion would be far beyond our possibilities. Having established that stochastic treatment is the way to proceed, it is instructive to write the path integral in Eq. (2.6.3c) as a finite sum over N randomly chosen field configurations weighted with their appropriate probability $P[\phi]$:

$$\langle \hat{O} \rangle \approx \frac{\sum_{\{\phi_i\}} P[\phi_i] \, O[\phi_i]}{\sum_{\{\phi_i\}} P[\phi_i]} \equiv \bar{O}. \tag{3.1.1}$$

In this thesis, a random sample (or random state) always refers to a snapshot of the auxiliary field ϕ. More generally, a sample can be anything that represents a term in the partition sum. Particularly visual examples include the two-dimensional Ising model, which is described as a square lattice with spin-up and -down values at every site, or the worldlines of particles moving in space. Both examples are depicted in Fig. 3.1. Furthermore, we note that the representation of samples for a given theory is by no means unique. Different algorithms will in general rely on different decompositions of the partition sum. In the context of auxiliary-field methods, for example, this could be done by using different Hubbard-Stratonovich transformations, as already remarked in the previous section.

Regardless of the exact nature of the samples, Eq. (3.1.1) clearly must be an approximation, since the true answer can only be obtained by collecting all possible configurations. Stated differently, $\bar{O} = \langle \hat{O} \rangle$ holds only in the limit of $N \to \infty$, which is impossible to reach in practice. Consequently, our estimate of the sample mean $\bar{O}$ will be different from the true expectation

---

[1]At the time of writing this thesis, the best computer in the TOP500 list was able to perform roughly 10^{25} FLOPS per year.

value of the observable $\langle \hat{O} \rangle$ by some error. This uncertainty is only of statistical nature and can be quantified by considering the variance of the mean,

$$\mathrm{Var}[\bar{O}] \equiv \sigma_{\bar{O}}^2 = \langle (\bar{O} - \langle O \rangle)^2 \rangle = \frac{1}{N} \mathrm{Var}[O], \tag{3.1.2}$$

which can be derived by invoking the central limit theorem (see, e.g., [111]). This is a major benefit of stochastic methods in general: not only do we get answers to the questions we asked, we also get a quality assessment of this answer in the form of an unbiased statistical uncertainty. Moreover, we can systematically improve this error by accumulating more samples, albeit at a rate that requires a hundred times more effort to gain another digit of precision. Note, however, that this uncertainty does not include systematic bias introduced, e.g., by the finite extent of the system under consideration.

To highlight a potential issue with this simple strategy, we may conduct the following thought experiment: say we have to stochastically integrate a strongly peaked function $f(x)$ in some finite interval $[a, b]$. According to the above procedure we would start by producing a set of evenly distributed x-values, evaluate the function at this point and finally average according to Eq. (3.1.1). Since the function is strongly peaked, however, we would "miss" with most of our random guesses, that is, we would sample in a region with no or little contribution to the total sum. This is a manifestation of the so-called overlap problem which causes a bad signal-to-noise ratio. Consequently, we will have to produce a large number of random samples to get results within reasonable accuracy.[2]

This issue would be mitigated if we were able to draw samples only from regions where $f(x)$ has decent support, i.e., only draw samples from regions that contribute significantly to the observable. In fact, the ideal case would be if our random samples were already be distributed according to the desired probability distribution - we would not have to worry about missing the distribution at all. In this case, Eq. (3.1.1) reduces to

$$\bar{O} = \frac{1}{N} \sum_{\{\phi_i\}} O[\phi_i]. \tag{3.1.3}$$

This strategy, referred to as importance sampling, reduces the variance of our estimated averages, and thus we obtain equally precise results at a cheaper numerical cost (i.e., with a lower amount of samples).

At first glance, this idea seems to merely be a neat optimization to save some computational effort. However, it becomes absolutely indispensable once we are interested in simulating quantum mechanical problems, where the space of configurations (i.e., the Hilbert space) grows exponentially with the system extent. Importance sampling ensures that we only consider a small, but representative, subspace of the vast configuration landscape. This allows us to obtain averages within a computational time that scales only polynomially with the system size (particle number, volume or inverse temperature) rather than exponentially.

While this strategy works in theory, there is a major potential bottleneck: for most problems of interest, the target probability density is either not known or it is exceedingly expensive to

---

[2]Equivalently, this can be considered as another manifestation of the dimensionality problem. We can conceptualized it as follows: consider two d dimensional spheres with radii $r_a = 0.99 r_b$. For very large d the ratio V_A / V_B is essentially zero and most of the weight lies close to the surface of the larger sphere. Uniform sampling in the d dimensional space will thus miss most of "the action".

compute. By examining Eq. (2.6.3c) we find that the partition sum appears in the denominator and we indeed face the issue of an unknown target density. The intuitive way to proceed would be to construct an algorithm that works with ratios of the target distribution rather than computing the full distribution. This allows for importance sampling in an efficient manner and, as we shall see in the following chapter, is the underlying idea of almost all state-of-the-art MC algorithms.

3.2 Markov chains

As established above, the quality of a stochastic calculation increases with the number of random samples. For precise measurements it is therefore of utmost importance to create a sufficient amount of configurations efficiently. From the previous discussion, it is evident that creating uniformly distributed samples from scratch at every iteration results in a bad signal-to-noise ratio as we will miss the important integration domain in most cases, particularly in a large number of dimensions.

An alternative approach is to take a configuration and introduce some change to it. For example, we can think of a spin-configuration for the Ising model on a finite lattice and simply flip a spin on a random site to produce a new configuration. Clearly, this is much cheaper than coming up with a new configuration altogether. Additionally, for many cases of interest it is possible to compute the weight of such a minimally changed sample with significantly reduced cost through some clever usage of linear algebra.[3] Repeated alteration of samples, referred to as updating, then leads to a time-ordered series of random states. If the process is memoryless, that is if the change to the next state only depends on the current one, we call the sequence Markov chain which represents a certain kind of discrete random process. So, by altering states, rather than inventing new ones from scratch every time, we ultimately perform a random walk in the space of configurations.

While the idea is conceptually intuitive, the main question still needs to be addressed: does such a procedure reproduce correctly distributed samples? Luckily, the concept of random processes and Markov chains reaches far beyond MC algorithms, and consequently we can draw from a vast literature on the topic. In the following, we merely lay out the basic properties that random processes have to fulfill in order to be useful for numerical calculations. For advanced treatment see, e.g., [113].

The above considerations are best formalized by considering the transition matrix $T_{\phi\phi'}$ whose elements are given by the probability to jump from the state ϕ to ϕ':

$$T_{\phi\phi'} \equiv P(\phi \rightarrow \phi').$$ (3.2.1)

To represent probabilities, the matrix has to obey $\sum_{\phi'} T_{\phi\phi'} = 1$ and $T_{\phi\phi'} \geq 0$. If we let the matrix act on some probability density $\pi[\phi]$ we obtain a "propagated" distribution function

$$\tilde{\pi}[\phi'] = \sum_{\phi} \pi[\phi]\, T_{\phi\phi'}$$ (3.2.2)

which represents one step in the discrete random process. Repeated application of the matrix moves through states along the Markov chain, and, by virtue of power iteration, factors out the

---

[3]If matrix inversion is involved in the weight calculation the paradigmatic example is the Sherman-Morrison formula [112].

dominant eigenstate

$$P[\phi] = \lim_{N \to \infty} \sum_{\{\phi_k\}} \pi[\phi_1] \, T_{\phi_1 \phi_2} \, \cdots \, T_{\phi_{N-1} \phi_N} \equiv \lim_{N \to \infty} T_{\phi_1 \phi_N}^{(N)} \tag{3.2.3}$$

It can be shown that $P[\phi]$ is indeed the desired target probability density if the following two important conditions are fulfilled:

(i) The process needs to be ergodic. This means it needs to be possible to reach every configuration in a finite sequence of steps. Formally this can be expressed by requiring that there exists a finite N such that

$$T_{\phi \phi'}^{(N)} \neq 0. \tag{3.2.4}$$

Stated differently, we need to formally be able to scan the full configuration space to obtain the correct expectation values.

(ii) The limit of Eq. (3.2.3) has to exist, i.e., the random process needs to arrive at some equilibrium distribution which is a left eigenstate of the transition matrix:

$$P[\phi'] = \sum_{\phi} P[\phi] \, T_{\phi \phi'}. \tag{3.2.5}$$

which makes it a stationary process. The condition is automatically fulfilled if the process obeys the stronger requirement of detailed balance:

$$P[\phi] \, T_{\phi \phi'} = P[\phi'] \, T_{\phi' \phi}. \tag{3.2.6}$$

Assuming that these conditions are fulfilled, we arrive at the practical protocol: we may start out with a random configuration, evolve it probabilistically according to the transition matrix and ultimately end up with a distribution that reflects the problem under investigation.[4] Generically, we may write for the next sample in the sequence

$$\phi^{(n+1)} = F[\phi^{(n)}] \tag{3.2.7}$$

where the subscript n corresponds to the "time" that has passed in the Markov process. The time average over these samples, after discarding N_{th} equilibration steps, then gives us the expectation value according to Eq. (3.1.3):

$$\bar{O} = \frac{1}{N - N_{\text{th}}} \sum_{i = N_{\text{th}}+1}^{N} O[\phi^{(i)}]. \tag{3.2.8}$$

While the above theoretical framework tells us *that* such a prescription works, it does not tell us *how* we can implement it. It turns out that there is quite some freedom to construct a valid

---

[4]Following the power-method argument, this implies that all but the dominant eigenvalues of $T_{\phi \phi'}$ have a magnitude smaller than unity. The gap to the next-to-leading eigenvalue then determines the rate of decay to the equilibrium distribution.

transition matrix. This has led to a large variety of MCMC methods specialized for specific problems. The details of the various algorithms relevant for this work are presented in Chapter 4.

3.2.1 Autocorrelation

The usage of Markov chains introduces the problem of correlation between subsequent samples. This causes two distinct phenomena which need to be addressed in order to trust the values that our simulation produces (see [114] for a comprehensive formal treatment).

First of all, we have to monitor the convergence to the equilibrium distribution. Since the stochastic process starts with an initial random configuration it is necessary to discard some samples at the beginning to avoid so-called initialization bias. By virtue of the conditions discussed above, convergence to the appropriate probability distribution is guaranteed. However, we do not know when this happens. The rate of convergence is determined by the so-called exponential autocorrelation time τ_{ext} which turns out to be very challenging to extract in practice [114].

Without knowledge of τ_{ext} the assessment of the number of steps to discard becomes nontrivial, and typically one resorts to a heuristic estimation. The rule of thumb in practical applications ranges from discarding 10% up to 50% of the samples but this is in general algorithm dependent. Moreover, we could face the issue of metastability, which means that we have hit a region in the configuration space that is hard to escape. This could lead to a serious underestimation of the equilibration time and thus wrong results due to a systematic bias. A way to address this issue is to check the consistency of the results amongst runs with different initial conditions as well as monitoring the running average of observables.

The second issue concerns the statistical independence of the samples for the error estimate. Since we only update an existing state by some small deviation it is unsurprising that two subsequent samples will not yield fundamentally different results. As a consequence, we may underestimate the error by simply using Eq. (3.1.2) which assumes statistically independent samples. To incorporate the effect of correlations we instead have to use

$$\sigma_{\bar{O}} = \sqrt{\mathrm{Var}[O]\,\frac{1 + 2\tau_{\mathrm{int}}}{N}}, \tag{3.2.9}$$

where τ_{int} denotes the so-called integrated autocorrelation time. It quantifies the number of samples that are to be discarded between two statistically independent measurements or, in other words, effectively reduces the number of independent samples.[5] It is important to differentiate between τ_{int} and the previously discussed exponential autocorrelation time: While the latter is a measure for the equilibration time, the former dictates the total runtime of our simulation. Clearly, the most efficient algorithms are the ones with the lowest autocorrelation and indeed τ_{int} is often used as a benchmark quantity to compare across algorithms.

A straightforward way to calculate τ_{int} is to use the convolution theorem to obtain the autocorrelation function and subsequently integrate over this function. However, this strategy can be cumbersome and plagued by a large amount of statistical noise which often leads to a wrong estimate of τ_{int}. Alternatively, unbiased error estimates may also be obtained with various other techniques such as binning [111], jackknife[115] and bootstrap [115]. A brief overview, as well as the derivation of Eq. (3.2.9), is given in Apppendix B.

---

[5]Simply stated, we cannot learn as much about the average from correlated samples as from uncorrelated ones - the integrated autocorrelation time quantifies that.
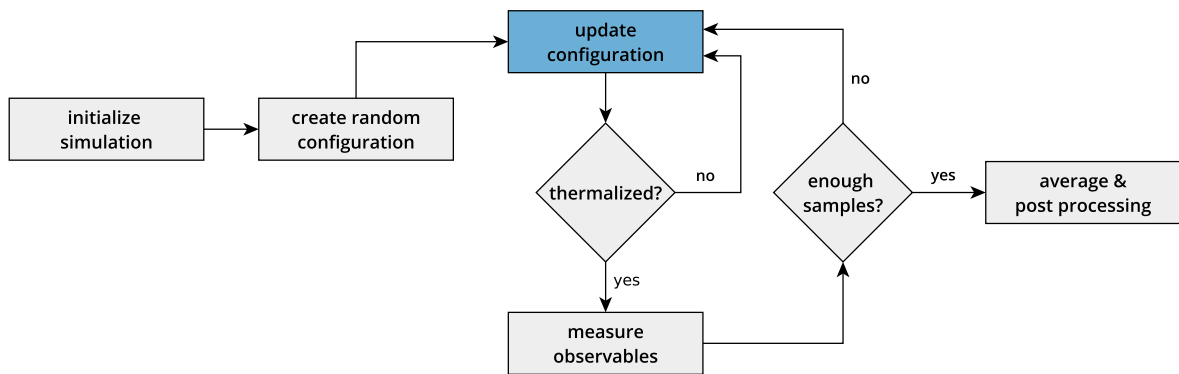
Figure 3.2: The flow diagram depicts a generic MCMC scheme. The specific algorithm only manifests itself in the blue box, where the update scheme needs to be implemented.

The autocorrelation time generally differs between observables and also depends on numerical as well as physical parameters. The latter dependence becomes particularly severe in the vicinity of phase transitions: since τ_{int} may be viewed as a susceptibility, it diverges with the power of some critical exponent when approaching the critical point. This phenomenon, referred to as critical slowing down, implies that MC calculations quickly become costly in critical regions as it becomes more expensive to produce decorrelated samples. The algorithms applied in this work, however, do not suffer from this issue due to the usage of global updates rather than local ones (e.g. a single spin flip). The exact nature of these updates are discussed in the following chapter.

3.2.2 Generic Markov chain sampling

The preceding sections lay out the general theoretical framework for MCMC simulations and already hint at the large variety of its applications. The general structure of an MCMC implementation in practice, however, very often follows the same simple recipe:

(1) Initialize the simulation. This could range from the setup of external libraries at runtime, just-in-time compilation to the calculation of pre-computed factors.

(2) Pick a random initial state ϕ. There are various options how this can be implemented: a "hot start" typically refers to an unordered random state, while a "cold start" refers to a symmetry broken configuration (e.g. all spins in the same direction in the Ising model example). Alternatively, one could start at a pre-thermalized configuration from a previous simulation.

(3) Update the configuration according to the update rules of the specific algorithm.

(4) If the equilibration time has passed (also referred to as thermalization): measure the observables. If not: go back to step 3.

(5) If enough samples have been accumulated: compute averages and perform other post processing steps (data export, cleanup, etc.). The criterion "enough samples" could be decided through various mechanisms: a fixed number of configurations, by some numerical tolerance of the results or merely a fixed amount of CPU time. If more samples are required: go back to step 3.

The procedure is summarized in Fig. 3.2. Evidently, almost all steps of any MCMC simulation are generic with the exception of the update strategy and the computation of the observables. The generic structure allows for the setup of a modular general purpose machinery with the obvious advantage of reducing overhead coding concerning topics such as data persistence, integration issues on HPC environments and other similar tasks. As a part of this thesis such a general and extendable package for heavy duty MCMC calculations was developed and successfully employed to obtain numerical results presented in the later chapters. The implementation is completely devoid from any knowledge of the specific algorithm but merely provides the "empty hull" of an actual MCMC simulation. The details of the algorithm are introduced by extending a generic sampler class and providing essentially the update scheme as class function. A brief description containing an overview of the `gMacs` (generic Markov chain sampling) package, written in Python3, may be found in Apppendix F.

3.3 The sign problem

As mentioned in the beginning, stochastic methods opened up the possibility to study otherwise intractable problems. Over time, many efficient algorithms based on the above considerations, have been devised in order to study a large variety of physical systems. All of these algorithms operate under the crucial assumption that the weight for a given configuration is positive semidefinite and thus may be interpreted as a probability distribution. While this is the case for the simulation of classical theories, where the weight is typically given by the Boltzmann factor $P[\phi] = e^{-\beta E[\phi]}$, the situation is not *a priori* clear in the quantum-mechanical case. Especially in theories containing fermions, the mapping to a classical sum of weights does not necessarily produce positive terms. For the systems concerning the present work, this becomes visible by reexamining Eq. (2.4.8): the determinant changes sign upon exchange of rows or columns, which corresponds to the exchange of two fermions. More generally, the situation arises whenever the theory is described by a complex action, thus leading to negative or even complex contributions to the path integral. This issue, referred to as the sign or phase problem, is one of the most fundamental problems in theoretical physics, as it hinders the exploration of strongly correlated systems dramatically.

3.3.1 Reiweighting

At a first glance, the problem does not seem unsolvable. A naive strategy to remedy a negative sign is simply to rewrite Eq. (3.1.1) in terms of the absolute value of the probability density, known as reweighting:

$$\langle O \rangle = \frac{\sum_\phi P[\phi]\, O[\phi]}{\sum_\phi P[\phi]} = \frac{\sum_\phi e^{i\theta[\phi]} |P[\phi]|\, O[\phi]}{\sum_\phi e^{i\theta[\phi]} |P[\phi]|} \tag{3.3.1a}$$

$$= \frac{\sum_\phi e^{i\theta[\phi]} |P[\phi]|\, O[\phi]}{\sum_\phi |P[\phi]|} \frac{\sum_\phi |P[\phi]|}{\sum_\phi e^{i\theta[\phi]} |P[\phi]|} = \frac{\langle e^{i\theta} O \rangle_{\text{pq}}}{\langle e^{i\theta} \rangle_{\text{pq}}}. \tag{3.3.1b}$$

The subscript "pq" denotes expectation values with respect to the phase-quenched theory, whereas expectation values without the subscript are obtained with the full probability distribution.

Although this procedure produces weights that are guaranteed to be nonnegative, the required computational effort scales exponentially with the system size. To illustrate this, we first recall that the partition function may be written in terms of the free energy

$$\mathcal{Z} = \mathrm{e}^{-\beta\mathcal{F}} = \mathrm{e}^{-\beta f V} \tag{3.3.2}$$

with the volume V and the (intensive) free energy density f. Writing the average phase factor as the ratio of the partition functions of the full and phase-quenched theories, respectively, then yields

$$Q \equiv \langle \mathrm{e}^{\mathrm{i}\theta}\rangle_{\mathrm{pq}} = \mathcal{Z}/\mathcal{Z}_{\mathrm{pq}} = \mathrm{e}^{-\beta\Delta f V}. \tag{3.3.3}$$

Since the phase-quenched partition function represents a sum of nonnegative terms, it follows that $Z_{\mathrm{pq}} > Z$ or, equivalently, $\Delta f > 0$.[6] This implies that with increasing system size the average phase vanishes exponentially. Analogously, $\langle \mathrm{e}^{\mathrm{i}\theta}O\rangle_{\mathrm{pq}}$ can be shown to vanish exponentially, leaving $\langle O\rangle$ as the ratio of two exponentially small quantities. The evaluation of such a ratio is in general a challenging mission because of excessive statistical fluctuations. Considering the relative error

$$\frac{\sigma_Q}{Q} = \frac{\frac{1}{\sqrt{M}}\sqrt{\langle \mathrm{e}^{\mathrm{i}\theta}\rangle_{\mathrm{pq}}^2 - \langle(\mathrm{e}^{\mathrm{i}\theta})^2\rangle_{\mathrm{pq}}}}{\langle \mathrm{e}^{\mathrm{i}\theta}\rangle_{\mathrm{pq}}} \sim \frac{\mathrm{e}^{\beta V \Delta f}}{\sqrt{M}} \tag{3.3.4}$$

reveals the exponential growth of the uncertainty with system size and inverse temperature as a consequence of these large cancellations. Stated differently, this means that with increasing system size we need to exponentially increase the amount of random samples in order to compute the expectation value at a target precision.

Clearly, reweighting is not an efficient way to circumvent the exponential growth of the Hilbert space in quantum mechanical simulations - after all, we might as well fully diagonalize the problem, which shows similar scaling. Another naive approach, namely to simply ignore the sign of each configuration, was shown to be an uncontrolled approximation that can lead to wrong physical conclusions [116].

It turns out that there is no general prescription to deal with this issue and, even worse, it has been shown that the sign problem belongs to the complexity class NP-hard [2] (nondeterministic polynomial). A generic solution to the sign problem would imply a polynomial solution of all problems in the category NP. The fact that, despite intense investigation, it is still unknown if P = NP renders the chances of finding a general solution to the sign problem highly unlikely.

3.3.2 Tackling the sign problem - a brief overview

Although a general recipe for sign-free algorithms may forever be out of reach, many strategies have been found to surmount a sign problem in specific scenarios. This is based on the fact that the sign problem is not a fundamental property of a given problem and its badness often depends on the representation (see, e.g., [117]). Through smart resummations and usage of symmetries

---

[6]From Eq. (3.3.3) it is easy to falsely conclude that there exist complex partition functions, as the generally complex average phase-factor is given by the ratio of partition functions. However, this is only the case if the partition functions are evaluated partially, such as with stochastic sampling. For the full theory all the complex weights exactly cancel which leads to a real (and positive) average phase factor.

many solutions have been found for specific problems. Perhaps the most famous example is the repulsive Hubbard-model, which, for general densities, suffers from a severe sign problem. At half filling, however, particle-hole symmetry allows to rewrite the problem appropriately such that it can be simulated with conventional MC methods. For attractive fermionic systems relevant for this work, the requirement is slightly less restrictive: as long as we consider an even number of equally populated and otherwise identical spin species we may write for the weight

$$P[\phi] = \frac{1}{\mathcal{Z}} \left(\det M[\phi] \right)^{2n}, \tag{3.3.5}$$

since the determinants are equal for all $2n$ species. This causes the weight to be positive semidefinite and allows for a probabilistic treatment. In any other case, particularly at finite mass- and/or spin-imbalance, the sign problem prohibits a straightforward treatment.

A full categorization of whether a given theory can be formulated in a sign-free manner is challenging. However, recent advances based on symmetry considerations identified conditions for the absence of a sign problem and thereby significantly extend the list of sign-free models [118–120]. Moreover, worldline methods may be formulated in a way that one-dimensional problems are free of an oscillating sign regardless of any imbalance [121] (although 1D systems are often treated with tensor networks or the density-matrix renormalization group (DMRG) method, which are limited to low dimensionality). Recently, such an approach was applied to the few-body sector of mass-imbalanced fermions [122, 123]. Alternative approaches for the fermionic sign problem in lattices are based on suitable resummations [124] combined with the introduction of so-called "dual variables" or "fermion bags" [125–127].

While the so-far mentioned methods are mostly based on resummations or the exploitation of certain symmetries, there exists a variety of methods that attack the sign problem by escaping to the realm of complex numbers, dubbed "complex plane methods" in [82]. In this thesis, we shall heavily employ such an approach, namely the complex Langevin (CL) method, to circumvent the above mentioned sign problem for imbalanced Fermi gases. Additionally, we employ a different method that extends the imbalance parameter to the complex plane. Doing so renders the probability measure positive semidefinite and conventional sampling techniques may again be applied. The specifics of both approaches are discussed in detail in the following chapter.

Yet another complex-plane method, somewhat related to CL [128], is achieved by deforming the integration contour into the complex plane and sampling along trajectories of (approximately) constant complex phase, called "Lefschetz thimbles" [129–131]. Once such a thimble is identified, which itself is a challenging task that can be considered the bottleneck of the approach, the sampling can be performed with a mild residual sign problem through a convenient parameterization.

Finally, it should be mentioned that the recent surge of studies on the application of machine learning techniques in physics involve first results to address the sign problem [132], albeit with mixed success so far. In any case, note that this list of approaches to tackle the sign problem merely provides a brief overview and by no means can be considered exhaustive. A more thorough list of modern approaches to the sign problem, along with some algorithmic details, may be found in recent reviews on the topic [82, 133, 134].

4 | Global update algorithms

> *"It is a mistake to think you can solve any major problems just with potatoes."*
>
> Douglas N. Adams

So far, the general framework of determinantal Monte Carlo sampling, along with possible shortcomings of such a treatment, has been introduced. In this chapter, we lay out in detail the specific algorithms applied in this work, with the goal of arriving at algorithms that are free of the sign problem for imbalanced Fermi gases. The unifying concept is based on global updates, which we introduce in a first step and subsequently connect to the algorithms relevant for this work.

Along the way, the paradigmatic Metropolis algorithm [135] is discussed as a building block of the the Hybrid Monte Carlo (HMC) method [136], which we discuss in the context of non-relativistic physics. Although this approach relies on positive-semidefinite measures, and thus suffers from a sign problem in general, the sign problem is absent in the case of balanced Fermi gases. Moreover, we discuss an extension to so-called imaginary asymmetries, dubbed iHMC, as a way to treat imbalanced Fermi gases within this approach.

The second part of this chapter is devoted to the idea of stochastic quantization, which was introduced in the early 1980's by Parisi and Wu [137]. The concept not only offers an alternative interpretation of quantization in general, but also constitutes the basis of a class of powerful stochastic algorithms. We justify its validity and set up the framework with the aid of a pedagogical toy problem.

While stochastic quantization with real fields lacks the possibility to treat theories with complex actions, it can be extended via complexification of the fields. This results in the so-called complex Langevin (CL) method, which is the workhorse for subsequent chapters. Parisi proposed this method shortly after the introduction of stochastic quantization and famously remarked "Nothing forbids to write a Langevin equation for complex theories" in a seminal paper [138]. The potential to provide a way around the notorious sign problem serves as motivation to apply this method to non-relativistic Fermi gases. We shall see, however, that the mathematical justification of this step is far from trivial and, in fact, impossible to achieve analytically for all but the simplest toy models. Nevertheless, the success of the approach in a number of relativistic theories [139] as well as nonrelativistic toy models [140] motivates an extension to the low-energy physics of interest in this thesis.

4.1 Critical slowing down & global updates

A major bottleneck in MCMC simulations is the problem of critical slowing down, which arises in the vicinity of phase transitions. In such a regime, a slight perturbation away from equilibrium (as introduced by random fluctuations) takes a long time to decay back to a steady state.[1] Since we are interested in equilibrium properties, however, we have to wait a certain time for another appropriate sample which "knows nothing" about the previous perturbation. A related reasoning may be achieved by viewing the integrated autocorrelation time as a susceptibility [114] which diverges at a second-order phase transition. Mapped to Markov chains, this implies strong correlation between subsequent samples, and thus strongly increased numerical effort required to precisely measure observables.

To arrive at possible solutions of this issue, we may again invoke the Ising model. A straightforward update strategy for this model is to randomly flip single spins on the lattice, which essentially only affects the neighboring spins. To obtain decorrelated configurations, however, changes at length scales on the order of the correlation length ξ are necessary. For large correlation lengths, local updates will therefore perform poorly, as the perturbation wanders randomly on the spin lattice and thus takes a long time to move further than ξ [114]. This picture provides a physical motivation for so-called global updates, which, instead of locally perturbing the sample, introduce non-local changes. Unfortunately, these strategies are challenging to come by and often tailored for specific physical models. Famous examples include the Swendsen-Wang algorithm [141], Wolff cluster updates [142] and Fourier acceleration [143].

4.1.1 The drift term

All algorithms employed in this work share the common usage of a global update strategy that relies on the so-called drift term. For a given spacetime lattice site (i, τ), the drift is given by

$$K_{i\tau}[\phi] = -\frac{\delta S[\phi]}{\delta \phi_{i\tau}}. \tag{4.1.1}$$

This quantity plays a central role in the update strategy as it determines, in large part, the physical change towards the next state in the Markov chain (up to random fluctuations). With the determinantal formulation introduced in Chapter 2, along with the corresponding definition of the action in Eq. (2.4.9), the above expression may be rewritten as

$$K_{i\tau}[\phi] = \mathrm{Tr}\left\{M^{-1}[\phi]\frac{\delta M[\phi]}{\delta \phi_{i\tau}}\right\}. \tag{4.1.2}$$

The variation of the Fermi matrix (of a single species) is given by

$$\frac{\delta M_\sigma[\phi]}{\delta \phi_{i\tau}} = \frac{\delta}{\delta \phi_{i\tau}}\left[\mathbb{1} + \prod_{\omega=1}^{N_\tau} B_\sigma V_\sigma(\phi_\omega) B_\sigma\right] \tag{4.1.3a}$$

---

[1]This can be made clear by analyzing an expansion in the order parameter. Far away from the phase transition, the potential is (almost) harmonic, whereas at the phase transition it is at least quartic. In the former case the state rapidly falls back to the equilibrium, whereas for the quartic potential a "creeping" solution is the case.

$$= \sum_{\kappa=1}^{N_\tau} \left\{ \prod_{\omega=1}^{\kappa-1} T(\omega, \omega - 1) \left[\frac{\delta}{\delta\phi_{i\tau}} T(\kappa, \kappa - 1) \right] \prod_{\omega'=1}^{\kappa-1} T(\omega', \omega' - 1) \right\} \tag{4.1.3b}$$

where

$$\frac{\delta}{\delta\phi_{i\tau}} T(\kappa, \kappa - 1) = B_\sigma \frac{\delta V_\sigma(\phi)}{\delta\sigma_{i\tau}} B_\sigma \tag{4.1.4a}$$

$$= B_\sigma \left[\rho_{\sigma,i} A \cos(\phi_{i\tau}) \right] B_\sigma, \tag{4.1.4b}$$

Note that this derivation is generic until Eq. (4.1.4a). The dependence on a specific HS transformation only comes in by explicitly performing the variation, which was performed in Eq. (4.1.4b).

The inverse of the Fermi matrix in Eq. (4.1.2) essentially dictates the computational effort. However, the benefit of decreasing the decorrelation time often outweighs this cost and therefore renders such an approach highly efficient. Moreover, this quantity is a necessary ingredient for stochastic quantization, as shown below.

The variation of the action with respect to the auxiliary field, which formally requires ϕ to be continuous, motivates the particular form of the HS transformation employed in this thesis. As remarked already above, it is possible to describe fermionic lattice theories with a discrete HS field, which is more efficient to store in memory (see, e.g., [144] for a state-of-the-art implementation). The usage of the drift term, however, prevents such a treatment.

4.2 Interlude: the Metropolis algorithm

Having introduced the general principles of Markov chains, we now discuss efficient algorithms for producing such sequences of states. Among the many possible ways to do this, the so-called Metropolis algorithm (or the slightly more general Metropolis-Hastings algorithm) is most often the method of choice [135, 145].[2] Before diving into the non-local update algorithms relevant for this work, we briefly elaborate on this algorithm as it is a part of the HMC method.

The underlying idea of the Metropolis algorithm is to first *propose* some change to a given configuration ϕ and then to accept or reject this change based on its relative probability. If the proposed configuration ϕ' corresponds to a higher probability density $P[\phi']$, it is always accepted. If its probability is lower than $P[\phi]$ (i.e., the current one), the new state is only accepted with a certain probability. The smaller the ratio

$$r = \frac{P[\phi']}{P[\phi]}, \tag{4.2.1}$$

the less likely it is for the new state to be accepted. If it is rejected, the next state in the Markov chain is again taken to be the current one, which effectively amounts to an increased sampling in regions with a large probability density. Nevertheless, configurations with lower probability are still sampled (as required by ergodicity) which allows the algorithm to accurately scan the entire state space.

An intuitive understanding of this procedure can be gained by considering physical simulations.

---

[2]In fact, the algorithm is used so frequently that it was selected to be among the top 10 algorithms "with the greatest influence on the development and practice of science and engineering in the 20th century" [146].

Typically, the target probability is given by the Boltzmann factor $\mathrm{e}^{-\beta E[\phi]}$, where $E[\phi]$ is the energy of a given configuration ϕ. The acceptance probability is then given by $r = \mathrm{e}^{\beta(E[\phi']-E[\phi])} \equiv \mathrm{e}^{-\beta \Delta E}$. This implies that moves to states with larger energies ($\Delta E > 0$) are accepted only rarely, whereas energetically favorable configurations ($\Delta E < 0$) are accepted with certainty.

Formally, the Metropolis-Hastings algorithm can be constructed by again considering the detailed balance condition Eq. (3.2.6). The key step is to split the transition probabilities into a proposal probability and an acceptance probability, such that the detailed balance condition reads

$$P[\phi]\, q_{\phi\phi'}\, \alpha_{\phi\phi'} = P[\phi']\, q_{\phi'\phi}\, \alpha_{\phi'\phi}. \tag{4.2.2}$$

The above expression states that we propose a move from ϕ to ϕ' with the probability $q_{\phi\phi'}$ and accept it with the acceptance rate

$$\alpha_{\phi\phi'} = \min\left[1, \frac{P[\phi']}{P[\phi]} \frac{q_{\phi'\phi}}{q_{\phi\phi'}}\right]. \tag{4.2.3}$$

Without loss of generality, we have used $\alpha_{\phi'\phi} = 1$. For symmetric proposal probabilities, i.e., $q_{\phi\phi'} = q_{\phi'\phi}$, the Metropolis algorithm is recovered as a special case of the more general Metropolis-Hastings algorithm. In this case, the acceptance rate reduces to Eq. (4.2.1). For an educational in-depth derivation of the algorithm see, e.g., [147].

In practice, the update step of the MCMC flow (blue box in Fig. 3.2) can be summarized as follows:

1. Create a new configuration ϕ' and calculate its weight $P[\phi']$.

2. Draw a random number x with uniform probability in the interval $[0, 1]$.

3. If $x < r$ accept ϕ' as the new state, otherwise re-use the current state ϕ.

Evidently, the algorithm does not require the full probability distribution, but merely the ratio of weights. Therefore, the strategy is particularly useful in cases where direct sampling is difficult due to an unknown target distribution. Nonetheless, there is a severe restriction when it comes to the sign of the weights: only positive ratios are eligible, and thus the sign problem sets the limits of this otherwise powerful algorithm. In certain cases, as we shall also discuss below, the problem may be mitigated by a suitable reformulation of the weights.

4.3   Hybrid Monte Carlo

The Hybrid Monte Carlo (HMC) algorithm, originally proposed in the context of lattice gauge theories [136], constitutes a powerful global update algorithm heavily used in lattice QCD studies. Here, we show how this technique can be used for the simulation of nonrelativistic fermions [86]. The central idea of HMC is to use molecular dynamics (MD) to explore the configuration space of the auxiliary field ϕ. To obtain a suitable representation, an additional fictitious field π is introduced, which plays the role of the conjugate momentum of the field variable:

$$\mathrm{e}^{-S[\phi]} \to \mathrm{e}^{-S[\phi]-\frac{1}{2}\sum_{i\tau} \pi_{i\tau}^2} \equiv P[\phi, \pi]. \tag{4.3.1}$$
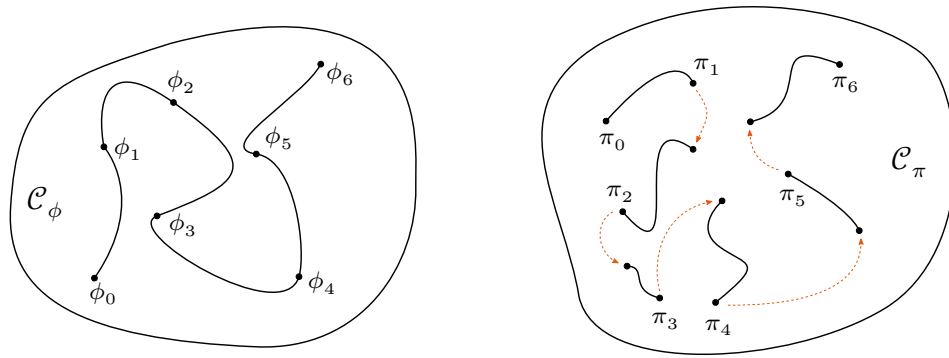
Figure 4.1: Update procedure of the HMC algorithm. Black solid lines represent the MD evolution of the fields, which start and terminate at the black dots. While the states ϕ move smoothly through the configuration space $\mathcal{C}_\phi$, the values of the π-field are randomized after every sweep (indicated through the dashed arrows) and thus jump discontinuously in their state space $\mathcal{C}_\pi$.

The integral over the π field merely constitutes a multiplicative factor in the partition sum and therefore leaves the physics untouched. Consequently, the modified probability distribution $P[\phi, \pi]$ is proportional to the physical one we want to sample.

To obtain a new, globally updated field configuration ϕ', both fields are propagated along a trajectory in the fictitious time t_H, according to Hamilton's equations of motion:

$$\frac{\partial \phi_{i\tau}}{\partial t_H} = \pi_{i\tau}, \tag{4.3.2a}$$

$$\frac{\partial \pi_{i\tau}}{\partial t_H} = K_{i\tau}[\phi]. \tag{4.3.2b}$$

For the numerical integration of these equations, a finite time step Δt_H needs to be introduced. In practice, the length of a trajectory between two decorrelated configurations is typically taken to be on the order of 1 such that a total of $\sim 1/\Delta t_H$ integration steps have to be performed per update. Since the above expression now contains the drift term $K_{i\tau}[\phi]$, this is a costly task and ideally Δt_H is chosen to be as large as possible while still being numerically stable. Moreover, the finite step Δt_H introduces a systematic error which needs to be addressed. This is where the "hybrid" part of the algorithm comes in: to ensure that the correct probability distribution $P[\phi, \pi]$ is sampled, a Metropolis accept-reject step is performed after evolving the fields along the trajectory.[3] According to the discussion in the previous section, the new configuration will be accepted with the probability

$$r_{\text{HMC}} = \min\left[1, \frac{P[\phi', \pi']}{P[\phi, \pi]}\right]. \tag{4.3.3}$$

It can be shown that the proper evolution of the fields according to Eq. (4.3.2) conserves the energy (also called on-shell propagation) [136]. Therefore, the acceptance rate is almost unity and only affected by numerical shortcomings of the integration. Finally, after checking the

---

[3]The Metropolis step, loosely speaking, acts as a "safety net". Should something go wrong in the propagation of the field values (say, for instance, a singular drift appears), the accept-reject step takes care of that and the algorithm tries to find a different next sample. This does not imply, however, that the HMC algorithm can operate at arbitrarily large step sizes Δt_H.

acceptance of the new configuration, the momentum field is randomized by drawing from a Gaussian distribution. This shifts the configuration to a different energy shell and, loosely speaking, changes the direction of the propagation in the state space of ϕ.

The update procedure can be summarized as follows (also schematically depicted in Fig. 4.1):

1. Randomly draw the field π from a Gaussian distribution.

2. Evolve both fields ϕ and π according to the MD equations (4.3.2) for a trajectory of length ~ 1.

3. Draw a random number x with uniform probability in the interval $[0, 1]$.

4. If $x < r_{\text{HMC}}$ accept ϕ' as the new state, otherwise re-use the current state ϕ.

One may now wonder about the validity of such an approach. As hinted above, the integration of Eq. (4.3.2) conserves the phase-space volume and is time-reversible, according to Liouville's theorem. However, this is only the case if a so-called symplectic (or geometric) integrator is applied, which respects the symmetries of the equations. The most commonly used variant of such an integration scheme is the Leapfrog algorithm, which we also apply in the studies presented in this thesis. The conservation of the phase-space volume as well as time-reversibility suffice to respect the detailed balance condition posed in Eq. (3.2.6). Specifically, the proposal probability is symmetric, such that the Metropolis algorithm may safely be applied.

Despite the fact that the HMC algorithm is the workhorse in high-energy physics, its applications to nonrelativistic systems remain relatively scarce. An early study, shortly after the initial proposal of the method, applied the algorithm to the 3D Hubbard model [148]. Similarly, the method was revisited recently in this context [149] and it was found to be inferior to state-of-the-art determinantal MC implementations [144]. The unfavorable behavior of HMC in this setting can be traced back to the computation of determinants of the large $N_s \times N_s$ Fermi matrix, where N_s is the number of spacetime lattice points. The algorithms applied in [148, 149] rely on a stochastic evaluation of the fermion determinant (specifically, the pseudofermion method) combined with a conjugate gradient procedure [150]. For such an approach to scale efficiently, the Fermi matrix needs to be well conditioned, which does not seem to be the case for the Hubbard model, in particular at large coupling and low temperatures. However, it was found that the method performs exceptionally well for studies with electron-phonon interactions [149].

Other studies, including the ones presented in this thesis, implement the method similarly to the original formulation of the determinantal MC algorithm [103], sometimes referred to as determinatnal HMC (DHMC). The key step of this approach is given by Eq. (2.4.7): instead of taking the determinant of the large $N_s \times N_s$ matrix, the approach requires taking determinants of a $N_x \times N_x$ matrix that has previously been propagated in imaginary time.[4] In the context of ultracold Fermi gases, the method has been applied to the unitary Fermi gas at finite temperature [151, 152] and the ground state [98] as well as to lower dimensional Fermi gases with contact interaction in 2D [153, 154] and 1D [78, 155–158] geometries. Additionally, a variant suitable for the study of entanglement properties has been proposed [159, 160].

Further applications of HMC in a nonrelativistic setting include effective theories in nuclear physics (see, e.g., [102]), the study of properties of graphene [161–164] and related models [165–168] as well as carbon nanotubes and the Hubbard model on the hexagonal lattice [169–171].

---

[4]An additional benefit of this approach is the applicability of Fourier acceleration in the imaginary time propagation.
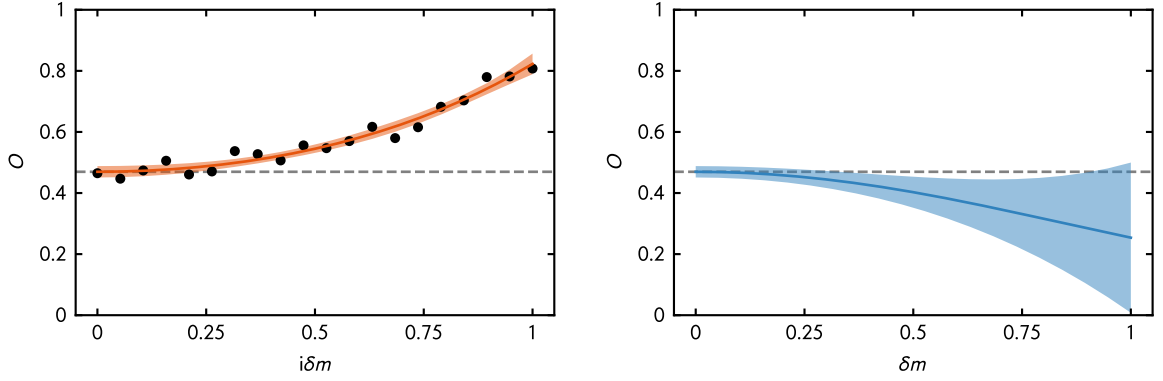
Figure 4.2: Schematic representation of the analytic continuation from imaginary to real asymmetries. (Left) Symbols show the observable as function of the real imbalance as obtained from an MC run, the solid line represents a fourth order polynomial fit along with a confidence interval. (Right) Analytically continued function along with the propagated confidence interval. The analytic continuation causes the error to blow up.

4.3.1 Imaginary asymmetries: iHMC

The HMC algorithm, although powerful, is not capable of treating imbalanced Fermi systems due to the occurrence of a sign problem. Here, an extension of the method to imaginary asymmetries is introduced, which again allows for efficient sampling. To distinguish from the symmetric counterpart, we shall refer to this strategy as iHMC.

To discuss the iHMC approach, we consider mass-imbalanced two-component fermionic systems. In this case, the mass is flavor-dependent which causes the determinants to be unequal and Eq. (3.3.5) no longer applies. An elegant way to circumvent this issue is to consider complex particle masses and introduce the imbalance as

$$m_\uparrow = m_0 + \mathrm{i}\delta m \tag{4.3.4}$$

$$m_\downarrow = m_0 - \mathrm{i}\delta m. \tag{4.3.5}$$

In this case, the masses are complex conjugates of each other, which translates to the transfer matrices defined in Eq. (2.4.5):

$$B_\uparrow = \mathrm{e}^{\sum_k \frac{k^2}{2m_\uparrow}} = \mathrm{e}^{\sum_k \frac{k^2}{2(m+\mathrm{i}\delta m)}} = \left(\mathrm{e}^{\sum_k \frac{k^2}{2(m-\mathrm{i}\delta m)}}\right)^* = \left(\mathrm{e}^{\sum_k \frac{k^2}{2m_\downarrow}}\right)^* = (B_\downarrow)^*. \tag{4.3.6}$$

This, in turn, allows us to write the probability measure as the absolute square of the determinants

$$P[\phi] = \frac{1}{\mathcal{Z}} \left|\det M_\phi^\uparrow\right|^2 = \frac{1}{\mathcal{Z}} \left|\det M_\phi^\downarrow\right|^2, \tag{4.3.7}$$

which is a positive semidefinite quantity by definition and may be sampled by the HMC algorithm (or, in fact, any other suitable MC implementation).

The above procedure allows for a simulation of mass-imbalanced fermions with imaginary asymmetry. For physical insight, however, it would be nice to know the results for *real* mass imbalances. This is achieved by computing an observable $O(\mathrm{i}\delta m)$ as a function of the imaginary imbalance and subsequently performing an analytic continuation to the real line. Practically,

this is achieved by performing either a polynomial fit or a Padé approximant for $O(\mathrm{i}\delta m)$ and subsequently setting $\delta m \to -\mathrm{i}\delta m$ (this is depicted in Fig. 4.2). Strictly speaking, such an approach is only permissible if the partition function is an analytic function of the mass imbalance δm, which is challenging to show in practice. For analytic insights on this procedure we refer to [172, 173].

It is important to note that this procedure constitutes a fully nonperturbative approach. The systematic uncertainties are equivalent to the determinantal MC algorithm (discretization of spacetime and finite system size) and are fully controllable by definition. The dependence on the analytic continuation, however, poses certain limitations and, as will be discussed in the later chapters of this thesis, causes the method to break down at very large imbalances. Another drawback of the method is the necessity to compute observables for a multitude of parameter values, as only then is an analytic continuation of numerical results possible at all. Compared to the direct evaluation at a single given value of the imbalance parameter, this introduces some extra computational effort.

In this thesis, we exploit the above procedure to study the ground state of mass imbalanced fermions in 1D. Technically, the approach can be extended to mass imbalanced systems at finite temperature, however, this is not pursued in this work. At finite temperature, i.e., in the grand canonical ensemble, it is even possible to formulate the approach for imaginary mismatch of chemical potentials. In fact, this marks the origin of the above procedure which can be traced back to a study of the 2D Hubbard model [174]. The strategy was also exploited in the lattice QCD community to circumvent a sign problem introduced with a finite real chemical potential [175, 176] and was later also proposed for nonrelativistic spin-polarized Fermi gases [172]. Finally, the iHMC method was applied to study the mass-imbalanced unitary Fermi gas in the ground state [63] as well as mass-balanced but spin-imbalanced 1D Fermi gases at finite temperature [177].

4.4 Stochastic quantization

Stochastic quantization is an intuitive tool to understand the quantization of field theories. The approach was initially proposed in the early 1980s by Parisi and Wu [137] and relies on the connection between Euclidean field theories and statistical systems coupled to an external heat reservoir.[5] The idea has led to major success in the study of quantum field theories in a variety of settings. Some of the early applications, as well as an educational overview of the approach, may be found in the famous review by Damgaard and Hüffel [180].

We may conceptualize the idea by considering the partition function of a given Euclidean field theory as a path integral:

$$\mathcal{Z} = \int \mathcal{D}\phi \, \mathrm{e}^{-S[\phi]} \equiv \int \mathcal{D}\phi \, P[\phi], \tag{4.4.1}$$

where the second equality defines the (unnormalized) probability measure of the field ϕ. The coupling to the heat reservoir can be understood by introducing a fictitious time t, in which the Euclidean field ϕ evolves under the influence of a randomly fluctuating force. This random force, referred to as the noise field or simply the noise, emulates thermal fluctuations stemming

---

[5]Stochastic quantization can also be formulated for real-time theories (i.e., in Minkowski metric), however, we only consider the case of Euclidean field theories in this work. For recent applications see, e.g., [178, 179].

from the heat bath. In the long-time limit, the system equilibrates with the heat bath whose temperature is set by the amplitude of the fluctuations. The fictitious time evolution of the real field ϕ is then described by a stochastic differential equation, namely the Langevin equation:[6]

$$\frac{\partial \phi(t)}{\partial t} = -\frac{\delta S[\phi]}{\delta \phi} + \eta. \tag{4.4.2}$$

This equation defines a random process for the variable $\phi = \phi(\vec{x}, \tau)$ and may be interpreted as a (continuous) random walk in the configuration space of ϕ. The first term on the right hand side is called the drift term, in analogy to the considerations of Section 4.1. In the literature, this term is also referred to as the classical flow of the theory, as it constitutes the deterministic part of the time-propagation of the field. The second term represents the fluctuating force and is given by a white-noise with the properties

$$\langle \eta(\tau) \rangle = 0, \tag{4.4.3a}$$

$$\langle \eta(\tau)\eta(\tau') \rangle = 2\delta(\tau - \tau'). \tag{4.4.3b}$$

The key ingredient of stochastic quantization is now the observation that the equilibrium distribution (if it exists) of the $d + 1$ dimensional random process in Eq. (4.4.2) corresponds to the probability measure in the path integral Eq. (4.4.1), associated with a d-dimensional Euclidean field theory. The "extra" dimension is simply the fictitious time t.

It is instructive to consider the above stochastic differential equation without the noise term. In that case, Eq. (4.4.2) reduces to a deterministic differential equation and its form is nothing but that of a gradient descent. Starting out at a random (non-pathological) state, this implies that the solution will converge to a stationary point of the action, which is the "mean-field" or classical solution. The simple interpretation of the noise term is that it represents quantum fluctuations around this classical solution.[7] In order to reproduce the correct physics, we have to "add the correct amount of fluctuations" which is set by the Fluctuation-Dissipation theorem. Thus, stochastic quantization can be viewed as a very explicit form of quantization.

Time-ordered realizations of the field ϕ, which have been obtained by a fictitious time evolution of Eq. (4.4.2), are called solutions of the Langevin equation. We shall denote these as $\phi_\eta(t)$, where the subscript η highlights the dependence on the specific noise realization. Fig. 4.3 depicts a schematic representation of these solutions. Mapped to our lattice problem discussed in Section 2.3, this implies that we obtain a sequence of auxiliary field configurations. For a given point in the fictitious time evolution of the fields, we may write the expectation value of an observable as the average over all possible realizations of the noise:

$$\langle O[\phi_\eta(t)] \rangle = \int \mathrm{d}\eta \, P[\eta, t] O[\phi_\eta(t)], \tag{4.4.4}$$

where $P[\eta, t]$ defines the distribution of the noise that has to obey Eq. (4.4.3). In the limit of large Langevin time, the random process reaches its equilibrium distribution, and as shown below, it holds that the expectation values of the Euclidean field theory correspond to the ones

---

[6]For convenience, we do not explicitly write the arguments of the field $\phi = \phi(\tau, \vec{x})$ in the following discussion.

[7]Essentially, the thermal fluctuations from the fictitious heat bath are mapped to quantum fluctuations of a Euclidean field theory.
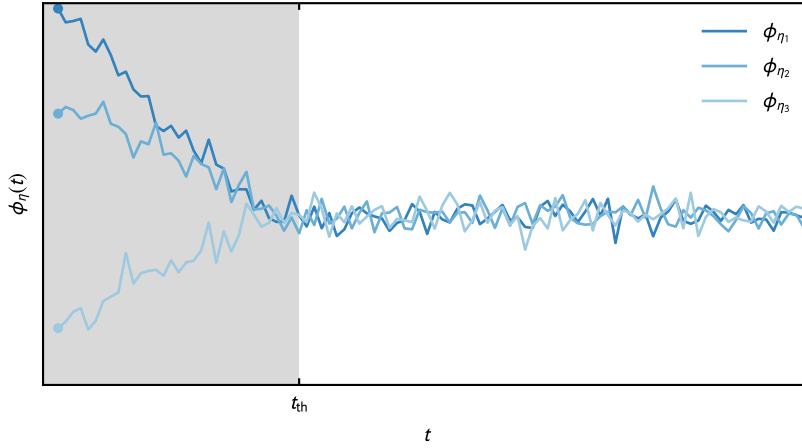
Figure 4.3: Schematic representation of multiple solutions of the Langevin equation in Eq. (4.4.2). The plot shows three different realizations that converge to the steady state (marked by fluctuations about a plateau) after the thermalization time has elapsed (indicated by the shaded area).

over the noise correlations:

$$\langle O \rangle = \lim_{t \to \infty} \langle O[\phi_\eta(t)] \rangle. \tag{4.4.5}$$

In practice, however, it may be costly to obtain a large number of solutions $\phi_\eta(t)$ at sufficiently large t. Conveniently, once the steady state of the random process is reached, we may obtain equivalent expectation values by performing a fictitious-time over a single trajectory

$$\langle O \rangle \approx \frac{1}{T} \int_{t_{\mathrm{th}}}^{t_{\mathrm{th}}+T} \mathrm{d}t \; O[\phi_\eta(t)], \tag{4.4.6}$$

where t_{th} reflects the equilibration time that is needed to approach the stationary probability distribution. This so-called thermalization time is indicated by the shaded area in Fig. 4.3.

4.4.1 Justification of stochastic quantization

Having layed out the conceptual groundwork of stochastic quantization, we now justify the approach by showing that the equilibrium distribution of the random process Eq. (4.4.2) is indeed the desired probability measure of our path integral. To investigate this issue, we lean on the discussion in [181] (a more formal justification may be found in, e.g., [182]).
We start by rewriting the expectation value $\langle O \rangle$ as an functional integral over the solutions of the random process:

$$\langle O[\phi_\eta(t)] \rangle = \int \mathcal{D}\phi \; P[\phi,t]O[\phi], \tag{4.4.7}$$

where $P[\phi,t]$ defines the time-dependent distribution function of the field ϕ. In other words, we have traded an integral over all noise configurations for a functional integral over all realizations of the field $\phi(t)$ weighted with the appropriate factor $P[\phi,t]$.

To study the fictitious time-dependence behavior of the probability measure, we may consider the fictitious-time derivative

$$\frac{\mathrm{d}\langle O[\phi_\eta(t)]\rangle}{\mathrm{d}t} = \int \mathcal{D}\phi \, \frac{\mathrm{d}P[\phi, t]}{\mathrm{d}t} O[\phi], \tag{4.4.8}$$

where we have used that only the probability measure carries a dependence on the Langevin time.

Alternatively, we may perform the same fictitious-time derivative by expanding the observable to second order in its ϕ dependence[8]

$$\mathrm{d}O[\phi] = \frac{\delta O[\phi]}{\delta\phi}\mathrm{d}\phi + \frac{1}{2}\frac{\delta^2 O[\phi]}{\delta\phi^2}(\mathrm{d}\phi)^2. \tag{4.4.9}$$

To obtain the field increment $\mathrm{d}\phi$, it is necessary to rewrite Eq. (4.4.2) in a discrete version, which is achieved by simply integrating both sides over the time interval $\mathrm{d}t$:

$$\int_t^{t+\mathrm{d}t} \mathrm{d}\tau \, \frac{\partial\phi(\tau)}{\partial\tau} = \int_t^{t+\mathrm{d}t} \mathrm{d}\tau \, K[\phi] + \int_t^{t+\mathrm{d}t} \mathrm{d}\tau \, \eta(\tau) \tag{4.4.10}$$

where $K[\phi] = -\frac{\delta S[\phi]}{\delta\phi}$ denotes the drift term. The left-hand side of the expression is readily evaluated and is given by the increment of the field $\mathrm{d}\phi = \phi(t + \mathrm{d}t) - \phi(t)$. Furthermore, the second integral is trivial, since the drift does not explicitly depend on the Langevin time t. For the proper definition of the first term on the right-hand side, however, some care has to be taken. Formally, the approximating sum of the integral is not uniquely defined and could depend on the intermediate points chosen for the partition.[9] We refrain from a discussion of the technical subtleties at this point and refer to [180] for a treatment of the issue. Pragmatically assuming that the integral can be suitably defined, we arrive at the discrete Langevin equation

$$\mathrm{d}\phi = K[\phi]\mathrm{d}t + \mathrm{d}w, \tag{4.4.11}$$

where $\mathrm{d}w$ denotes the so-called Wiener increment with the property

$$\langle\mathrm{d}w^2\rangle = \int_t^{t+\mathrm{d}t} \mathrm{d}\tau \int_t^{t+\mathrm{d}t} \mathrm{d}\tau' \, \langle\eta(\tau)\eta(\tau')\rangle = 2\mathrm{d}t. \tag{4.4.12}$$

We can now substitute Eq. (4.4.11) into Eq. (4.4.9) to obtain

$$\mathrm{d}O[\phi] = \frac{\delta O[\phi]}{\delta\phi}\left(K[\phi]\mathrm{d}t + \mathrm{d}w\right) + \frac{1}{2}\frac{\delta^2 O[\phi]}{\delta\phi^2}\left(K[\phi]\mathrm{d}t + \mathrm{d}w\right)^2 \tag{4.4.13a}$$

$$= \frac{\delta O[\phi]}{\delta\phi}K[\phi]\mathrm{d}t + \left(\frac{\delta O[\phi]}{\delta\phi} + \frac{\delta^2 O[\phi]}{\delta\phi^2}K[\phi]\mathrm{d}t\right)\mathrm{d}w + \frac{1}{2}\frac{\delta^2 O[\phi]}{\delta\phi^2}\mathrm{d}w^2. \tag{4.4.13b}$$

Note that terms of order $\mathrm{d}t^2$ have been discarded in the last equality, which corresponds to

---

[8]Note that the expansion to second order is required since ϕ is no ordinary variable but a random process and thus has to be treated with stochastic calculus [180].

[9]This distinguishes the Ito calculus from the Stratonovich calculus which are the two most commonly employed prescriptions to deal with integrals of this type.

Euler-Maruyama discretization [183]. The expectation value of the fictitious-time derivative then becomes

$$\left\langle \frac{\mathrm{d}O[\phi_\eta(t)]}{\mathrm{d}t} \right\rangle = \frac{\mathrm{d}\left\langle O[\phi_\eta(t)] \right\rangle}{\mathrm{d}t} \tag{4.4.14a}$$

$$= \left\langle -\frac{\delta O[\phi]}{\delta\phi}\frac{\delta S[\phi]}{\delta\phi} + \frac{\delta^2 O[\phi]}{\delta\phi^2} \right\rangle \equiv \langle L_\mathrm{R}O \rangle, \tag{4.4.14b}$$

where Eq. (4.4.12) was used, as well as the fact that terms proportional to $\mathrm{d}w$ vanish because of the vanishing expectation of the Wiener increment $\langle dw \rangle = 0$. Eq. (4.4.14b) implicitly defines the so-called Langevin operator[10]

$$L_\mathrm{R} = \int \mathrm{d}\tau\mathrm{d}^d x \left(\frac{\delta}{\delta\phi} + K[\phi] \right) \frac{\delta}{\delta\phi}. \tag{4.4.15}$$

We may again write this in terms of the time-dependent probability measure defined in Eq. (4.4.7):

$$\frac{\mathrm{d}\left\langle O[\phi_\eta(t)] \right\rangle}{\mathrm{d}t} = \int \mathcal{D}\phi \left(-\frac{\delta O[\phi]}{\delta\phi}\frac{\delta S[\phi]}{\delta\phi} + \frac{\delta^2 O[\phi]}{\delta\phi^2} \right) P[\phi, t] \tag{4.4.16a}$$

$$= \int \mathcal{D}\phi\, O[\phi] \left(-\frac{\delta}{\delta\phi}\frac{\delta S[\phi]}{\delta\phi} + \frac{\delta^2}{\delta\phi^2} \right) P[\phi, t]. \tag{4.4.16b}$$

The last line in the above expression was obtained through partial integration and the assumption of vanishing boundary terms, or at least a sufficiently fast decay in the case of a noncompact integration region. The assumption is in fact crucial and will be subject to further discussion below.

Finally, we compare the expressions in Eq. (4.4.8) and Eq. (4.4.16) to arrive at the Fokker-Planck (FP) equation for the probability distribution $P[\phi, t]$:

$$\frac{\mathrm{d}}{\mathrm{d}t}P[\phi, t] = L_\mathrm{R}^\mathrm{T} P[\phi, t]. \tag{4.4.17}$$

The operator L_R^T, referred to as the FP operator (or FP Hamiltonian), represents the formal adjoint of Eq. (4.4.15):

$$L_\mathrm{R}^\mathrm{T} = \int \mathrm{d}\tau\mathrm{d}^d x\, \frac{\delta}{\delta\phi} \left(\frac{\delta}{\delta\phi} - K[\phi] \right). \tag{4.4.18}$$

The procedure so far has led us to the FP equation for the probability distribution $P[\phi, t]$. It is now straightforward to check whether the probability measure of the path integral is indeed a stationary distribution of the random process: we simply plug $P[\phi]$, as defined in Eq. (4.4.1), into Eq. (4.4.17) to obtain

$$L_\mathrm{R}^\mathrm{T} P[\phi] = \int \mathrm{d}\tau\mathrm{d}^d x\, \frac{\delta}{\delta\phi} \left(\frac{\delta}{\delta\phi} - K[\phi] \right) P[\phi] \tag{4.4.19a}$$

---

[10]The integral over spacetime in Eq. (4.4.15) should merely be viewed as a shorthand notation and essentially reflects a sum over all possible degrees of freedom.

$$= \int \mathrm{d}\tau \mathrm{d}^d x \, \left\{ \frac{\delta}{\delta\phi} \left(\frac{\delta}{\delta\phi} \mathrm{e}^{-S[\phi]} \right) - \frac{\delta}{\delta\phi} \left(K[\phi] \mathrm{e}^{-S[\phi]} \right) \right\} \tag{4.4.19b}$$

$$= \int \mathrm{d}\tau \mathrm{d}^d x \, \left\{ \frac{\delta}{\delta\phi} \left(-\frac{\delta S[\phi]}{\delta\phi} \mathrm{e}^{-S[\phi]} \right) - \frac{\delta}{\delta\phi} \left(K[\phi] \mathrm{e}^{-S[\phi]} \right) \right\} = 0, \tag{4.4.19c}$$

as it should be for the stationary distribution. Note that this "proof of existence" alone does not guarantee the uniqueness of the stationary distribution. The latter can be achieved by performing a similarity transformation of $P[\phi]$ which leads to a FP equation with a positive semidefinite operator with a unique lowest eigenstate. A version of such a proof can be found in [82, 181]. The above procedure shows that the random process in Eq. (4.4.2) produces field configurations'ϕ distributed according to the Boltzmann weight of our path integral. Hence, we have arrived at an equivalent representation of a given theory that is valid for real fields ϕ.

4.4.2 Stochastic quantization as a numerical method

So far, we have discussed the idea of stochastic quantization as a general tool to quantize Euclidean field theories. Here, we want to exploit these considerations to construct an efficient numerical method, dubbed real Langevin (RL).

We start by considering the properties of the noise term in Eq. (4.4.3) which reveal the Markov nature of the random process through the δ-correlation of noise values at different times. Therefore, we may connect the discrete Langevin equation (4.4.11) by recasting it into the general form proposed in Eq. (3.2.7):

$$\phi^{(n+1)} = \phi^{(n)} + K[\phi_n]\Delta t + \sqrt{2\Delta t}\,\eta. \tag{4.4.20}$$

Here, the noise term η is written as a random variable with vanishing mean and $\langle \eta^2 \rangle = 1$, in accordance with the properties proposed above. In principle, it is possible to choose any distribution that satisfies these constraints, however, the predominant choice for η is a standard Gaussian.[11]

The update step (corresponding to the blue box in Fig. 3.2) can be summarized as follows:

1. Evaluate the drift term for the sample $\phi^{(n)}$ and multiply it by the integration step Δt.

2. Draw a random vector $\eta^{(n)}$ with the same size as the field.

3. Add the drift and the random vector to $\phi^{(n)}$ to obtain the next step in the sequence.

As opposed to the Metropolis-based algorithms discussed above, no accept-reject step is necessary to obtain a new state. As a consequence, we do not have to calculate the weight of a given configuration (which may be a challenging task) but "only" the drift term. This freedom allows us later to extend the method to the more general case of complex actions, as discussed below. By virtue of the discussion in the previous section, we know that in the long-time limit the samples $\phi^{(n)}$ follow the desired probability distribution of the path integral. Therefore, the strategy to evaluate the random sequence is identical to the one in regular Monte Carlo approaches: after starting out from a randomly produced configuration, we let the sampling process equilibrate for a certain thermalization time (typically a few multiples of the autocorrelation time) before we

---

[11] Overly broad distributions, for instance some power law, could lead to numerically inconvenient behavior due to excessive fluctuations and therefore longer convergence time.

start to collect samples. The measurement of observables and their statistical evaluation follows the procedure discussed in Section 3.2.

Systematic bias: time-step dependence & higher order integration

It is important to note that the statistical uncertainty is not the only source of error, as we have introduced a systematic bias through the discretization of the Langevin equation in Eq. (4.4.20). This raises the necessity to extrapolate results to the limit of $\Delta t \to 0$ or, alternatively, to resort to sufficiently small step sizes to suppress the systematic errors below an acceptable threshold. The standard form of discretization in Eq. (4.4.20) corresponds to Euler-Maruyama integration and leads to a linear dependence on the integration step Δt. A naive guess to improve this scaling would be to increase the order of numerical integration of the drift term, e.g. by a Runge-Kutta scheme of higher order, and subsequently add in the noise. However, such a strategy does not alter the linear dependence on the step size, although it comes at a considerably higher numerical cost due to repeated evaluation of the drift term.

To actually improve the scaling, higher-order discretizations taking into account the noise term have been investigated in the literature. A convenient explicit algorithm, proposed in [184], takes the following form:

$$\chi^{(n)} = \phi^{(n)} + \frac{\Delta t}{2} K[\phi^{(n)}], \tag{4.4.21a}$$

$$\psi^{(n)} = \chi^{(n)} + \frac{3\sqrt{\Delta t}}{4} \left(\eta + \frac{1}{\sqrt{3}}\zeta \right), \tag{4.4.21b}$$

$$\phi^{(n+1)} = \phi^{(n)} + \frac{\Delta t}{3} \left(K[\chi^{(n)}] + 2K[\psi^{(n)}] \right) + \sqrt{\Delta t}\,\eta, \tag{4.4.21c}$$

which leads to three evaluations of the drift term. The algorithm relies on two independent noise fields η and ζ which both satisfy the condition (4.4.3). It was shown analytically that the algorithm leads to corrections of the order $\mathcal{O}(\Delta t^2)$ for a single degree of freedom and $\mathcal{O}(\Delta t^{\frac{3}{2}})$ for coupled systems. In a later study, the above prescription was extended to the complex case [185] where the same scaling was observed. In fact, the prefactor of the polynomial was observed to be tiny, at least for the models under study, such that the dependence on the integration step is almost entirely suppressed. We revisit this topic in a concrete numerical setting in Section 5.6. Other integration schemes have been investigated in the past [186–188]. Within the models addressed with a variant of an improved integration scheme, success was achieved in reducing computational cost at equal systematic bias in terms of Δt as well as to eliminate finite-step dependence altogether within the statistical uncertainty. The majority of stochastic quantization studies, however, still rely on the linear discretization as it is often sufficient to get reasonable results at modest computational effort. Unless otherwise noted, we shall use the linear integration scheme in this thesis.

4.4.3 Toy problem I: simple integrals as 0+0 dimensional field theory

In order to illustrate the RL method in a concrete numerical setting, we consider a simple integral as a toy problem for a $0 + 0$-dimensional field theory. In other words, the field ϕ depends on neither space nor time. This purely serves an illustrative purpose - we are not interested in a detailed study of the specific model at hand but rather aim to investigate the behavior of the RL
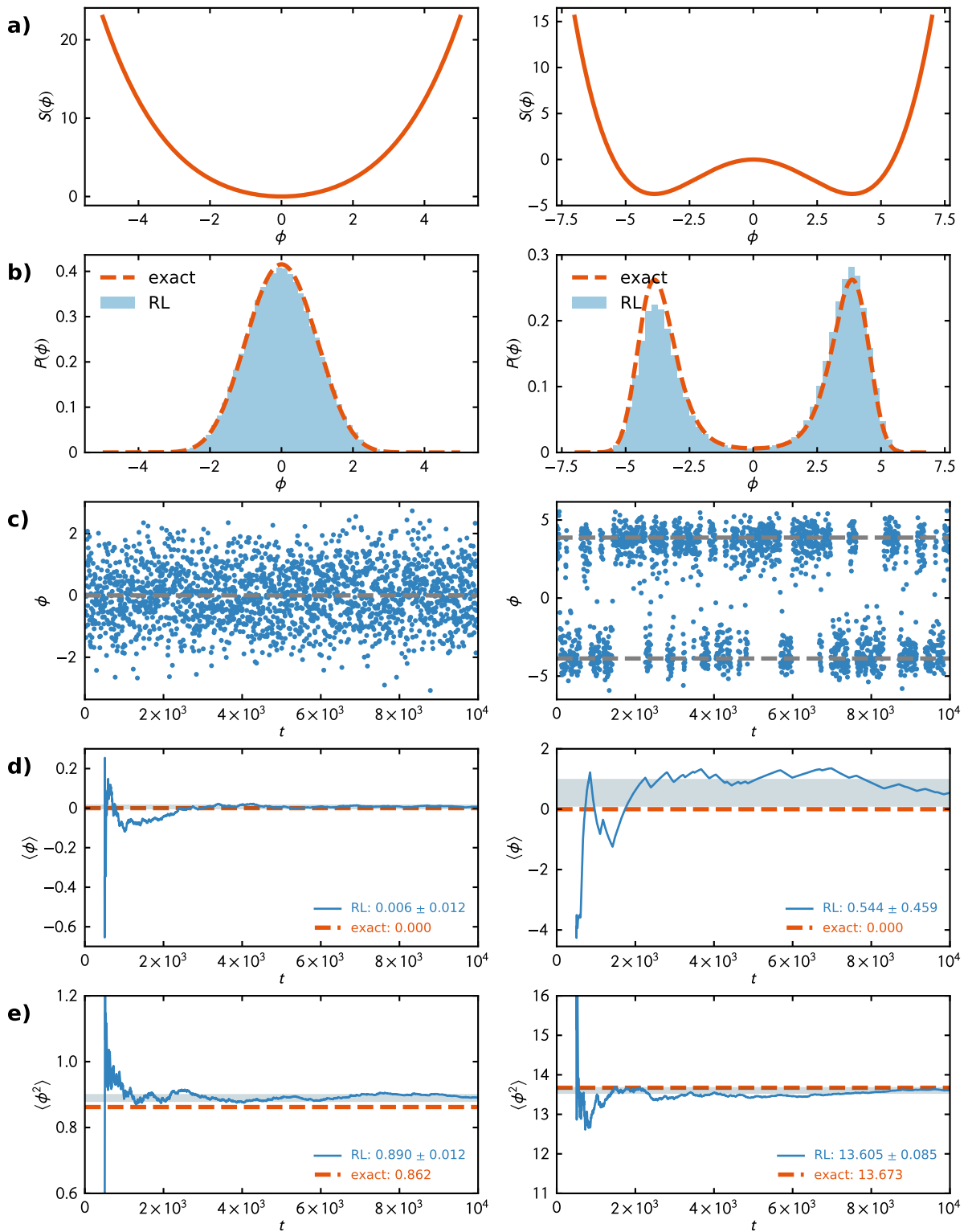
Figure 4.4: (a) Action as a function of the real variable ϕ. (b) Probability distribution $e^{-S[\phi]}$ (dashed lines) along with the sampled histogram (bins). (c) Measured values of ϕ as a function of Langevin time. (d) Running average of $\langle\phi\rangle$ compared to the exact solution (orange dashed line) (e) Running average of $\langle\phi^2\rangle$ compared to the exact solution (orange dashed line). The shaded areas correspond to the statistical uncertainty after the full run, i.e, $t = 10^4$ for the present example.

method in a straightforward case. Of course, it is highly inefficient to use RL for the solution of this simple problem, however, the section serves as a basic example of an application of the method. Furthermore, conclusions that generalize to more involved problems can be drawn by this simple analysis.

We consider the action

$$S(\phi) \;=\; \frac{\mu}{2}\phi^2 \;+\; \frac{\lambda}{4!}\phi^4, \tag{4.4.22}$$

with real couplings μ and λ. In the spirit of a real field theory, we will keep λ positive and thus end up with two distinct scenarios: one in which $\mu > 0$ (single-well anharmonic potential) and one in which $\mu < 0$ (double-well potential).

We readily derive the discrete Langevin equation for our toy problem, according to Eq. (4.4.20):

$$\phi^{(n+1)} = \phi^{(n)} - \left(\mu\phi^{(n)} + \frac{\lambda}{6}(\phi^{(n)})^3\right)\Delta t \;+\; \sqrt{2\Delta t}\,\eta, \tag{4.4.23}$$

where η denotes a standard Gaussian white noise. In principle, this is everything needed to calculate expectation values of the form Eq. (4.4.6).

In Fig. 4.4, a detailed analysis of two simulations at fixed $\lambda = 0.4$ and $\mu = \pm 1$ is presented (left and right columns, respectively). The second row from the top shows the histograms of the sampled field values, which should follow the distribution $e^{-S(\phi)}$ (exact solution shown with dashed lines) in the limit of large Langevin time $t \to \infty$. While in the single-well system (left column) this is the case to a good approximation, it is apparent that the double-well scenario still suffers from a slight asymmetry. This can occur when the random process gets "stuck" in an area of configuration space and does not easily move to another high-probability area of configuration space (i.e. the other well).

This behavior can be further elucidated by the measured field values as a function of t, depicted in row (c): on the left we essentially see white noise centered around the expected value of 0, whereas on the right we observe several correlated plateaus, corresponding to either the negative or the positive well. As a consequence, we face a signal-to-noise issue in the calculation of the expectation value $\langle\phi\rangle$, which is shown in row (d): when the trajectory is located in the left (right) well, the currently sampled values are negative (positive) such that adding these values to the estimate of the expectation value causes it to shift towards negative (positive) values. This leads to cancellations visible as zig-zag movements of the running average. Moreover, the autocorrelation between subsequent samples increases and with it the statistical error, as indicated by the large uncertainty band (shaded area in the plot). Due to the symmetry of the problem, however, the running average for $\langle\phi^2\rangle$ converges to the exact value relatively smoothly in both cases. Thus, by investigating only one observable, no profound statements can be made about a different one. While the autocorrelation of observable A may be small and its statistical errors under control, observable B could display erratic behavior and suffer from extremely slow convergence.

By tuning the parameters of the model, one could even study the extreme case where the two wells are separated by a barrier that cannot be surmounted by the random walk (signaling a breakdown of ergodicity). In such a situation, the expectation value $\langle\phi\rangle$ would indicate that the discrete symmetry is broken, which certainly is not a physical result for our model. This reflects the problem of meta-stability of any Markov chain method, which is often very hard to detect *a*
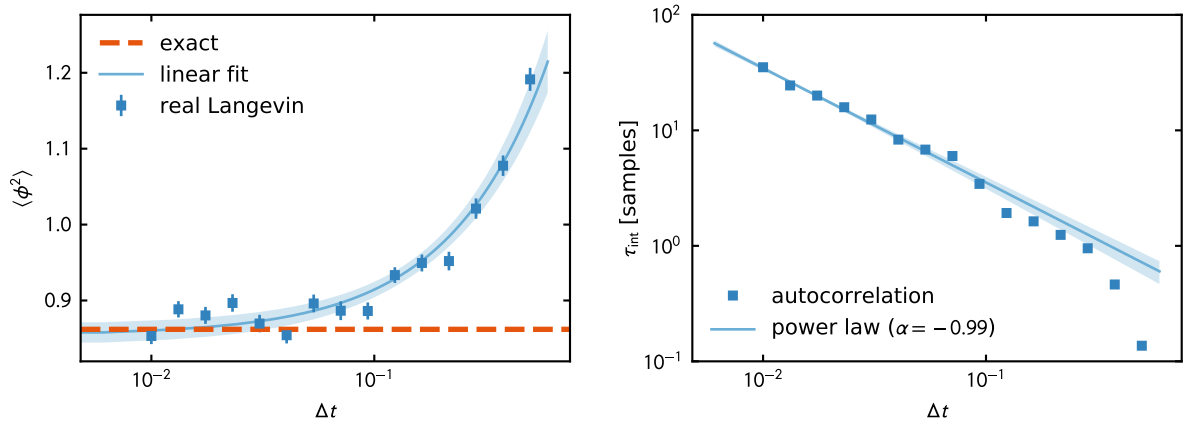
Figure 4.5: Real Langevin results for the simulation parameters $\mu = 1$, $\lambda = 0.4$ and a total Langevin-time of 10^4. (Left) Symbols reflect RL results for $\langle \phi^2 \rangle$ along with the statistical errorbars as a function of integration time-step Δt (note that the x-axis features a log-scale). The solid line represents a linear extrapolation to the limit $\Delta t \to 0$, along with the 95% confidence band (shaded area). The horizontal dashed line shows the exact result. (Right) Integrated autocorrelation time of the observable $\langle \phi^2 \rangle$ in units of samples as a function of Δt on a double-logarithmic scale. The solid line shows a power-law fit with exponent ~ -1, along with the 95% confidence band (shaded area).

priori. Generally, careful analysis of this issue is necessary in real simulations, for example by sweeping numerical parameters in a systematic manner.

As remarked above, the RL method suffers from a systematic bias that enters through the finite integration step Δt. We analyze the behavior of the expectation value $\langle \phi^2 \rangle$ in the left panel of Fig. 4.5. Indeed, we observe a systematic linear behavior of $\langle \phi^2 \rangle$, which is expected due to the order of the Langevin equation. The plot also features a linear extrapolation to the limit $\Delta t \to 0$, which is in excellent agreement with the exact result (dashed line).

Finally, by inspecting the Langevin equation 4.4.23, it becomes apparent that the integrated autocorrelation time τ_{int} between samples should be inversely proportional to the Langevin time-step Δt. Stated differently, statistically independent samples will be more expensive as the integration step decreases. On the other hand, a coarser integration step yields a larger systematic error and thus a balance must be found where both the computational effort as well as the precision are within reasonable bounds. This behavior is illustrated in the right panel of Fig. 4.5, where we show the dependence of τ_{int} (for the observable $\langle \phi^2 \rangle$) on the integration step size Δt on a double-logarithmic scale. A power-law fit reveals that τ_{int} scales as Δt^{-1} for sufficiently small integration steps. For $\Delta t \gtrsim 0.3$, subsequent samples are essentially uncorrelated. For this reason, a precise estimate of τ_{int}, which is smaller than 1 in this parameter range, is challenging, and the values deviate from the exact scaling due to noise.

4.5 The complex Langevin method

The above discussion shows that stochastic quantization is a valid description for theories with real actions. Sometimes, however, we are required to consider the more general case of complex actions - specifically in light of the sign problem: whenever we encounter negative contributions to the partition sum, we know that this can only originate from a complex valued action in

the exponent (after all, a real quantity in the exponent always leads to something positive). The occurrence of a complex action has serious implications and may spoil the construction of an efficient numerical method for such theories. Nevertheless, there are certain models that can efficiently be treated by extending the idea of real Langevin to the more general complex Langevin method. Here, we first explore this matter from a practical viewpoint and later discuss its formal aspects along with possible shortcomings of such a treatment.

4.5.1 A practical guide to complex Langevin

Before bothering with the formal background of the approach, we take the practical route to the CL method. We start by recognizing that the drift term is in general a complex quantity if the action itself is complex. In this case, a step in the Markov process according to Eq. (4.4.20) results in an imaginary contribution to the field value ϕ. A pragmatic solution is to simply extend the manifold of the field ϕ to the complex plane by setting

$$\phi \rightarrow \phi_R + i\phi_I, \tag{4.5.1}$$

which implies the analytic continuation

$$S[\phi] \rightarrow S[\phi_R + i\phi_I]. \tag{4.5.2}$$

Naturally, this step is only allowed if the action is a holomorphic function of ϕ. As a consequence of the complexification, we obtain a system of coupled stochastic differential equations which we may write in discrete form:

$$\phi_R^{(n+1)} = K_R[\phi^{(n)}]\Delta t + \sqrt{N_R \Delta t}\, \eta_R, \tag{4.5.3a}$$

$$\phi_I^{(n+1)} = K_I[\phi^{(n)}]\Delta t + \sqrt{N_I \Delta t}\, \eta_I. \tag{4.5.3b}$$

As before, the noise terms η_R and η_I are standard Gaussians centered around zero and represent two independent Wiener processes. However, in order to satisfy the dissipation-fluctuation theorem, the noise amplitudes are related through

$$N_R - N_I = 1. \tag{4.5.4}$$

While $N_I \neq 0$ is required to solve the associated Fokker-Planck equation, there is no such restriction when solving the above Langevin equations. In practice, it is typical to use $N_I = 0$ as this was shown to be numerically most favorable [189].

The respective drift terms in Eq. (4.5.35) are given by the real and imaginary parts of the functional derivative of the complex action

$$K_R[\phi^{(n)}] = -\mathrm{Re}\frac{\delta S[\phi]}{\delta \phi}\bigg|_{\phi=\phi^{(n)}} \tag{4.5.5a}$$

$$K_I[\phi^{(n)}] = -\mathrm{Im}\frac{\delta S[\phi]}{\delta \phi}\bigg|_{\phi=\phi^{(n)}} \tag{4.5.5b}$$
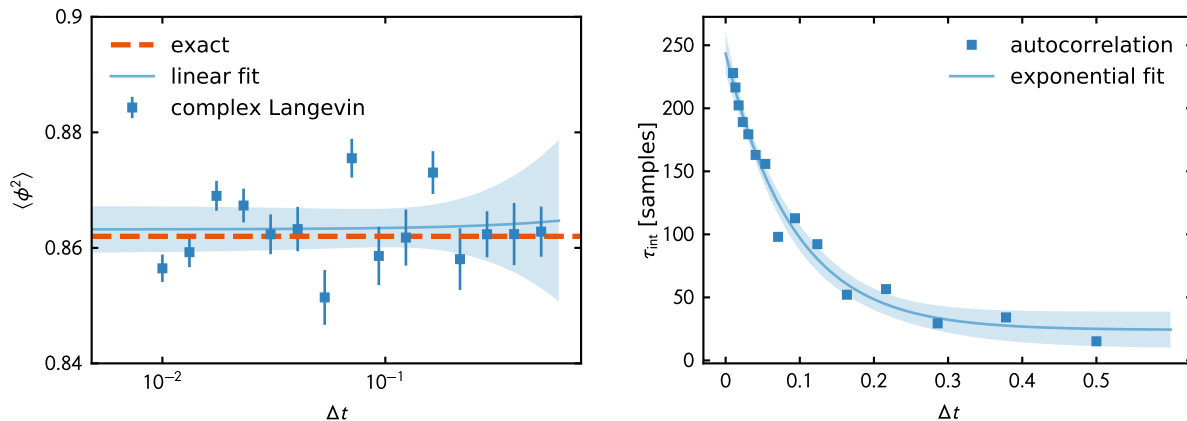
Figure 4.6: CL analysis for the action Eq. (4.4.22) with $\mu = 1.0$ and $\lambda = 0.4$, corresponding to the single well potential. (Left) Integration step dependence of the second moment $\langle\phi^2\rangle$ as obtained with CL (symbols). The solid line represents a linear fit to the data in order to extrapolate to $\Delta t \to 0$ and the dashed line shows the exact result. (Right) Step dependence of the integrated autocorrelation time for $\langle\phi^2\rangle$. The solid line represents an exponential fit. Shaded areas represent a 95% uncertainty bands of the corresponding fits.

and are responsible for the coupling of the two stochastic differential equations. As for all algorithms discussed in this section, it is the computationally most costly task to evaluate these expressions. However, no severe additional cost was introduced through the complex fields.

From a computational viewpoint the change from real to complex Langevin is indeed marginal: instead of performing the random walk on the real line we have to randomly explore the complex plane. Everything else stays exactly as in the real case. But we have to be careful: This somewhat leisurely look at the method would imply a general solution to the sign problem. It cannot be stressed enough that this is not the case, and sure enough, the sign problem will return in some other way. However, before turning to these subtleties, we discuss the approach with an illustrative example.

4.5.2 Toy problem II: a complex toy problem

In order to see the CL machinery at work, we build on the toy problem in Section 4.4.3. As remarked above, from a computational standpoint, CL is largely just the Langevin process of stochastic quantization with complex variables.

A straightforward way to construct a complex field theory would be to consider complex-valued couplings μ and λ in Eq. (4.4.22), which in fact has been considered before, see, e.g., [181]. However, this would amount to solving a different theory as the couplings necessarily take on different values than in the real case. For an alternative treatment, we may rewrite the above problem with a suitable Hubbard-Stratonovich transformation which merely amounts to a different representation of the same "physical" scenario. Moreover, this is very much in the spirit of our approach to fermionic theories, where we use a HS transform to construct a path integral. We start by inserting a suitable factor of 1 into the partition function in terms of an auxiliary variable σ:

$$\mathcal{Z} = \int_{-\infty}^{\infty} d\phi \; e^{-S(\phi)} \tag{4.5.6a}$$

$$= \sqrt{\frac{\lambda}{24\pi}} \int_{-\infty}^{\infty} d\sigma \; e^{-\frac{\lambda}{24}\sigma^2} \int_{-\infty}^{\infty} d\phi \; e^{-\frac{\mu}{2}\phi^2 - \frac{\lambda}{24}\phi^4} \tag{4.5.6b}$$

A shift $\sigma \to \sigma + i\phi^2$ allows us to write

$$\mathcal{Z} = \sqrt{\frac{\lambda}{24\pi}} \int_{-\infty}^{\infty} d\sigma \int_{-\infty}^{\infty} d\phi \; e^{-\phi^2 \left(\frac{\mu}{2} + \frac{i\lambda\sigma}{12}\right) - \frac{\lambda}{24}\sigma^2} \tag{4.5.7}$$

and subsequently to integrate out the dependence on the old field ϕ (note that this is only possible in the case $\mathrm{Re}[\mu] > 0$). Ultimately, we obtain the "bosonized" version

$$\mathcal{Z} = \int_{-\infty}^{\infty} d\sigma e^{-\frac{\lambda}{24}\sigma^2 + \frac{1}{2}\log\frac{\lambda}{12\mu + 2i\lambda\sigma}} \equiv \int_{-\infty}^{\infty} d\sigma \, e^{-S_{\mathrm{B}}(\sigma)}, \tag{4.5.8}$$

where we defined the "bozonized action"

$$S_{\mathrm{B}}(\sigma) = \frac{\lambda}{24}\sigma^2 - \frac{1}{2}\log\frac{\lambda}{12\mu + 2i\lambda\sigma}, \tag{4.5.9}$$

which is, by construction, a complex quantity. According to the discussion in the previous section we can still evaluate expectation values stochastically by using the complex Langevin equation

$$\sigma_R^{(n+1)} = \sigma_R^{(n)} - \Delta t \; \mathrm{Re}\left[\frac{\lambda}{12}\sigma^{(n)} + i\frac{\lambda}{12\mu + 2i\lambda\sigma^{(n)}}\right] + \sqrt{2\Delta t}\eta, \tag{4.5.10a}$$

$$\sigma_I^{(n+1)} = \sigma_I^{(n)} - \Delta t \; \mathrm{Im}\left[\frac{\lambda}{12}\sigma^{(n)} + i\frac{\lambda}{12\mu + 2i\lambda\sigma^{(n)}}\right]. \tag{4.5.10b}$$

To compute the expectation value of $\langle\phi^2\rangle$ we have to express it in terms of the new field σ:

$$\langle\phi^2\rangle = \left\langle \frac{6}{6\mu + i\lambda\sigma} \right\rangle_\sigma \tag{4.5.11}$$

where the subscript σ denotes averaging over different realizations of σ.

From this point on, we proceed exactly as in the real case, with the exception that we now have to deal with a complex variable σ. The qualitative dependence of the numerical results on the integration step size Δt should still be linear. This is indeed the case, as apparent from the left panel of Fig. 4.6, where we show CL results for the model given by Eq. (4.4.22) with parameters $\mu = 1.0$ and $\lambda = 0.4$. We observe that CL correctly reproduces the exact result. Interestingly, the CL values show an extremely mild dependence on the integration step, which is likely a consequence of the specific representation and in any way should not be interpreted as a general result. Additionally, we show the dependence of the integrated autocorrelation time as a function of the integration step in the right panel of Fig. 4.6. As in the real case, the autocorrelation time increases with smaller timestep. Interestingly, though, in contrast to the real case, the correlation between samples seems to exponentially grow with decreasing Δt. Regardless of the actual functional form, the autocorrelation time at large Δt seems to be slightly higher for this specific model than for RL.

Besides the actual results of the calculation, it is instructive to investigate the behavior of the drift term. In Fig. 4.7 we show the so-called classical flow pattern, which corresponds to the
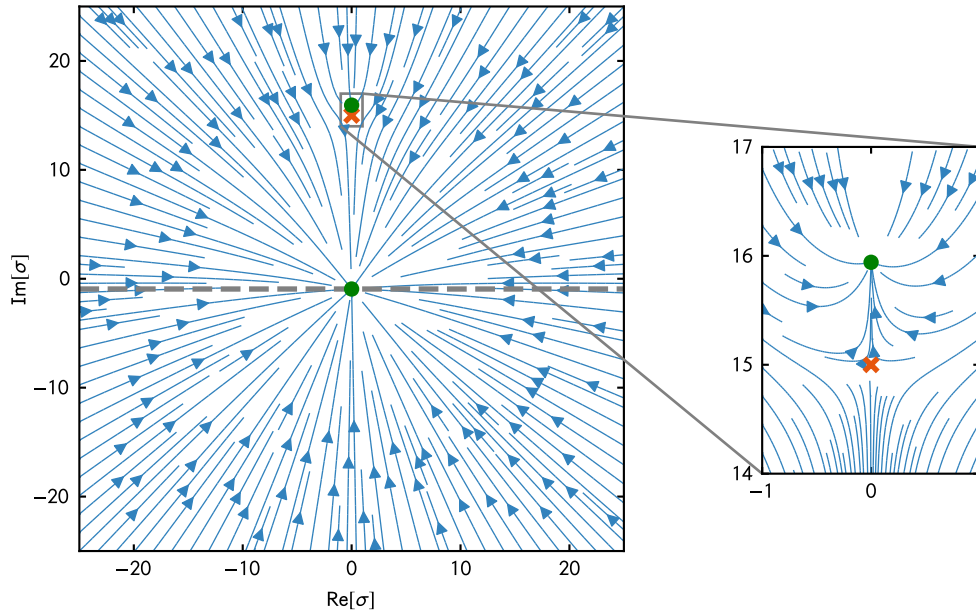
Figure 4.7: Classical flow diagram with attractive fixed points (green dots) and the pole associated with the branch point of the action (red cross). The gray dashed line represents the domain of the equilibrium probability distribution.

direction of the drift in the complex plane. We can immediately identify an attractive fixed point, i.e. a point in the complex plane with stationary action and a drift that is pointing towards it from any direction (lower green dot). It is conceivable that such a point is responsible for a steady state in the random process, as it will pull the field values towards it. Although the noise term will cause the field to fluctuate around this point, the field value can only rarely escape such a point. In fact, the existence of a sufficiently strong attractive fixed point has been shown to be necessary condition for the existence of an equilibrium distribution of the Langevin process [190, 191]. Luckily, this appears to be the case for the systems of interest in this thesis.

The situation might change drastically if poles are encountered inside the domain of the distribution. This could lead to a breakdown of ergodicity, due to a breakdown of holomorphicity of the action (the issue is revisited below). In the model considered here, we can indeed find a pole at the point $\sigma = 6\frac{\mu}{\lambda}$, which corresponds to the branch point of the action (marked by the red cross). At first glance, this looks very "dangerous" as there is also another attractive stationary point (upper green dot) in the vicinity of the pole. Generally, this could suggest faulty behavior. However, the imaginary part of the drift points away from the pole. Thus, even if a trajectory approaches this area of configuration space, fluctuations (which only occur in the real direction) will "kick the process back" into a stable trajectory that decays towards the attractive fixed point below. In equilibrium, the distribution will therefore be confined to the gray dashed line far away from the pole, ensuring correct behavior (i.e. it is approximately shifted from the real axis by a constant offset).

In Fig. 4.8 we show the Langevin time evolution of an actual random process as it was sampled with an integration step of $\Delta t = 0.01$. In the left panel we show the sampled field values σ in
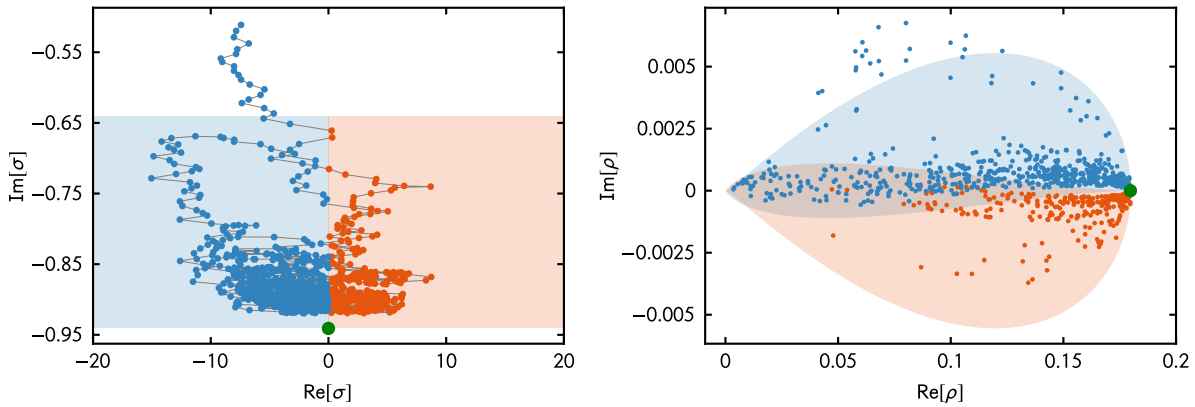
Figure 4.8: Sampling process in the complex plane. The sampled values of the auxiliary field σ are shown on the left. The corresponding values of the complex measure are shown in the right panel. The shaded areas represent areas with positive and negative real parts of σ (orange and blue, respectively) and map onto each other. The dots outside the shaded areas are early samples in the stochastic series which then converges to the attractive fixed point (green dot).

the complex plane. The process starts at a random point (top left in the plot), somewhat far away from the lower attractive fixed point (green dot). After a while, the imaginary part relaxes towards the attractor and the (real) noise causes the field value to fluctuate around it. This indeed corresponds to sampling the complex distribution defined in Eq. (4.5.8) as is shown in the right panel of Fig. 4.8. Shaded areas correspond to regions of positive (orange) and negative (blue) values of $\mathrm{Re}[\sigma]$. While these areas are rectangular in the σ-plane (left plot), they are deformed in the half-circles in the complex plane of $\rho(\sigma)$. The attractive fixed point sits exactly at $\mathrm{Re}[\sigma] = 0$ such that the trajectories in the right panel pass this point when switching from one domain to the other.

4.5.3 A closer look on complex measures & boundary terms

The above example shows that there is at least one case in which a complexified random walk leads to correct answers. To further formalize the approach, we take a closer look into the behavior of the various probability distributions to gain insights as to when the method is expected to deliver accurate results.

We start by writing the complex probability density of the physical expectation values given by

$$\rho[\phi_R] = \frac{1}{\mathcal{Z}} \mathrm{e}^{-S[\phi_R]}. \tag{4.5.12}$$

Note that this function defines a map from the real line (denoted by ϕ_R) to the complex plane. The expectation value of a given observable is then written as

$$\langle O \rangle_{\rho(t)} = \int \mathcal{D}\phi_R \, O[\phi_R] \rho[\phi_R, t], \tag{4.5.13}$$

where the average with respect to $\rho[\phi, t]$ is denoted in the subscript. Analogously to the derivation in Section 4.4.1, the fictitious time evolution can be obtained by a temporal differentiation of the

expectation values, which leads to the Fokker-Planck equation

$$\frac{\mathrm{d}}{\mathrm{d}t}\rho[\phi_R, t] = L_0^{\mathrm{T}}\rho[\phi_R, t] \tag{4.5.14}$$

with the FP operator

$$L_0^{\mathrm{T}} = \int \mathrm{d}\tau \mathrm{d}^d x \; \frac{\delta}{\delta\phi_R}\left(\frac{\delta}{\delta\phi_R} + \frac{\delta S[\phi_R]}{\delta\phi_R}\right). \tag{4.5.15}$$

To investigate the actually sampled probability density, we recall that we extended the random walk to the complex plane. Thus, the Langevin process in Eq. (4.5.35) will sample field values according to the density

$$P[\phi_R, \phi_I] = \frac{1}{\mathcal{Z}}\mathrm{e}^{-S[\phi_R + \mathrm{i}\phi_I]} \tag{4.5.16}$$

with the time-dependent expectation values

$$\langle O \rangle_{P(t)} = \int \mathcal{D}\phi_R \mathcal{D}\phi_I \; O[\phi_R, \phi_I] P[\phi_R, \phi_I, t]. \tag{4.5.17}$$

Unlike the complex distribution $\rho[\phi_R]$, the above probability measure maps from the complex plane to the set of real numbers. Since $P[\phi_R, \phi_I, t]$ is a positive semidefinite function by construction, it is a well-defined probability measure. Again, temporal differentiation of the above expression yields the associated Fokker-Planck equation

$$\frac{\mathrm{d}}{\mathrm{d}t}P[\phi_R, \phi_I, t] = L^{\mathrm{T}}P[\phi_R, \phi_I, t] \tag{4.5.18}$$

with yet another FP operator:

$$L^{\mathrm{T}} = \int \mathrm{d}\tau \mathrm{d}^d x \; \left\{\frac{\delta}{\delta\phi_R}\left(N_R\frac{\delta}{\delta\phi_R} - K_R\right) + \frac{\delta}{\delta\phi_I}\left(N_I\frac{\delta}{\delta\phi_I} - K_I\right)\right\}. \tag{4.5.19}$$

The central question is whether the expectation values obtained by this complexified random walk agree with the ones from the original, but complex, density $\rho[\phi_R, t]$. Stated differently, it is necessary to show that

$$\langle O \rangle_{\rho(t)} = \langle O \rangle_{P(t)}. \tag{4.5.20}$$

This equality should hold for all times, if the initial conditions of the two distributions agree. It is not obvious *a priori* whether this equation holds. In fact, it is not even clear that the process would converge and if it does, whether it converges to the correct answer. Indeed, following the steps outlined in Section 4.4.1 for the case of real Langevin, one finds that the resulting FP operator is neither self-adjoint nor positive semidefinite, such that the proof of convergence to the desired probability distribution is spoiled. In [189], some of the mathematical questions are investigated, however, general results remain scarce. Numerical evidence, on the other hand, points to the existence of a stationary distribution as well as correct answers for some models but faulty behavior for others.

In order to investigate the validity of Eq. (4.5.20) we closely follow the strategy devised in Refs. [189, 192]. The key step is to define an interpolating function

$$F(t,\tau) = \int \mathcal{D}\phi_R \mathcal{D}\phi_I \, O[\phi_R + \mathrm{i}\phi_I, \tau] P[\phi_R, \phi_I, t - \tau] \tag{4.5.21}$$

which corresponds to the limits

$$F(t,0) = \langle O \rangle_{P(t)}, \tag{4.5.22a}$$

$$F(t,t) = \langle O \rangle_{\rho(t)}. \tag{4.5.22b}$$

It is straightforward to verify Eq. (4.5.22a) by simply evaluating Eq. (4.5.21) at $\tau = 0$, which then yields an expression identical to the definition in Eq. (4.5.17). On the other hand, some work has to be done to show the second limit. First of all, we may choose the initial conditions

$$P[\phi_R, \phi_I, 0] = \rho[\phi_R, 0] \, \delta(\phi_I - \chi). \tag{4.5.23}$$

without loss of generality. This corresponds to an initial distribution that varies in the real direction but is confined to a certain point on the imaginary axis. Inserting the initial condition into Eq. (4.5.21) allows us to integrate over the imaginary direction:

$$F(t,t) = \int \mathcal{D}\phi_R \mathcal{D}\phi_I \, O[\phi_R + \mathrm{i}\phi_I, t] \, P[\phi_R, \phi_I, 0] \tag{4.5.24a}$$

$$= \int \mathcal{D}\phi_R \, O[\phi_R + \mathrm{i}\chi, t] \, \rho[\phi_R, 0] \tag{4.5.24b}$$

$$= \int \mathcal{D}\phi_R \, \mathrm{e}^{tL} O[\phi_R + \mathrm{i}\chi, 0] \, \rho[\phi_R, 0] \tag{4.5.24c}$$

$$= \int \mathcal{D}\phi_R \, O[\phi_R + \mathrm{i}\chi, 0] \, \mathrm{e}^{tL^{\mathrm{T}}} \rho[\phi_R, 0] \tag{4.5.24d}$$

$$= \int \mathcal{D}\phi_R \, O[\phi_R + \mathrm{i}\chi, 0] \, \rho[\phi_R, t] = \langle O \rangle_{\rho(t)}. \tag{4.5.24e}$$

For the third equality, we have exploited the fictitious-time evolution of the observable, in accordance with Eq. (4.4.14):

$$\frac{\mathrm{d}}{\mathrm{d}t} O[\phi, t] = L_{\mathrm{C}} O[\phi, t], \tag{4.5.25}$$

where $\phi = \phi_R + \mathrm{i}\phi_I$ is simply the complex field-value such that the associated complex FP operator reads

$$L_{\mathrm{C}} = \int \mathrm{d}\tau \mathrm{d}^d x \, \left(\frac{\delta}{\delta\phi} + \frac{\delta S[\phi]}{\delta\phi} \right) \frac{\delta}{\delta\phi}. \tag{4.5.26}$$

The formal solution of Eq. (4.5.25) is given by

$$O[\phi, t] = O[\phi, 0] \mathrm{e}^{tL_{\mathrm{C}}}. \tag{4.5.27}$$

Furthermore, we exploit that the operators L_{C} and L act equivalently on holomorphic observables

due to the Cauchy-Riemann equations and thus may be used interchangeably. The crucial step in this derivation is given by an integration by parts that shifts the time dependence from the observable to the probability distribution $\rho[\phi_R, t]$. This allows us to rewrite Eq. (4.5.24d) as the desired expectation value $\langle O \rangle_{\rho(t)}$ under the assumption that the boundary terms of this integration vanish.

The above discussion proves that $F(t, \tau)$ indeed interpolates between the appropriate limits (under certain conditions). If the function is independent of τ altogether, that is, if

$$\frac{\mathrm{d}}{\mathrm{d}\tau} F(t, \tau) = 0, \tag{4.5.28}$$

it follows that Eq. (4.5.20) holds. Upon performing the temporal differentiation we obtain

$$\begin{aligned}
\frac{\mathrm{d}}{\mathrm{d}\tau} F(t, \tau) = \int \mathcal{D}\phi_R \mathcal{D}\phi_I \Big\{ &P[\phi_R, \phi_I, t - \tau] \, LO[\phi_R + \mathrm{i}\phi_i, \tau] \\
&- L^{\mathrm{T}} P[\phi_R, \phi_I, t - \tau] \, O[\phi_R + \mathrm{i}\phi_i, \tau] \Big\},
\end{aligned} \tag{4.5.29}$$

which can be shown to vanish via integration by parts. Again, this proof operates under the critical assumption that the boundary terms vanish. Nonvanishing boundary terms are a potential source of problems within the CL approach as it has been shown that in such a case, the method sometimes produces spurious results by converging to the wrong limit [193, 194]. This contributed to the mixed success of CL over the years, as the issue was not thoroughly investigated up until recently. The requirement of vanishing boundary terms, however, allows us to arrive at a conclusion to determine whether we may trust the values from a CL calculation [189]. More precisely, if the product

$$P[\phi_R, \phi_I, t - \tau] \, O[\phi_R + \mathrm{i}\phi_I, \tau] \tag{4.5.30}$$

does not decay fast enough towards the boundaries of the integration domain, the formal argument underlying the complexification of the random process is spoiled. Hence, in this case it cannot be guaranteed that the expectation values obtained with a complexified random walk converge to the correct values.

While the condition of fast decay was recognized in [189, 192], the required rate was not immediately clear. In [195], the above arguments were reviewed by considering a finite step size in Langevin time. It was then found that integration by parts is valid if the probability distribution of the drift term falls off faster than any polynomial of the drift value towards large magnitudes.[12]

Criteria for correctness

The preceding discussion clearly shows the requirement for the validity of the CL method. However, the time-dependent probability distribution in Eq. (4.5.30) is hard to evaluate in practice. After all, we are typically interested in the equilibrium distribution to obtain equilibrium expectation

---

[12]It is noted that a few technical subtleties with respect to the definitions of the various FP operators have to be considered. Treating those, however, is beyond the scope of this thesis and it is simply referred to, e.g., Refs. [189, 192] for further details.
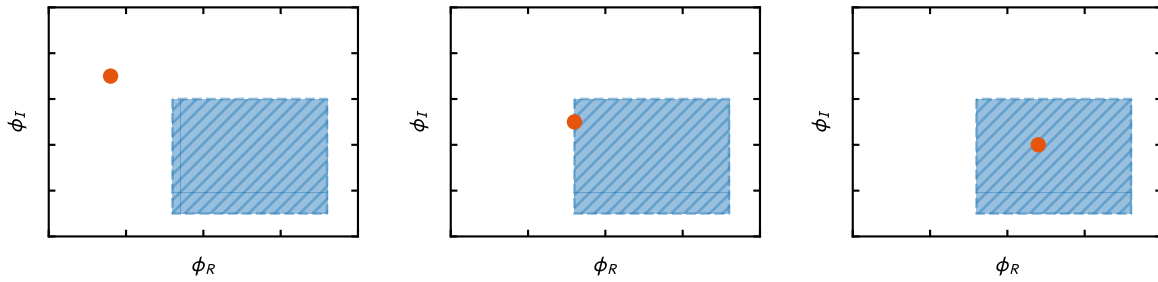
Figure 4.9: Schematic representation of possible pole positions. The shaded area represents the domain of the equilibrium distribution and red dots indicate nonanalytic points of the action. (Left) Pole outside the distribution. (Center) Pole at the edge. (Right) Pole inside the distribution.

values. In [189], the temporal behavior of Eq. (4.5.28) was thoroughly investigated for a few toy models and it was shown that the fictitious-time dependence is largest at $\tau = 0$, such that the knowledge of the time-dependence of the boundary terms is not required. These considerations culminated in a practical condition for the correctness of a CL simulation:

$$\langle LO \rangle = 0. \tag{4.5.31}$$

Technically, this has to be the case for all observables, which would correspond to an infinite number of conditions to check. Practically, however, this is not feasible and one may at least check the above condition for the observables of interest. If it holds, the check constitutes a strong argument for the validity of the results, whereas a violation renders the results unreliable.

4.5.4 Meromorphic drifts

Up to this point, our discussion of the validity of the CL approach relies on the important assumption of holomorphic actions. The fermionic theories of interest in this thesis require a determinant as the probability measure in the path integral, see Eq. (2.4.8). Since we define our action as

$$S[\phi] = e^{-\ln P[\phi]} = e^{-\ln \det M[\phi]}, \tag{4.5.32}$$

it is immediately apparent that zeroes of the fermion determinant lead to nonanalytic behavior of the action and thus require us to revisit the formal arguments presented above. Here, we only briefly discuss the central aspects in this regard and follow the conclusions of a recent extensive study of this issue [190].

The problems arise due to the singularities at zeroes of the determinant. The strategy to address this issue is to consider the integration domain without the pole region, that is, by manually cutting out a region around the singularity. In other words, we extend the boundary of the integration domain to include the contour of the region around the pole. The central question is then similar as before: how does the probability distribution $P[\phi]$ behave at the boundary around the poles? Naively, we could argue that $P[\phi]$ has a zero at the pole, and the random process will therefore never reach this point. As in the discussion above, though, it is not the vanishing of the probability at the pole but the decay towards it, which triggers correct or incorrect behavior.

If $P[\phi]$ decays only power-like, problematic contributions of these singularities may be observed. To further understand the implications on the sampled expectation values, three distinct scenarios have been considered in [190], which are also schematically depicted in Fig. 4.9.

Poles on the outside Naturally, poles outside the region of the equilibrium distribution are unproblematic, since after some thermalization the influence of the pole will be lost and expectation values are unbiased. Note that this is also the case for the toy problem discussed in Section 4.5.2 (visible as the red dot in Fig. 4.7 whereas the equilibrium distribution lies near the gray dashed line).

Poles at the edge It is essential to monitor the behavior of $P[\phi]$ around these points on the edge, and it has been found that for certain toy problems, such an occurrence could spoil the correctness [190]. This rules out an earlier explanation for the failure of CL, which rested on the winding of the process around the singularities [196].

Poles on the inside The main issue related to a pole inside the domain of the equilibrium distribution is the potential occurrence of bottlenecks, as the probability measure vanishes directly at the singularity. This, in turn, could lead to wrong expectation values due to a statistical underrepresentation of some subspace of the configuration space.[13]

Unfortunately, analytic insight into the pole structure is limited to simple toy problems. To investigate if a calculation suffers from the above issues in full-fledged many-body applications, it is important to closely monitor the sampled probability distribution. In [190], a variety of toy problems, as well as some high-energy-like models, have been investigated thoroughly in this regard.

4.5.5   Practical aspects

Aside from the conceptual issues of the CL method, there are some practical shortcomings that have to be properly addressed in order to obtain stable results. Here, we briefly outline the two main strategies relevant for this thesis.

Adaptive integration step

An early identified problem of Langevin methods is the appearance of numerically unstable averages. These so-called runaway solutions are the consequence of uncontrolled excursions of the random process, specifically in the imaginary direction. The issue is related to the accuracy of the integration of the drift term and may be conceptualized via the classical flow-diagram: an accumulated numerical error could push the CL process onto unstable trajectories that diverge towards large imaginary values. Since these trajectories are only reached through numerical noise, they do not belong to the dynamics of the problem. As a consequence, the running averages of the measured observables show unstable behavior and, depending on the frequency of such an occurrence, may fail to arrive at converged expectation values.

A naive way to address this issue is to use a tiny timestep in order to suppress the accumulation of numerical noise. However, this approach does not constitute a general solution of the problem. Additionally, the exploration of configuration space will be much slower which leads to increased

---

[13]This problem is related to the issue of meta-stability as remarked already in the discussion of Markov chains in Section 3.2.

numerical effort. In [197], instabilities have been cured by introducing an adaptive integration step. The idea is to rescale the integration step depending on the magnitude of the drift term in order to avoid problematic regions in the flow diagram. It was shown that such an approach provides a full solution to the problem of instabilities and has thus become standard in CL applications.

In this thesis, we apply a strategy along the lines of an algorithm proposed in [197] and simply rescale the timestep with the maximal value of the drift at every iteration:

$$\Delta t^{(n)} = \Delta t_0 \frac{K_0}{\max_{i\tau} |K[\phi^{(n)}]|}. \tag{4.5.33}$$

Here, $\Delta t^{(n)}$ is the new timestep used for the present update and Δt_0 is the average or target timestep. The parameter K_0 denotes the target drift, whose value may either be set manually or pre-computed during thermalization. In any case, only the product $\Delta t_0 K_0$ is of importance, such that in practice $K_0 = 1$ (with appropriate units) is a legitimate choice. Note that whenever we perform an extrapolation $\Delta t \to 0$, it is actually the target timestep Δt_0 that is extrapolated.

The regulator

A separate potential issue of CL simulations, as discussed at length above, is the insufficient decay of the probability distribution towards infinity. This leads to excursions to remote areas away from the region of interest and therefore may cause unstable behavior.[14] For the systems relevant in this work, the problem becomes apparent by re-examining the specific form of the Hubbard-Stratonovich transformation in Eq. (2.4.2a) which is proportional to $\sin \phi$. For real fields, the decoupling results in a compact integration domain. For complex-valued ϕ, on the other hand, we obtain

$$\sin \phi = \sin \phi_R \cosh \phi_I + i \cos \phi_R \sinh \phi_I, \tag{4.5.34}$$

which is unbounded in the imaginary direction and thus could lead to faulty behavior. To prevent uncontrolled excursions, a harmonic confinement of ϕ was proposed [198], such that the Langevin equations read

$$\phi_R^{(n+1)} = K_R[\phi^{(n)}]\Delta t + 2\xi\Delta t\phi_R^{(n)} + \sqrt{2\Delta t}\,\eta_R, \tag{4.5.35a}$$

$$\phi_I^{(n+1)} = K_I[\phi^{(n)}]\Delta t + 2\xi\Delta t\phi_I^{(n)}. \tag{4.5.35b}$$

Here, ξ is referred to as the regulator strength that keeps ϕ from wandering off. The modified Langevin equations then correspond to an action with an additional mass-like term

$$S[\phi] \to S[\phi] + \int d\tau d^d x \, \xi\phi(x,\tau), \tag{4.5.36}$$

---

[14]Note that the symptoms of this issue are similar to those of numerical instabilities. However, these trajectories belong to the dynamics of the physical problem and are not of accidental nature, in contrast to the ones that are produced through numerical noise.

which introduces a systematic bias in the computed expectation values. Therefore, it is necessary to check that the results are either insensitive to the regulator strength ξ or, equivalently, an extrapolation $\xi \to 0$ has to be performed. Stated differently, the idea is to simulate a series of well-behaved systems in order to extrapolate to the physically correct point.

It was observed that a regulator is a requirement to simulate nonrelativistic fermions via CL in a stable manner [78, 79, 198]. This is certainly true for the HS transform defined in Eq. (2.4.2a). However, other HS transforms exist which are self-regulated in the sense that a mass-like term naturally appears. To our knowledge, this avenue has not yet been pursued in nonrelativistic calculations.

Finally, it should be pointed out that the strategy is related to other ideas in the context of relativistic field theories. A mathematically well-defined solution to stabilize CL simulations of QCD-like models is the usage of gauge-cooling, which keeps the sampled configurations close to the desired manifold via suitable gauge transformations [199–202]. Another practical approach is the idea of dynamical stabilization, which was developed to further mitigate the excursion problem. The idea is to confine the non-compact directions of the configurations by a function that rapidly grows with the distance to the desired manifold. Although the approach cannot be derived from the action, it can be shown to vanish in the continuum limit [203–205].

Part II

Ultracold Fermi gases: insights from stochastic lattice approaches

5 | Fermi gases in one dimension

"60% of the time, it works every time."

Brian Fantana, Channel 4 News Team

The numerical study of one-dimensional (1D) quantum systems has received substantial attention in recent years, not least due to advances in experiments with tightly confined cold quantum gases. The stochastic approaches developed in the preceding sections may be formulated for 1D Fermi systems, which considerably reduces the numerical burden compared to higher dimensional systems. Naturally, this is a good starting point for the way towards the characterization of our many-body framework in the context of ultracold Fermi gases.

As already remarked in the introduction, a variety of 1D systems is solvable in closed form by the Bethe ansatz (BA) [70, 71]. The procedure provides closed expressions for many quantities of interest in the form of coupled integral equations (for continuous systems). To obtain concrete values, however, the roots of these equations have to be determined numerically which makes it difficult to obtain exact results beyond the few-body regime. In the thermodynamic limit (TL), corresponding to the limit of infinite particle number and volume at fixed density, expansions for several observables exist in both the weak and strong coupling limits. These allow for an important sanity-check of numerical values in the limit of large particle numbers.

While spin-imbalanced Fermi gases are accessible with the BA, a mass-asymmetry between the spin species restricts the otherwise powerful approach to selected points of certain symmetries [206–208]. This calls for numerical treatment, as also the mean-field method is actually less suitable for low-dimensional systems owing to the the enhanced influence of fluctuations.

Several numerical methods specialized to 1D systems are available such as the density-matrix renormalization group (DMRG) [209, 210] or tensor-network based methods [211], which exploit the low amount of entanglement in the system. In the few-body regime, reasonable system sizes can be computed with exact diagonalization due to a lower degree of degeneracy of the energy states. Moreover, through the usage of certain transformations in combination with worldline or worm-type algorithms, many 1D models may even be treated with MC methods without a sign problem despite the presence of imbalances. The reduced computational effort, as well as the abundance of benchmark methods, render 1D systems an ideal testbed for newly developed many-body methods. An extensive 1D benchmark study of several state-of-the-art many-body approaches may for instance be found in [212].

In the following, we investigate the ground state of 1D Fermi gases via the projective formulation of the lattice approaches discussed in Chapter 2. We start by benchmarking the HMC approach in the crossover from few to many fermions with equal masses and spin populations [78]. This initial study sets the methodological stage for the subsequent exploration of systems with either

one of these two conditions dropped. For the purely mass-imbalanced case, we cross-validate results from the iHMC and CL methods to establish both approaches as a useful tool for these otherwise challenging systems [79]. Subsequently, we focus solely on the CL method to investigate the pairing situation in spin-imbalanced gases. Finally, we combine both imbalances to address both spin- and mass-asymmetric Fermi gases.

A central quantity of interest is the ground-state energy, which we use to benchmark our results against existing results in the literature wherever available. Besides this "integrated" quantity, it is necessary to compute suitable two-body correlation functions in order to study the pairing structure of spin-up and -down particles. Although true long-range ordering in 1D is prohibited by the Mermin-Wagner theorem [213], quasi long-range order may still be the case in the sense of power-law rather than an exponential decay of the appropriate correlation functions. In the presence of spin imbalance, 1D systems are expected to favor correlations of the FFLO type as the leading instability. A particularly interesting quantity in this regard, with clear markers for the pairing patterns, is given by the so-called shot noise which constitutes an exciting opportunity also for experimental measurements [214].

5.1   Model & scales

The model under consideration in this chapter is the one-dimensional analogue of Eq. (2.1.1) which simplifies to

$$\hat{H} = \int_0^L \mathrm{d}x \left\{ \sum_{\sigma \in \{\uparrow,\downarrow\}} \hat{\psi}_\sigma^\dagger(x) \left(-\frac{1}{2m_\sigma} \frac{\partial^2}{\partial x^2} \right) \hat{\psi}_\sigma(x) + g\, \hat{\psi}_\uparrow^\dagger(x)\hat{\psi}_\downarrow^\dagger(x)\hat{\psi}_\downarrow(x)\hat{\psi}_\uparrow(x) \right\}. \qquad (5.1.1)$$

Throughout this chapter we employ periodic boundary conditions, which minimize the influence of the finite box size L. The model is often referred to as the Gaudin-Yang model [67, 68] and can be solved in closed form by the Bethe ansatz for the case $m_\sigma = m$, i.e., in the mass-balanced case.

The coupling g sets the interaction strength and is related to the 1D s-wave scattering length a through $g = 2/a$ (see, e.g., [12]). To facilitate a comparison to the literature, the dimensionless coupling

$$\gamma = \frac{g}{n} \qquad (5.1.2)$$

is introduced, where n denotes the total particle density $n = n_\uparrow + n_\downarrow$. Loosely speaking, γ quantifies the ratio of potential energy to kinetic energy such that $|\gamma| \gg 1$ corresponds to the strongly interacting regime and $|\gamma| \ll 1$ to the weakly interacting limit.[1]

In the following, all results are presented in dimensionless form. For a single species, the ground-state energy of the noninteracting Fermi gas is obtained by integrating the energy density of states, defined in Eq. (1.4.1), up to the Fermi energy and is is given by

$$E_{\mathrm{F}G,\sigma} = \int_0^{\varepsilon_{\mathrm{F},\sigma}} \mathrm{d}\varepsilon\, \varepsilon\, \rho^{\mathrm{1D}}(\varepsilon) = \frac{1}{3} N_\sigma \varepsilon_{\mathrm{F},\sigma}, \qquad (5.1.3)$$

---

[1]Especially in BA studies, treacherous factors of 2 may occur. Unless otherwise noted, we assume $m = 1$ in the mass-balanced case. In the literature, $2m = 1$ is sometimes used.

with the Fermi energy

$$\varepsilon_{\mathrm{F},\sigma} = \frac{k_{\mathrm{F},\sigma}^2}{2m_\sigma} \tag{5.1.4}$$

and the corresponding Fermi momentum

$$k_{\mathrm{F},\sigma} = \pi \frac{N_\sigma}{L} = \pi n_\sigma. \tag{5.1.5}$$

For a two-component gas we obtain

$$E_{\mathrm{FG}} = E_{\mathrm{FG},\uparrow} + E_{\mathrm{FG},\downarrow} = \frac{\pi^2}{6L^2}\left[\frac{N_\uparrow^3}{m_\uparrow} + \frac{N_\downarrow^3}{m_\downarrow}\right] \tag{5.1.6}$$

which reduces to

$$E_{\mathrm{FG}} = \frac{\pi^2}{24}\frac{N^3}{L^2} \tag{5.1.7}$$

in the spin- and mass-balanced case with total particle number $N = N_\uparrow + N_\downarrow$ and $m_\sigma = 1$.

5.2 From few to many in 1D balanced Fermi gases

As a first step on our way towards imbalanced Fermi gases, we benchmark our lattice approach in the balanced scenario, i.e., equally populated spin species of equal mass. In this simplest case, the determinants over the Fermi matrices of both spin species are equal such that

$$P[\phi] = (\det M[\phi])^2 \geq 0 \tag{5.2.1}$$

according to Eq. (3.3.5). This eliminates the sign problem and allows us to study these systems with the Metropolis-based HMC method.

With this tool, we explore some essential properties in the crossover from few to many fermions. It turns out that the question of how many is many strongly depends on the dimension and it is found that already the modest amount of $\sim 5\uparrow +5\downarrow$ particles is relatively close to the many-body limit in 1D. A qualitatively similar trend was observed in recent few-body experiments, which explore the convergence to the macroscopic limit one particle at a time, albeit in the presence of a harmonic trap [215, 216].

The results in the present section reflect an extension of an earlier work on these systems, where we have studied ground-state as well as the lowest excited energies and the contact parameter from few to many particles [155]. Here, we aim to extract information on the pairing properties via suitable correlation functions to set the stage for subsequent investigations of spin-imbalanced systems.

5.2.1 Numerical parameters

Unless otherwise noted, all results for correlation functions in this section are obtained for lattices of $N_x = 80$, which was found to be close to the infinite-volume limit. Along the same lines, the

one- and two-body correlation functions were found to be sufficiently converged to the ground state for $\beta \varepsilon_{\mathrm{F}} \approx 2.5 - 4.0$, slightly depending on the particle number. Since the extent of the imaginary-time axis is rescaled with the Fermi energy, the temporal lattice sizes vary for different particle densities as we have kept the discretization fixed at $\Delta\tau = 0.05$.

All our values represent averages over ~ 5000 statistically independent samples, allowing a relative uncertainty of $\sim 1 - 2\%$. To accumulate this number of samples, several trajectories reflecting different initial conditions have been combined. Decorrelation between the samples was ensured by separating measurements of observables by an average MD-trajectory length of $T_{\mathrm{MD}} = 1$. The trajectories are probed with a discrete step of $\Delta t_{\mathrm{MD}} = 0.05$ such that on average 20 transient states are sampled between subsequent measurements. This procedure yields an autocorrelation time on the order of 10^{-2} for all observables and parameter values studied.

5.2.2 Energy equation of state

To cross-check the present work with existing results, we re-computed values for the ground-state energy as a function of the coupling strength and particle number. The ground-state energy is defined as

$$E \equiv \langle \hat{H} \rangle = -\frac{\partial \ln \mathcal{Z}}{\partial \beta}, \tag{5.2.2}$$

which results in the following expression within our auxiliary-field lattice approach:

$$E = -\sum_{\sigma \in \{\uparrow,\downarrow\}} \int \mathcal{D}\phi \, P[\phi] \mathrm{Tr} \left\{ [M_\phi^\sigma(\beta)]^{-1} \frac{\partial M_\phi^\sigma(\beta)}{\partial \beta} \right\}, \tag{5.2.3}$$

in accordance with the discussion in Section 2.6. Note that this form also allows to compute the kinetic and interaction energies separately.

In Fig. 5.1, we compare our results for $E/E_{\mathrm{F}G}$ with the weak-coupling expansion,

$$\frac{E}{E_{\mathrm{F}G}} = 1 + \frac{6\gamma}{\pi^2} - \frac{\gamma^2}{\pi^2} + \dots \, , \tag{5.2.4}$$

and the strong-coupling expansion,

$$\frac{E}{E_{\mathrm{F}G}} = -\frac{3}{\pi^2}\gamma^2 + \left(\frac{\gamma}{1+2\gamma}\right)^2 \left(1 + \frac{4\pi^2}{15(1+2\gamma)^3}\right) + \dots \, , \tag{5.2.5}$$

in the TL as obtained from the BA [217, 218], where $E_{\mathrm{F}G}$ is given by Eq. (5.1.7). We observe that our results are in excellent agreement with the weak-coupling expansion for $|\gamma| \lesssim 2$ and with the strong-coupling expansion for $\gamma \lesssim -2$. The TL appears to be approached rather rapidly, which is evident from the inset of Fig. 5.1. With increasing particle number, the energy obtained on the lattice oscillates around the TL result with a decreasing amplitude.

The exact (binding) energy of one spin-up and one spin-down fermion interacting via a contact interaction in the infinite-volume limit is given by

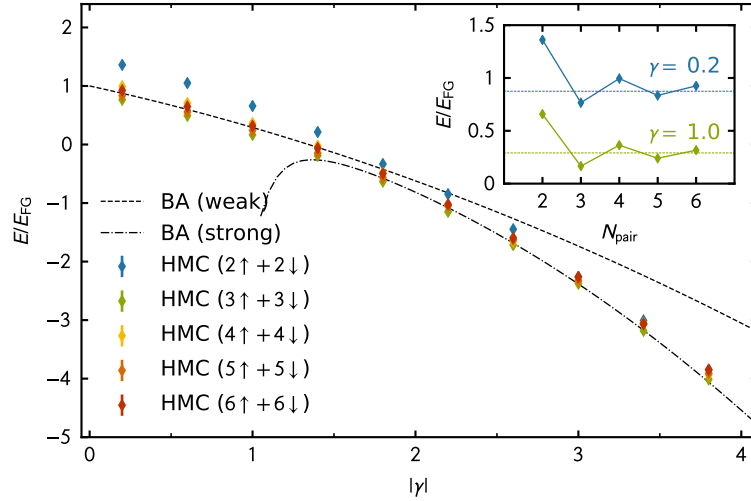$$E_{1+1} = -g^2/4 = -3\gamma^2/\pi^2 \, E_{\mathrm{F}G}. \tag{5.2.6}$$

Figure 5.1: Equation of state for $N = 4$ to 12 particles as a function of $|\gamma|$, extrapolated to infinite volumes. The dashed and dot-dashed lines are the results from the BA [217] in the TL for weak and strong coupling, respectively. (Inset) Particle number dependence of E/E_{FG} for $\gamma = -0.2$ and $\gamma = -1.0$ compared to the BA.

From Eq. (5.2.5), we observe that the ground-state energy per pair is simply given by the energy of the $1 + 1$-body problem, $E/N_{\mathrm{pairs}} = -g^2/4$, at leading order in the strong-coupling expansion. Loosely speaking, the dynamics in the strong-coupling limit may therefore be viewed as dominated by the formation of tightly bound $\uparrow\downarrow$-pairs. In the strict infinite-coupling limit $1/\gamma \to 0$, the many-body system may be viewed as a gas of composite bosons, known as the Tonks-Girardeau gas [219].

In the weak-coupling limit, a finite gap $\Delta/E_{\mathrm{FG}} \sim |\gamma|e^{-\pi^2/(2|\gamma|)}$ has been found to emerge between the singlet ground state and the first triplet excited state together with gapless density fluctuations [217, 220–223]. Consequently, the dynamics of the many-body system in this limit is associated with a BCS superfluid. For a detailed discussion of the many-body phase diagram see, e.g., [223]. Here, we only highlight that a smooth crossover from the formation of tight bosonic molecules in the limit $1/\gamma \to \infty$ to Cooper pairing in the limit $1/\gamma \to -\infty$ is found to occur at $\gamma \sim -2$ in this system. At this point, the size of the bosonic pairs is of the order of the distance between the fermions [217, 223].

Indeed, for the two-body problem in the infinite-volume limit, the "diameter" d_0 of the bosonic pair is given by $d_0 = 2/|g|$, see, e.g., [224]. Thus, we have $d_0 n = 2/|\gamma|$ which may be viewed as a measure for the crossover point in terms of the coupling at which the properties of the system change significantly.[2]

In the following subsections we do not aim at a detailed quantitative discussion of the phase diagram but focus on our results for the momentum distribution as well as the one- and two-body density matrices.

---

[2]We define the diameter d_0 as $\frac{1}{e}|\Phi(0, d_0/2)|^2 = |\Phi(0, 0)|^2$, where $\Phi(x_\uparrow, x_\downarrow)$ is the ground-state wave function. Note that Φ is only a function of $|x_\uparrow - x_\downarrow|$ in the infinite-volume limit.

5.2.3 One-body response functions

The one-body density matrix ρ_σ in principle allows us to compute all single-particle expectation values and is defined as ground-state expectation value of a creation and annihilation operator:

$$\rho_\sigma(x, x') = \langle \hat{\psi}_\sigma^\dagger(x) \hat{\psi}_\sigma(x') \rangle, \tag{5.2.7}$$

where σ refers to the spin index and the operators $\hat{\psi}_\sigma$ ($\hat{\psi}_\sigma^\dagger$) denote annihilation (creation) operators, respectively. In terms of a general N-body wave function $\Phi(x_{\uparrow,1}, x_{\downarrow,1}, \dots, x_{\uparrow,N_\uparrow}, x_{\downarrow,N_\downarrow})$, the one-body density matrix associated with a single spin species is given by

$$\rho_\sigma(x, x') = N_\sigma \int_{-\frac{L}{2}}^{\frac{L}{2}} dy_2 \cdots \int_{-\frac{L}{2}}^{\frac{L}{2}} dy_N \ \Phi^*(x, y_2, \dots, y_N)\Phi(x', y_2, \dots, y_N). \tag{5.2.8}$$

The single-particle momentum distribution n_{kq}^σ is implicitly defined by the Fourier transform of the above expression:

$$\rho_\sigma(x, x') = \sum_{k,q} \varphi_k^*(x) \, n_{kq}^\sigma \, \varphi_q(x'), \tag{5.2.9}$$

where

$$\varphi_k(x) = \frac{1}{\sqrt{L}} e^{i\omega_k x} \tag{5.2.10}$$

and $\omega_k = 2\pi k/L$ for a periodic box of extent L considered in this work.

The one-body density matrix ρ_σ determines the overlap of a state in which a fermion with spin σ has been removed from the ground state at point x', with a state in which a fermion with the same spin σ has been removed at point x. Correspondingly, the associated single-particle momentum distribution determines the overlap of a state in which a fermion with spin σ and momentum q has been removed from the ground state, with a state in which a fermion with the same spin σ but momentum k has been removed. From the definition of the single-particle momentum distribution, it follows immediately that it is only finite for $|k| \leq k_{\mathrm{F}}$ and $|q| \leq k_{\mathrm{F}}$ in the noninteracting limit.

In a periodic box, the one-body density matrix of the noninteracting system can be computed analytically. We find

$$\rho_\sigma(x, x') = \frac{1}{L} \left\{ 1 + 2\sum_{j=1}^{\bar{N}_\sigma} \cos\left(\omega_j(x - x')\right) \right. \tag{5.2.11}$$

$$\left. + \delta_{(N_\sigma \bmod 2),0} \left[\cos\left(\omega_{\bar{N}_\sigma + 1}(x - x')\right) - \cos\left(\omega_{\bar{N}_\sigma + 1}(x + x')\right) \right] \right\},$$

where

$$\bar{N}_\sigma = \begin{cases} (N_\sigma - 1)/2 & \text{for } N_\sigma \text{ odd,} \\ (N_\sigma - 2)/2 & \text{for } N_\sigma \text{ even.} \end{cases} \tag{5.2.12}$$
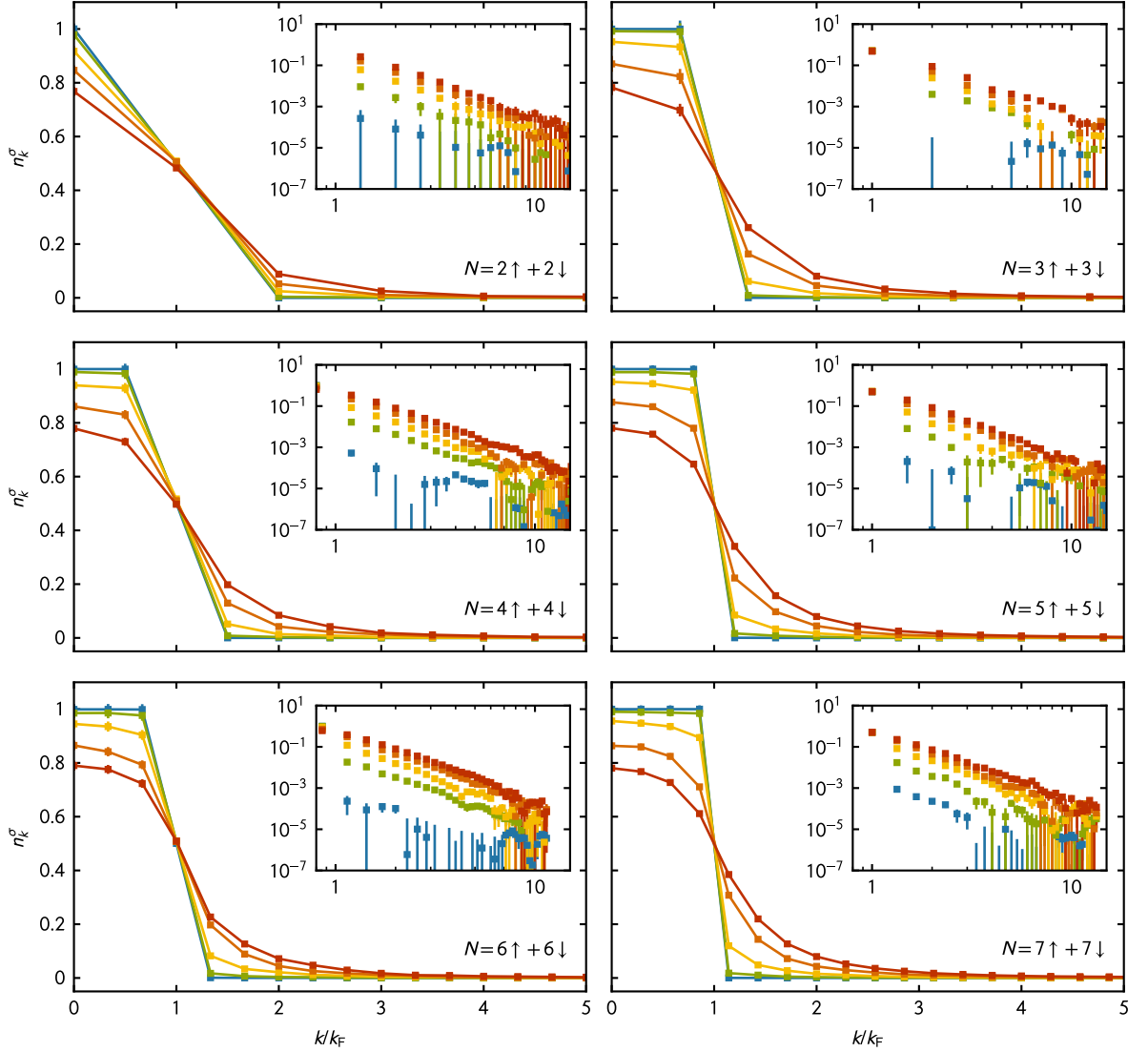
Figure 5.2: Diagonal part of the momentum distribution n_k^σ as a function of k/k_F for $\gamma = -0.2, -1.0, -2.0, -3.0, -4.0$ (blue, green, yellow, orange, red symbols, respectively) for various particle numbers N (different panels). Solid lines are guides to the eye. (Insets) Asymptotic behavior on a double logarithmic scale.

For odd N_σ, the one-body density matrix of the noninteracting system is a translation-invariant quantity as it only depends on the distance between x and x'. For even N_σ, however, the one-body density matrix of the noninteracting system is no longer translation-invariant in a periodic box but depends on x and x' separately, see Eq. (5.2.11). Nevertheless, in the large-N_σ limit, the term breaking translation invariance is only subdominant, implying that the one-body density matrix becomes a translation-invariant quantity in the TL, as it should be. In fact, we have

$$\rho_\sigma(x, x') = \frac{\sin\left(\pi n_\sigma |x - x'|\right)}{\pi |x - x'|} \qquad (5.2.13)$$

for fixed $n_\sigma = N_\sigma/L$ with $N_\sigma \to \infty$ and $L \to \infty$. We emphasize that the breaking of translation invariance in systems with even N_σ is a direct consequence of the fact that the ground-state wave function of the noninteracting system is not an eigenstate of the center-of-mass momentum operator $\hat{P}_{\text{tot}}$. It is, however, an eigenstate of $\hat{P}_{\text{tot}}^2$. For odd N_σ, on the other hand, the ground-state wave function is an eigenstate of $\hat{P}_{\text{tot}}$ with zero eigenvalue.[3] Since the ground-state wave function of the fully interacting system is effectively generated by exciting the ground-state wave function of the noninteracting system according to the momentum-conserving interaction, we conclude that translation invariance of the ground-state wave function is preserved in our MC studies for systems with odd N_σ but is violated for systems with even N_σ, see also [225] for a discussion of this issue for systems in (anti)periodic boxes. We return to this below when discussing our results for the one-body density matrix.

From the one-body density matrix in Eq. (5.2.11), the momentum distribution n_{kq}^σ of the noninteracting system is readily obtained. We find

$$n_{kq}^\sigma = \delta_{kq}\theta(\bar{N}_\sigma - |k|) \tag{5.2.14}$$
$$+ \frac{1}{2}\delta_{(N_\sigma \bmod 2),0}\left(\delta_{k,(\bar{N}_\sigma+1)} - \delta_{k,-(\bar{N}_\sigma+1)}\right) \times \left(\delta_{q,(\bar{N}_\sigma+1)} - \delta_{q,-(\bar{N}_\sigma+1)}\right),$$

where

$$\theta(x) = \begin{cases} 1 & \text{for } x \geq 0, \\ 0 & \text{otherwise.} \end{cases} \tag{5.2.15}$$

In Fig. 5.2, we show our results for the diagonal part of the momentum distribution $n_k^\sigma \equiv n_{kk}^\sigma$ for both spin species as a function of k/k_{F} for various particle numbers and coupling strengths γ. For small values of the coupling, $0 < |\gamma| \lesssim 1$, the momentum distribution is still well described by the noninteracting momentum distribution, independent of the total particle number N. For stronger couplings, $\gamma \lesssim -2$, the system is then dominated by the formation of tightly bound dimers where the crossover to this regime from the weakly coupled regime dominated by Cooper pairing occurs at $\gamma \sim -2$, as already remarked above. In the regime with $\gamma \lesssim -2$, the momentum distributions clearly deviate from their noninteracting counterparts. More specifically, even fermions which initially reside in states with low momenta are now excited above the Fermi point k_{F}. Loosely speaking, the momentum distributions effectively start to flatten out when the coupling is increased beyond $\gamma \lesssim -1$ and therefore these distributions lose their characteristic feature of a sharp drop present in the weak-coupling limit.

From the scaling behavior of the momentum distribution, further quantities such as the sound velocity [226, 227] and Tan's contact parameter [228–230] may be obtained. The former dictates the scaling behavior close to the Fermi point and may be computed, for instance, by performing a fit to the numerical data in the low-momentum regime $k \lesssim k_{\text{F}}$. Without discussing further details, it was found that the sound velocity remains close to the Fermi velocity for $|\gamma| \lesssim 2$. For $|\gamma| \gtrsim 2$, the sound velocity then starts to decrease rapidly, indicating that the system enters the crossover

---

[3]As the Hamiltonian and parity operators commute with each other, the ground-state wave function (including the center-of-mass motion) can be chosen to be an eigenstate of the parity operator. Note that the part of the ground-state wave function describing the relative motion of the fermions has even parity whereas the parity of the center-of-mass wave function can be chosen at will. In our numerical implementation, conventions effectively correspond to choosing the center-of-mass wave function to have odd parity for even N_σ. For odd N_σ, we choose the center-of-mass wave function to have odd parity if $(N_\sigma - 1)/2$ is odd, and otherwise even.

area between the regime dominated by Cooper pairing at small attractive couplings and a regime governed by the formation of a gas of tightly bound bosonic molecules, in accordance with earlier studies [223]. These findings are in good agreement with Bethe ansatz results in the TL at large and small coupling [220, 222].

To extract Tan's contact, it is possible to exploit the asymptotic behavior of the momentum distribution, which is related to the contact parameter C via

$$C \equiv \lim_{|k| \to \infty} k^4 n_k \,. \tag{5.2.16}$$

By performing a linear fit to n_k for momenta with $|k| > k_{\mathrm{F}}$ on a double-logarithmic scale we may extract C, see also the insets of Fig. 5.2. Note that, for very dilute systems, the high momentum part is subject to noise which explains the seemingly odd behavior at large momenta. In addition, the high-momentum occupancy is very sensitive to the finite size of the box. These effects complicate a determination of the contact parameter through this procedure. Nevertheless, agreement was observed with previously obtained results for even N_σ using a different route towards a determination of the contact parameter via the Feynman-Hellmann theorem [155]. The present determination, however, exhibits a larger errorbar and is therefore inferior to the more stable procedure in [155]. A detailed discussion of Tan's relation in 1D may be found in [231].

In addition to the momentum distribution, we here discuss results for the one-body density matrix. In Fig. 5.3, we present our results for ρ_σ as a function of the dimensionless coordinates $k_{\mathrm{F}} x$ and $k_{\mathrm{F}} x'$ in a periodic box for $N = 2\uparrow + 2\downarrow, 3\uparrow + 3\downarrow, 4\uparrow + 4\downarrow, 5\uparrow + 5\downarrow$ fermions (from left to right) and $\gamma = 0, -0.2, -3.0$ (from top to bottom). The color coding is associated with the value of the one-body density matrix at the point (x, x'). The results for finite γ represent numerical data from our MC calculations, whereas the result for the noninteracting system ($\gamma = 0$) was obtained analytically in Eq. (5.2.11).

The results shown in Fig. 5.3 exemplify our findings for other particle numbers. As suggested by the analytic solution for the noninteracting limit, we observe that the number of oscillations at fixed coupling and box size increases with increasing particle number. The scale for these oscillations is set by the density. The main maxima of the one-body density matrix are found along the lines with $|x - x'| = \nu L$, with $\nu \in \mathbb{Z}$. However, as already indicated above, we also clearly see that translation invariance is broken for even N_σ, whereas it is manifest for odd N_σ. Loosely speaking, this invariance is progressively restored as the particle number is increased. The mild violation of translation invariance for $\gamma = -3.0$ and odd N_σ in Fig. 5.3 is due to statistical uncertainties in our MC calculations at strong couplings.

5.2.4 Pair correlation function

In addition to the one-body quantities, we have calculated the pair-correlation function, also known as the on-site two-body density matrix. In one-dimensional systems, this function has attracted a lot of interest for instance in the search for FFLO phases [232]. It is defined as

$$\rho_{\uparrow\downarrow}(x, x') = \langle \hat{\psi}_\uparrow^\dagger(x) \hat{\psi}_\downarrow^\dagger(x) \hat{\psi}_\uparrow(x') \hat{\psi}_\downarrow(x') \rangle \,. \tag{5.2.17}$$
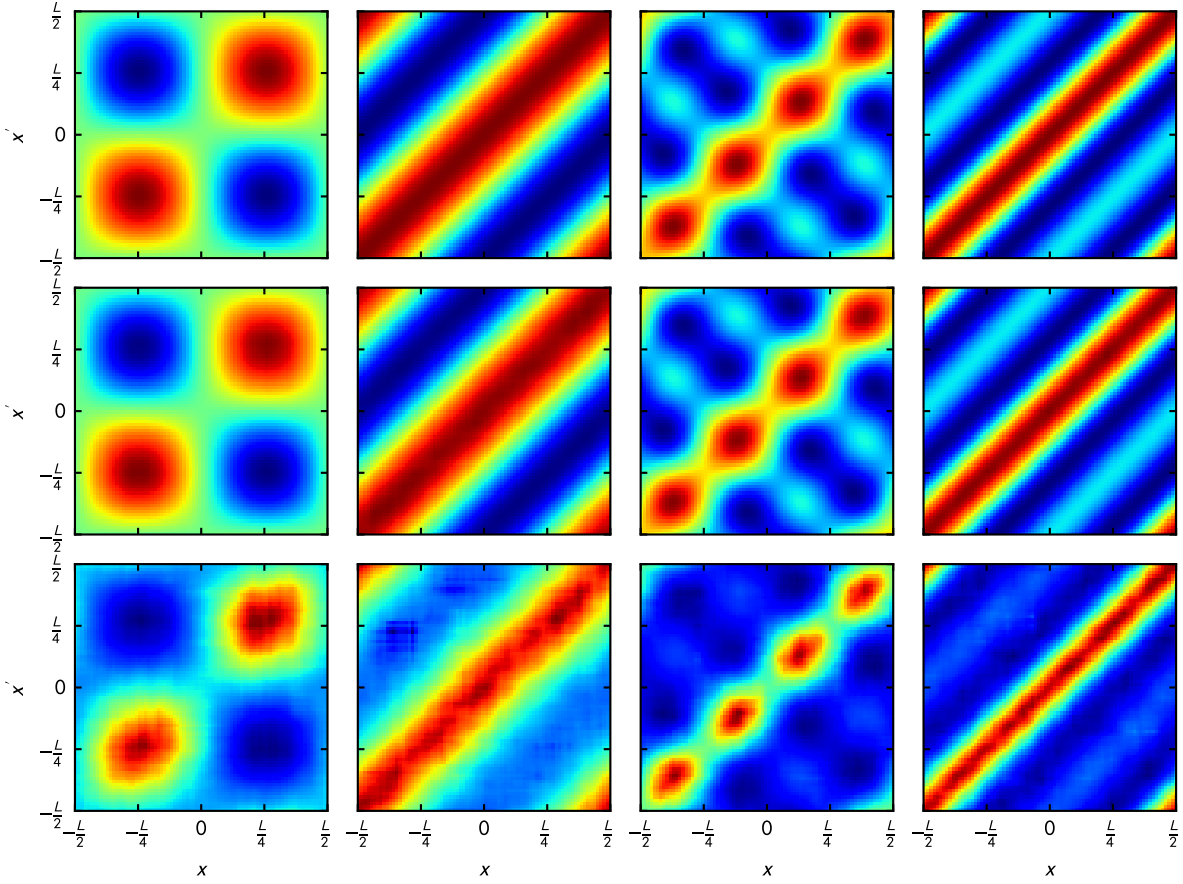
Figure 5.3: One-body density matrix $\rho_\sigma(x, x')$ as a function of the coordinates x and x' for $N = 2\uparrow +2\downarrow, 3\uparrow +3\downarrow, 4\uparrow +4\downarrow, 5\uparrow +5\downarrow$ fermions (from left to right) and $\gamma = 0, -0.2, -3.0$ (from top to bottom) in a periodic box with L. The analytic result for the noninteracting limit ($\gamma = 0$) is given in Eq. (5.2.11). The color coding is associated with the value of $\rho_\sigma(x, x')$ (largest values are colored red, lowest values are colored blue). The violation of translation invariance is clearly visible in the results for even N_σ but is continuously weakened for increasing N_σ, see main text for a detailed discussion.

This expression can be rewritten in terms of the ground-state N-body wave function Φ:

$$\rho_{\uparrow\downarrow}(x, x') = N_\uparrow N_\downarrow \int_{-\frac{L}{2}}^{\frac{L}{2}} \mathrm{d}y_3 \cdots \int_{-\frac{L}{2}}^{\frac{L}{2}} \mathrm{d}y_N \ \Phi^*(x, x, y_3, \dots, y_N) \times \Phi(x', x', y_3, \dots, y_N) \,. \quad (5.2.18)$$

Note that

$$\int_{-\frac{L}{2}}^{\frac{L}{2}} \mathrm{d}x \, \rho_{\uparrow\downarrow}(x, x) = \frac{N_\uparrow N_\downarrow}{L} \,, \quad (5.2.19)$$

where $N_\uparrow N_\downarrow$ is the number of all possible combinations of one spin-up fermion with one spin-down fermion in a system with $N = N_\uparrow + N_\downarrow$ fermions.

The pair-correlation function determines the overlap of a state in which a pair of one spin-up and one spin-down fermion has been removed from the ground state at point x', with a state in
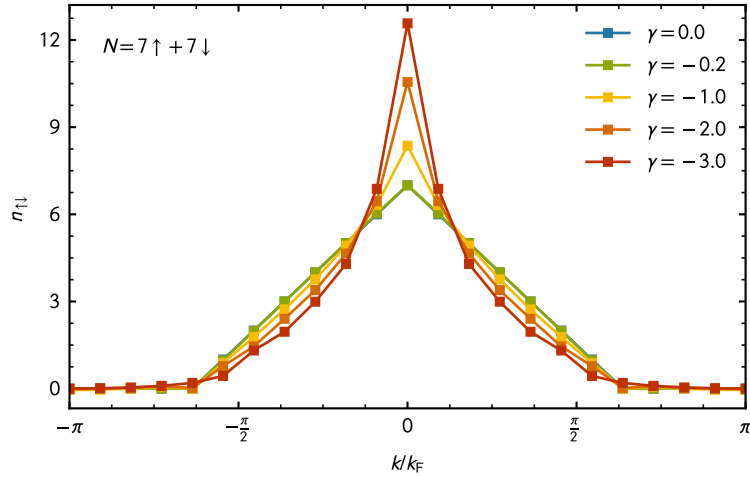
Figure 5.4: Pair-momentum distribution function $n_{\uparrow\downarrow}(k/k_{\mathrm{F}})$ for $N = 7 \uparrow +7 \downarrow$ fermions and different values of the coupling.

which such a pair has been removed at point x. Correspondingly, the so-called pair-momentum distribution $n_{\uparrow\downarrow}(k, q)$ determines the overlap of a state in which a pair of one spin-up and one spin-down fermion with momentum q has been removed from the ground state, with a state in which such a pair with momentum k has been removed. It is implicitly defined through the Fourier transform of the pair-correlation function

$$\rho_{\uparrow\downarrow}(x, x') = \sum_{k,q} \varphi_k^*(x) n_{\uparrow\downarrow}(k, q) \varphi_q(x') \,. \tag{5.2.20}$$

From Eq. (5.2.19), it follows immediately that

$$\sum_{k,q} n_{\uparrow\downarrow}(k, q) = \frac{N_\uparrow N_\downarrow}{L} \,. \tag{5.2.21}$$

Note that, by definition, the pair-momentum distribution is related to the propagation of a pair of vanishing size.

In the noninteracting limit, the pair-correlation function is simply the product of the one-body density matrices associated with the spin-up and spin-down fermions:

$$\rho_{\uparrow\downarrow}(x, x') = \rho_\uparrow(x, x') \rho_\downarrow(x, x') \,. \tag{5.2.22}$$

We immediately conclude that the pair-correlation function in a periodic box also suffers from terms violating translation invariance for even N_σ. Thus, the convergence to the TL is in general expected to be faster for odd N_σ. For our discussion of the pair correlation function in this work, we shall therefore focus on the latter case from now on. The associated pair-momentum distribution of the noninteracting system then reads

$$n_{\uparrow\downarrow}(k, q) = \frac{\delta_{k,q}}{L} \sum_{j=-\infty}^{\infty} \theta(\bar{N}_\uparrow - |j|)\theta(\bar{N}_\downarrow - |j + k|) \,. \tag{5.2.23}$$

Without loss of generality, we may now assume $\bar{N}_\uparrow \geq \bar{N}_\downarrow$ to obtain

$$
n_{\uparrow\downarrow}(k,q) = \frac{\delta_{k,q}}{L}\Big[(2\bar{N}_\downarrow + 1)\theta(|\bar{N}_\uparrow - \bar{N}_\downarrow| - |k| - 1) \tag{5.2.24}
$$
$$
+ (\bar{N}_\uparrow + \bar{N}_\downarrow + 1 - |k|)\theta(|k| - |\bar{N}_\uparrow - \bar{N}_\downarrow|) \times \theta(\bar{N}_\uparrow + \bar{N}_\downarrow - |k|)\Big],
$$

with the definition of $\theta(x)$ as in Eq. (5.2.15). From this expression, we observe that, for spin-balanced systems, the pair-momentum distribution assumes a global maximum for $k = q = 0$. Phenomenologically, this implies that finding an on-site pair with zero momentum is most probable. This observation is in line with standard BCS theory where pairing of spin-up and spin-down fermions both located on the Fermi surface but with opposite momenta is most favorable in the presence of an infinitesimally weak but finite attractive coupling, eventually leading to a destabilization of the Fermi surfaces.

We note that, for spin-imbalanced systems, the pair-momentum distribution of the noninteracting system remains constant up to momenta $q \sim |k_{F,\uparrow} - k_{F,\downarrow}|$ and then decreases monotonically. For interacting spin-imbalanced systems, the pair-momentum distribution has even been found to develop maxima at $\pm q$, see Refs. [232, 233]. Since q is associated with the center-of-mass momentum of the formed on-site pairs, the observation of such maxima may be viewed as a precursor for the formation of FFLO-type ground states, where q sets the scale for the periodic structure of the ground state in the many-body phase diagram [52, 53]. *A priori*, however, the mere existence of such maxima in the pair-correlation function does not necessarily entail that pairs with momenta q describe the lowest-lying two-body states in the spectrum and that a condensate is composed of these states, see, e.g., [234]. Still, (pronounced) maxima at $\pm q$ may be viewed as an indication that the formation of pairs with momenta q is favored.

In Fig. 5.4, as a concrete example for the pair-momentum distribution, we show our results for the diagonal part of $n_{\uparrow\downarrow}$ as a function of the momentum k for a spin-balanced system of $N = 7 \uparrow + 7 \downarrow$ fermions. For increasing coupling γ, we observe that the pair-momentum distribution progressively narrows, resulting in an increase of the maximum at vanishing momenta. This may be viewed as an indicator that it is energetically favored for pre-formed on-site pairs to occupy the state of zero center-of-mass momentum.

Finally, it is worthwhile to note that the observed progressive formation of a narrow maximum in the momentum distribution associated with the formation of on-site pairs is also consistent with the observation that the system is expected to undergo a smooth crossover from Cooper pairing at small attractive couplings to a gas of bosonic molecules at $\gamma \sim -2$, see the discussion above.

5.3   Mass-imbalanced fermions: equation of state

In this section, we extend our study of balanced Fermi gases to systems consisting of fermions with different masses. Given the rapid experimental progress in the context of mass-imbalanced quantum gases, this study aims at the further theoretical development of stochastic frameworks required for *ab initio* studies of such systems in any dimension. With these developments, we particularly aim at aspects which can currently be accessed only in a very limited fashion with conventional MC methods, if at all, as a consequence of the fermionic sign problem.

To test our developments, we examine the EOS of mass-imbalanced Fermi mixtures when confined to one spatial dimension. Although 1D systems are also experimentally relevant, as remarked

above, we do not aim at a high-precision calculation of the EOS with the present study. Our goals are rather of methodological nature. From this standpoint, the 1D limit is appealing since the running times of the computations are comparatively short and it is therefore possible to take vastly more data than in higher dimensions. This allows to reduce systematic errors (e.g., by studying large lattice sizes) and to focus on the underlying methods. Moreover, as it is well known, 1D systems of fermions with contact interaction are typically solvable by the Bethe ansatz for arbitrary particle numbers [71]. However, as remarked already above, an analytic solution is currently out of reach for systems involving particles of general unequal masses. While the two-body problem can of course be solved, the solution of mass-imbalanced few-body systems is restricted to specific mass configurations [206, 208], infinite interaction strength [207], or specific boson-fermion mixtures [235]. In any case, the existence of analytic solutions in some cases and the absence of theoretical results in other cases represents a further motivation for the developments discussed in this section.

It is worth noting that progress has been made in related cases such as the half-filled asymmetric Hubbard model in 1D [236] as well as 3D [237], which does not feature a sign problem and is directly connected to the Falicov-Kimball model in the limit of large asymmetry. Cases away from half filling were also studied in [238, 239] and the few-body limit was recently addressed by means of a suitable worldline algorithm that can be formulated without a sign problem in 1D [122, 123]. Furthermore, exact diagonalization studies have addressed harmonically trapped systems of up to $N_\uparrow + N_\downarrow = 10$ particles [240, 241]. While these methods provide results for the few-body regime, it is challenging to extend them beyond low particle numbers or to higher dimensions due to the prohibitive scaling of memory requirements. A recent review on one-dimensional few-body mixtures, involving mass-imbalanced systems, may be found in [242].

Below, we present our fully nonperturbative results for the ground-state energy of interacting fermions of unequal masses. We compare our results to those obtained by other methods wherever possible. Additionally, we show the EOS for the ground-state energy as a function of interaction strength across a wide range of mass imbalances. To the best of our knowledge, this is the first determination of the full EOS for mass-imbalanced fermions interacting via a contact interaction in 1D.

5.3.1   Scales & parameters

To quantify the mass imbalance between the two spin species, we introduce the dimensionless relative mass-asymmetry

$$\bar{m} = \frac{m_\uparrow - m_\downarrow}{m_\uparrow + m_\downarrow}, \tag{5.3.1}$$

which vanishes in the case of equal masses. For systems with balanced spin populations considered in this section, the results are invariant under the transformation $\bar{m} \to -\bar{m}$. Fixing the relative asymmetry only eliminates one degree of freedom, such that several choices of $(m_\uparrow, m_\downarrow)$ lead to the same value of $\bar{m}$. In the following, we choose to work at constant total mass $M = m_\uparrow + m_\downarrow$ which motivates to write the particle masses as

$$m_{\uparrow/\downarrow} = m_0 \pm \frac{\delta m}{2} \tag{5.3.2}$$

with

$$\bar{m} = \frac{\delta m}{2m_0}. \tag{5.3.3}$$

We set $m_0 = 1$ for the remainder of this section, which fixes the scale for the masses in our calculations. With these conventions, a mixture of ^{161}Dy and ^{40}K corresponds to $\bar{m} \approx 0.602$.

To calculate the noninteracting energy on the lattice, we simply sum the single-particle energies. As a function of the mass imbalance $\bar{m}$ we obtain

$$E_{\bar{m}} = E_0 \left[\frac{1}{1 - \bar{m}^2} \right], \tag{5.3.4}$$

where E_0 is the corresponding noninteracting energy for mass-balanced systems on the lattice. Note that the energy as obtained from a calculation in the mean-field approximation exhibits the same dependence on $\bar{m}$ as the noninteracting system (see, e.g., [63]).

Numerical parameters

Throughout this section, we set the number of 1D spatial lattice sites to $N_x = 40$, which was found to be sufficient for the methodological purpose of the present investigation. A scaling behavior of 1D mass-balanced Fermi gases was performed in an earlier investigation and may be found in [78, 155]. As before, the temporal lattice spacing was chosen to be $\tau = 0.05$ which is sufficient to study the interaction strengths under consideration, even in the presence of a mass asymmetry. Furthermore, we numerically extrapolate to the limit of large imaginary time $\beta \varepsilon_{\mathrm{F}}$ by averaging over a few results obtained at sufficiently large propagation times, following also the discussion for the balanced systems and [155]. To carry out that extrapolation, we performed calculations on temporal lattices as large as $N_\tau \sim 1500$, which we found in previous works to be sufficient for the particle numbers and couplings considered here.

Each data point shown was computed using an average of $\sim 5 \times 10^3$ decorrelated samples (both in the iHMC and CL approaches), which have been obtained via a few independent trajectories. For the iHMC results, we have relied on the same numerical parameters as in the balanced case. This leads again to an integrated autocorrelation time of $\tau_{\mathrm{int}} \approx 10^{-2}$, largely unaffected by the mass imbalance. For the CL study, we have employed an adaptive integration step whose influence on the ground-state energy is investigated below. The resulting autocorrelation is comparable to the ones from iHMC results. All in all, our choice of parameters allows us to determine observables within a statistical uncertainty of $\sim 1 - 2\%$.

Note that for mass-imbalanced systems the eigenvalues of the transfer matrix spread further as in the case of equal masses, as a consequence of the change of kinetic energy in the system. For sufficiently large mass asymmetry, the propagation could therefore become unstable, as floating point arithmetic is incapable of resolving the spread of the eigenvalues which ultimately leads to ill-conditioned Fermi matrices. The onset of this behavior was observed for the largest mass imbalances studied in this section. However, no problematic influence on our numerical results was observed. For larger lattice sizes, and particularly in higher dimensions, one should nevertheless carefully monitor this issue, as the problematic parameter range could then involve points of physical interest.

5.3.2 Imaginary mass imbalance

As a first step, we approach the mass-imbalanced problem with the iHMC method introduced in Section 4.3.1. The algorithm requires to shift the mass asymmetry to the complex plane which is achieved by applying the transformation

$$\delta m \to i\delta m. \tag{5.3.5}$$

As discussed in Section 4.3.1, this renders the path-integral measure positive-semidefinite and therefore allows us to employ a Metropolis-based algorithm. The left panel of Fig. 5.5 shows our results for the ground-state energy (black diamonds) for various couplings as a function of imaginary $\bar{m}$. The solid black line represents the corresponding noninteracting Fermi gas, according to the transformation of Eq. (5.3.4):

$$E_{\bar{m}} = E_0 \left[\frac{1}{1 + (-i\bar{m})^2} \right]. \tag{5.3.6}$$

This expression suggests the use of a Padé approximant to fit the data, which takes on the form

$$f(\bar{m}) = \frac{\sum_{i \geq 1} b_i \bar{m}^{2i}}{1 + \sum_{j \geq 1} c_j \bar{m}^{2j}}, \tag{5.3.7}$$

where the even powers reflect the symmetry under $\bar{m} \to -\bar{m}$, and the b_j's and c_j's are fit parameters. The colored lines in Fig. 5.5 represent a least-squares fit of the above form with a polynomial of order 2 (4) in the numerator (denominator). The nearly perfect agreement with the numerical data is crucial when performing an analytic continuation to real $\bar{m}$ as small variations in the fit parameters can greatly influence the final results for real mass imbalances. In principle, higher orders can be included in the polynomials which has been found, however, to limit the stability of the fit procedure. Therefore, we only use the aforementioned order of the Padé approximant in this work.

To obtain results for real $\bar{m}$, we perform an analytic continuation to the real axis via the inverse transformation of Eq. (5.3.5), namely $i\delta m \to \delta m$. The results of the analytic continuation are shown in the right panel of Fig. 5.5 along with the 95% confidence level (shaded bands). We find very good agreement with the form of the noninteracting result (solid black line) and the results for the energies are very stable with the order of the Padé approximant up to $\bar{m} \sim 0.5 \dots 0.6$. For mass imbalances beyond $\bar{m} \sim 0.6$, however, the associated uncertainties grow rapidly and a quantitative prediction for the ground-state energy (or any other observable) is not guaranteed, particularly at strong couplings. At very high imbalances (not shown in this plot), it is even possible that the qualitative trend as a function of $\bar{m}$ changes due to the effect of the higher-order terms in the functional form of the fit. A possibility to remedy this issue might be to use a larger amount of data and a finer grid for the $(-i\bar{m})$-axis. While this is feasible (albeit tedious) in 1D, the numerical effort in 2D and 3D would be definitely prohibitive.

5.3.3 CL & mass-imbalanced Fermi gases

To complement the iHMC study above, we exploit the CL method, as introduced in Section 4.5, to address mass-imbalanced fermions. This algorithm, as opposed to the HMC approach, introduces
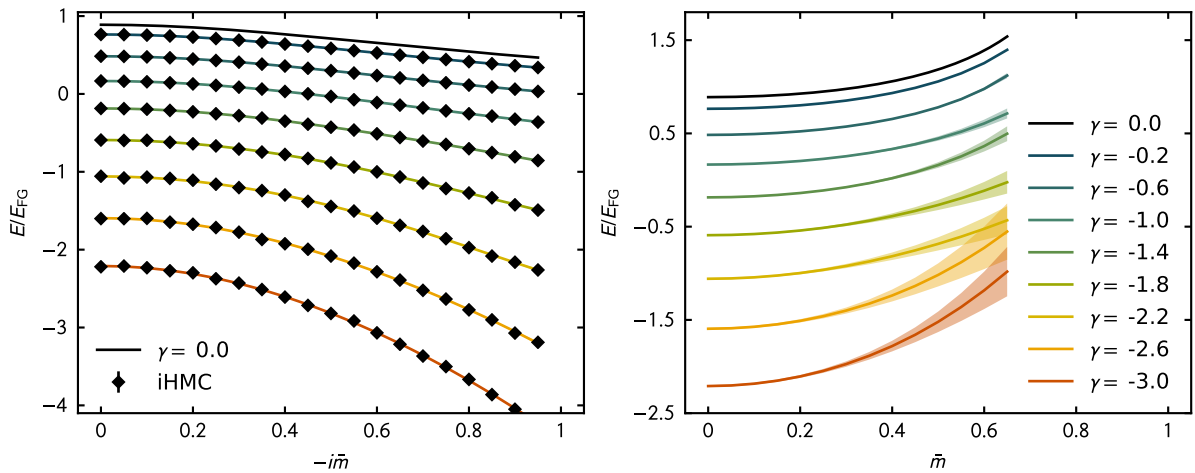
Figure 5.5: Ground-state energy of $N = 3\uparrow +3\downarrow$ fermions as a function of imaginary (left) and real (right) mass imbalance for various couplings γ from weak to strong attractive interaction (lines ordered from top to bottom). (Left) iHMC results for imaginary $\bar{m}$ (black diamonds, statistical error bars are of the size of the symbols) with Padé approximations according to Eq. (5.3.7) (solid colored lines). The black solid line shows the noninteracting result on the lattice. (Right) Analytically continued ground-state energies as a function of real mass imbalance (solid lines) along with the 95% confidence bands (shaded areas). The plot range in the right panel was limited to $\bar{m} = 0.65$ due to large uncertainties beyond that point.

a dependence of the integration step which needs to be addressed before being able to discuss results as a function of physical parameters. After an investigation of these systematic effects, we proceed with a benchmark of the CL method for balanced systems and a cross-check of the CL results to the above-discussed iHMC values in the mass-imbalanced case. Finally, we present the full energy dependence on the interaction strength over a wide range of mass imbalances.

Numerical artifacts

Before studying our results as a function of physical parameters, we here investigate potential systematic bias stemming from numerical artifacts. As already discussed in Section 4.4.2, the use of CL implies a finite integration step Δt of the Langevin equation. Here and in all CL investigations to follow, we employ an adaptive integration step which was found to be crucial in order to stabilize the CL trajectories [192].[4] Furthermore, in order to stabilize the calculations against uncontrolled excursions in the complex plane, the auxiliary field is confined around the origin by a harmonic confinement of strength ξ, dubbed the regulator (see Section 4.5.5). We investigate the influence of both parameters for a system of $N = 5+5$ particles with $\bar{m} = 0.3$. The choice of these parameters is essentially arbitrary and only exemplifies the numerical accuracy of all other datasets. To facilitate a comparison to the iHMC results above, we chose an attractive coupling of $\gamma = -1.0$.

The dependence of the ground-state energy on Δt for the above systems is shown in the left panel of Fig. 5.6. Within the statistical uncertainty, the trend may assumed to be linear, which

---

[4]The adaptive step size implies that Δt is not constant throughout the propagation in Langevin time, such that Δt should be more correctly referred to as average integration step. In the following, we use both terms interchangeably, as is common in the literature.
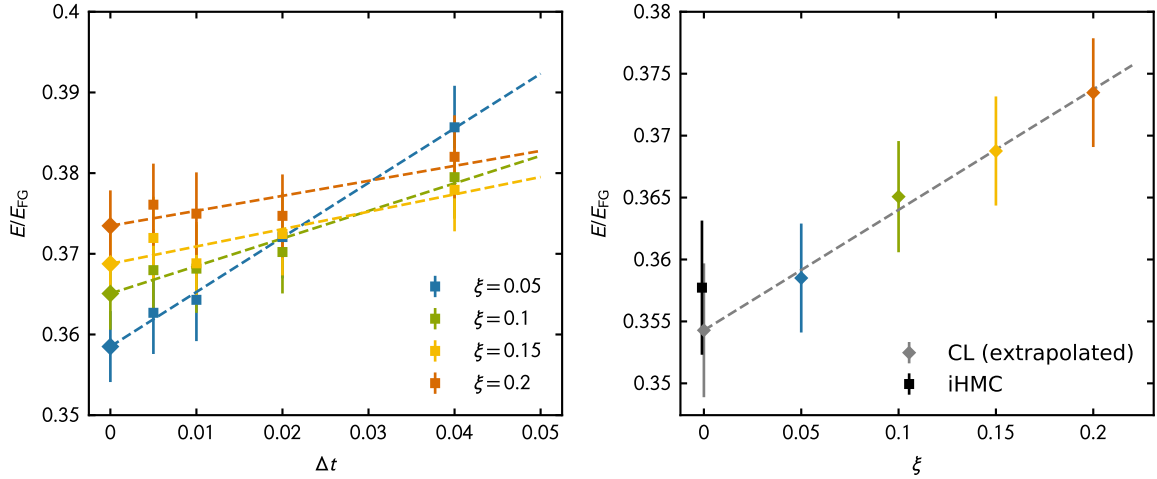
Figure 5.6: Ground-state energy for a $5 \uparrow +5 \downarrow$ system with $\bar{m} = 0.3$ and $\gamma = -1.0$. (Left) Dependence on the integration step Δt for various values of the regulator strength ξ. (Right) $\Delta t \to 0$ extrapolated values as a function of ξ, along with a comparison to iHMC results (black square at $\xi = 0$). In both panels, linear fits are shown as dashed lines and the extrapolated values are indicated by symbols in the appropriate limit.

we exploit to extrapolate the ground-state energy to the limit $\Delta t \to 0$ via a least-squares fit (diamonds at $\Delta t = 0$). For $\xi \gtrsim 0.1$, the dependence on Δt appears to be relatively mild.

In the right panel of Fig. 5.6, ground-state energies are shown after an extrapolation $\Delta t \to 0$ as a function of the regulator ξ. The results in the considered regulator range display almost perfect linear behavior which allows a relatively precise extrapolation to vanishing ξ. At $\xi = 0$ we compare the extrapolated result to the iHMC value from our previous calculation and observe excellent agreement.

The above procedure was found to be essentially independent of the order of extrapolations, i.e., it does not matter if $\xi \to 0$ is extrapolated before the step-size dependence or vice versa. In any case, the variation of our numerical results for different ξ and Δt is only of a few percent such that an exact extrapolation to the appropriate limits may be omitted for a first benchmark. Based on this analysis, we chose the strength of the regulator to be $\xi = 0.1$ and the average CL integration step $\Delta t = 0.01$ for the discussion of the following results. For high-precision results beyond these first methodological benchmarks, however, extrapolations should be carried out explicitly.

Benchmark: Equal masses at arbitrary interaction

We begin by considering the mass-balanced scenario in order to conduct a detailed benchmark study of the CL method in the context of nonrelativistic fermions. In the left panel of Fig. 5.7 we compare our results for attractive interactions, i.e., $\gamma < 0$, with a variety of other methods across a wide range of interaction strengths. We find good agreement with the results discussed in Section 5.2, which in turn have been found to agree with exact results from the BA in the TL (also shown in the plot). The small discrepancy at large negative values of γ originate from the finite system size considered in this work, while the previous HMC results are extrapolated to infinite volumes. Additionally, we show results from a renormalization-group approach to density functional theory based on the microscopic interactions defining our model [243]. We abbreviate
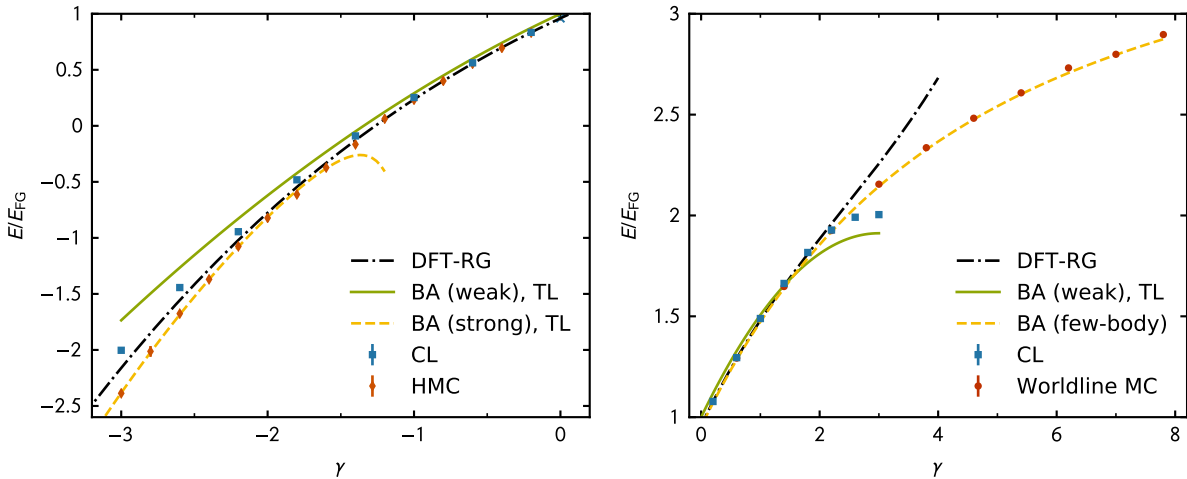
Figure 5.7: Ground-state energy of $N = 5 \uparrow + 5 \downarrow$ fermions of equal mass ($\bar{m} = 0$) as a function of interaction strength. (Left) Attractive interaction. CL results (blue squares) compared to HMC results (red diamonds), DFT-RG [243] (dashed-dotted line) and BA expansions in the TL for weak (solid line) and strong (dashed line) attraction [217, 218]. (Right) Repulsive interaction. CL results (blue squares) compared to DFT-RG (dashed-dotted line), weak BA expansion in the TL (solid line), exact few-body BA results (dashed line) and worldline MC values (red circles) [122].

this approach as DFT-RG which was put forward in Refs. [244–247]. As shown in Fig. 5.7, we find excellent agreement with this method for $-2 \lesssim \gamma$. Note that $|\gamma| \lesssim 2$ is roughly the range where the DFT-RG approach is able to formulate reliable predictions based on state-of-the-art truncations presently restricted to mass-balanced systems.

In the right panel of Fig. 5.7, we benchmark our values for repulsive interactions, i.e., $\gamma > 0$, which were previously inaccessible with the HMC method because of the sign problem. Agreement between the weak coupling expansion results from the BA (solid line), DFT-RG and our CL values is observed up to $\gamma \lesssim 2$. While the former two methods are restricted to interactions in this regime, the CL method in principle does not have a constraint in terms of the interaction strength. A comparison to a very recent determination of the ground-state energy based on a sign-free worldline MC algorithm [122, 123], however, reveals some discrepancy between the methods for $\gamma \gtrsim 2.0$. While the CL results seem to level off, the worldline results continue to grow. The latter is in agreement with exact BA results for the $5 \uparrow + 5 \downarrow$ system (dashed line), taken from [122]. At first glance, the relative discrepancy at $\gamma = 3.0$, which is the largest value considered in the present work, seems to be comparable to the deviation at the largest couplings on the attractive side. While the attractive values have been observed to converge to the appropriate values with increasing system size, a finite-size investigation up to $N_x \approx 100$ on the repulsive side did not change the outcome significantly.

The faulty values at large repulsion raise some concern regarding the reliability of the CL approach. To further investigate this issue, the histograms of the sampled values for the ground-state energies at large attraction ($\gamma = -3.0$) and large repulsion ($\gamma = 3.0$) are shown in Fig. 5.8. A comparison highlights the fundamentally different behavior: While the distribution $P[E]$ is well localized (and in fact almost perfectly Gaussian) on the attractive side, the repulsive system exhibits so-called "fat tails" which refers to slowly decaying skirts of the histogram. Their appearance
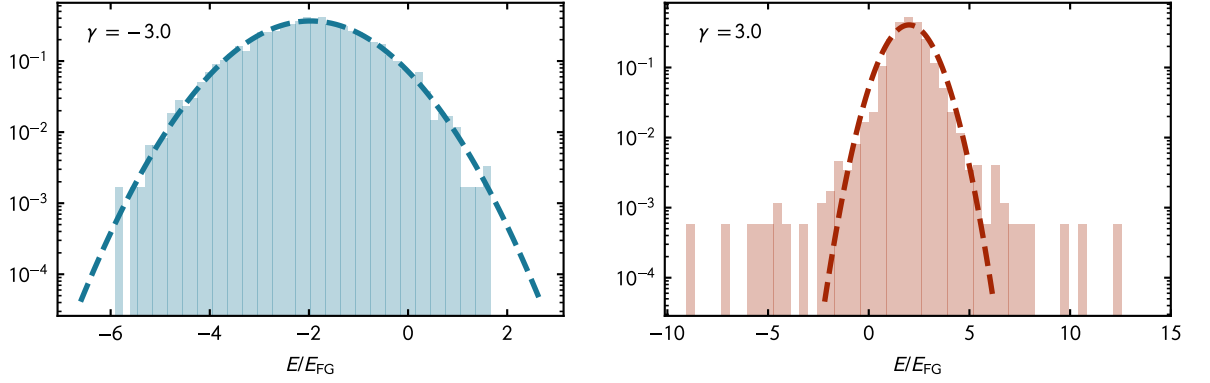
Figure 5.8: Histograms of the samples ground-state energies for strongly attractive (left) and repulsive (right) interactions of $|\gamma| = 3.0$. The dashed lines represent a Gaussian with the estimated sample values for the mean and the variance.

is problematic in several ways: First of all, a slowly decaying probability function might not have a well-defined second moment which would imply infinitely large error bars. Practically, this means that the variance of the sampled observable diverges with an increasing number of samples, thereby nullifying the advantage of MC approaches altogether. Such a behavior could originate for instance from an overlap problem of the trial wavefunction an the actual physical distribution, which ultimately leads to a poor signal to noise ratio. Alternatively, this could be the hallmark of numerical instabilities in the imaginary time propagation, leading to frequent outliers.

The second problematic aspect is the formal validity of the CL approach, as discussed in Section 4.5.3. The fat tails of the observables may be related to the appearance of boundary terms, which in turn invalidate the proof of correctness of the CL method. A detailed investigation of the faulty behavior is necessary to conclusively identify the true reason for the frequent outliers. Such a study is beyond the scope of the present thesis and is deferred to a future project.

We note that the onset of these problems is already visible, to some extent, for weaker repulsion where the CL results agree (quite well) with other methods. The frequency of the sampled outliers, however, is much lower in these systems such that the statistics is sufficient to "override" the few faulty values. As a consequence of the problematic behavior at large repulsion, we shall only consider attractive systems in the following.

Comparison among stochastic methods for general mass imbalances

Motivated by the excellent agreement between CL and other methods in mass-balanced systems, we expand our investigation to mass-imbalanced systems. As mentioned above, there is no need for analytic continuation, which saves computational effort since we only have to compute single data points (as opposed to a grid of data points with subsequent fitting). Although it is possible to run calculations for an arbitrary configuration of the fermion masses $m_\uparrow$ and $m_\downarrow$, we stick to the definition Eq. (5.3.2) introduced with the iHMC method to facilitate a straightforward comparison.

A comparison of iHMC and CL results is shown in the left panel of Fig. 5.9 for a system of $N = 4\uparrow + 4\downarrow$ fermions at various attractive coupling strengths. We find excellent agreement between the methods up to $\bar{m} \sim 0.5 - 0.6$, where the iHMC algorithm starts to develop large
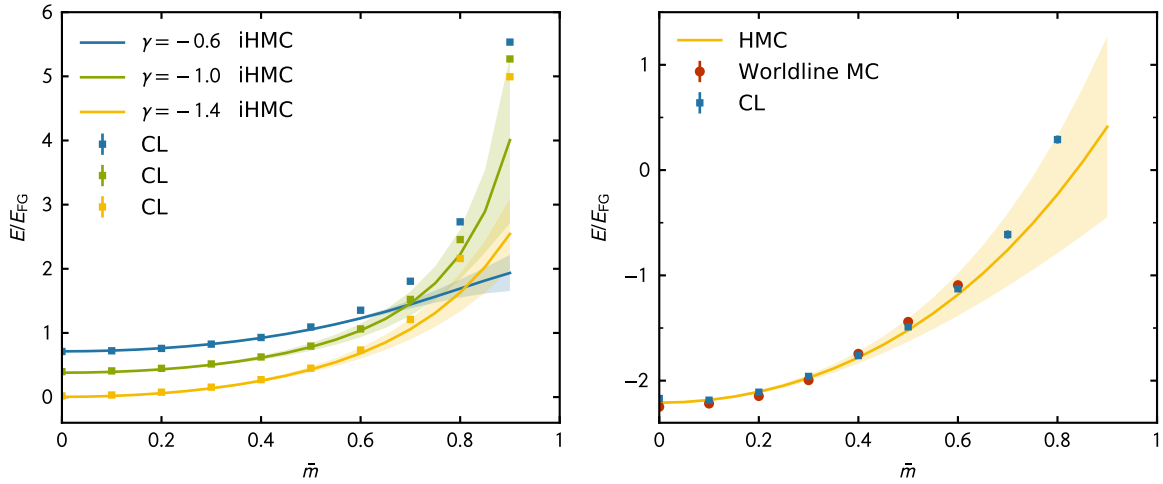
Figure 5.9: Ground-state energy as a function of mass imbalance. (Left) Comparison of iHMC (lines) and CL (symbols) results for $4\uparrow+4\downarrow$ fermions for $\gamma=-0.6,-1.0$ and -1.4. (Right) Comparison for systems of $3\uparrow+3\downarrow$ fermions at $\gamma=-3.0$ between CL (squares), iHMC (line) and worldline MC (circles) [122]. In both panels the shaded areas represent the 95%-confidence interval of iHMC data, the statistical uncertainties of the CL data are smaller than the symbol sizes.

uncertainties. Remarkably, the results obtained with the CL algorithm continue to be smooth well beyond this regime and the statistical uncertainties are of roughly constant magnitude across all considered imbalances.

In the right panel of Fig. 5.9, we compare our results to the worldline MC approach from [122, 123] which became available after our initial calculations for mass-imbalanced systems. This approach may be formulated without a sign-problem in 1D, however, a sign-free generalization to higher dimensions of this strategy is not possible as opposed to CL. Moreover, the worldline method appears to be best suited in the few-body regime, whereas the CL approach readily extends to many-body systems, as further discussed below. We observe excellent agreement between all three stochastic methods across all mass imbalances available which verifies the applicability of iHMC and CL for general mass-imbalanced systems.

Equation of state for mass-imbalanced fermions

Thus far, we have compared our CL results to various methods and found excellent agreement for all cases considered. Most of the parameter space, however, is generally difficult to access due to analytic and numerical problems, as pointed out above. The CL method is, however, able to predict values for arbitrary $\bar{m}$ and across a wide range of both attractive and repulsive interaction strengths, although the results for strong repulsion ($\gamma \gtrsim 1$) display problematic tails of the sampled histograms, as our discussion above shows.

To underscore this ability, we present in Fig. 5.10 our determination of the EOS for mass-imbalanced fermions. As apparent from the figure, the results are smooth as a function of interaction strength and mass imbalance and intersect the correct noninteracting results on the vertical line at $\gamma = 0$. It is also evident in Fig. 5.10 that the EOS becomes linear in a region around $\gamma = 0$. This linear region can be compared with a first-order perturbative calculation of
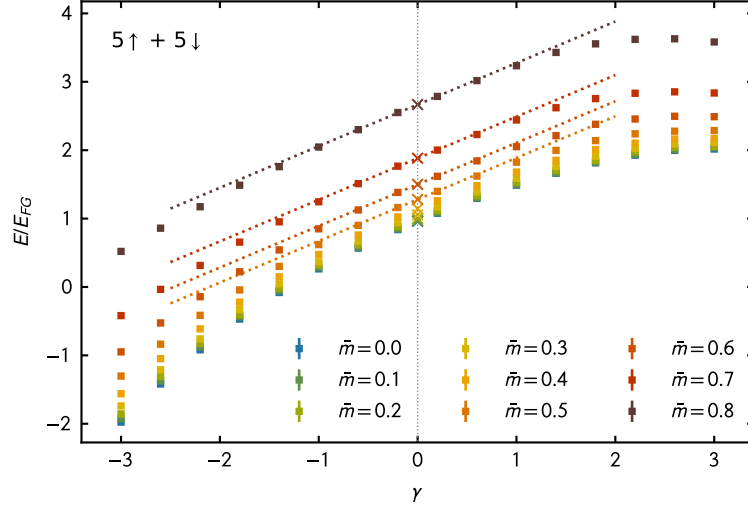
Figure 5.10:   Ground-state energy of $N = 5 \uparrow + 5 \downarrow$ fermions as a function of the dimensionless coupling γ for several mass imbalances $\bar{m}$ as obtained from our CL approach. Error bars are of the size of the symbols and smaller. The dashed-dotted lines show the first-order perturbative results as given in Eq. (5.3.8).

the ground state energy, as shown in Fig. 5.10, which is given by

$$\frac{E}{E_{\mathrm{FG}}} = \frac{E_{\bar{m}}}{E_{\mathrm{FG}}} + \gamma \frac{24}{\pi^2} \frac{N_\uparrow N_\downarrow}{(N_\uparrow + N_\downarrow)^2} + \mathcal{O}(\gamma^2) \,, \tag{5.3.8}$$

with $E_{\bar{m}}$ as in Eq. (5.3.4). Note that the first-order correction in γ does not depend on the mass imbalance $\bar{m}$, which is reflected in Fig. 5.10 by the fact that the slope at $\gamma = 0$ does not change as $\bar{m}$ is increased. Moreover, we observe that our numerical data agrees very well with this perturbative result around $\gamma = 0$, indicating that our CL approach indeed works reliably, at least in the weak-coupling limit. Interestingly, we deduce from this comparison that the size of the linear region depends on $\bar{m}$ and on the sign of the coupling γ. In fact, the size of the linear region is not symmetric around $\gamma = 0$ and even appears to increase with increasing $\bar{m}$ for attractive couplings ($\gamma < 0$).

Our results make the versatility of our CL approach evident. In fact, very promisingly, this enables us to predict values for the ground-state energy at couplings and mass imbalances relevant to experimental setups where analytic expressions are not available and stochastic calculations have only been of limited use so far because of the sign problem. Such experiments include for instance mixtures of the fermionic atoms ^{6}Li and ^{40}K corresponding to $\bar{m} \approx 0.74$ but also mixtures with smaller values of $\bar{m}$ realized with a variety of suitably chosen different fermion species (such as ^{6}Li, ^{40}K, ^{161}Dy, ^{163}Dy, and ^{167}Er) in the future (see, e.g., [248–250]).

Finally, it is worth noting the peculiar flattening of the EOS. Initially, our analysis suggested that this behavior could hint at the so-called fermionization, referring to the fact that an interacting system of distinguishable fermions becomes equivalent to a system of noninteracting identical fermions in the limit of infinite repulsion. Such a behavior was discussed for mass-balanced systems (see, e.g., [219, 251, 252]) and evidence for this behavior has even been observed in experiments [215, 253–255]. As the discussion above clearly shows, however, our CL results are

compromised for large repulsive interactions such that this conclusion is in fact wrong. The effect of flattening can be traced back to shortcomings of our numerical treatment whose investigation will be the target of future efforts.

5.4 Spin-polarized fermions in 1D

In this section, we continue our characterization of imbalanced Fermi gases by considering two-component systems with a population imbalance. As already mentioned in the introduction, the spin asymmetry is quantified by the relative polarization

$$p \equiv \frac{n_\uparrow - n_\downarrow}{n_\uparrow + n_\downarrow}, \tag{5.4.1}$$

which is confined to the interval $p \in [-1, 1]$. In the case of equal masses of the spin species, which we address in this section, all results are invariant under the transformation $p \to -p$. Without loss of generality, we consider $p > 0$ in the following such that the up-component is also referred to as the majority species.

At $p = 0$ it follows that $n_\uparrow = n_\downarrow$, such that the system is balanced and therefore amenable to MC treatment free of the sign problem, as was discussed in Section 5.2. In this limit, particles tend to form $\uparrow\downarrow$-pairs and the ground state is protected by the uniform energy gap Δ. At full polarization, i.e., $p = 1$, on the other hand, only majority particles are present such that the gas is noninteracting as a consequence of the Pauli principle. The interesting question is now the intermediate regime for p in the interval $(0, 1)$: As opposed to the three-dimensional case discussed in the introduction, no real symmetry breaking can occur in 1D as a consequence of the Mermin-Wagner theorem [213]. Thus, no real phase transition can be expected but rather, if anything, a smooth crossover between different regimes.

It turns out that for equal masses the Hamiltonian in Eq. (5.1.1) is integrable by means of the BA for arbitrary polarizations [256, 257]. This technique was employed to study the full phase diagram of 1D Fermi gases with attractive interaction in dependence of the chemical potential μ vs. the Zeeman-field h. Indeed it was found that FFLO-type pairing is the leading instability in a wide parameter range which was further consolidated by numerical evidence obtained in DMRG [258–261] and MC studies [232, 262]. This is in contrast to strongly interacting 3D Fermi gases where the FFLO phase is conjectured to be present only in a small region of the phase diagram, if at all. Hence, experiments with 1D Fermi gases constitute a promising approach to finally observe the elusive inhomogeneous pairing mechanism (see, e.g., [71] for a recent review).

The study of the pairing mechanisms at work necessitates the calculation of suitable two-body correlation functions. Within the BA framework, however, this proves to be challenging such that numerical methods are more than just a useful alternative. In this section, we extend the CL approach to study spin-imbalanced systems in the few- and many-body regimes. In the following, we again start by considering the ground-state energy for various interaction strengths in order to validate the CL approach for these systems. We then move to the main goal of this section, namely the characterization of pairing in spin-imbalanced Fermi gases through the calculation of the pair-momentum distribution functions and density-density correlations in momentum space.
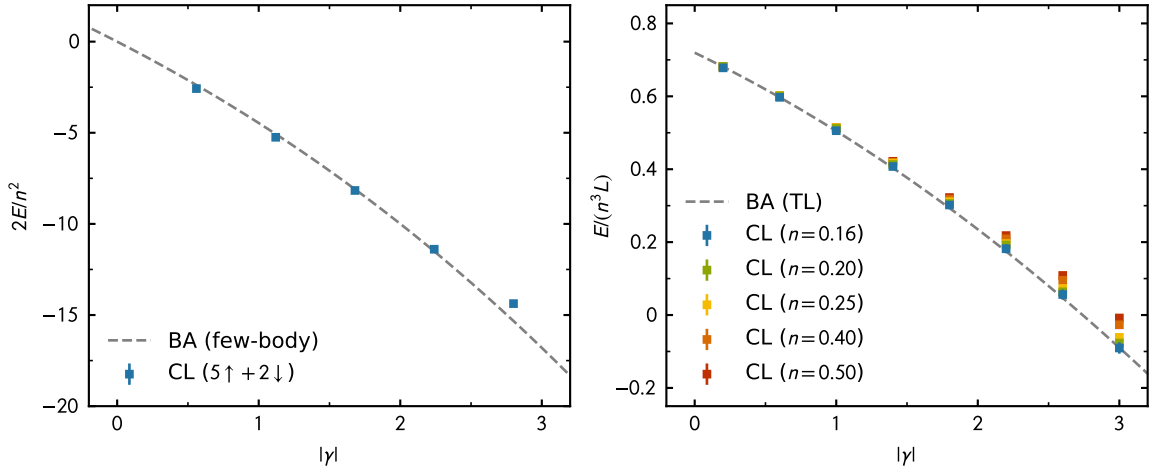
Figure 5.11: Ground-state energy of spin-polarized fermions as a function of attractive interaction γ. (Left) Few-body CL results (blue squares) in units of $n^2/2$ compared to exact few-body BA calculations (dashed line). (Right) Many-body CL results in units of n^3L for various values of the particle density (squares) compared to the BA expansion in the TL (dashed line) [263].

Numerical parameters

As in our previous investigations, we integrate the Langevin equation up to trajectory lengths of $T_L \approx 1000$ during which we measure observables after intervals of ~ 1 "Langevin seconds". Averaging over ~ 5 independent trajectories, corresponding to different initial conditions, and accounting for autocorrelation effects yields a relative statistical accuracy in the range of $1 - 2\%$ for all observables under consideration.

Unless otherwise noted, we employ an adaptive integration step with the target value $\Delta t = 0.04$, below which the qualitative trend of all correlation functions remained unaltered. Furthermore, the regulator is fixed to $\xi = 0.1$ which yields stable results within reasonable accuracy, as discussed in detail above.

5.4.1 Equation of state for finite spin-polarization

As a first step, we benchmark the CL approach for spin-imbalanced systems via the computation of the ground-state energy as a function of attractive interaction strength $\gamma \leq 0$. In the left panel of Fig. 5.11, we present our results for $5 \uparrow + 2 \downarrow$ particles extrapolated to the limits $\Delta t \to 0$ and $\xi \to 0$ in order to facilitate a precise benchmark to the exact BA solutions at the corresponding particle content [264]. We observe excellent agreement across the entire interaction range studied, except of the largest value at $\gamma = -2.8$, for which the CL value slightly overestimates the exact BA result. Similar to the discussion in Section 5.3.3, we attribute this deviation to the finite extent of the box, which was only taken to be $N_x = 39$ for this calculation.

In the right panel of Fig. 5.11, we show our results for the ground-state energy in the many-body regime at fixed polarization of $p = 0.5$. In order to work at constant polarization but varying density in the canonical ensemble, it is necessary to slightly vary the lattice sizes. For the presented results at $n = 0.5, 0.4, 0.25, 0.2$ and 0.16 we have chosen the parameters $(N_x, N_\uparrow + N_\downarrow) = (136, 51 + 17), (130, 39 + 13), (112, 21 + 7), (140, 21 + 7)$ and $(125, 15 + 5)$, respectively. These lattice sizes are large enough to suppress finite-size effects and can be hence

considered as sufficiently close to the infinite-volume limit. The comparison to the BA solution in the TL [263] reveals that the CL results converge to the expected solution with decreasing density. This is indeed not unexpected, as the BA model exactly solves the zero-range model whereas our lattice treatment introduces some residual finite range of the interaction. Only in the dilute limit these effects are small, which is precisely reproduced by our results.

The above analysis verifies the applicability of the CL method in the case of general spin-imbalances for attractive coupling, at least for ground-state energies. Motivated by this agreement with BA results, we now turn to the discussion of correlation functions for the spin-polarized 1D Fermi gas.

5.4.2   Singlet pairing in spin-imbalanced 1D Fermi gases

In order to investigate the pair-formation in spin-polarized systems we compute the on-site pair-density matrix

$$\rho_{\uparrow\downarrow}(x, x') = \langle \hat{\psi}_\uparrow^\dagger(x)\hat{\psi}_\downarrow^\dagger(x)\hat{\psi}_\downarrow(x')\hat{\psi}_\uparrow(x')\rangle, \tag{5.4.2}$$

which was already introduced in the discussion of spin-balanced systems in Section 5.2.4. The above quantity encodes information on singlet pairing, i.e., the formation of ↑↓-molecules. For the study of other instabilities, such as triplet pairing of spin alike particles or charge-density waves, alternative two-body correlation functions need to be computed (see, e.g., [260]).

Regardless of the exact nature of the instability, true long-range order in 1D systems is destroyed through "energetically cheap" long-wavelength fluctuations. Nevertheless, these systems may feature quasi long-range ordering which manifests itself through polynomially decaying correlation functions instead of an exponential decay. The strength of a particular ordering is then described by the asymptotic behavior of the corresponding correlation function, which follows a power law with the correlation coefficient α implicitly defined as

$$\rho_{\uparrow\downarrow}(x, x') \propto |x - x'|^{-\alpha}. \tag{5.4.3}$$

The leading instability is reflected by the smallest exponent α. Stated differently, the system will exhibit the ordering pattern according to the mechanism whose correlation function decays slowest. In spin-balanced Fermi gases, it was found that singlet paring is the dominant instability, which is in line with our discussion in Section 5.2 (see also [72, 265]).

Using BA techniques [260], it was shown that the formation of ↑↓-pairs is also the preferred ordering mechanism in the presence of spin imbalance across essentially the entire parameter range.[5] The mismatched Fermi surfaces cause the particles to pair at a non vanishing center-of-mass momentum given by

$$q = |k_{F,\uparrow} - k_{F,\downarrow}|. \tag{5.4.4}$$

As a consequence, the spatial correlation functions display spatial oscillations such that their

---

[5] Compared to the balanced case, the singlet-pairing correlations decay faster in spin-imbalanced systems. Formally, this is true even for infinitesimal polarization and described by a discontinuous jump of $1/2$ in the correlation coefficient $\alpha(p)$ at $p = 0$. For even larger values of p, $\alpha(p)$ was found to decrease slightly with increasing polarization [260].
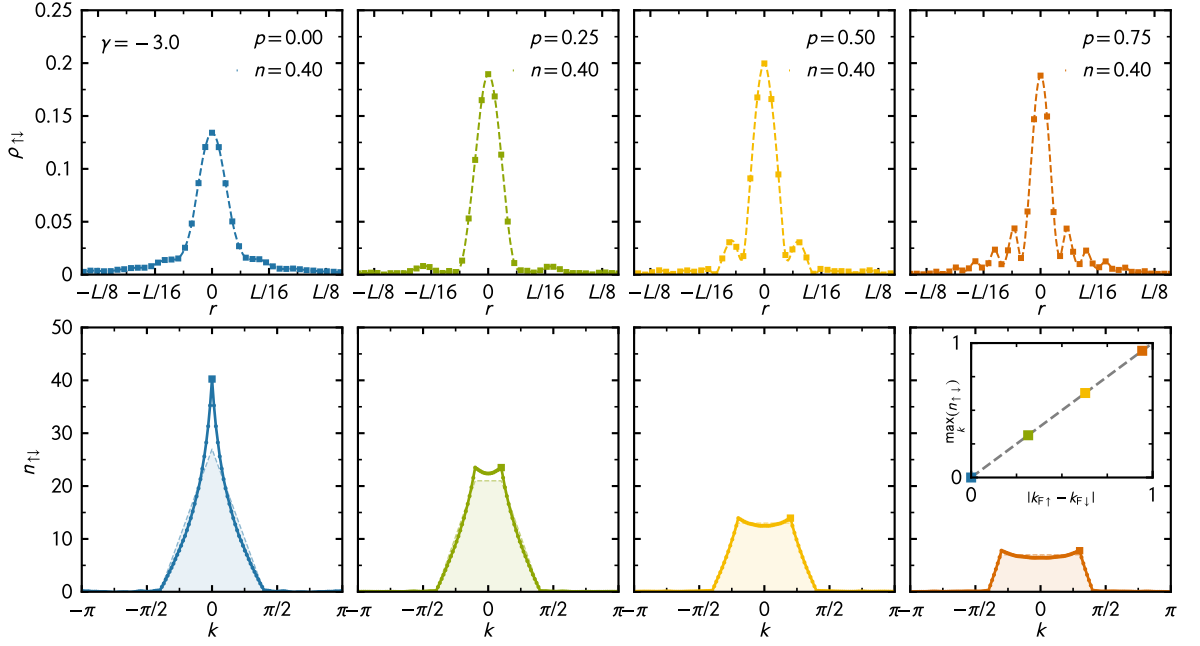
Figure 5.12: (Top) On-site pair-density matrix for systems at fixed density of $n = 0.4$ and polarizations of $p = 0.0, 0.25, 0.5$ and 0.75 (from left to right) as a function of $r = |x - x'|$. The dashed lines represent cubic spline interpolations. (Bottom) Pair-momentum distribution in the first Brillouin zone for the same system. The dashed shaded area represents the corresponding noninteracting pair-momentum distribution. (Inset) The position of the off-center peak as a function of polarization.

asymptotic behavior is given by

$$\rho_{\uparrow\downarrow}(x, x') \propto \frac{|\cos(q|x - x'|)|}{|x - x'|^{\alpha(p)}}, \tag{5.4.5}$$

with the polarization-dependent correlation coefficient $\alpha(p)$. Such an oscillating behavior of the pair-density matrix, which may be related to a spatially varying order parameter, is the signature of FFLO-type pairing, as already discussed in Section 1.3. For a more detailed discussion see, e.g., [265].

On-site pair-density matrix

In the top row of Fig. 5.12, we present our many-body results for $\rho_{\uparrow\downarrow}(x, x')$ at a density of $n = 0.4$ and at various polarizations sufficiently close to the TL. The leftmost column represents the balanced system, which shows a monotonic decay towards large spatial separation $r = |x - x'|$. The light modulation should not be confused with the spatial inhomogeneity of the order parameter. It is rather a residual effect that originates from the kinematically possible pairing at non-zero center-of-mass momenta even in the spin-balanced case. The effect is expected to fade out with increasing interaction.

In the second, third and fourth column of Fig. 5.12, spin-imbalanced systems with $p = 0.25, 0.5$ and 0.75 are shown. With growing polarization the spatial fluctuation of $\rho_{\uparrow\downarrow}$ become more pronounced, in accordance to Eq. (5.4.5). The nodes of $\rho_{\uparrow\downarrow}$ have in fact an intuitive physical

interpretation: The excess fermions tend to reside near the zeros of the spatially oscillating order parameter, which, loosely speaking, reflects the locally vanishing energy gap [265]. Note that the minima of the oscillating correlation function should drop to zero. The finite resolution of the lattice, however, introduces a slight deviation from this behavior. Nevertheless, our results for the on-site pair-density matrix are in excellent agreement with the expected behavior for FFLO-type pairing.

Pair-momentum distribution

To learn about pairing in the system, it is very instructive to study the pair-momentum distribution $n_{\uparrow\downarrow}$, defined as the Fourier transform of the on-site two-body density matrix, see Eq. (5.2.20). It quantifies the likelihood of finding a pair with a given momentum in the system, or in other words, characterizes where in momentum space the on-site pairing between up and down particles is most likely to take place. The quantity was discussed in Section 5.2 for balanced Fermi gases, where it was shown to be peaked at vanishing momentum. The hallmark of FFLO pairing are off-center peaks in this quantity, which indicate the formation of pairs with non-zero center-of-mass momentum given by Eq. (5.4.4).

In the bottom row of Fig. 5.12, we show the pair-momentum distribution $n_{\uparrow\downarrow}$ for the same systems as before. The leftmost column displays again a strongly peaked behavior at $k = 0$, as expected from our previous calculations. The quantity is analogous to the scenario studied in Fig. 5.4, however, at larger lattices and particle content.

The situation changes as soon as we turn to polarized systems. Immediately upon turning on a finite spin imbalance we find peaks in the pair-momentum distribution at $k \neq 0$ as a consequence of pairing across incommensurate Fermi surfaces. The position of the off-center peaks follows the linear trend expected for FFLO-type pairing. This can be seen in the inset of Fig. 5.12, where we plot the dependence of the peak positions as a function of polarization. This type of pairing is observed for all polarizations studied, indicating the absence of a "critical polarization" in 1D above which singlet pairing ceases to be the leading instability. This finding is in agreement with earlier numerical studies [260, 262].

Shot-noise correlations

Besides the two-body correlation functions presented above, density-density correlations, also referred to as shot-noise correlations, provide a valuable tool to probe the pairing mechanism in ultracold atom systems [214]. Experimentally, the quantity is accessible through statistical analysis of the measured spin-selective momentum distributions of the interacting system, which are proportional to the spatial density distributions after the trapping potential has been switched off.

We define the density-density correlation function in momentum space as

$$
\begin{aligned}
G_{\sigma\sigma'}(k, k') &\equiv \langle \delta\hat{n}_{k,\sigma}\, \delta\hat{n}_{k',\sigma'}\rangle \\
&= \langle \hat{n}_{k,\sigma}\, \hat{n}_{k',\sigma'}\rangle - \langle \hat{n}_{k,\sigma}\rangle \langle \hat{n}_{k',\sigma'}\rangle,
\end{aligned}
\tag{5.4.6}
$$

where $\delta\hat{n}_{k,\sigma}$ denotes the fluctuations of the single-particle momentum distribution about its mean value. Although we will focus on spin-resolved density-density correlations in the following, we
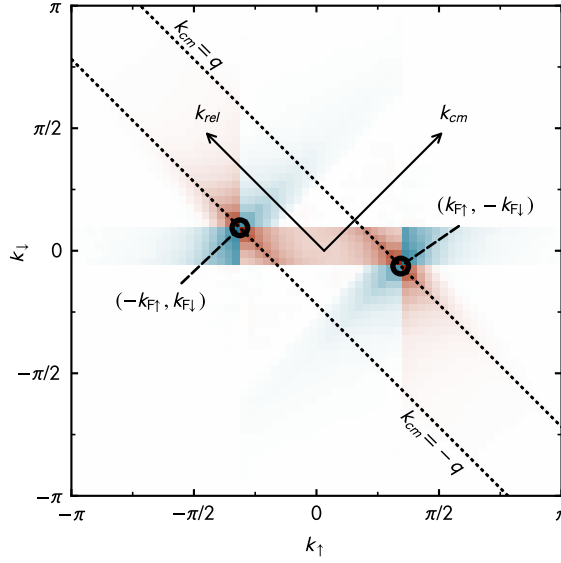
Figure 5.13: Density-density correlation function $G_{\uparrow\downarrow}(k_\uparrow, k_\downarrow)$ for a system of $N = 21 \uparrow + 5 \downarrow$ particles. The direction along the diagonal defines the center-of-mass momentum k_{cm} of a pair whereas its orthogonal direction defines the relative momentum k_{rel}. The two dashed gray lines show lines of constant $k_{\mathrm{cm}} = \pm q$ which include the points at opposite Fermi momenta (marked with black circles).

point out that one could also study the total density-density correlation function

$$G_{\mathrm{tot}}(k, k') \equiv \sum_{\sigma,\sigma'} G_{\sigma\sigma'}(k, k') \tag{5.4.7}$$

and extract essentially the same information about pairing in the system.

The calculation of this quantity allows us to study the internal momentum structure of a bound pair of fermions in our system. The two momentum space coordinates $(k + k')/2$ and $k - k'$ may be interpreted as the center-of mass and relative momentum of the two fermions in a pair, respectively, see Fig. 5.13. To understand the quantity itself, we may picture it as the covariance matrix of the single-particle momentum distributions $n_\sigma(k)$ and $n_{\sigma'}(k')$. Positive values of $G_{\sigma\sigma'}(k, k')$ mark situations where high (low) values of $n_\sigma(k)$ occur along with high (low) values of $n_{\sigma'}(k')$. Negative values, on the other hand, correspond to the opposite situation, where high (low) $n_\sigma(k)$ occur along with low (high) $n_{\sigma'}(k')$. The two cases can physically be identified with particle-particle and particle-hole correlations, respectively. Within this picture, it is also straightforward to see that the density-density correlation function equals zero for noninteracting systems, as the two single-particle distributions are then statistically independent.

We show in Fig. 5.14 the density-density correlation functions for a variety of polarizations at the total particle number $N_\uparrow + N_\downarrow = 26$. The lattice size is fixed to $N_x = 64$, resulting in a constant total density of $n \approx 0.41$. In the top left plot, we show the balanced system, consisting of $N_\uparrow = N_\downarrow = 13$ particles and we observe the expected positive peak at the momentum space coordinates $(\pm k_{\mathrm{F},\uparrow}, \mp k_{\mathrm{F},\downarrow})$. Since the Fermi momenta for the two species coincide in this case, the peaks occur on the anti-diagonal and thus indicate pairing with a center-of-mass momentum of $q = 0$. This is the expected BCS-type behavior for balanced Fermi gases and is in line with our discussion of the pair-momentum distribution above.
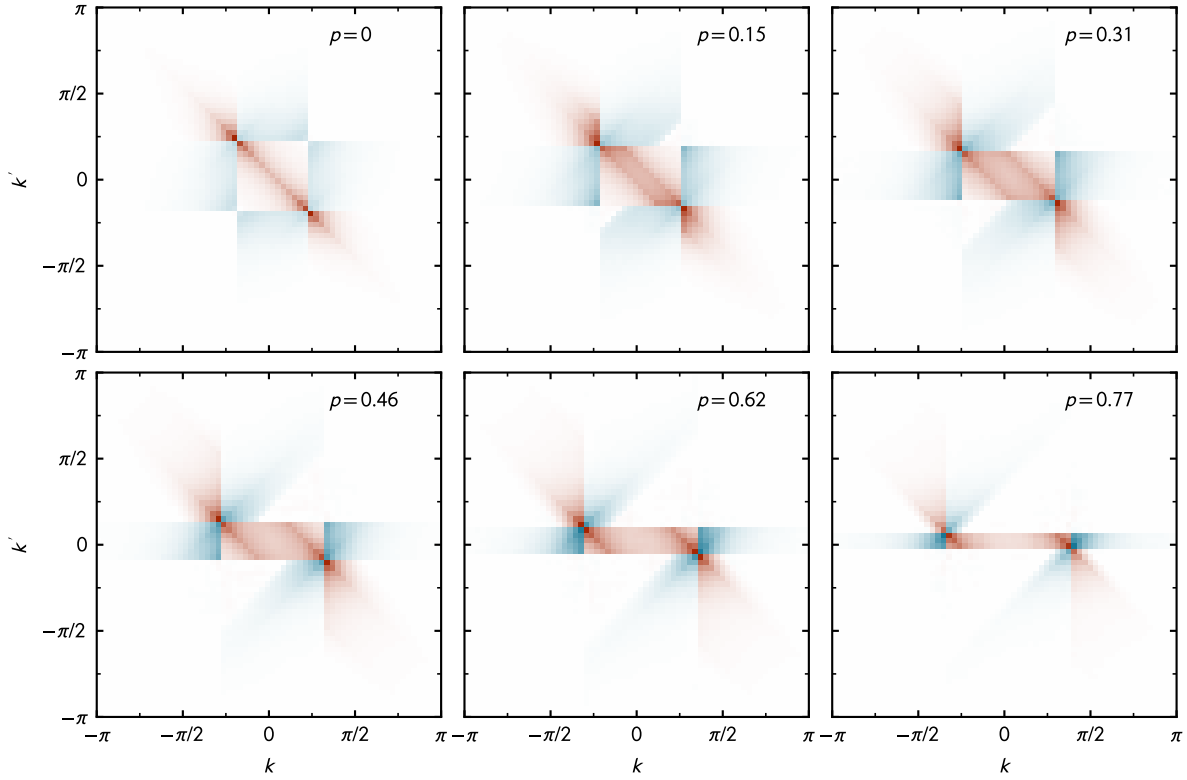
Figure 5.14: Density-density correlations according to Eq. (5.4.6) for systems of $(N_\uparrow, N_\downarrow) = (13, 13), (15, 11), (17, 9), (19, 7), (21, 5)$ and $(21, 3)$ from top left to bottom right. Positive (negative) correlations are indicated by red (blue) color coding, white indicates no correlation.

For non-zero polarizations, we can clearly see a deviation from this behavior as the peaks shift outwards from the central diagonal line by an offset of $|q|$. Still, however, we can clearly observe a formation of sharp peaks around the opposite Fermi points which constitutes a pristine signal of FFLO-type pairing.

Another interesting feature is the "checkerboard" pattern that separates the $k - k'$ space into segments of positive and negative correlations at the intersection lines of the Fermi surfaces. By the statistical argument from above, we expect 4 particle-hole like areas with negative correlation along with 5 particle-particle (or hole-hole) regions with positive correlation. Clearly, this is what we observe in our numerical data and this picture is in agreement with the observations in [260]. We note here that, for the balanced case, the checkerboard structure washes out with increasing interaction strength while it is extremely stable in the spin-imbalanced case, indicating the preservation of the respective Fermi surfaces, at least for the interactions studied here.

Numerical challenges at large momenta

A word of caution is in order regarding the high-momentum part of the presented correlation functions: Statistical fluctuations cause the distributions of the sampled observables to decay only polynomially towards the tails. As discussed in Section 5.3.3, this could lead to biased expectation values in the case of excessive fluctuations. Near the Fermi surfaces, where most of our physical discussion takes place, the fluctuations appear to be under control, allowing a

qualitative discussion of the associated effects.

Nevertheless, an investigation of this matter is necessary to rule out any systematic bias stemming from the numerical treatment. Interestingly, the same shortcomings were observed in the HMC treatment, implying that the issue does not originate from the complexification of the auxiliary field and the associated potential formal issues (see Section 4.5.3). As remarked earlier, a likely culprit could be an overlap problem between the trial wavefunction, which we take to be a Slater determinant, and the true ground state of the system. In this regard, a finite-temperature treatment should mitigate the issue as such an approach does not rely on the use of trial wavefunctions but rather considers the full single-particle basis (hence, the higher numerical effort). First tests indeed suggest the validity of this interpretation and the obtained correlation functions at $T > 0$ are free of excessive noise, even in the large momentum tails. A straightforward one-to-one comparison to the ground-state results, however, requires particle projection to fixed particle number since the finite-temperature simulations are presently performed in the grand-canonical ensemble. Alternatively, more sophisticated trial wavefunctions, such as a BCS-type ansatz, should improve the situation with the benefit of staying at $T = 0$, i.e., circumventing the need for particle projection. Both approaches, however, are beyond the scope of the present thesis and are deferred to future studies.

5.5 Mass- and spin-imbalanced systems

Having treated mass-imbalanced and spin-polarized Fermi gases separately, we now proceed with our investigation of imbalanced 1D Fermi gases by combining these two deformations. Although purely spin-imbalanced 1D Fermi gases have been under intense investigation in the past, the combination with unequal masses remains surprisingly scarce in the literature, not least due to the increased complexity as a consequence of a reduced symmetry. Here, we investigate the effect of unequal masses of the two fermionic species on the pairing structure of spin-imbalanced systems. A question of particular interest is the fate of the FFLO-type behavior in the presence of a finite mass asymmetry.

To quantify the mass asymmetry we use the mass ratio

$$\kappa = m_\uparrow/m_\downarrow \tag{5.5.1}$$

as opposed to the discussion in Section 5.3, where the relative mass imbalance $\bar{m}$ was used. Positive (negative) values of $\bar{m}$ then correspond to $\kappa > 1$ ($\kappa < 1$), respectively. In contrast to the investigation above, the physical results are not invariant under the transformations $\kappa \to \kappa^{-1}$ and $p \to -p$ separately. The combined transformation $(\kappa, p) \to (\kappa^{-1}, -p)$, however, again leaves the results unchanged. Without loss of generality, we always assume $p > 0$, such that the up component is always the majority species. Moreover, we fix the mass of the lighter species to $m = 1$ such that the total mass, and thus the reduced mass, is not constant for varying values of κ.

A meaningful comparison of systems associated with different mass ratios κ requires to identify a scale which is kept fixed to the same value in all systems. Unlike in the purely mass-imbalanced systems discussed above, where we operated at constant total mass $M = m_\uparrow + m_\downarrow$, we shall keep the two-body binding energy ε_B fixed in the following discussion. From the solution of the
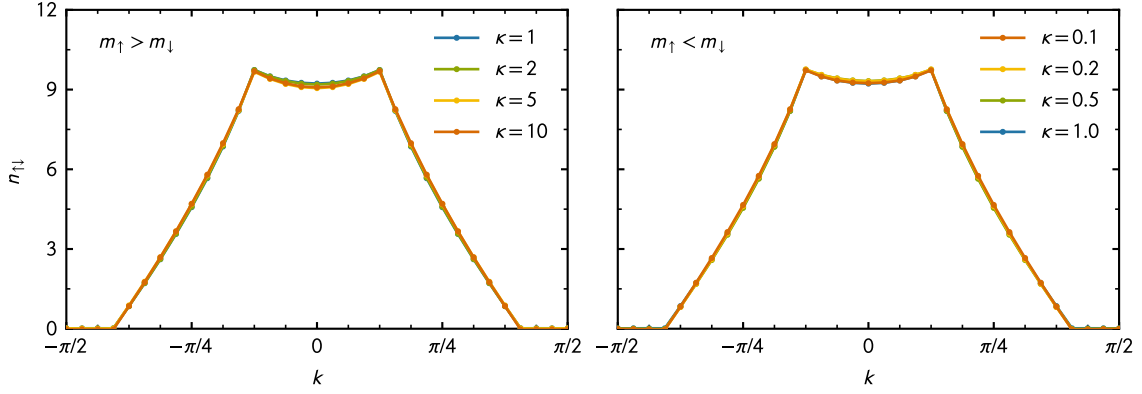
Figure 5.15: Pair-momentum distribution for $N = 17 \uparrow + 9 \downarrow$ particles on a lattice of $N_x = 64$ sites and $\tilde{\gamma} = -2.0$. (Left) Heavy-majority systems with mass ratios $\kappa = 1.0, 2.0, 5.0, 10.0$. (Right) Heavy-minority systems with mass ratios $\kappa = 1.0, 0.5, 0.2, 0.1$.

two-body problem we obtain the binding energy as

$$\varepsilon_{\rm B} = -\frac{m_{\rm r}}{2} g^2 \tag{5.5.2}$$

where $m_{\rm r}$ is the reduced mass which is related to κ via

$$m_{\rm r} = \frac{m_\uparrow m_\downarrow}{m_\uparrow + m_\downarrow} = m_\downarrow \frac{\kappa}{1 + \kappa} = m_\uparrow \frac{1}{1 + \kappa}. \tag{5.5.3}$$

Analogously to the discussion above, we define the dimensionless coupling constant

$$\tilde{\gamma} \equiv \sqrt{m_{\rm r}}\, \gamma, \tag{5.5.4}$$

which reduces to the definition in Eq. (5.1.2) for the mass-balanced case.[6] Since the effect of the mass imbalance is already incorporated at the two-body level, any residual effect that is observed by varying κ at constant $\tilde{\gamma}$ must originate from many-body physics.

The combined spin and mass asymmetry leads to two distinct physical possibilities: more particles of the larger mass ($\kappa > 1$), referred to as heavy majority, or more particles with the smaller mass ($\kappa < 1$), called heavy minority. As we shall see below, these different scenarios lead to physically distinct pairing patterns.

Pair-momentum distribution

As in the previous section, we start our investigation by computing the pair-momentum distribution $n_{\uparrow\downarrow}(k, k')$ according to the definition in Eq. (5.2.20). The quantity is shown in Fig. 5.15 for a system of $N = 17 \uparrow + 9 \downarrow$ particles and a variety of mass imbalances. We observe that the pair-momentum distribution is largely independent of κ and, most importantly, no variation of the pairing-peak position is apparent. This indicates the stability of FFLO-type correlations with finite center-of-mass pairing for all mass imbalances considered here. In both cases, heavy majority and heavy minority, the mechanism does not necessarily imply that pairs are only found at $k_{\rm cm} = \pm|k_{\rm F,\uparrow} - k_{\rm F,\downarrow}|$. Other combinations of pairs at $k_{\rm cm} \neq \pm q$ are kinematically possible

---

[6]Note that $m_{\rm r}$ is dimensionless in our units.

but the ones at the FFLO-momentum are most likely to be present. As a consequence of the negligible variation of the pair-momentum distribution, the spatial modulation of the order parameter remains effectively unchanged. The discussion of our results for this specific particle configuration carries over to other values of the polarization, where the same qualitative trends have been observed.

Opposed to the above findings, several studies on the asymmetric Hubbard model, where the mass imbalance corresponds to asymmetric hopping amplitudes, suggest the breakdown of singlet superconductivity at some critical mass imbalance. In the spin-balanced case, a crossover to either a charge-density wave (CDW) [266, 267] or a collapse of the heavy particles featuring a non-uniform density [268] was proposed. For the spin-imbalanced scenario, it was argued that FFLO-type pairing is confined to a smaller parameter regime [269] and worldline MC studies found non-uniform density profiles for large attractive interactions and mass imbalances [238]. A possible explanation of the apparent discrepancy to our CL results might be the different dispersion relations: While at very low densities the Hubbard model and the quadratic dispersion are practically identical, the former flattens towards the edges of the first Brillouin zone (BZ) as opposed to the monotonically increasing quadratic dispersion employed in this work. Consequently, the energy cost for excitations at densities beyond the dilute regime are different for the two models which ultimately prohibits a straightforward comparison. Moreover, the studies mentioned for the Hubbard model have been performed at low albeit finite temperatures and some even in the grand-canonical ensemble, which could also lead to qualitatively different behavior to the strict zero-temperature limit. To resolve whether these studies are actually in contradiction to our CL results, a more detailed scan of the parameter space, along with additional correlation functions for CDW and other ordering mechanisms, is necessary. Such a study, however, is beyond the scope of the present thesis.

Shot-noise correlations

In order to better understand the influence of mass imbalance on the pairing behavior, we again turn to the investigation of the shot-noise correlations. In Fig. 5.16, we show our results for the same systems as in the above discussion for heavy-majority (top row) and heavy-minority (middle row) configurations. Although the pair-momentum distributions remain roughly the same, we observe changes in the density-density correlation functions. Besides the regular pairing-peak at the opposite Fermi points $(\pm k_{\mathrm{F}}^{\uparrow}, \mp k_{\mathrm{F}}^{\downarrow})$, we observe the emergence of an additional peak with increased mass asymmetry. Consistent with the observation of constant peak positions in the pair-momentum distribution, the "spectral weight" is only shifted along lines of constant center-of-mass momentum. This implies that merely the internal structure, i.e., the relative momentum of up and down particles, changes with the mass ratio.

The appearance of the additional peaks may be understood through the fact that the spacing between the energy states is reduced for the heavy component: With the same energy cost, the heavy particle can scatter into higher lying momentum states.

Heavy majority   At first, let us consider the heavy-majority scenario (top row of Fig. 5.16) in more detail. As discussed above, pair formation happens at lines of constant center-of-mass momentum $k_{\mathrm{cm}} = \pm q$, which corresponds to $k' = k \pm q$ (dashed lines in the lower left panel of Fig. 5.16) and reflects the positions of the two maxima in the pair-momentum distribution discussed above. We
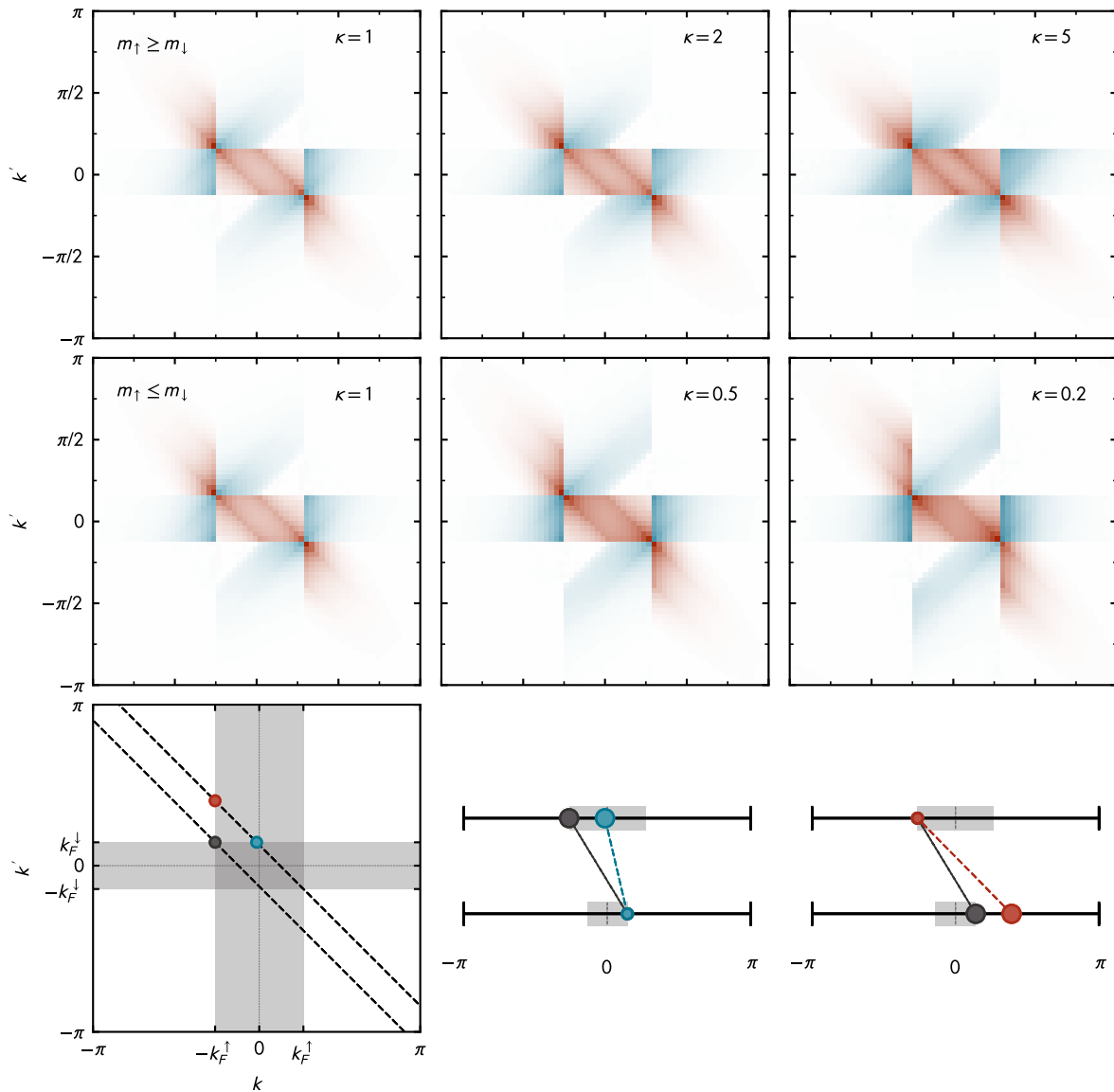
Figure 5.16: Density-density correlations for $N = 17 \uparrow +9 \downarrow$ particles on a lattice of $N_x = 64$ sites and $\tilde{\gamma} = -2.0$. (Top row) Heavy majority with $\kappa = 1, 2, 5$. (Center row) Heavy minority with $\kappa = 1, 0.5, 0.2$. (Bottom row) Pairing of mass-imbalanced fermions in momentum space. (Bottom row, left) Momentum plane with marked positions of the emerging peaks: regular pairing at the Fermi surfaces (gray circle), shift of the heavy majority (blue circle) and shift of the heavy minority (red circle). The two dashed lines correspond to $k_{\mathrm{cm}} = \pm q$ and shaded areas reflect the respective Fermi surfaces. (Bottom row, center and right) Sketch of the single-particle momentum space for the heavy-majority (bottom, center) and heavy-minority (bottom, right) scenario. Upper lines represent the k-space of majority particles, the lower lines correspond to the k-space of the minority species.
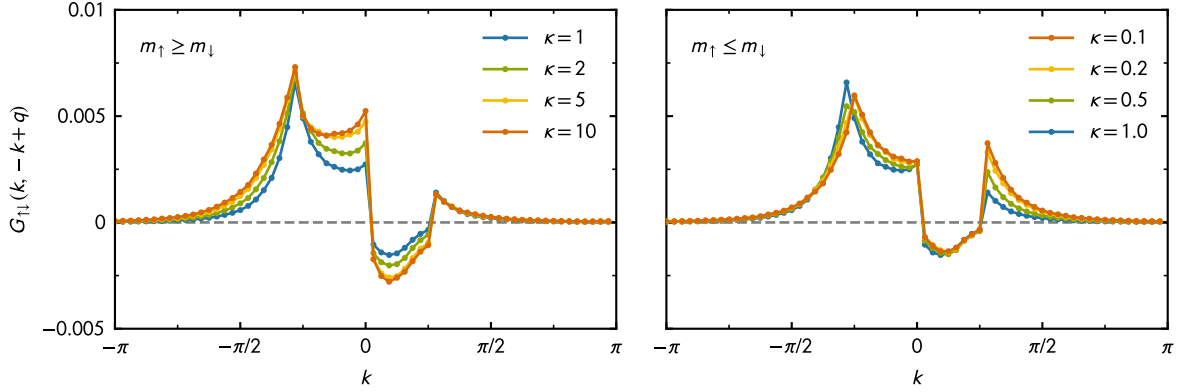
Figure 5.17: Cuts in momentum space along a constant center-of-mass momentum k_{cm} of the pairs for the systems shown in Fig. 5.16. (Left) Heavy majority. (Right) Heavy minority.

observe peaks at $(\pm k_{\mathrm{F},\uparrow}, \mp k_{\mathrm{F},\downarrow})$ which mark the expected FFLO-type pairing in the vicinity of both Fermi surfaces. With increasing κ, additional peaks emerge at $(\pm k_{\mathrm{F},\uparrow} \mp 2q, \mp k_{\mathrm{F},\downarrow})$, indicated by stronger particle-particle correlations (i.e., deeper red coloring). For clarity, only the point at $(-k_{\mathrm{F},\uparrow} + 2q, k_{\mathrm{F},\downarrow})$ is marked with a blue circle in the lower left panel of Fig. 5.16.

The lower central panel of Fig. 5.16 reveals the occurring mechanism: For large enough mass imbalance it becomes energetically favorable to scatter with heavy particles from far below the Fermi surface while still obeying the constraint $|k_{\mathrm{cm}}| = |q|$. The sketch depicts the perspective of the lighter particle at the Fermi surface: In addition to scatter with an up-particle at $k_\uparrow = -k_{\mathrm{F},\uparrow}$ (gray circle), there is now an increased likelihood to pair with a particle at $k_\uparrow = -k_{\mathrm{F},\uparrow} + 2q$ (blue circle). Note, however, that the center-of-mass momentum of such a pair jumps from $k_{\mathrm{cm}} = -q$ to $k_{\mathrm{cm}} = +q$, which corresponds to switching between the two dashed lines in the lower left panel of Fig. 5.16.

Heavy minority   Turning to the heavy-minority scenario (middle row of Fig. 5.16) reveals a similar picture with reversed role of the majority/minority particles. For the same mass imbalances as before, we now observe additional peaks at $(\pm k_{\mathrm{F},\uparrow}, \pm k_{\mathrm{F},\downarrow} \mp 2k_{\mathrm{F},\uparrow})$. The situation is depicted in the lower right panel of Fig. 5.16, where scattering of a light majority particle at its Fermi surface is now favored to happen with either a heavy-minority particle at its Fermi point (gray circle) or far above it (red circle). Similar to the heavy-majority case, the latter scattering option becomes energetically more favorable with larger mass ratio since the energy states may be reached more easily. The corresponding peak in the shot-noise correlation function is marked with a red circle in the lower left panel of Fig. 5.16.

A more detailed illustration of the buildup of the additional peaks for both scenarios is shown in Fig. 5.17, where cuts along the line of $k_{\mathrm{cm}} = -q$ for heavy-majority (left) and heavy-minority (right) systems are plotted as a function of the momentum k of the up-component. In the former case, the emergence of a second peak at $k = -k_{\mathrm{F},\uparrow} + 2k_{\mathrm{F},\downarrow}$ is clearly visible. For heavy-minority systems, the additional peak at $k_\uparrow = k_{\mathrm{F},\uparrow}$ is apparent. A mirrored but otherwise identical picture applies for $k_{\mathrm{cm}} = +q$, which is not shown in the plot.

As already discussed above, it appears that the mass imbalance does not destroy the FFLO-type behavior and pairing still predominantly happens with $|k_{\mathrm{cm}}| = |q|$. If this condition were to be

broken, other momentum states than the ones corresponding to the above-discussed peaks would be populated. This, in turn, would cause the oscillations of the order parameter to wash out, as more modes with $k \neq \pm q$ would interfere with the oscillatory behavior. As a consequence, the pairing gap would not vanish periodically, which implies that the excess fermions cannot minimize their energy by residing in regions with a locally vanishing pairing gap.

While this behavior may be explained physically, the numerical issues discussed in Section 5.5 could interfere with this interpretation, particularly at large momenta. Although unlikely, the effect could be a statistical anomaly and further checks, including larger system sizes, are needed to fully resolve the situation.

5.6 Excursion: higher-order CL integration

All our CL results for the above discussion of 1D Fermi gases have been computed with an integration scheme corresponding to Euler-Maruyama (EM) discretization of the Langevin equation. As discussed already in Section 4.4.2, this strategy introduces a systematic bias that scales linearly with the integration step Δt and the slope typically increases with the strength of the bare interaction strength. Since the EM integration scheme is often sufficiently accurate, and also due to its straightforward implementation, it remains the predominant choice for CL studies despite the existence of higher-order integration schemes.

For a CL study of the $SU(3)$ spin model, on the other hand, higher order integration was found to be a crucial ingredient in order to reach sufficient accuracy at reasonable computational cost [185]. The applied integration scheme was introduced in Eq. (4.4.21), which is expected to introduce a systematic error that scales with $\Delta t^{\frac{3}{2}}$. While the improvement seems relatively modest in terms of the computational complexity, it was found that the leading coefficient is strongly suppressed such that finite step size corrections seem to be eliminated altogether, at least for the specific model and parameter values studied.

Motivated by the almost total suppression of discretization effects, we here present numerical tests for the higher-order integration scheme in Eq. (4.4.21). The improved integration strategy requires to evaluate the drift three times, thereby increasing the numerical effort at constant Δt by that factor. To combine this strategy with the adaptive step size introduced in Section 4.5.5, we define the improved drift

$$K_{\mathrm{imp}} \equiv \frac{\Delta t}{3} \left(K[\chi^{(n)}] + 2K[\psi^{(n)}] \right), \tag{5.6.1}$$

such that the step size is rescaled like

$$\Delta t^{(n)} = \frac{\Delta t}{\max_{i\tau} |K_{\mathrm{imp}}[\phi^{(n)}]|}. \tag{5.6.2}$$

As opposed to EM integration, some random noise already enters the improved drift term which is used to rescale the step size in the above expression. Note also that the regulator term is included in each evaluation of the drift function $K[\phi]$.
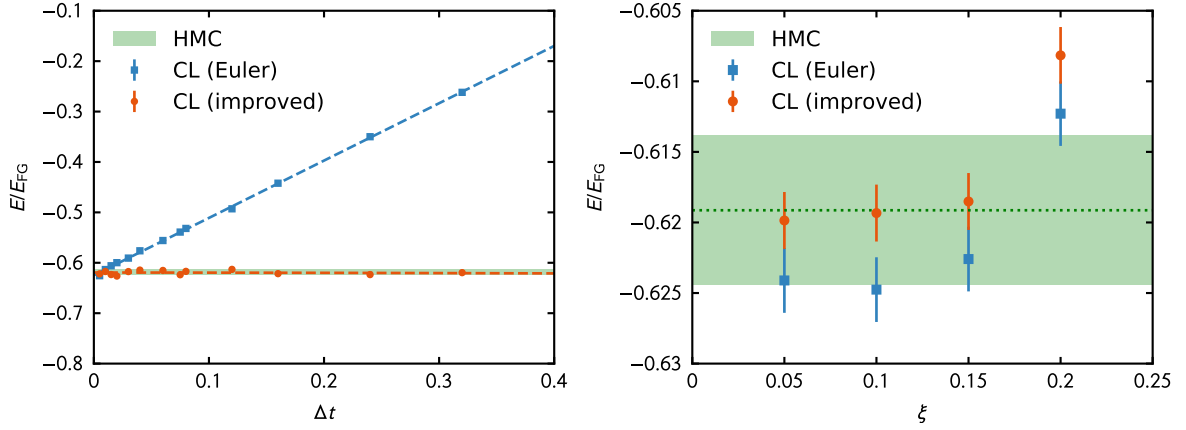
Figure 5.18: (Left) Ground-state energy as a function of the integration step Δt. EM integration (blue squares) and improved integration (red circles) are compared to the HMC result (green band). Dashed lines are polynomial fits of the appropriate order. (Right) Regulator dependence of the ground-state energy extrapolated to $\Delta t \to 0$. In both panels, the green HMC band reflects 1σ uncertainty.

5.6.1 Canonical ensemble in the ground state

We compare the two integration schemes for a mass-balanced system of $N = 5 \uparrow + 5 \downarrow$ particles at a spacetime lattice of $N_x \times N_\tau = 40 \times 100$ and the moderate attractive interaction strength $\gamma = -2.0$. The choice of these parameters allows a comparison to results obtained with the HMC algorithm. In order to precisely filter out the systematic effects we have accumulated 2×10^5 samples per data point. Results for the ground-state energy in dependence of the step size Δt are shown in the left panel of Fig. 5.18 for a regulator strength of $\xi = 0.1$. An extrapolation to the limit $\Delta t \to 0$ for both CL integration algorithms displays excellent agreement with the HMC results. While the results from EM integration deviate already for relatively small values of Δt, the improved values stay roughly within one standard deviation of the HMC results (reflected by the green band) for all values of Δt under study.

In the right panel of Fig. 5.18, the regulator dependence of the $\Delta t \to 0$ extrapolated ground-state energies is shown. We observe a delicate systematic difference between the EM and improved results although the error bars overlap in some cases and thus the results may be considered equivalent for all practical purposes. For sufficiently small values of ξ, all results are observed to lie within one standard deviation of the HMC results, regardless of the integration type. Remarkably, the qualitative behavior of the ground-state energy as a function of ξ does not seem to depend on the employed integration algorithm.

5.6.2 Grand canonical ensemble at finite temperature

To complement the investigation of the ground state, we have also implemented the higher-order scheme for finite temperature calculations and tested its behavior across a variety of interaction strengths and densities. The latter is dictated by the parameter $\beta\mu$, where β is the inverse temperature and μ is the chemical potential. To compare the integration schemes we have accumulated 10^4 decorrelated samples per data point at a spacetime lattice of $N_x \times N_\tau = 41 \times 160$. As above, we have fixed the regulator to $\xi = 0.1$ and kept the inverse temperature at the moderate value of $\beta = 8.0$.
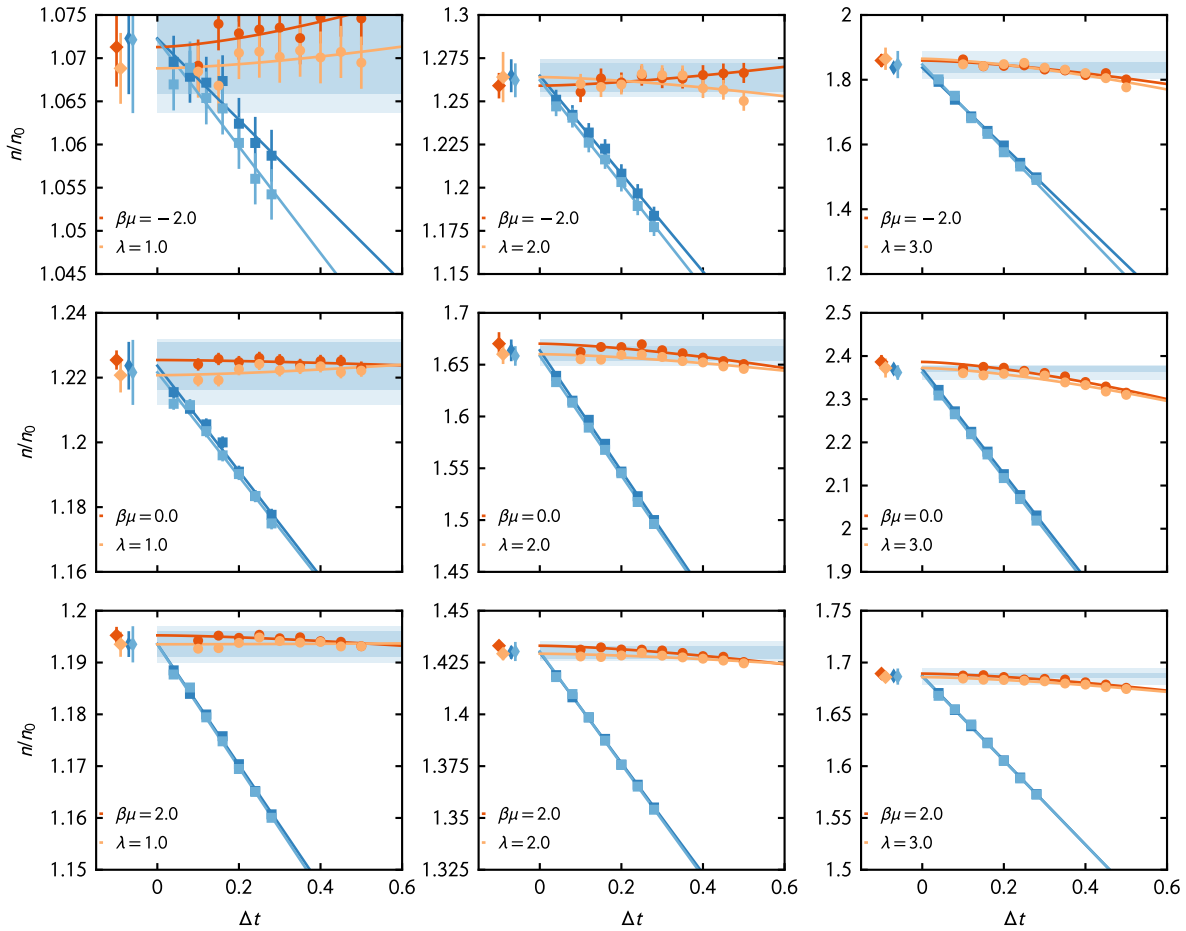
Figure 5.19: Comparison of EM (blue symbols) and improved (orange symbols) integration schemes for various couplings and densities. The values at $\Delta t < 0$ depict results extrapolated to $\Delta t \to 0$ with the propagated statistical errors. Blue shaded bands are the errors of the extrapolated values of the EM scheme. Solid lines are polynomial fits to the numerical data.

The results for the density at various values of $\beta\mu$ and the dimensionless coupling $\lambda = \sqrt{\beta}g$ are shown in Fig. 5.19. To indicate the variation of different initial conditions, two lines per algorithm and parameter set are shown (marked with similar colors). The extrapolated results are shown at negative values of Δt for clarity and are found to agree in all cases within statistical uncertainty.

The conclusion regarding the dependence on the integration step largely carries over from the ground-state investigation: While results obtained with the EM integration scheme scale linearly and the slope strongly increases with the coupling λ (left to right at constant $\beta\mu$), the dependence on Δt of the improved results remains relatively mild. The improved results deviate from the error band of the extrapolated EM values (blue shaded bands) only beyond large values of $\Delta t \gtrsim 0.35$ for the strongest interactions considered here. Similar to the EM values, the improved results show an increase of the scaling prefactor, however, even in the strongly interacting regime at $\lambda = 3.0$ the dependence is relatively mild.

This analysis essentially implies an elimination of finite step bias within practical statistical accuracy. Rather than resorting to tiny integration steps in order to reach sufficient accuracy, it

seems to be enough to work at a relatively large steps without the need of extrapolating $\Delta t \to 0$. This drastically reduces the computational effort for both ground-state and finite-temperature calculations.

5.7 Summary & Outlook

The goal of the present section was to fully characterize the lattice approaches developed in the first part of this thesis in a concrete physical setting. While the HMC algorithm is an established tool in many branches of physics, the present study of 1D Fermi gases is among the first systematic applications of its extensions to imaginary asymmetries (iHMC) as well as the CL approach in the context of nonrelativistic fermionic systems.

As a first step, we have investigated the crossover from few to many fermions via the HMC approach in order to identify appropriate numerical and physical parameter regimes, which carry over to all lattice approaches applied in this thesis. Concretely, we have found excellent agreement with BA expansions at weak and strong coupling and have showed that the lattice treatment allows for a suitable computation of one- and two-body correlation functions. Most notably, the pair-momentum distribution was computed in the balanced case, and it was found that the formation of zero center-of-mass momentum pairs is favored as the attractive interaction increases, in accordance with the literature. This quantity later played an important role in the characterization of pairing in spin-imbalanced systems, as it shows clear signals of FFLO-type pairing in the form of off-center peaks.

After setting the methodological stage for our lattice treatment, we have investigated fermionic systems with unequal masses. The reduction of symmetry inhibits the efficient use of plain HMC as a consequence of the sign problem and also renders BA techniques inapplicable. To surmount the sign problem we employed the iHMC and CL approaches which displayed excellent agreement for attractively interacting systems up to mass-imbalances of $\bar{m} \lesssim 0.6$, beyond which results obtained through the iHMC approach exhibit large uncertainties. Remarkably, the CL values do not suffer from such a shortcoming and the method seems to be applicable for systems with arbitrary mass imbalance. While these results have been confirmed by a sign-free implementation of the worldline algorithm [122, 123] on the attractive side, our values at large repulsive interactions have been shown to be problematic. This shortcoming did indeed not come unexpected, as the histogram of the sampled ground-state energies displayed fat tails which cause biased expectation values in this parameter regime. Our determination of the EOS for attractive interactions marks the first systematic study of 1D fermions with contact interaction for general mass imbalances.

The success of the CL method for attractively interacting fermions allowed us to subsequently extend our study to spin-imbalanced systems. Since the mass-balanced case is again integrable, we were able to benchmark against BA results in both the few- and many-body sectors and found excellent agreement. Despite the applicability of the exact BA for purely spin-imbalanced systems, correlation functions are challenging to compute within this approach which necessitates numerical treatment. We have shown that the CL method is able to accurately compute two-body correlation functions and found that FFLO-type pairing is the dominant instability for all values of the relative polarization under study. This finding, which is supported by the occurrence of off-center peaks in the pair-momentum distribution, is in accordance to earlier studies on the subject [260]. An exciting possibility to resolve the internal structure of the fermionic pairs was

shown to be the computation of the density-density correlations in momentum space, which feature distinct imprints of FFLO-type pairing. These quantities were also found to be in excellent agreement with earlier results obtained by the means of DMRG [259, 260] and are in principle accessible in experimental setups [214].

As a final step, we have combined both asymmetries to study the influence of mismatched particle masses on the FFLO pairing pattern. While the pair-momentum distribution was found to be largely unaffected by the mass imbalance, the shot noise revealed distinct changes in the pairing pattern. Interestingly, FFLO-type behavior was found to prevail for all mass-imbalances under study. However, the relative momentum of the pairs changes as higher momentum states become energetically accessible. To the best of our knowledge, this type of pairing was observed for the first time in this study. It will be interesting to see if these predictions withstands experimental verification.

Our extensive study of 1D imbalanced Fermi gases shows the excellent applicability of stochastic lattice approaches, and most specifically of CL, in the context of low-dimensional ultracold Fermi gases. Benchmarks to known results in the literature have shown the accuracy and reliability in many cases and faulty behavior has been found to be accompanied by distinct imprints on the histograms. This yields an optimistic outlook for the application of CL in more diverse studies otherwise plagued by a sign problem and, most promisingly, the extension to larger spatial dimensions, as also discussed in the subsequent chapter.

As remarked already above, the CL treatment of Fermi gases with large repulsive interactions yielded polynomially decaying histograms which could be the sign of a formal failure of the CL method. A similar issue was found for the tails of one-body correlation functions in momentum space, which ultimately limits the predictive power of the CL in this regime. A necessary further step in the development of CL for ultracold Fermi gases is therefore the detailed investigation of this shortcoming by clarifying the exact nature of the issue. Possible strategies involve the use of improved trial wavefunctions, finite temperature calculations, alternate Hubbard-Stratonovich transformations, and, most importantly, stabilized imaginary time propagation. We shall briefly elaborate on these techniques in the general outlook in Chapter 7.

With a more sophisticated implementation of the above described lattice approaches it should then become possible to study the correlation functions of various ordering mechanisms in more detail. In particular, a study of the dependence of the different correlation coefficients on polarization and mass asymmetry is of interest as this helps to unambiguously identify the leading instability.

The perhaps most exciting possible avenue pursued in this chapter is the study of so-called shot-noise correlations, which allow a close look at the pairing structure in 1D Fermi gases. An extension to higher dimensional systems is certainly feasible and could be fruitful in the discussion of exotic superfluid phases in the phase diagram of the spin-polarized UFG, as discussed in the upcoming chapter.

6 | The spin-polarized unitary Fermi gas

> *"Bei diesem Blatt kann ich frohlocken und möchte ewig weiterzocken."*

> Johnny Firpo in "Zwei sind nicht zu bremsen"

Without a doubt, one of the most intensely studied many-body systems in recent years is the unitary Fermi gas. It is situated right "in the middle" of the BCS-BEC crossover and corresponds to the regime with the strongest possible s-wave interaction while still satisfying the unitarity of the scattering matrix. As a result, Fermi gases exhibit a scale invariance in this regime and it is possible to write any thermodynamic quantity as a dimensionful factor (typically its noninteracting value) multiplied by a *universal* dimensionless scaling function which only depends on temperature and density [270]. For example, the energy of the UFG may be written as

$$E = E_{\text{FG}} \, f_E(n/k_{\text{F}}^3, T/T_{\text{F}}) \, . \tag{6.0.1}$$

Such a relation holds irrespective of the nature of the thermodynamic phase such that the thermodynamic behavior at unitarity is described by only a few universal numbers. Mapped to experiments, universality implies that the same function f_E must be measured regardless of the fermionic atom species which indeed has been confirmed in a range of experiments over the past two decades (see, e.g., [20, 35]).

In this chapter we explore the thermodynamics of the UFG in the presence of a finite spin imbalance. At low temperatures, when the system is superfluid, a large enough polarization will destroy superfluidity, often referred to as the Chandrasekhar-Clogston limit [29, 30], as discussed in Chapter 1. Precisely how that happens, and what other exotic superfluid phases may be traversed in the process, has remained a controversial topic. Part of the challenge in answering such questions is that the UFG (not unlike QCD and many other systems) is a strongly correlated many-body system lacking a small parameter and therefore can only be tackled with nonperturbative methods such as the CL approach.

To discuss the physics of the UFG, our main quantity of interest is the density equation of state (EOS), which is a direct output of our numerical calculation in the grand canonical ensemble. In the case of different chemical potentials for the spin species, the densities of up and down particles will generally differ, which opens the possibility to study the "magnetic" properties of the system. In addition to a precise density equation of state, we obtain a variety of other thermodynamic quantities through the use of thermodynamic relations and compare them to

other approaches wherever available. A central tool in this regard, at least at high temperatures,[1] is the virial expansion, which gives a power series representation of the partition sum at low fugacities. We shall demonstrate that all our quantities agree with the virial expansion in the expected limit and thus survive an important sanity check.

To further validate the numerical approach, which we have applied to the UFG for the first time, we perform an extensive benchmark for the spin-balanced gas. In this limit, precise experimental values have been obtained [271] and, since the balanced system does not suffer from a sign problem, exact calculations from other stochastic schemes are available [152, 272–275]. Beyond the balanced limit, however, benchmark values at finite temperatures are relatively scarce since MC studies face a severe sign problem. The problem was nevertheless attacked via the standard worm algorithm combined with re-weighting [276, 277] which shed some light on the critical temperature in the presence of slight spin asymmetry. Besides the mentioned MC study, there are other results obtained via mean-field treatment as well as more sophisticated methods albeit with potentially uncontrolled approximations (see [57–59] for reviews). The here presented *ab initio* results mark the first unbiased, experimentally testable predictions for a range of thermodynamic properties of the spin-polarized UFG at finite temperature.

6.1 Model, scales & scattering on the lattice

Fermions in the unitary limit are governed by a Hamiltonian with a nonrelativistic dispersion relation and a zero-range interaction,

$$\hat{H} = \int d^3x \, \hat{\psi}_s^\dagger(x) \left(-\frac{\hbar^2 \nabla^2}{2m} \right) \hat{\psi}_s(x) - g \int d^3x \, \hat{n}_\uparrow(x) \hat{n}_\downarrow(x), \tag{6.1.1}$$

which corresponds to the three-dimensional version of the model introduced in Eq. (2.1.1). Since we must discretize the problem for our numerical treatment, the coupling g needs to be tuned such that our lattice theory reproduces the desired scattering properties. This can be done by first considering the so-called finite-range expansion [278] which allows us to write the low-energy scattering phase shift of sufficiently short-ranged interaction potentials in terms of the momentum:

$$p \cot \delta(p) = -\frac{1}{a} + \frac{1}{2} r_{\text{eff}} p^2 + \mathcal{O}(p^4). \tag{6.1.2}$$

For the unitary point, where the scattering length a diverges and the effective range r_{eff} tends to zero, this yields a phase-shift of $\delta = \frac{\pi}{2}$ independent of the (small) momentum.

The above expansion holds for continuous systems in the limit of infinite volumes. For finite system sizes in the continuum, on the other hand, we may exploit Lüscher's formula [89]. It relates the scattering phase shift to the energy spectrum of the two-body problem in a periodic box of length L via

$$p \cot \delta(p) = \frac{1}{\pi L} S(\eta) \tag{6.1.3}$$

with $\eta = \frac{Lp}{2\pi}$ and the three-dimensional zeta function $S(\eta)$ as defined, e.g., in [91]. Tuning the

---

[1]Sometimes also referred to as the Boltzmann regime.

phase shift to unitarity, i.e., $\delta = \frac{\pi}{2}$, then corresponds to finding the roots of the zeta function.[2] We use the root closest to the origin, located at $\eta^2 = -0.0959007$, as it relates to the smallest value of the coupling that obeys the unitarity condition and therefore minimizes lattice spacing effects.

In order to match the lattice theory to the continuum, we must solve the Schrödinger equation of the two-body problem on the lattice. For a zero-range potential, the relation between coupling and energy reads

$$\frac{1}{g} = \frac{1}{L^3} \sum_{\vec{k}} \frac{1}{E - 2\varepsilon_{\vec{k}}}, \tag{6.1.4}$$

where the sum is over all momentum states $\vec{k}$ on the lattice and $\varepsilon_{\vec{k}} = \frac{1}{2m}\vec{k}^2$ is the dispersion relation. The coupling is then obtained by inserting the energy $E = \frac{\eta^2}{2m_r}(\frac{2\pi}{L})^2$ evaluated at a root of $S(\eta)$. To minimize cutoff effects we evaluate the sum for a large value of L and find a value of $g \approx 5.14435$ for the unitary point in our formulation. More details on this procedure may be found, e.g., in [98, 102, 279].

Note that the above prescription only matches the lowest energy value of the lattice problem to the continuum. Higher energy states will generally differ and thus the exact physics is only reproduced in the very dilute limit where only a small number of momentum states are occupied. To remedy this issue, parameters additional to the coupling have to be introduced and appropriately tuned. Such an improved strategy has been applied before [91, 93, 107], however, it is not pursued in this thesis.

6.1.1 The grand canonical ensemble

To study the thermodynamics of the UFG, we consider the grand-canonical partition function

$$\mathcal{Z} = \text{Tr}[e^{-\beta(\hat{H} - \mu_\uparrow \hat{N}_\uparrow - \mu_\downarrow \hat{N}_\downarrow)}], \tag{6.1.5}$$

where $\beta = 1/T$ is the inverse temperature and μ_σ is the chemical potential coupled to the number operator $\hat{N}_\sigma$ for the species σ. Through the variable transformation

$$\mu = \frac{1}{2}(\mu_\uparrow + \mu_\downarrow) \tag{6.1.6a}$$

$$h = \frac{1}{2}(\mu_\uparrow - \mu_\downarrow) \tag{6.1.6b}$$

we can rewrite the partition function as

$$\mathcal{Z} = \text{Tr}[e^{-\beta(\hat{H} - \mu\hat{N} + h\hat{M})}], \tag{6.1.7}$$

where μ is the average chemical potential and h is the relative chemical potential mismatch coupled to the total number operator $\hat{N} = \hat{N}_\uparrow + \hat{N}_\downarrow$ and the so-called magnetization operator $\hat{M} = \hat{N}_\uparrow - \hat{N}_\downarrow$, respectively. Often, h is referred to as the effective Zeemann field or merely magnetic field since it causes a spin-selective shift of the Fermi surfaces around the average

---

[2]The evaluation of $S(\eta)$ might be tricky due to numerical cancellations. A useful technique may be found in the appendix of Ref. [91] along with tabulated values of the roots of $S(\eta)$.
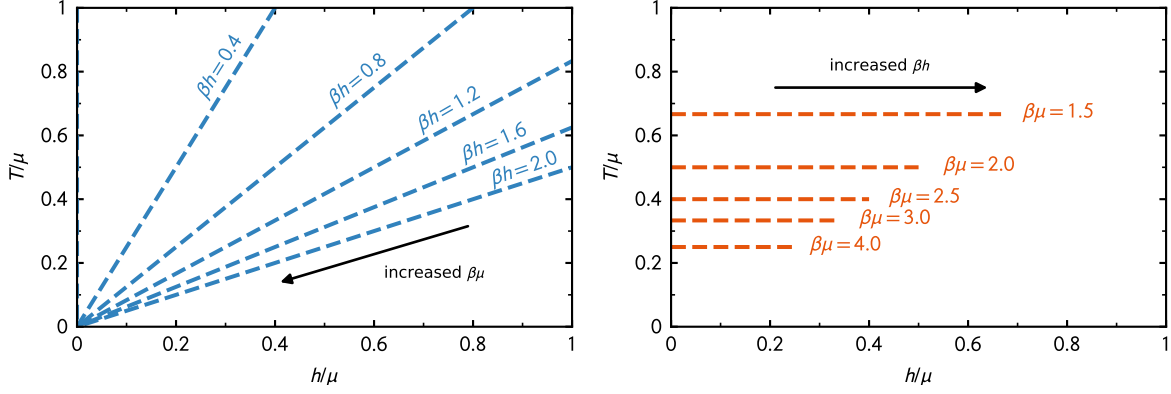
Figure 6.1: Sketch of the grand-canonical parameter space $1/\beta\mu$ vs. h/μ. The lower left corner corresponds to large chemical potential, i.e., low T/T_F, where the superfluid phase is present. (Left) Lines of fixed βh. Varying $\beta\mu$ implies moving along the dashed lines. (Right) Lines of fixed $\beta\mu$. Varying βh corresponds to moving along horizontal lines.

Fermi surface, as already discussed in the context of the CC limit in Section 1.3. Without loss of generality, we set $h > 0$ which implies that the up component is set to be the majority species.[3] In Fig. 6.1 scans through the parameter plane $1/\beta\mu$ vs. h/μ at fixed values of βh are depicted to guide the reader through our studies.

6.1.2 Units & scales

In the following, all results are presented in dimensionless form. As remarked above, computations are carried out in the grand-canonical ensemble which implies fixing the parameters μ and h to obtain the average density as a result of the calculation. Due to the units we have chosen, temperatures as well as chemical potentials carry the units of L^2 which we exploit to define the dimensionless parameters $\beta\mu$ and βh to fix the physics.

A characteristic length scale in the system is given by the thermal de Broglie wavelength $\lambda_{\mathrm{T}} = \sqrt{2\pi\beta}$. In order to avoid strong discretization and finite-size effects, other parameters must be chosen such that,

$$\ell \ll \lambda_{\mathrm{T}} \ll N_x\ell \tag{6.1.8}$$

where N_x is the number of spatial lattice sites per dimension. The above expression encodes part of the computational challenge when moving to low temperatures: due to the increased thermal wavelength, the box size needs to be scaled appropriately which renders the computation more costly. Luckily, however, λ_{T} grows only with $\sqrt{\beta}$ such that sufficiently low temperatures may be reached within reasonable computational effort.

Characteristic energy scales in the system are given by the Fermi energies of the spin species $\varepsilon_{\mathrm{F},\sigma} = \frac{1}{2}k_{\mathrm{F},\sigma}^2$ with the Fermi momenta

$$k_{\mathrm{F},\sigma} = (6\pi^2 n_\sigma)^{1/3}. \tag{6.1.9}$$

---

[3]Note that this is only permissible in the case of equal spin species. Otherwise, for instance in the case of a mass imbalance between the species, the situation for h and $-h$ correspond to different physical scenarios.

Note that our units imply $\varepsilon_F = T_F$ such that the Fermi energy may be used to rescale energies as well as temperatures.[4]

Finally, all thermodynamic properties are presented in the units of the corresponding quantity of the noninteracting gas (either in the ground state or at the corresponding temperature). A detailed derivation of the expressions may be found in Apppendix C.

6.1.3 Numerical parameters

For the numerical determination of the EOS, a range of physical as well as numerical parameters have to be specified. As already remarked in Section 2.3, we fix the lattice spacing to $\ell = 1$ such that the temporal time step $\Delta\tau$ sets the lattice units. Technically, in order to eliminate the effect of the imaginary-time discretization, an extrapolation $\Delta\tau \to 0$ needs to be performed. Since the temporal discretization only yields an error on the order of $\Delta\tau^2$, however, we have found it sufficient to set $\Delta\tau = 0.05$ for all numerical calculations to follow, which is below the statistical accuracy of the present study.

Moreover, we consider a fixed value of $\beta = 8.0$ which amounts to $N_\tau = 160$ temporal lattice sites and fixes the thermal wavelength to $\lambda_T \approx 7.09$. To minimize contamination from finite-size effects, the spatial extent of the box needs to be chosen such that Eq. (6.1.8) is satisfied. Unless otherwise noted we chose the moderate volume $V = 11^3$ which is sufficient to capture the physics in a wide temperature range.

All results presented below have been obtained by averaging over three independent trajectories of 10^3 samples. We refer to a sample as a measurement after the CL time evolution of length ~ 1 in Langevin time which corresponds to a variable number of actual CL updates due to the usage of an adaptive CL step. For every trajectory, which merely reflects different initial field configurations, the first 10% of the samples have been discarded to avoid initialization bias. All in all, our total number of samples allows us to obtain a relative statistical error of roughly 2%. Finally, we have checked the influence of the regulator strength on our results, which we found to be negligible, at least for small enough values of ξ. In the following we use $\xi = 0.1$ which represents a pragmatic choice and appears to be large enough to stabilize trajectories over a broad range of temperatures and also small enough as to avoid large bias in the final results. The discretization of Langevin time, however, has been found to have impact on the obtained results and therefore the extrapolation $\Delta t \to 0$ is necessary, as discussed further below.

6.2 Data post processing & systematic error control

Before being able to discuss the thermodynamic behavior of the UFG as a function of physical parameters, we have to address potential numerical artifacts. In the following we show the statistical validity of our results by detailing the post processing applied to the raw simulation data and commenting on possible issues and their implications. Subsequently, we address systematic errors introduced by the CL treatment and extrapolate where necessary.

---

[4]The definition of the Fermi momentum of a single species in Eq. (6.1.9) should not be confused with the often used expression for a two-component gas: $k_F = (3\pi^2 n)^{1/3}$ where $n = n_\uparrow + n_\downarrow$ denotes the total density. The latter is used in particular in studies of the balanced UFG, where it is equivalent to the above definition.
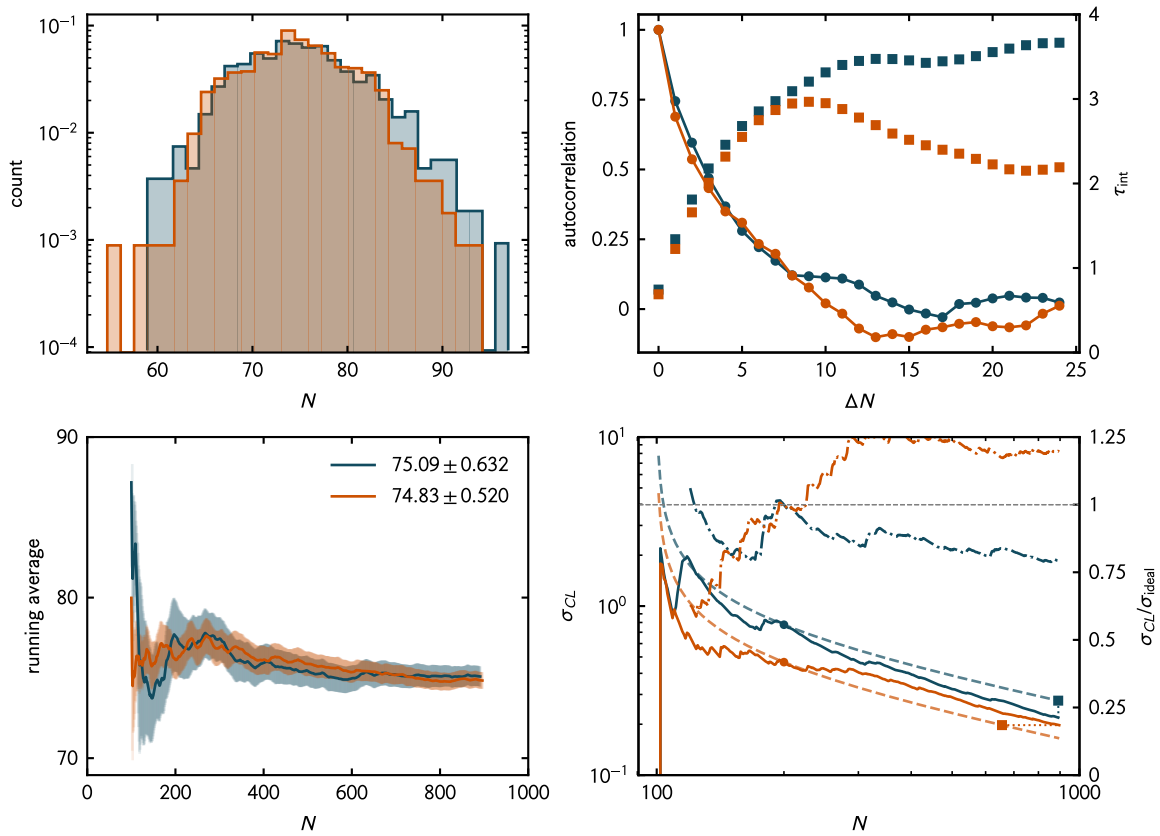
Figure 6.2: Statistical evaluation details for the total density with the parameters $\beta\mu = 2.0$, $\beta h = 1.2$ and $\Delta t = 0.04$. The colors correspond to two different initial conditions, i.e., two trajectories. (Top left) Sampled histogram on a log scale. (Top right) Autocorrelation function and integrated autocorrelation time as a function of sample lag ΔN. (Lower left) Running average with statistical error estimate. (Lower right) Error estimate as function of sample number. Solid lines are the actual error, dashed lines are the expected $N^{-1/2}$ decay from the reference point (dot) and dashed-dotted lines are the ratio of actual error to ideal error (scale on the right).

6.2.1 Statistical evaluation & error estimation

Part of every MC calculation is the statistic evaluation of single runs at fixed parameter sets. While plain averages are readily evaluated, some more effort has to be put forward to ensure the validity of the values and to reliably estimate the errors. This is not only because of autocorrelation between samples, but could also originate from more subtle effects like a distribution overlap problem, numerical instabilities or, as in the case of CL, potential conceptual barriers of the method. Here, we show a detailed investigation of the particle density for the parameters $\beta\mu = 2.0$, $\beta h = 1.2$ and $\Delta t = 0.04$ and all other parameters as discussed above. This specific dataset serves to exemplify the quality of our data - other parameter sets are of equivalent statistical accuracy.

A central tool to study the behavior of the simulation is the histogram of the sampled values. The expected functional form of the distribution depends on the observable as well on the representation and the applied algorithm and is in general unknown. Nevertheless, it is important that the histogram is somewhat localized such that it decays quickly towards large values of the

observable on either side. In the case of large statistical weight towards the wings[5] the results suffer from slow convergence since frequent outliers increase the variance of the sampled values which in turn reduces the statistical accuracy dramatically. In extreme cases, namely when the distribution decays slower than a power law with exponent $\alpha = 3$, the second moment of the distribution formally diverges and is no longer well defined. Practically, this implies that accumulating more samples will not increase the statistical accuracy and the simulation fails to deliver arbitrary precise measurements. We show histograms for two trajectories in the top left panel of Fig. 6.2 and observe almost perfect Gaussian behavior which is well localized and therefore no issues are expected.

To complement the histogram, running averages are shown in the lower left panel of Fig. 6.2. After the first discarded 10% of the samples, the averages (lines) relatively quickly approach a stationary value and stay, mostly, within the decreasing statistical error (shaded area). Outliers in the histograms, which could be caused by various issues, would correspond to a sudden jump in the running average. While single or few outliers are washed out by a sufficient amount of samples, too frequent outliers prevent the trajectory from stabilizing and no reliable values may be obtained.[6] For all parameter values studied in this chapter, outliers pose no problem and the running averages are observed to be smooth. For increasing values of $\beta\mu$, however, we observe a small number of atypical contributions which is likely caused by a singular Fermi matrix due to the increased density in the system. It is expected that this trend becomes more severe at larger lattices and lower temperatures, where the eigenvalues of the Fermi matrix spread beyond the capabilities of floating point arithmetic. Consequently, numerical noise washes out the lowest lying eigenstates. The issue may be controlled by suitably stabilizing the imaginary time propagation via matrix decomposition (typical strategies rely on either the singular value decomposition or the QR-decomposition [100]). Further, we note that an ill-conditioned Fermi matrix is not the only source of potential outliers and, specifically for CL simulations, uncontrolled excursions in the complex plane could lead to destabilized trajectories and need to be carefully monitored, as discussed below.

In the same way as the running average, the evolution of the statistical error is plotted as a function of the sample number in the lower right panel of Fig. 6.2 (note the double logarithmic scale). For large N the variance of the mean should decay as $N^{-1/2}$. This is indicated by the dashed lines, which show the ideal decay starting from a reference point at $N_{\text{ref}} = 100$ samples after thermalization (indicated by the dot). We observe that the errors indeed follow the trend with some fluctuations around it. For a frequent number of outliers, the estimated error would level off at some plateau which sets the limit of precision that can be achieved for the observable without resorting to an exponential increase in sample number. We do not observe such a problematic behavior across all parameter values studied.

Finally, in order to correctly estimate the statistical error, we have to take into account the effect of autocorrelation for which we employ the Jackknife method [115]. Additionally, we show the autocorrelation function for the total density in the top right panel of Fig. 6.2. As we measure observables only after a certain Langevin time has passed, the correlation between the samples is generally rather low as can be seen from the curve. As apparent from the figure, the estimation of the integrated autocorrelation time from the autocorrelation function is challenging and oscillates

---

[5]Large tails are also called fat tails, long skirts or Pareto tails in the literature.

[6]Regardless of the ability to treat single outliers, their occurrence should always be investigated as it could be the onset of numerical problems.

due to statistical noise. Therefore we estimate the quantity with the Jackknife method and observe that τ_{int} is always below ~ 4. Furthermore, τ_{int} somewhat depends on the discretization step $\Delta\tau$ as well as mildly on the physical parameter $\beta\mu$.

6.2.2 Imaginary parts of observables

Besides the regular statistical evaluation of Markov chain data shown above, the usage of CL requires us to also check the imaginary parts of sampled observables. For all physical quantities, the imaginary part needs to vanish, or at least be sufficiently small. Any deviation from that may spoil the formal argument of the CL method and thus marks a shortcoming of the method for the corresponding parameter regime.

In Fig. 6.3 we show how the imaginary part of the total density evolves in Langevin time for a system with the parameters $\beta h = 1.2$ and $\Delta t = 0.04$ for multiple values of $\beta\mu$. Across all values, the trajectory initially starts out at a relatively large value of $\text{Im}[n]$, which stems from a random start in the field space. As time progresses, we observe an exponential decay of the imaginary part which is expected for physical results. Eventually, the decay stops and levels off at a plateau as a consequence of the finite precision of floating point arithmetic. Naturally, we can use the onset of the plateau as indication for a sufficiently thermalized random process. As apparent from Fig. 6.3, the plateau occurs after ~ 200 decorrelated samples, which is a typical thermalization time used throughout this work.

While for negative values of $\beta\mu$ (i.e., the virial regime) the trajectories settle at $\sim 10^{-16}$, which reflects the limit set by floating point arithmetic, the magnitude of the plateaus grows as $\beta\mu$ is increased. Although the imaginary part is larger than in the virial regime, the magnitude is still $\sim 10^{-10}$ for systems with $\beta\mu \leq 1.5$ which is well beyond a problematic order of magnitude. However, further increasing $\beta\mu$ reveals potential issues as the trajectory fails to sufficiently decay towards a stable value. Beyond $\beta\mu \approx 2.5$ (which roughly corresponds to the phase transition temperature as discussed below) the decay is almost entirely suppressed and the imaginary part, while still some orders of magnitude smaller than the corresponding real part, does not sufficiently vanish. It is therefore expected that the CL results are compromised in this regime as a consequence of the broken formal argument. Indeed, as discussed further below, we observe deviation from benchmark data even in the balanced case.

Of course, the absence of a sufficient decay is a symptom of an underlying problem. The exact reason, however, is relatively challenging to identify as there are several possible mechanisms that could cause such a behavior. First of all, it is possible that a so-called distribution overlap problem prevents the values from converging to a stable trajectory due to frequent outliers. However, judging from the above discussion of the statistical evaluation for the same parameter set, this is an unlikely root of the problem backed by the well behaved nature of the real part.

A close inspection of the trajectories in Fig. 6.3, particularly of the lower central panel ($\beta\mu = 2.0$), reveals an interesting behavior: there are frequent occurrences of a large imaginary part of the density followed by a decay back towards small values of $\text{Im}[n]$. This implies an occasional large value of the drift term in the imaginary direction during the Langevin propagation and thus possible faulty behavior as already discussed in Section 4.5.3. We observe that the number of exceptional drift values rises with the chemical potential, i.e., with increased density in the system. As already mentioned above, this could be a consequence of ill-conditioned Fermi matrices which is expected to become a problem with increasing particle density. In fact, similar
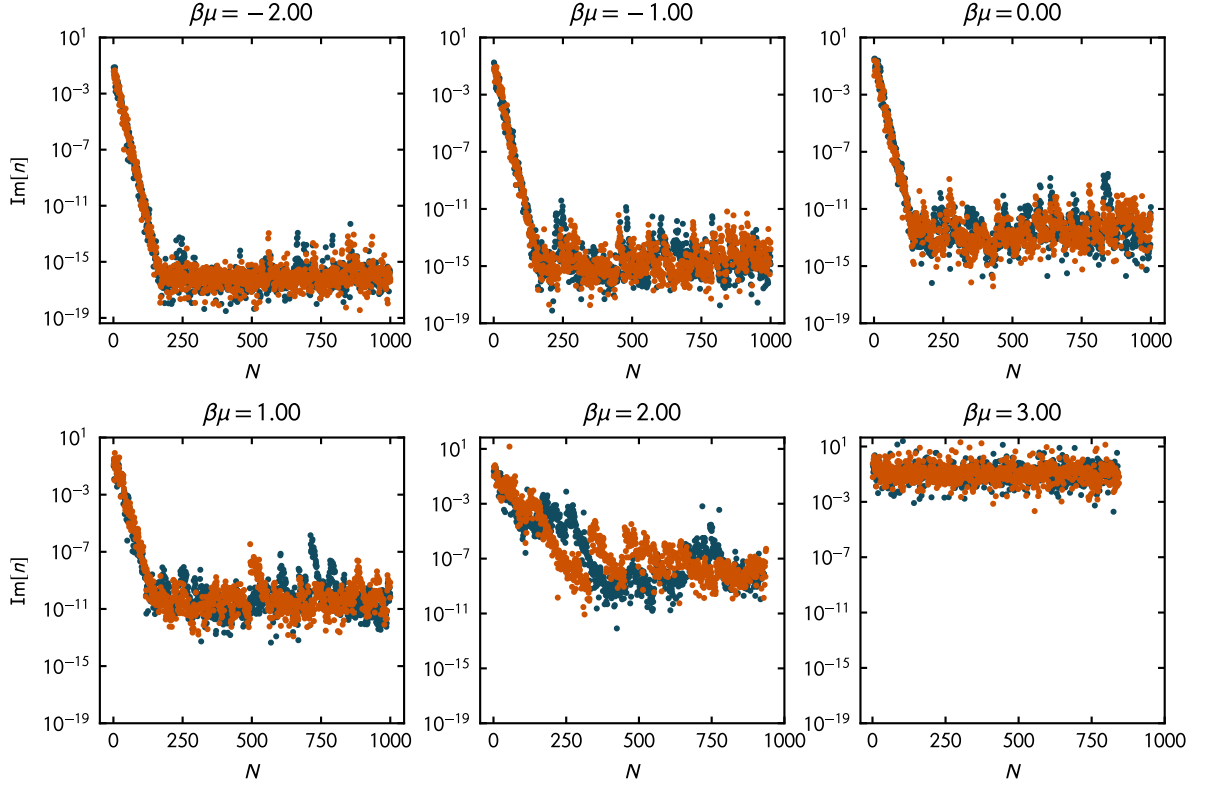
Figure 6.3: Imaginary part of the density as a function of the sample number with $\beta h = 1.2$ and $\Delta t = 0.04$. The colors denote two different initial values. The panels correspond to $\beta \mu = -2.0, -1.0, 0.0, 1.0, 2.0$ and 3.0 (top left to bottom right).

behavior regarding the singularity of the Fermi matrix for increased system sizes and densities was observed for HMC simulations of the balanced UFG without a stabilization procedure [98]. Additionally, an extensive analysis of the issue in ground-state calculations, which we have performed in a separate project, displays essentially the same features and thus further suggests this mechanism as the likely culprit. It is therefore expected that a proper stabilization of the imaginary-time propagation will diminish this shortcoming. However, the implementation and proper testing of the procedure is beyond the scope of the present thesis and deferred to a future study on the topic.

Although the above explanation yields a consistent picture, it should be noted that the CL method may generally fail in some parameter regimes. Without first eliminating other possible issues, however, it is challenging to conclusively identify whether this is the case for the present system or not.

6.2.3 Finite-volume effects

Our procedure of evaluating the path integrals for the UFG involves discretizing spacetime using a (3+1)-dimensional lattice. As already remarked in Section 2.3, this imposes certain limitations that need to be addressed in order to obtain physically correct results.

First of all, the box extent $L = N_x \ell$, which sets the IR cutoff, should be larger than any physical length scale in the system. In particular, L should exceed the thermal wavelength λ_{T} leading

to the requirement of large lattice sizes at low temperature. Moreover, at the superfluid phase transition, the correlation length diverges and, even below the phase transition, the dynamics are then governed by massless excitations (associated with the appearance of Goldstone bosons). This further strengthens the need for large lattices in this regime.

The lattice size, however, is not the only source of systematic error. Indeed, simply increasing the lattice size by itself would not be enough to ensure accuracy at low temperature. The latter is essentially controlled by the dimensionless parameter $\beta\mu$: Increasing β or increasing μ will have the same effect in the sense that both lead to an increased density and therefore larger lattice-spacing effects.[7] These translate into finite-range effects which can be best understood by again looking at the finite range expansion of the scattering phase-shift in Eq. (6.1.2): While in the continuum $r_{\mathrm{eff}} = 0$ by definition, the corresponding effective range on the lattice will generally be finite [91]. This implies that particles in momentum states other than $p^2 = 0$ feel a finite-ranged two-body potential and thus a deviation from the unitary limit. As stated above, the effect worsens with increased density in the system as the particle spacing approaches the induced finite range of the potential.

A somewhat different way of looking at this is to realize that the lattice spacing determines the UV cutoff in the calculation. From this standpoint, an increase of the density then corresponds to filling momentum states. If the spacing is too large (or the UV cutoff is too small), then already a substantial amount of momentum states will be occupied in the noninteracting limit and therefore excitations to higher states are no longer possible when the interaction is turned on. To investigate the effects of the finite box size, we consider spatial volumes $V = (N_x)^3$ with $N_x = 7, 9, 11$ and periodic boundary conditions. In Fig. 6.4, we display the behavior of the density in units of λ_{T}^3, for a selected set of parameter values $(\beta\mu, \beta h)$ as a function of inverse spatial volume. Our CL results for the interacting density exhibit a behavior which follows closely the trend of the density of the noninteracting system on an appropriately sized lattice (shown as gray lines). Moreover, where applicable, our results also show very good agreement with the results from the virial expansion. The scaling of the noninteracting system suggests that our largest lattice sizes are already close to the infinite limit for a wide range of $\beta\mu$ values.

It should be mentioned that our choice for the lattice parameters is appropriate for a computation of "integrated quantities", such as the density EOS. For an accurate calculation of other observables, such as correlation functions, this may not be the case. In fact, a computation of the contact in [151] relied on equivalent lattice parameters as the present work and showed that the one-particle momentum distributions were not obtained sufficiently accurate at very large momenta. At least for the calculation of the density EOS and related quantities, however, this effect seems to be subleading.

As we shall discuss further below, our values in the normal phase at lattice sizes of $N_x = 11$ are in excellent agreement with a variety of benchmark values in the spin-balanced case, both from experiment and theory. There is no reason to believe that this should change in the spin-imbalanced case. However, in order to extract precise continuum properties, a finite-size scaling is a necessary next step. Typically, this is done via a filling-factor extrapolation to zero density or, equivalently, infinite volume. The strategy is to fix the particle number, i.e., to work in the canonical ensemble, and then subsequently study the same particle content at increasingly larger lattices. At finite temperatures, such a treatment requires a projection to a fixed number of particles as proposed in several MC studies [280–282] as well as a recent CL application for

---

[7]In the condensed matter literature, the density on the lattice is also referred to as filling factor.
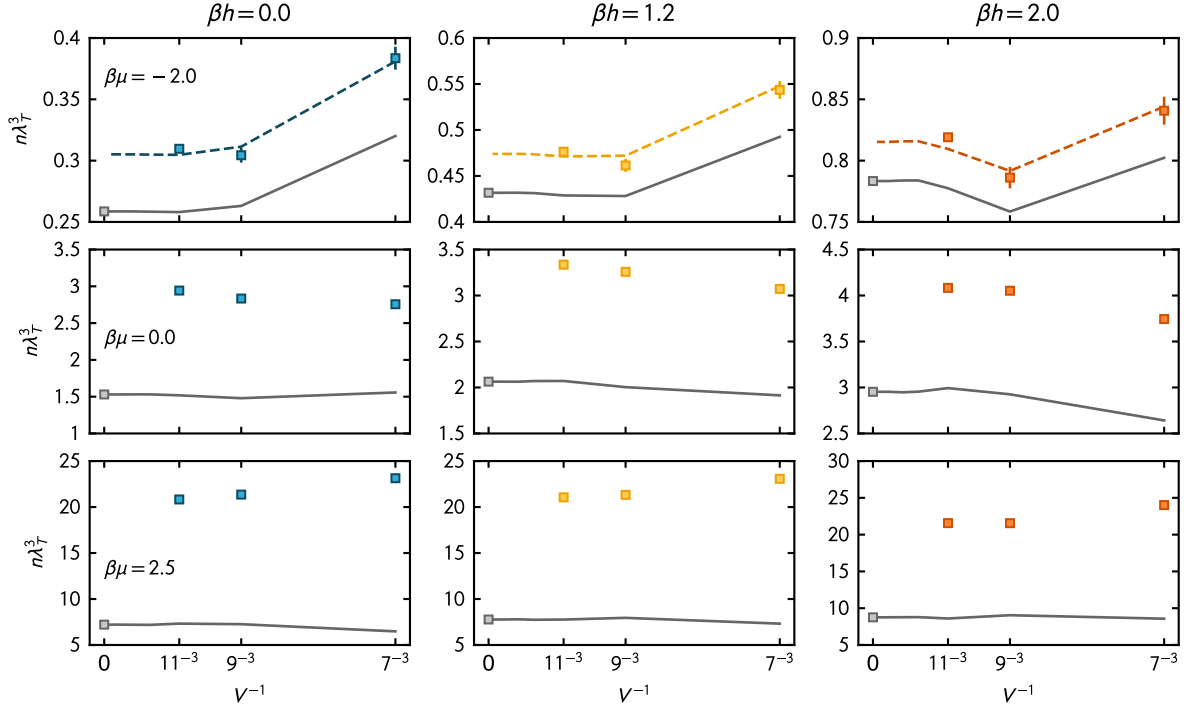
Figure 6.4: Dimensionless density $n\lambda_T^3$ as a function of inverse volume for selected values of $(\beta\mu, \beta h)$ together with the noninteracting values on the lattice (solid lines) and the values in the infinite-volume limit (symbols at $V^{-1} = 0$) as well as, where applicable, the results from the virial expansion (dashed lines).

low dimensional Fermi systems [283]. In this thesis, however, such an approach was not explored and left for future investigations.

Finally, the influence of an effective finite range of the interaction potential may be mitigated by better matching the scattering properties of the lattice theory to the continuum. The obvious benefit of such an approach, as compared to simply increasing the lattice size, is the drastically lower numerical cost since better continuum results are achieved at a constant lattice size. Several strategies have been devised in this regard, especially in the high-energy lattice community where samples at large lattices are exceedingly expensive to compute. For the UFG, early approaches involved matching the second-order virial coefficients [279]. Recently, improved transfer-matrices have been used to accurately compute ground-state properties [93] and so-called improved operators have been proposed for unitary fermions in the ground state [91]. The latter approach holds particular promise for the present system. However, it has never been applied to the UFG at finite temperature, to the best of our knowledge.

6.2.4 Step size dependence & extrapolation

Apart from finite-volume effects, Langevin-type approaches suffer from the use of a finite step size Δt which is required to solve the CL equations.[8] With the integration method applied in

---

[8]This dependence may be considered a general drawback compared to Metropolis-based approaches, where the accept-reject step eliminates this systematic bias.
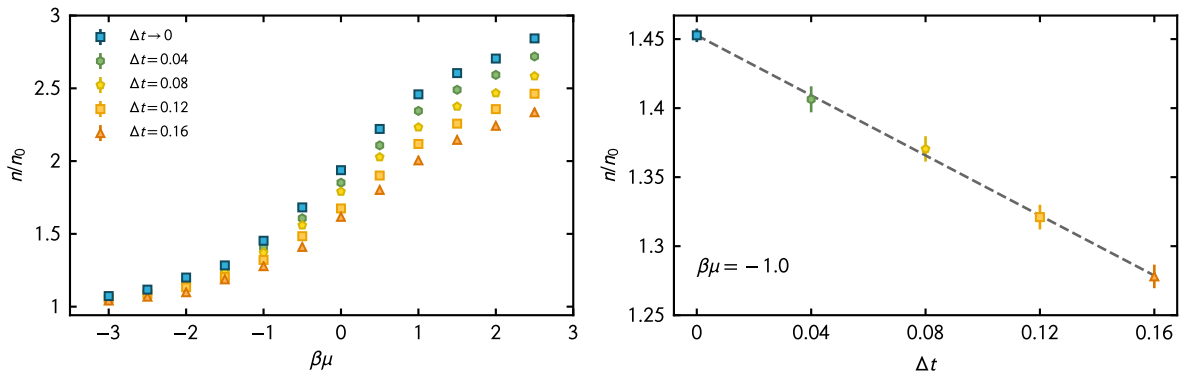
Figure 6.5: (Left) Density EOS of the balanced gas for CL integration step sizes of $\Delta t = 0.16, 0.12, 0.08$ and 0.04, together with values extrapolated to $\Delta t \to 0$. (Right) Density EOS for $\beta\mu = -1.0$ as a function of $\Delta t \to 0$.

this work, the computational effort scales linearly with the inverse step size, however, so does the systematic bias. As already remarked in Section 4.4.2, this requires to either settle for parameters with sufficient accuracy at reasonable cost or to perform an extrapolation $\Delta t \to 0$. The latter strategy has the obvious advantage of completely eliminating the systematic bias but also comes at the price of running multiple simulations at various values of the Δt parameter.

The dependence of our results on Δt is shown in Fig. 6.5, along with the extrapolation to vanishing step size. The left panel of Fig. 6.5 shows the density EOS in the balanced case for various values of the adaptive integration step Δt, together with the extrapolated values. We observe that the results for the EOS somewhat strongly depend on the step size, and the dependence is stronger the larger $\beta\mu$ is.

As an example, this linear behavior is illustrated in detail for $\beta\mu = -1.0$ in the right panel of Fig. 6.5. Indeed, we in general observe an almost perfect linear behavior which allows for a precise extrapolation to the limit $\Delta t \to 0$ and thus for an elimination of the systematic error associated with a finite integration step.

The right panel of Fig. 6.5 also highlights the necessity of an extrapolation. As apparent from the figure, the results at the lowest considered step size $\Delta t = 0.04$ deviate from the extrapolated value by $\sim 5\%$ which is well above the statistical accuracy (indicated by the errorbars) and even larger when we move towards denser systems. Although the computational cost is still modest at $\Delta t = 0.04$, smaller values of Δt become increasingly expensive and, while still feasible at the lattice sizes considered for this work, smaller values might be prohibitive at larger lattices. Therefore, we found it most convenient to extrapolate the step size with the help of larger integration steps of $\Delta t = 0.08, 0.12$ and 0.16 which we perform for all our results to follow. Note that it is certainly possible to shift the extrapolation to larger values of Δt, however, at some point accuracy will suffer due to the "long distance" that the extrapolation has to bridge. Generally, the choice of Δt is specific to the problem at hand and should be addressed to obtain reliable results.

The specific choice of parameters for the discussion of this systematic error serves to exemplify the analysis. Other values for $\beta\mu$ and βh yield results with equivalent accuracy.

6.3 Thermodynamics of the spin-polarized unitary Fermi gas

Having addressed the numerical artifacts introduced by the lattice treatment, we are now in a position to explore the thermodynamics of the UFG. We start by considering the balanced case, which has been under intensive experimental as well as theoretical investigation over the past two decades. Therefore, the system provides an excellent benchmark for our CL results and serves to validate our approach for the spin-imbalanced scenario.

Our strategy is to consider the UFG at fixed values of the imbalance parameter βh (which vanishes in the balanced limit) and varying the dimensionless average chemical potential $\beta\mu$. For large negative values of $\beta\mu$, the system will be dilute as it is energetically costly for particles to enter the system. In this regime no real Fermi surface exists and the gas is dominated by the thermal energy $k_B T$, i.e., approaching the classical regime. Here, only few-body correlations are of importance due to a small scattering cross section which is proportional to the square of the small thermal wavelength λ_{T}. This leads to the applicability of the so-called virial expansion (VE), which is a power-series representation of the partition function in terms of the fugacities $z_\sigma = \mathrm{e}^{\beta\mu_\sigma}$ and may be written as

$$\ln \mathcal{Z} = Q_1 \sum_{n,m} z_\uparrow^n z_\downarrow^m b_{nm}. \tag{6.3.1}$$

The parameters b_{nm} are called virial coefficients and may be obtained by solving the $n + m$ body problem.[9] The maximal radius of convergence of the above series in the balanced case is $z = 1$, corresponding to $\beta\mu = 0$. Beyond that point the fugacity ceases to be small and the expansion breaks down. For the polarized case the majority species features a larger fugacity than $\beta\mu$ such that the convergence radius in terms of $\beta\mu$ is reduced and the VE breaks down already at $\beta\mu < 0$.

Increasing the chemical potential, and particularly proceeding to positive values of $\beta\mu$, results in larger densities of the gas and therefore larger values of the Fermi energy ε_{F} which will eventually be dominant. The increased value of the Fermi energy leads to lower values of T/T_{F} and ultimately to a sufficient build-up of the Fermi surface such that pairing between the particles occurs. In the balanced gas, pairing becomes dominant and causes a phase transition from the strongly interacting normal phase to a superfluid phase at $T \approx 0.17 T_{\mathrm{F}}$, which is an unusually high transition temperature compared to conventional BCS-type superfluids. The transition is smooth, i.e., of second order, and has been precisely characterized in experimental measurements [32, 271]. The phase transition leaves a distinct imprint on the thermodynamic properties and, most notably, causes the specific heat to diverge at the critical temperature.[10] As remarked in the introduction, numerous quantitative studies have been conducted for the balanced case which allows us to extensively compare our results in this limit.

In the presence of a nonvanishing chemical potential mismatch, i.e., $\beta h > 0$, the system is effectively subjected to a magnetic field which causes a spin-selective energy shift of the single-particle levels. As remarked already in the introduction, this leads to a competition between spin alignment and pair formation, causing the superfluid to vanish above the critical field h_c. At

---

[9]A practical overview of the VE along with values for the coefficients and expressions for the specific observables discussed below may be found in Apppendix D.

[10]The shape of the curve for the specific heat resembles the Greek letter λ and hence is sometimes referred to as λ-transition.

zero temperature, the transition was found to be of first order, although with varying predictions of the exact value of the critical imbalance (see discussion below). Consequently, a tri-critical point needs to exist where the nature of the phase transition changes from second to first order. While mean-field considerations provide some knowledge on the phase diagram in the BCS and BEC limits, the unitary regime so far lacks a full characterization of its phase structure. Experimentally, superfluid behavior of the UFG has been observed in the presence of spin polarization [31–36] but the exact nature of the observed phases remains a puzzle.

6.3.1 Density equations of state

The central thermodynamic properties of interest in this thesis are the densities of the spin components. The total particle density is obtained via differentiation of the partition function with respect to $\beta\mu$:

$$n \equiv \frac{1}{V}\langle\hat{N}\rangle = \frac{1}{V}\frac{\partial\ln\mathcal{Z}}{\partial(\beta\mu)}. \tag{6.3.2}$$

Unless otherwise noted, we normalize our results with the noninteracting density n_0 of the balanced gas at the corresponding average chemical potential and temperature which is obtained via numerically integrating the Fermi-Dirac distribution (see Apppendix C).

Benchmark for the spin-balanced UFG

As a first step, we consider the density EOS for the balanced UFG to benchmark our values against existing values in the literature. The results are shown in the top panel of Fig. 6.6 as a function of $\beta\mu$. The CL values vary smoothly across a wide range of chemical potentials which may be translated into a range of $T/T_{\rm F}$ values. The statistical errorbars, which do not contain any estimates of systematic errors, are small and on the order of the symbol sizes. Our results are in excellent agreement with an experimental determination of the EOS by the MIT group [271, 272] across almost all shown values of $\beta\mu$. In the fully quantum degenerate regime at large values of $\beta\mu$, some deviation is observed near the transition to the superfluid phase (gray shaded area) which is located at $(\beta\mu)_c \approx 2.5$. This discrepancy, as remarked above, is most likely the consequence of a combination of numerical instabilities and the intermediate system size considered here. Our values beyond $(\beta\mu)_c$ show a qualitatively similar behavior to the experiment, however, they are in quantitative disagreement and thus not shown here.

On the theoretical side, we may compare our values with various other methods, most notably, MC results from the determinantal Hybrid Monte Carlo (DHMC) approach [152] as well as the bold-diagrammatic Monte Carlo (BDMC) method [272]. The former is a lattice technique relying on an equivalent representation of the partition function as the CL approach. Agreement is excellent across the entire parameter range, however, the approach suffers from similar shortcomings regarding the lattice cutoff. The BDMC method relies on a diagrammatic summation of relevant skeleton diagrams which is done directly in the thermodynamic limit (TL). Naturally, the calculation of observables in the TL provides a tremendous advantage as it circumvents the need for finite-size error correction. However, the BDMC method suffers from convergence issues which seem to be particularly severe towards the phase transition. Moreover, the symmetry broken phase seems to be presently inaccessible via this otherwise powerful method [272, 274, 284].

Figure 6.6:   (Top) Density of the balanced UFG obtained by CL (blue squares), in units of the noninteracting unpolarized density n_0 as a function of the dimensionless average chemical potential $\beta\mu$. Also shown, third-order VE (dashed line), experimental results [271] (red circles), and theoretical results obtained by bold diagrammatic Monte Carlo calculations [272] (dark diamonds) and determinantal hybrid Monte Carlo calculations [152] (light diamonds). (Middle) Detailed comparison of CL data (symbols) with 1st, 2nd and 3rd orders of VE (lines). (Bottom) Detailed comparison of CL results for $n\lambda_T^3$ (squares) to DHMC values [274] (diamonds) as well as experiment (circles) at $\beta\mu = 0.0$ and $\beta\mu = 2.0$ (left and right, respectively).

Coincidentally, the BDMC method deviates from the experimental measurement in the same way as the DHMC and CL results, albeit, due to different reasons. In the lower panels of Fig. 6.6 we perform a more detailed comparison of our EOS to experiment and more recent BDMC determinations [274] and find agreement at the 1% level at $\beta\mu = 0.0$ and $\sim 4\%$ at $\beta\mu = 2.0$. We emphasize that the CL errorbars only contain systematic uncertainties whereas the uncertainty of the benchmark data also includes an estimate of systematic bias.

Additionally, results obtained via the Luttinger-Ward (LW) approach [38] are shown in Fig. 6.6 which we find to be in good agreement in the low density regime. However, with increasing chemical potential, the LW approach seems to systematically overestimate the density. The resolution of the density dependence on the chemical potential seems to be a general shortcoming of the LW theory in ladder approximation [285] which otherwise gives consistent results for various thermodynamic quantities, most notably thermodynamic response functions (see below). Similar behavior of an equivalent LW implementation [286] has been already remarked in [271]. Finally, we compare our results in the low density limit to the VE as depicted in the central panel of Fig. 6.6. At third order, the expression for the density reads

$$n_{\text{VE3}}(\beta\mu, \beta h) = n_0(\beta\mu, \beta h) + \frac{Q_1}{V} \left[2z^2 \Delta b_2 + 3z^3 \Delta b_3 \cosh(\beta h) \right], \qquad (6.3.3)$$

which is also valid for polarized systems (see Apppendix D for a derivation). We find excellent agreement in this limit and observe that the VE approaches our results order-by-order. Beyond $\beta\mu \approx -1.0$ the third-order VE curve dips to lower densities which marks the limited applicability of the expansion whereas the CL values continue smoothly towards larger densities, as expected. This extensive benchmark of the density EOS of the balanced UFG shows remarkable agreement among a variety of methods and renders the CL approach valid for a study of the resonant Fermi gas, at least in the balanced limit. The observed discrepancies at low temperature, which are shared amongst all state-of-the-art theoretical methods, are expected to be cured by a more numerically stable implementation of the CL method and larger lattice sizes.

Density EOS of the polarized UFG

Having ensured that the CL method gives reliable values in the known limits, we now move towards unexplored territory, i.e., the polarized case which is accessible via the CL method with essentially the same numerical effort. We show our determination of the density EOS in Fig. 6.7 again as a function of $\beta\mu$ for values of $\beta h = 0.0$ to 2.0.

The sole benchmark for the density EOS at finite temperature in terms of the grand-canonical variables $\beta\mu$ and βh was found to be the VE which shows excellent agreement for all values of βh studied here, in the regime where the VE is applicable. As already pointed out earlier, the radius of convergence for the VE is expected to shrink with increasing βh as a consequence of the additional scale in the system. Indeed, we find this behavior and the third-order VE already starts to deviate from our results at $\beta\mu \approx 1.5$.

Beyond the virial regime, our values continue to evolve smoothly and we observe the polarized system to approach the EOS balanced system from above. This is not unexpected, as the relative asymmetry h/μ decreases when $\beta\mu$ is increased at fixed βh. Of course, the approach to the balanced EOS should happen at progressively larger values of $\beta\mu$ when βh is increased, which is indeed the case and can be seen in Fig. 6.7. As the balanced system is known to be governed by a
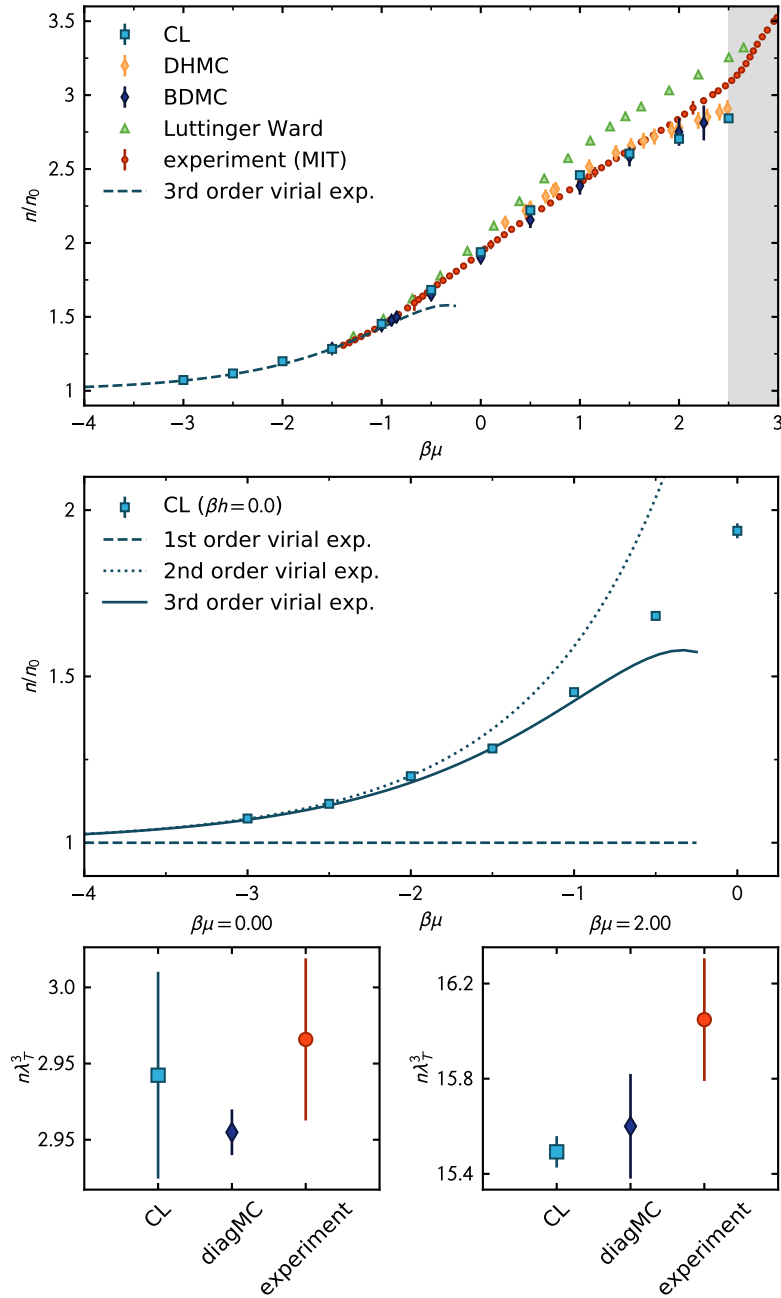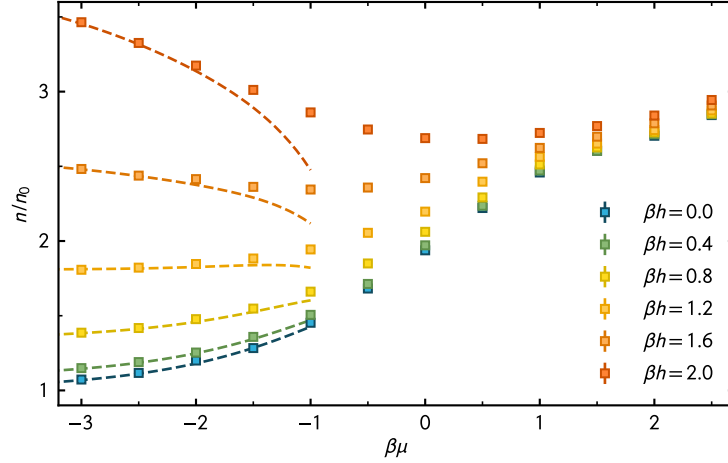
Figure 6.7: Density of the polarized UFG obtained by CL, in units of the noninteracting unpolarized density n_0 as a function of the dimensionless average chemical potential $\beta\mu$ for various fixed values of the dimensionless Zeemann field βh (symbols). Dashed lines correspond to the third-order VE at the according field strengths.

superfluid ground state above $(\beta\mu)_c$, this observation also suggests that the critical temperature decreases with increasing spin asymmetry, in line with (semi-)analytic studies [37, 38, 63, 287] and lattice MC studies of a slightly spin-imbalanced UFG using reweighting techniques [276, 277].

To the best of our knowledge, the here presented EOS for the polarized UFG represents the first systematic study of this quantity based on *ab initio* methods. Our results should be experimentally testable via essentially the same procedure as in [271], where the chemical potential was obtained via the local change of the density with respect to the position in the trap. However, it is unclear at this point if the spin-selective measurement of the chemical potential holds unforeseen experimental roadblocks.

Note that the value of $\beta h = 2.0$ by no means reflects the boundaries of our approach. To reliably study systems at larger values of $\beta h = 2.0$, however, box effects certainly need to be addressed due to a strongly increased density of the majority species.

Magnetization & Polarization

The unequal densities of spin-up and -down particles allow for an investigation of magnetic properties of the UFG. The difference of spin-up and -down densities is just the magnetization which can be written as the derivative of the partition function with respect to the effective Zeemann field:

$$m \equiv \frac{1}{V}\langle \hat{M} \rangle = \frac{1}{V}\frac{\partial \ln \mathcal{Z}}{\partial(\beta h)}. \tag{6.3.4}$$

Alternatively, we may normalize the magnetization with the total density to obtain the relative polarization

$$p \equiv \frac{m}{n} = \frac{n_\uparrow - n_\downarrow}{n_\uparrow + n_\downarrow}, \tag{6.3.5}$$
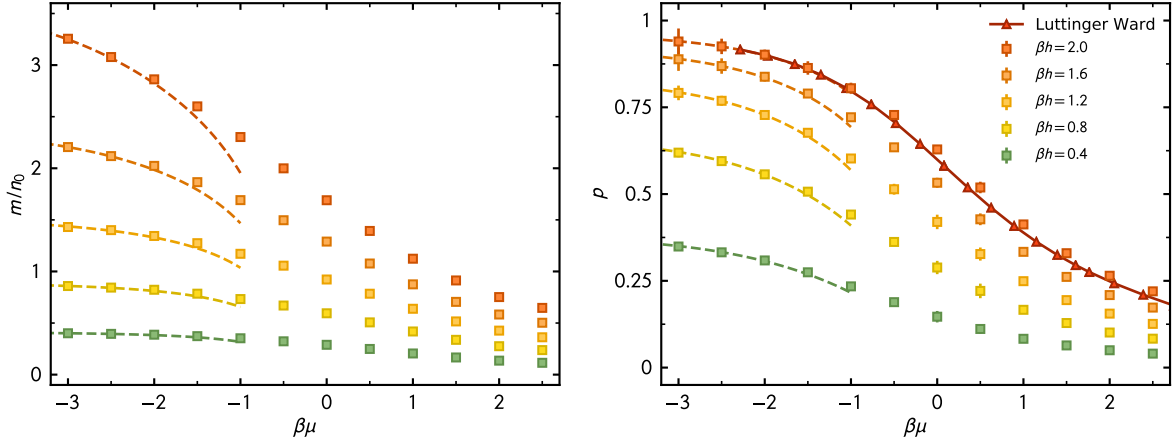
Figure 6.8: (Left) Magnetization normalized by the corresponding noninteracting density as a function of $\beta\mu$ (Right) Relative polarization as a function of $\beta\mu$. At $\beta h = 2.0$ results from the LW approach [38] are available and compared to CL. Dashed lines correspond to the third-order VE.

which is more commonly used in the literature. Our results for the magnetization are shown in the left panel of Fig. 6.8 as a function of $\beta\mu$. At high temperature we can again compare to the third-order VE, which reads

$$m_{\text{VE3}}(\beta\mu, \beta h) = m_0(\beta\mu, \beta h) + \frac{Q_1}{V}\Delta b_3 z^3 \sinh(\beta h). \tag{6.3.6}$$

Similar to the density, the results for the magnetization match the VE for large negative values of $\beta\mu$ and start to deviate at $\beta\mu \sim -1.0$. For $\beta\mu = 2.0$, which is close to the critical value of the balanced system, we observe that the magnetization only shows a very mild dependence on βh.

As discussed above, the magnetization is supposed to be small in the superfluid phase since pairing is energetically more favorable, or equivalently, the response to an external magnetic field is suppressed by the pairing gap (see, e.g., [56, 288]). Therefore, our results suggest that the system remains close to the superfluid phase for $\beta h \leq 2.0$, provided that $\beta\mu$ is fixed close to its critical value $(\beta\mu)_c$ for the balanced case. Sufficiently below the critical regime, i.e., at sufficiently high temperature, the system can "easily" respond to the magnetic field by flipping spins to lower its total energy (see discussion above).

In the right panel of Fig. 6.8, we present results for the relative polarization p. At large temperature and chemical potential asymmetry, the system is highly polarized and essentially dominated by a single spin species. With increasing $\beta\mu$, the polarization quickly is suppressed until it drops to $p \lesssim 0.25$ at $(\beta\mu)_c = 2.5$. Additionally, we compare our results for p at $\beta h = 2.0$ to the LW approach [38] which, to date, seems to be the only quantitative benchmark in the literature.[11] We find excellent agreement across all values of $\beta\mu$, in contrast to the density EOS before, where the LW values showed some deviation at low T/T_{F}. This observation suggests that the systematic error of the LW approach tends to cancel out for the polarization [285].

---

[11]Many more values of βh have been studied in [38]. Due to an unlucky choice of parameter values, however, the $\beta h = 2.0$ line is the only parameter set that allows for a comparison without interpolation.
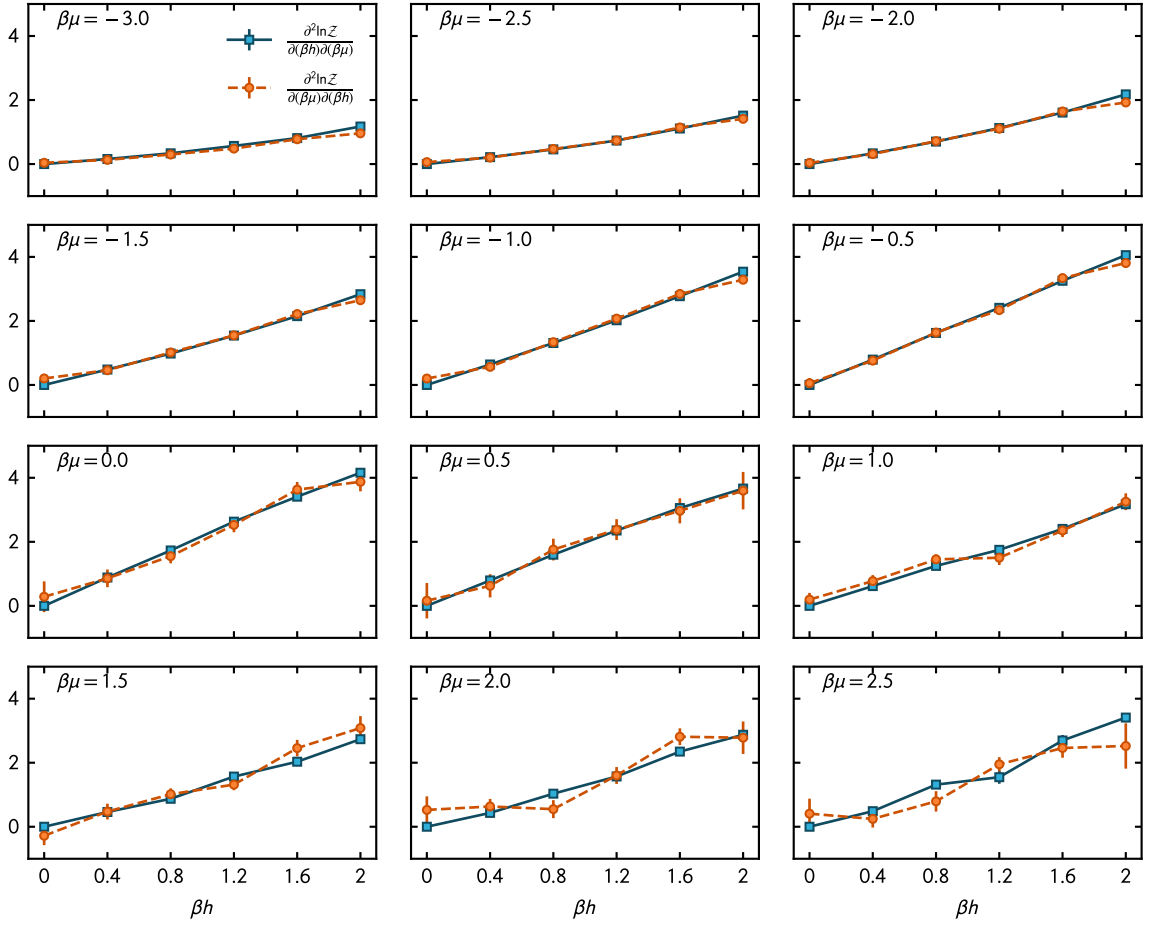
Figure 6.9: Second derivatives of $\ln \mathcal{Z}$ with respect to $\beta\mu$ and βh (blue squares) and with respect to βh and $\beta\mu$ (red circles) as a function of βh for values of $\beta\mu = -3.0, -2.5, -2.0, \dots, 2.5$. Solid and dashed lines are introduced to guide the eye.

6.3.2 Maxwell relations: a valuable cross-check

The above analysis shows that benchmark data is abundant for the balanced UFG. For the polarized case, however, quantitative studies are scarce. To further verify the internal consistency of our results even beyond the virial regime we may exploit some Maxwell relations. Specifically, the relation

$$\left(\frac{\partial n}{\partial (\beta h)} \right)_{\beta\mu} \overset{!}{=} \left(\frac{\partial m}{\partial (\beta\mu)} \right)_{\beta h} \tag{6.3.7}$$

must hold because the order of the derivatives should not matter mathematically. Since the data points at different $(\beta\mu, \beta h)$ values are statistically independent as they stem from different simulations, this check further backs the physical soundness of the CL results.

The outcome of this analysis is depicted in Fig. 6.9, where we show the above second derivatives of $\ln \mathcal{Z}$ as a function of βh for multiple values of fixed $\beta\mu$. We find good agreement for almost all values of $\beta\mu$ considered except for the largest value at $\beta\mu = 2.5$, which is also where our results for the density EOS start to deviate from the experimental values.
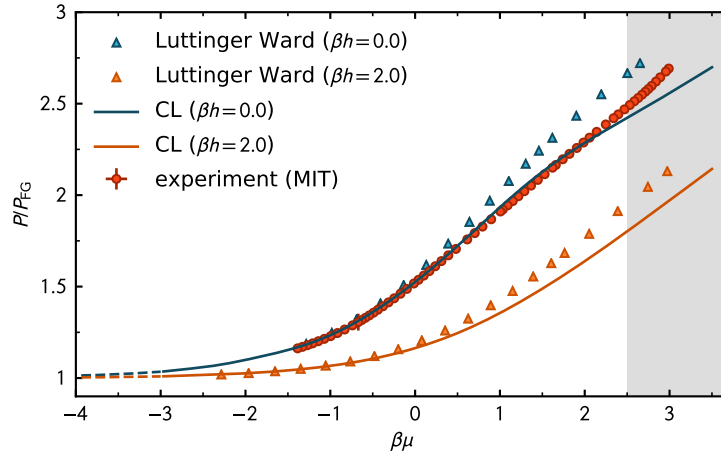
Figure 6.10: Pressure in units of the noninteracting pressure $P_{\mathrm{FG}} = P_{\mathrm{FG}}(\beta\mu_\uparrow) + P_{\mathrm{FG}}(\beta\mu_\downarrow)$ as a function of $\beta\mu$. CL values (lines) are shown at fixed values of $\beta h = 0.0$ (blue) and $\beta h = 2.0$ (orange). Also shown are the experimental values from [271] (red circles) and LW results from [38]. The gray shaded area reflects the superfluid phase.

The derivatives have been obtained numerically from the above presented equations of state. The procedure first involves a cubic spline interpolation with natural boundary conditions which then allows for a simple derivative of the spline polynomials. Note that such an approach might be problematic for overly noisy data [289]. Here, however, the strategy yields very stable and trustworthy results for the first derivatives of the density and magnetization EOS. Naturally, the method fails for higher order derivatives as a consequence of the order of the spline.

Of course, this internal check should not be understood as a sufficient condition to ensure the validity of our results. Rather, we may view it as a necessary condition that needs to be satisfied in order to assume that the results are physically meaningful at all. A failure to meet the condition, on the other hand, indicates faulty behavior of the simulation and needs to be investigated.

6.3.3 Pressure scaling function

Knowledge of the density EOS allows us to obtain a variety of other quantities via suitable thermodynamic relations. As a first step, we deduce the pressure, which is often measured in experiment via the local change of the density profiles in the trap and related to the total energy of the gas [271, 272, 290]. We can obtain the pressure via numerically integrating the Gibbs-Duhem relation,

$$P(\beta\mu) = \frac{1}{\beta} \int_{-\infty}^{\beta\mu} n(x) \, dx, \tag{6.3.8}$$

at fixed value of βh. The integration domain starts at $-\infty$ which implies that we have to use the VE up to a cutoff value. Above the cutoff, we integrate the numerical CL results. In our case, the cutoff is located at $\beta\mu = -3.0$ which does not introduce any bias due to the excellent agreement in this regime.

This procedure allows us to compute the dimensionless scaling function for the pressure

$$P(\beta\mu, \beta h) = P_{\mathrm{FG}}(\beta\mu, \beta h)\, f_P(\beta\mu, \beta h) \tag{6.3.9}$$

which only depends on the two parameters $\beta\mu$ and βh as proposed in [270], being a consequence of the universality in the unitary regime. Our results are shown in Fig. 6.10 for values of $\beta h = 0.0$ and $\beta h = 2.0$ as a function of the dimensionless chemical potential.[12]

As before, we compare to the experimental values in the balanced case [271] and observe reasonable agreement up to the superfluid transition point. This analysis shows that our density EOS is smooth enough to infer related thermodynamic properties within reasonable accuracy.

Moreover, we compare our values to a recent calculation based on LW theory [38]. To the best of our knowledge, this LW study constitutes the only quantitative determination of the pressure scaling function for general temperatures and imbalances beyond the mean-field level, besides the present work. In both, the balanced and polarized case, we find good agreement up to values of $\beta\mu \lesssim 0.5$. Similar as for the density, the LW approximation seems to slightly overestimate the pressure in the high density, i.e., low temperature limit.

6.3.4 Energy equation of state

From the pressure EOS we immediately are able to extract the energy of the system via the relation

$$P = \left(\frac{\partial E}{\partial V}\right)_{N,T} = \frac{2}{3}\frac{E}{V} + \frac{1}{12\pi a}\frac{C}{V}, \tag{6.3.10}$$

which holds for the entire BCS-BEC crossover region. Here, C is the so-called contact parameter which is an essential thermodynamic property quantifying the strength of short-range correlations in the system [228–230]. Its value for the UFG has been extensively studied in the literature (see, e.g., [151, 273, 284, 291–293]) and has been recently determined experimentally as a function of temperature [55, 294]. The quantity is notoriously difficult to estimate at finite lattices, as it is extremely sensitive to the UV behavior, and thus to the cutoff induced by the lattice spacing. Therefore, the investigation of the contact is beyond the scope of the present thesis.

Luckily, the contact term in the above expression enters with the *s*-wave scattering length a in the denominator such that the relation for the UFG takes on the simple form

$$PV = \frac{2}{3}E, \tag{6.3.11}$$

which coincides with the expression for a classical Boltzmann gas as a consequence of the scale invariance. In the literature, the energy is typically written via a dimensionless scaling function:

$$E(\beta\mu) = E_{\mathrm{FG}}\, f_E(\beta\mu, \beta h), \tag{6.3.12}$$

where E_{FG} denotes the ground-state value of the Fermi energy at the corresponding density. At

---

[12]Our results for $\beta h = 0.4, 0.8, 1.2$ and 1.6 are omitted to avoid clutter but lie between the two shown curves in Fig. 6.10.
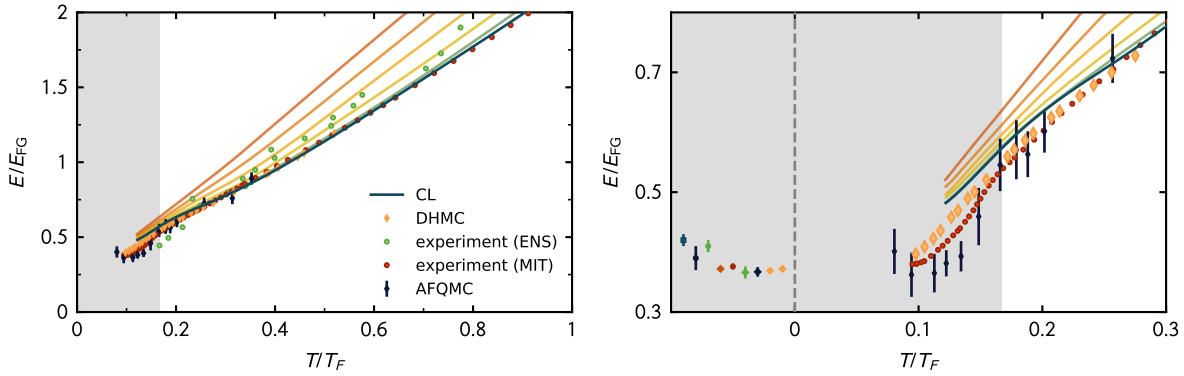
Figure 6.11: Energy in units of the free gas energy E_{FG} as a function of T/T_{F}. CL values (lines) are shown at several values of βh and are compared to various other results for the balanced case: experimental values from [271] (red circles) and [43] (green circles), DHMC [152] (yellow diamonds) and AFQMC [293] (dark diamonds). (Left) Full range including temperatures up to $T/T_{\mathrm{F}} = 1.0$. (Right) Zoom to the phase transition including several determinations of the Bertsch parameter (see text).

zero temperature, the ratio defines the so-called Bertsch parameter ξ via

$$E = \xi E_{\mathrm{FG}}, \tag{6.3.13}$$

which is a central universal number of the UFG as it also determines multiple other properties. Over the years, it has become by far the most intensely studied property of the UFG and, since ξ has been studied extensively via a variety of many-body approaches, it has somewhat evolved into a benchmark number to compare the accuracy of various methods and optimization schemes. We show our dimensionless energy scaling function, as obtained via Eq. (6.3.12), in Fig. 6.11 as a function of T/T_{F}. The comparison to the experiment [271] reveals excellent agreement in the balanced case for $T/T_{\mathrm{F}} \gtrsim 0.25$, below which we observe a slight overestimation of the energy. We also show other theoretical values obtained in the grand-canonical ensemble via DHMC [152] as well as recent AFQMC results for fixed particle numbers of $N_\uparrow = N_\downarrow = 33$ obtained via particle projection [293]. While the former results have been obtained at finite (yet large) lattices, the latter study used volumes up to $V = 13^3$ in combination with a detailed finite size extrapolation to obtain remarkable accuracy. In addition to the balanced case, we show the first determination of the spin-imbalanced energies which, as expected from the discussion of the pressure EOS, approach the balanced result at low temperature.

To set our values in perspective to the zero-temperature extrapolation, a small selection[13] of determinations of the Bertsch parameter is shown in the right panel of Fig. 6.11. Early studies, relying on Fixed-Node Diffusion Monte Carlo (FN-DMC) [295], estimated $\xi = 0.42(1)$. Over the years, the value settled to $\xi \approx 0.37$ as confirmed in multiple experimental measurements by various groups [43, 44, 271, 296] and a variety of unbiased Monte Carlo determinations: AFDMC with giant lattice sizes up to $V = 27^3$ [107] obtained $\xi = 0.372(5)$, highly optimized ground-state lattice MC studies [93] up to particle numbers of $N = 66$ computed $\xi = 0.366(11)$ and a recent AFQMC study [293] with finite size scaling up to $V = 15^3$ finds $\xi = 0.367(7)$. Finally, a very recent determination employed the HMC method up to volumes of only $V = 11^3$ in combination

---

[13]For a more comprehensive overview on the determinations of the Bertsch parameter see, e.g., [93, 293].

with a precise matching of the scattering properties to the continuum [297]. The procedure yields a remarkably good estimate of $\xi = 0.369(2)$ and $\xi = 0.372(2)$ (depending on the details of the extrapolation) and highlights the relevance of improved lattice operators.

Clearly, our estimated value for the energy is neither close to zero temperature nor in exact agreement with the values at $T > 0$ due to the reasons already discussed above. However, the CL results do align with comparable early lattice studies without severe optimizations [101, 102] which encourages the use of future optimizations and yields an optimistic outlook. Finally, it is noted that the determination of the Bertsch parameter is best done directly in the ground state, which allows for a much more efficient implementation based on the projective formulation (see Section 2.5). We will briefly return to this topic below.

6.3.5 Thermodynamic response functions

Up to this point, the discussion revolves around the equations of state for pressure, energy and densities. However, these functions, although precise, only show subtle traces of the superfluid phase transition. A precise determination of critical properties, such as the superfluid transition temperature T_c, from these equations of state is therefore extremely challenging to measure experimentally. In the latter, it is more common to rely on thermodynamic response functions such as the compressibility or the specific heat to identify the phase transition point.

This can be reasoned by considering the role of fluctuations near a second-order phase transition. Far away from the critical regime, a local perturbation will only affect a local region of the system, or equivalently, the correlation length is small. Towards the phase transition, the correlation length grows until it eventually diverges at the critical point and therefore the system becomes very susceptible to microscopic fluctuations. In other words, small local changes will have a macroscopic impact on the state of the system.

We further elucidate this instance by considering the isothermal compressibility, defined via

$$\kappa = \frac{1}{n}\left(\frac{\partial n}{\partial P}\right)_{T,V} = \frac{1}{n^2}\left(\frac{\partial n}{\partial(\beta\mu)}\right)_{T,V}. \tag{6.3.14}$$

We may rewrite this as a second derivative of the partition sum which in turn may be expressed as the variance of the density[14]

$$\left(\frac{\partial n}{\partial(\beta\mu)}\right)_{T,V} = \frac{1}{V}\frac{\partial}{\partial(\beta\mu)}\left(\frac{1}{\mathcal{Z}}\frac{\partial\mathcal{Z}}{\partial(\beta\mu)}\right) \tag{6.3.15a}$$

$$= \frac{1}{V}\left(-\frac{1}{\mathcal{Z}^2}\frac{\partial\mathcal{Z}}{\partial(\beta\mu)}\frac{\partial\mathcal{Z}}{\partial(\beta\mu)} + \frac{1}{\mathcal{Z}}\frac{\partial^2\mathcal{Z}}{\partial(\beta\mu)^2}\right) \tag{6.3.15b}$$

$$= \frac{1}{V}\left(\langle N^2\rangle - \langle N\rangle^2\right). \tag{6.3.15c}$$

Due to the large impact of fluctuations at the critical point, quantities of this type will generally feature a clear signal of the phase transition and are therefore routinely used as a probe in experiment as well as theoretically. In fact, the divergence near a second-order phase transition follows universal scaling laws which may be characterized with critical exponents (see, e.g., [298]).

---

[14]A similar derivation holds for all other susceptibilities we consider in this work and is shown in Apppendix E.
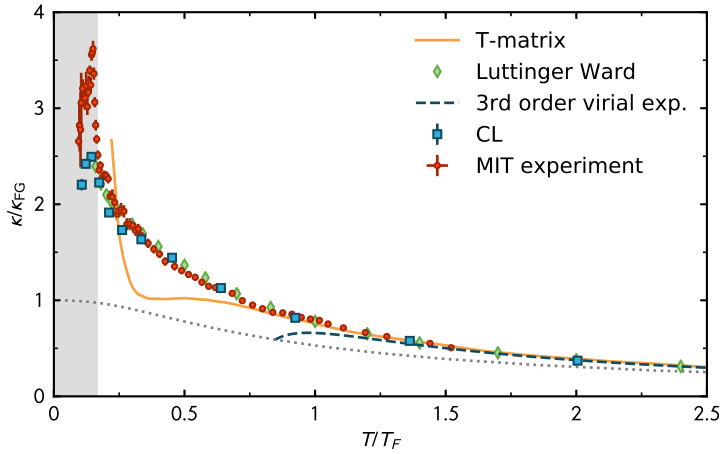
Figure 6.12: Compressibility κ in units of the noninteracting compressibility at zero temperature κ_{FG} in dependence of T/T_{F} as obtained by CL (blue squares). Also shown are experimental values (red circles) [271] as well as theoretical results from T-matrix [299] (yellow line) and LW [300] (green diamonds) approaches. At high temperature, the VE of third order (dashed line) is shown. The dotted line shows the noninteracting compressibility.

For finite systems, such as the ones we consider in this work, the divergence is naturally washed out since Eq. (6.3.15) represents a finite sum. Nevertheless, the critical exponents may be obtained by finite size scaling over a variety of system sizes. In the present work, however, we do not perform such an analysis but rather present our results at finite lattices as a first step towards the characterization of thermal susceptibilities of the spin polarized UFG. Moreover, we do not rely on a determination of the response via a fluctuation relation of the above type, but rather obtain the thermodynamic response via numeric differentiation of the density or magnetic EOS, as discussed in Section 6.3.2. We found this procedure to yield more stable results. The obvious drawback is a difficult error estimation which in such a case has to be carried out through linear error propagation.

As shown below, our thermodynamic response functions match state-of-the-art results from other methods as well as experiment away from the critical regime. Naturally, we observe deviations from experiment at the critical point, however, we successfully recover the qualitative features which allow us to draw conclusions on the underlying physics.

Compressibility

As remarked above, we obtain the isothermal compressibility κ, defined in Eq. (6.3.14), via a numeric differentiation of the density EOS. Our results for κ as a function of T/T_{F} are shown in Fig. 6.12. Across all temperatures, the strongly correlated gas is more compressible as the ideal Fermi gas, which is a consequence of the attractive interaction. Slightly below the superfluid phase transition, which is indicated by a rapid increase of the compressibility, we find a maximum and a subsequent suppression of κ in line with expectations. A precise determination of the critical temperature, however, is challenging due to the roundoff stemming from the finite system size (see discussion above).

Throughout the entire range above the critical temperature T_c, we observe remarkable agreement with experimental values [271]. Additionally, we compare our results to a recent T-matrix
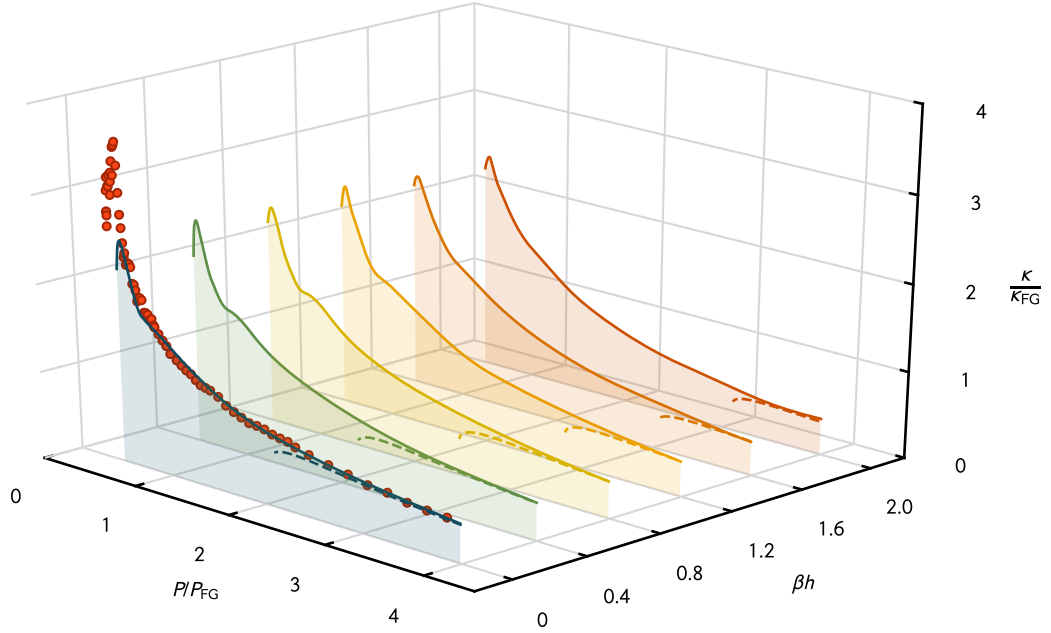
Figure 6.13:   Compressibility for the spin-polarized UFG in units of the noninteracting compressibility κ_{FG} as a function of P/P_{FG} as obtained by CL (lines). The lines correspond to $\beta h = 0.0, 0.4, 0.8, 1.2, 1.6$ and 2.0 (front to back, respectively). Also shown is the experimental determination in the balanced case [271] (red symbols) and the third-order VE (dashed lines).

calculation [299] which does show a rapid increase at low temperature but starts to deviate from the CL values and experiment at $T/T_{\mathrm{F}} \approx 0.75$. Finally, we also show the compressibility obtained via LW theory [24], which is in excellent agreement with our CL results.

In Fig. 6.13, the same quantity is shown in dependence of the pressure scaling function P/P_{FG}.[15] The figure also contains our results for the imbalanced UFG at various values of βh. For all studied chemical potential asymmetries we find perfect agreement with the third-order VE at large P/P_{FG}

$$\kappa_{\mathrm{VE3}} = \kappa_{\mathrm{FG}}(\beta\mu, \beta h) + \frac{1}{(n_{\mathrm{VE3}})^2} \frac{Q_1}{V} \left[4z^2 \Delta b_2 + \frac{9}{2} z^3 \Delta b_3 \cosh(\beta h) \right]. \tag{6.3.16}$$

At low temperatures near the critical region, the above mentioned issues carry over to the imbalanced case. Therefore, the presentation on a three-dimensional grid is deliberately chosen to highlight the qualitative nature of our results in this regime.

We observe that the position of the maximum depends only weakly on βh, suggesting an almost constant critical temperature (within our accuracy) as a function of βh, at least within the considered parameter range $\beta h \leq 2.0$. This conclusion is in line with our previous interpretation based on the magnetic EOS. Lattice MC studies for slight imbalances [276, 277] as well as an

---

[15]Using the pressure as x-scale circumvents the issue of thermometry in the experimental setup which is a challenging task particularly in the strongly interacting regime.
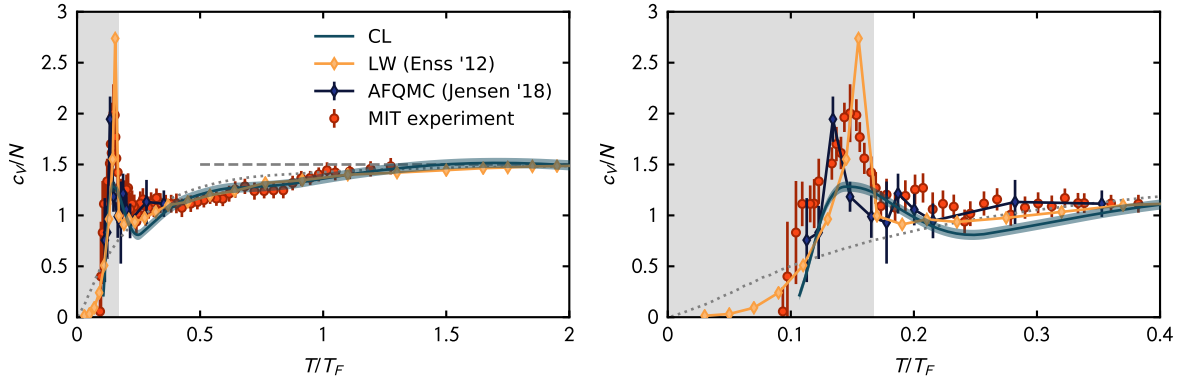
Figure 6.14: Specific heat per particle of the balanced UFG as a function of T/T_{F}. The dotted line shows the noninteracting Fermi gas at the corresponding temperature and the dashed line represents the classical limit $c_V/N = \frac{3}{2}$ (Dulong-Petit law). (Left) Full range including the high-temperature regime. (Right) Zoom to the critical region (superfluid phase marked as gray shaded area). Also shown: MIT experiment [271], LW theory [24] and recent AFQMC values [275].

investigation based on the functional renormalization group [37] reached similar conclusions for this part of the phase diagram.

Specific heat

To complement our discussion of the thermodynamic response, we investigate the specific heat (at constant volume) for the spin-balanced UFG. It is defined as the response of the energy to a change of temperature and may be written as

$$\frac{C_V}{N} = \left(\frac{\partial E}{\partial T}\right)_{N,V} = \frac{3}{2}\left(\frac{T}{T_F}\right)^{-1}\left[\frac{P}{P_{\mathrm{FG}}} - \frac{\kappa_{\mathrm{FG}}}{\kappa_T}\right]. \tag{6.3.17}$$

In analogy to the compressibility discussed above, the specific heat relates to the energy fluctuations via

$$\frac{C_V}{N} = \beta^2\left(\langle E^2\rangle - \langle E\rangle^2\right) \tag{6.3.18}$$

and is therefore expected to show a clear hallmark of the second order phase transition. It is important to note that the derivative in Eq. (6.3.17) has to be carried out at constant particle number N, which is *a priori* impossible to do in the grand-canonical ensemble (which is formally coupled to a particle reservoir). Through several thermodynamic relations as well as the universal scaling of the UFG, however, a suitable expression may be obtained which was also used in an experimental investigation to compute the specific heat from density measurements [271]. A detailed derivation may be found in Apppendix E.

Our results for C_V/N in dependence of T/T_{F} are shown in Fig. 6.14. At large temperature, the specific heat reaches its classical value of $\frac{3}{2}$ as dictated by the Dulong-Petit law. At lower temperature, but still above the superfluid phase, we observe that C_V/N follows the value of the ideal Fermi gas (shown as the dotted gray line) surprisingly close almost until the critical temperature. At the transition we observe a washed out peak which nevertheless shows a hallmark

of the experimentally observed lambda transition [271]. Below T_c, the specific heat quickly drops, as it is expected in the symmetry broken phase where the pairing gap exponentially suppresses the ability of the system to accommodate thermal excitations.

Being a second derivative of the partition function, the specific heat is a notoriously challenging quantity to measure in experiment but also to determine theoretically. This instance is reflected by the somewhat increased errorbars of all benchmark values shown in Fig. 6.14, including an experimental determination [271] and a recent AFQMC study at finite particle number of $N = 80$ at a lattice of $V = 11^3$. Moreover, a comparison to results obtained from LW theory [24] is shown.

The specific heat capacity may be used to probe pairing above the critical temperature, often referred to as pseudogap regime. In the case of substantial pairing in the system, C_V/N should be suppressed already above the superfluid phase. We indeed observe a slight suppression at around $T/T_{\mathrm{F}} \approx 0.25$, however, the effect is too delicate to account for substantial pairing in the system. We rather attribute this behavior to systematic shortcomings of our treatment. This conclusion is consistent with the other studies shown in Fig. 6.14.

Regarding the determination of the critical temperature, we unfortunately come to the same conclusion as for the compressibility: The considered system sizes are too small to reliably address this quantity which calls for further calculations including proper finite-size scaling.

6.3.6 The fate of Pauli magnetism at unitarity

The possibility to study spin-imbalanced Fermi gases with the CL method allows us to investigate the linear response of thermodynamic quantities to an "external magnetic field". The strength of this field is given by the mismatch of the chemical potentials h, defined in the grand canonical partition sum above. A central quantity of interest to consider is the magnetic or spin susceptibility, defined as the derivative of the magnetization with respect to the external field:

$$\chi_{\mathrm{M}} \equiv \left(\frac{\partial M}{\partial h} \right)_{T,V,\mu}. \tag{6.3.19}$$

It quantifies how the system reacts to external magnetic fields in the same way as the compressibility tells us about the change of volume with applied pressure. Equivalently, χ_{M} is a second derivative of the partition sum with respect to the effective Zeemann field and therefore relates to the fluctuations of the magnetization via

$$\chi_{\mathrm{M}} = \beta \left(\langle M^2 \rangle - \langle M \rangle^2 \right). \tag{6.3.20}$$

Early studies of this quantity have been performed by Pauli in order to understand the magnetic properties of certain alkali metals. Due to the large Fermi temperature in these systems, the electrons in the metals may be considered as a highly degenerate Fermi gas and therefore are well described by the noninteracting theory, at least in a first approximation. By doing so, it became possible to explain the weak temperature dependence of χ_{M} in these paramagnetic materials. Near the ground state, the dependence of χ_{M} on T/T_{F} may be obtained via a Sommerfeld
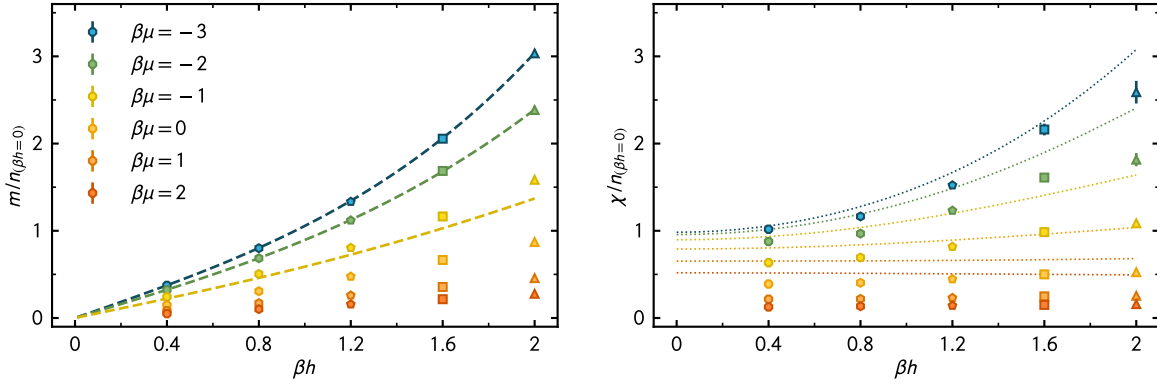
Figure 6.15: (Left) Magnetization in units of the interacting density for the balanced system as a function of βh for several values of $\beta\mu$. For $\beta\mu \leq -1.0$, third-order VE is shown with dashed lines. (Right) Dimensionless magnetic susceptibility $\chi_M/n(\beta h = 0)$ as a function of βh (symbols) compared to the corresponding susceptibility of the free Fermi gas (dotted lines) at equal chemical potential and asymmetry (color and shape coding as in other panel).

expansion which, at leading order, reads

$$\chi_M = \chi_P \left[1 - \frac{\pi^2}{12} \left(\frac{T}{T_F} \right)^2 \right] \tag{6.3.21}$$

with the Pauli susceptibility

$$\chi_P = \frac{3}{2} \frac{n}{\varepsilon_F}. \tag{6.3.22}$$

To leading order, the Pauli susceptibility does not depend on h, which implies a linear growth of the magnetization with the applied field. As a consequence of the Pauli principle, the susceptibility is nonzero even in the ground state, in contrast to a classical gas, which would saturate towards low temperatures (or large fields) and therefore show a vanishing response to a magnetic field. A comprehensive discussion of these considerations may be found in [298].

At large temperature, on the other hand, the system enters the Boltzmann regime and should therefore follow Curie's law which predicts a decay with $\chi_M = CT^{-1}$ where C is the material-specific Curie constant.[16]

Again, rather than relying on the expression given in Eq. (6.3.20), we compute this quantity for the UFG by performing numerical derivatives of the magnetization EOS at fixed values of $\beta\mu$. The benefit of this approach is the ability to also extract the magnetic susceptibility at zero-field, which would otherwise be impossible due to the vanishing value of $\langle M \rangle$ for $\beta h = 0$. However, since we only consider six different values of βh, the values at the largest asymmetries slightly depend on the boundary conditions used for the spline interpolation, which we fix to be open. The associated uncertainty is not considered in the statistical errorbars.

---

[16]For completeness it is noted here that the charge degree of freedom would introduce more subtle effects due to the spin-orbit coupling. In particular, a diamagnetic contribution arises which is often called Landau diamagnetism. Depending on the effective mass this effect may even be the dominant. Further, due to the occurrence of so-called Landau levels, the magnetization and hence the susceptibility are periodic functions of the applied field, a consequence called the de-Haas-van-Alphen effect. For details see, e.g., Ref. [298].

We show the results from this analysis in Fig. 6.15 at fixed values of $\beta\mu$ as a function of βh. In the left panel of Fig. 6.15, the magnetization, in units of the noninteracting density at $\beta h = 0$, is shown and found to be in excellent agreement with the third-order VE for $\beta\mu \lesssim -1.0$. With growing chemical potential, we observe an increasingly linear behavior of the magnetization. As remarked above, this is exactly the behavior that is expected for a free Fermi gas at low temperature. It is surprising, however, that this feature survives in the strongly interacting regime.

To further quantify this observation, the spin susceptibility is shown in the right panel of Fig. 6.15. As anticipated from the above considerations, the susceptibility becomes field-independent at low temperature, i.e., large $\beta\mu$. Additionally, the corresponding susceptibilities for the ideal Fermi gas are shown in the plot and observed to scale remarkably similar. Surprisingly, it seems that the susceptibility of the strongly interacting Fermi gas scales almost identically to the noninteracting case, although rescaled by a temperature dependent factor. For the lowest values of $\beta\mu$ the noninteracting system even shows quantitative agreement with the results for the UFG at low fields (a similar observation holds for the specific heat discussed above). To the best of our knowledge, this constitutes the first determination of the spin susceptibility for general fields $h > 0$. It will be interesting to see how these values compare to experimental measurements.

6.3.7 The spin susceptibility as a probe for the pseudogap

A central question in the study of strongly interacting Fermi gases is the nature of pairing just above the critical temperature. While particle paring occurs in the superfluid phase, which comes along with the formation of a gap in the energy spectrum, it is unclear how this feature evolves above the phase transition. The situation for the UFG has been investigated via an array of theoretical methods and has even been addressed experimentally [301–303]. The conclusions, however, remain controversial and clear signals are still absent from the literature.[17] This is of course a consequence of the strongly-correlated nature of the UFG which poses severe limitations to theoretical investigations. For an extensive overview on advances on pseudogap physics in cold Fermi gases we refer to the recent reviews on the topic [28, 304, 305].

One reason for the interest in this regime is the possible connection to cuprate superconductors, which, amongst multiple other phases, feature a pseudogap. It must be noted, however, that the scenario in these systems is much more complicated and involves the competition of several instabilities. The pairing gap in the high-T_c superconductors may therefore be the consequence of this competition, whereas a possible pseudogap in the UFG must be a consequence of pre-formed pairs present above the critical temperature. Nevertheless, investigation of both scenarios could lead to a knowledge transfer between the fields.

It has been argued that the spin susceptibility may be used as a probe to study the pseudogap [288, 309]. The argument follows the discussion on the CC limit in Section 1.3: in the BCS phase the energy gap protects the pairs against spin flips caused by the magnetic field. This hinders the system to react to an applied magnetic field and consequently the magnetic susceptibility will be small in this regime. Equivalently, a pseudogap should cause a suppression of χ_M at low temperature as a consequence of pre-formed pairs in the system.

---

[17]Part of the confusion about the subject stems from the absence of a stringent definition of the term as well as different nomenclature proposed by varying authors. An excellent introduction to this matter may be found in [304].
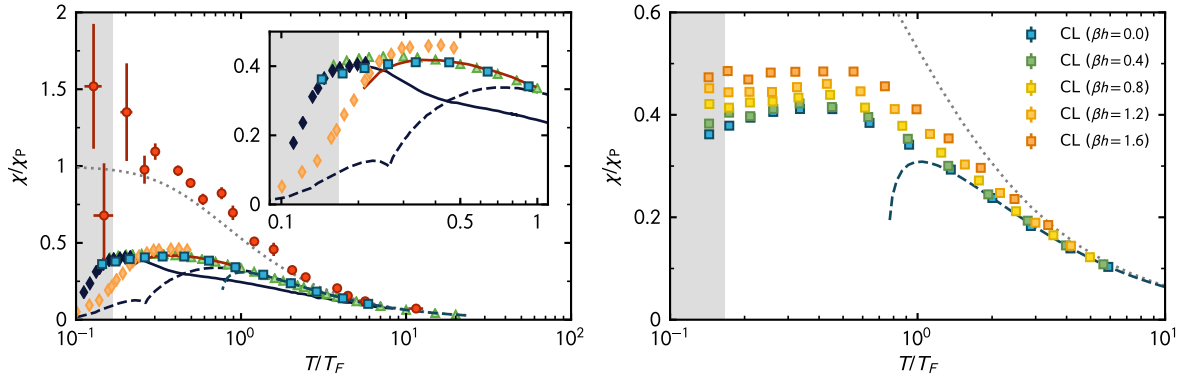
Figure 6.16: Spin susceptibility χ in units of the Pauli susceptibility χ_P as a function of T/T_F. The gray shaded area shows the superfluid phase and the dotted line represents the noninteracting normalized susceptibility. (Left) CL values (squares) are compared to experimental values [302] (red circles) as well as theoretical results from LW [300] (green triangles), T-matrix [306] (dark dashed line), extended T-matrix [307] (red line), NSR [299] (dark solid line), spherical cutoff AFQMC [308] (yellow diamonds) and AFQMC [28] (dark diamonds). (Inset) Zoom to the critical region. (Right) CL results for the susceptibility for finite polarization compared to the third-order VE (dashed lines).

To facilitate a comparison to the literature, we show our results for the spin susceptibility as a function of T/T_F in Fig. 6.16. Across all temperatures we find a lower spin susceptibility as for the ideal Fermi gas (dotted line). In line with our previous discussion of χ_M, we observe only a mild dependence on the temperature in the normal phase to an extent that is comparable to the low temperature expansion given by Eq. (6.3.21). This again highlights the similarity of Pauli magnetism an the magnetic behavior of the normal phase at unitarity. Similar to other quantities, we observe a convergence to the classical prediction at large temperature where the spin susceptibility decays like $\propto T^{-1}$ according to Curies law.

Additionally to our CL results, a variety of other determinations of the spin susceptibility of the balanced UFG are shown in Fig. 6.16. All theoretical values, including the third-order VE, seem to agree in the regime above $T/T_F \gtrsim 1.0$. Below this point, curves obtained via the Nozières-Schmitt-Rink (NSR) formalism [299] as well as varying T-matrix approaches [306, 307] predict a substantial suppression of χ_M far above T_c. Interestingly, also an AFQMC study in the grand-canonical ensemble [308] predicts a suppression at $T/T_F \approx 0.25$ which is in contradiction to a recent AFQMC study at fixed particle number [293]. The resolution of this conundrum is based on the lattice momentum cutoff which apparently shows a pronounced impact on this quantity: while the earlier study relied on a spherical cutoff in momentum space, the latter considered the full Brillouin-Zone [28]. Our CL results agree very well with the latter MC study as well as with results obtained from LW theory [24] across the entire temperature range. Most confusingly, perhaps, all theoretical values are far off the experimental determination [302] (red circles). This is likely a consequence of the trap-averaging procedure that has been applied in the latter.

In the right panel of Fig. 6.16, we show the same quantity including our results for all values of $\beta h \leq 1.6$. At large temperature, the curves for the imbalanced systems converge to the VE and eventually to the noninteracting line, as in the balanced case. Moreover, we observe a mild shift to larger values with increasing βh, which is not unexpected, as the system tends to evolve
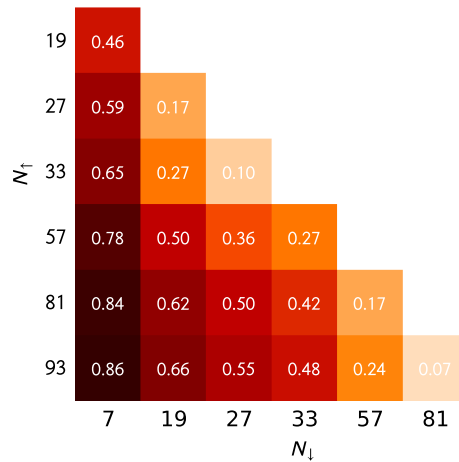
Figure 6.17: Particle numbers and polarizations corresponding to $(N_\uparrow, N_\downarrow)$ configurations of closed energy shells on a 3D lattice.

slowly towards the noninteracting gas with increasing polarization.

Most interestingly, the results at $\beta h > 0$ follow a qualitatively similar trend as for the balanced gas and show no sign (within our accuracy) of suppression as the temperature is lowered. From this analysis, we conclude that the pairing temperature T^* only differs slightly, if at all, from the critical temperature T_c.

6.4 Excursion: the spin-polarized UFG at zero temperature

As remarked already above, exotic superfluid phases are expected to be stable, if at all, only at low temperatures. This regime could be challenging to reach with the finite-temperature methods applied so far, due to the increased numerical effort that follows from larger values of the inverse temperature β. This motivates to work directly in the ground state which may be done by employing a projective version of the CL method in analogy to our discussion of 1D fermions in Chapter 5. In this section, we present results for the ground-state energy EOS of the spin-polarized UFG from a first exploratory study. This study serves as a first benchmark in order to establish the CL method as a reliable tool for ground-state calculations in three spatial dimensions.

As opposed to the finite-temperature approach, which is formulated in the grand-canonical ensemble and therefore assumes fixed chemical potentials, the projective formulation requires fixed particle numbers which corresponds to the canonical ensemble. In order to approach the thermodynamic limit, it is technically necessary to increase successively the particle number and volume at constant densities. However, to study ground-state energies it was found sufficient to consider particle numbers $N \lesssim 100$ at fixed system sizes [310]. In order to minimize finite size effects, particle configurations are chosen such that the total momentum is zero and the noninteracting many-body state respects the cubic symmetry of the lattice. These configurations correspond to the full occupation of all available degenerate energy levels, i.e., the full occupation
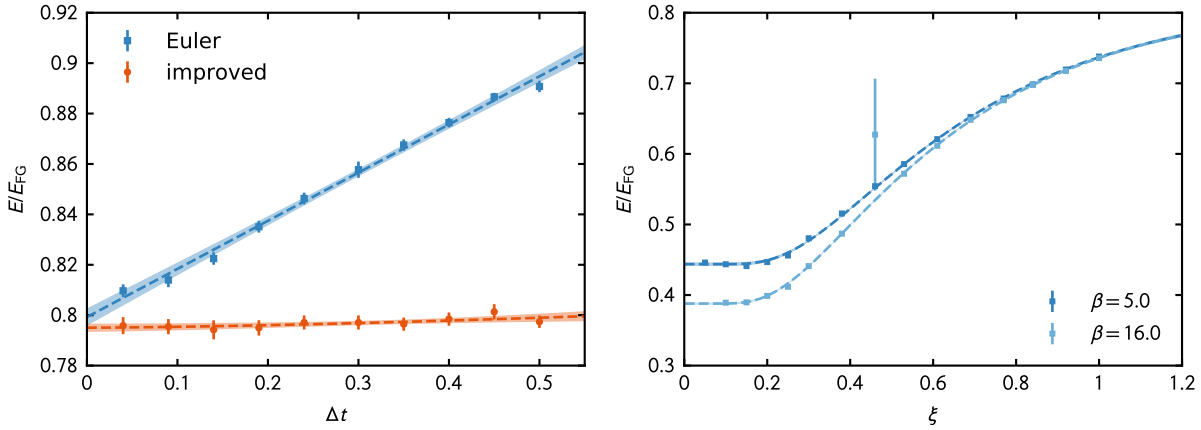
Figure 6.18: (Left) E/E_{FG} as a function of the integration step Δt for EM discretization (blue squares) and improved integration (orange circles). Dashed lines represent a polynomial fit. (Right) Regulator dependence of the ground-state energy for $\beta = 5$ and $\beta = 16$. The dashed lines represent fits according to Eq. (6.4.1). Shaded areas represent 95%-confidence bands in both panels.

of energy shells comparable to a full shell of atomic orbitals in the ground-state. The first few of these "magic numbers" on a 3D lattice are $N_\sigma = 1, 7, 19, 27, 33, \ldots$ and are summarized in Fig. 6.17, where also possible values of the polarization, constructed out of combinations of these values, are shown. Note that particle numbers other than these closed-shell configurations are accessible with similar numerical effort, however, the results could potentially suffer from subtle lattice artifacts.

6.4.1 Numerical parameters & extrapolations

In the following, all results reflect averages over 4 trajectories of 2×10^3 decorrelated samples which results in a statistical uncertainty of $1 - 2\%$. Moreover, all energies are obtained at lattices of $N_x = 9$, which introduces a systematic bias that is not considered in the presented uncertainties, see also the discussion below. To reach the ground state, the extrapolation $\beta \to \infty$ needs to be performed for which we considered values of $\beta \leq 20$ (in lattice units) and subsequently performed an fit to an exponentially decaying function. This parameter range reflects the current limitations of our CL implementation, as numerical instabilities inhibit simulations at larger inverse temperatures [311].

To study the potential systematic bias of the CL method, we briefly address the influence of the finite integration step Δt and the regulator strength ξ on our results. In the left panel of Fig. 6.18, the ground-state energy for a system of $N = 19 \uparrow +19 \downarrow$ fermions as a function of Δt is shown. Both approaches, the Euler-Maruyama (EM) discretization and the improved integration scheme defined in Section 4.4.2, yield consistent values in the limit $\Delta t \to 0$, which is reached via a polynomial fit to the numerical data. The results reveal a qualitatively similar picture as discussed in Section 5.6: While the EM discretization yields a linear behavior that displays a relatively steep slope, the higher-order integrator yields essentially constant results for all values of Δt under study. It is interesting to see that this property seems to hold even for the strongly interacting UFG. This allows us to simply use the improved scheme with a relatively crude step of $\Delta t = 0.2$ in the following.
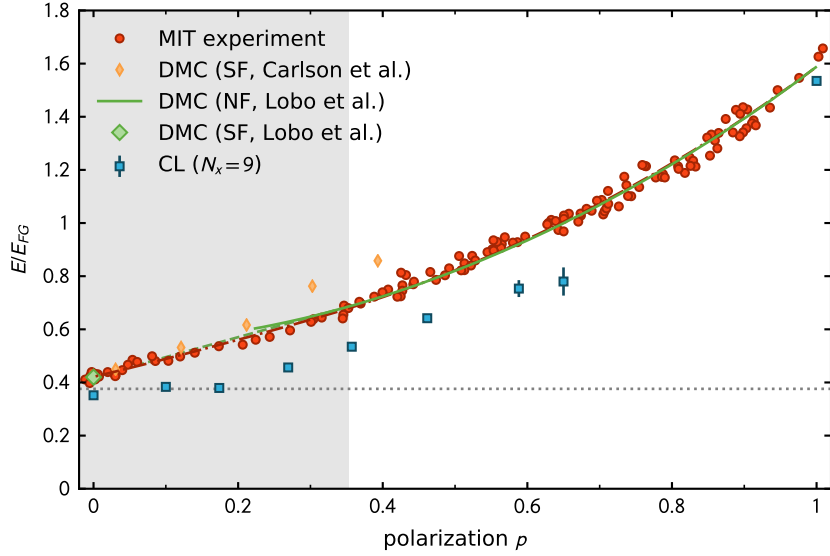
Figure 6.19: Ground-state energy in units of the noninteracting energy E_{FG} as function of the relative polarization p. CL values (blue squares) are compared to experiment [312] (red circles) and various DMC determinations [39, 313]. The gray shaded area indicates the superfluid phase [39].

In Fig. 6.18, the ground-state energy of the same system is depicted as a function of the regulator strength ξ for two values of β. The symbols show the numerical CL data and the dashed lines correspond to a fit of the form

$$E(\xi)/E_{\mathrm{FG}} = a + \xi^b \, \mathrm{e}^{-c/\xi}, \tag{6.4.1}$$

which is empirically motivated and appears to fit the data reasonably well [311]. Interestingly, the ground-state energy seems to level off to a plateau at low regulator strength, similar to the results shown in Section 5.6. This suggests that extrapolation $\xi \to 0$ may be omitted by working at a sufficiently small value of ξ, where the systematic bias introduced by the regulator is negligible to a good approximation.

6.4.2 Energy equation of state

Having addressed the numerical artifacts of our ground-state lattice treatment, we now discuss the ground-state EOS as a function of polarization, as shown in Fig. 6.19. A comparison to an experimental determination of the EOS [312] as well as several FN-DMC calculations [39, 313] reveals that our CL values yield qualitatively similar results, however, at some offset to the expected values. The systematic underestimation of E/E_{FG} displayed by our CL results originates, most likely, from the considered lattice size which was fixed to the relatively small value $N_x = 9$. First calculations at $N_x > 9$, which are not included in the present analysis, indeed have shown larger values for E/E_{FG} such that a proper finite-size scaling is expected to yield more accurate results for the EOS. At present, however, our implementation is not suited to study profoundly larger lattices due to numerical instabilities, as briefly discussed in Section 6.2.1.

The ground-state energy corresponds to the zero-temperature limit of the results discussed in

Section 6.3.4. At zero polarization, the energy should approach the Bertsch parameter $\xi \approx 0.37$, which is indicated by the gray dotted line in Fig. 6.19. Although it appears that our present CL determination reproduces the Bertsch parameter quite well, it should be noted that this is rather of coincidental nature: As discussed above, finite-size scaling will shift the energy to larger values and thus away from the physically expected result. The overestimation of the Bertsch parameter by "plain", i.e., unoptimized lattice methods has been observed before [63, 101, 102, 152] and is a consequence of the induced finite effective interaction range (see the discussion in Section 6.2.3). To remedy this issue, optimized lattice schemes have recently been employed which resulted in a greatly improved accuracy of the estimates for the Bertsch parameter [293, 297] as compared to earlier lattice studies. Alternatively, simply scaling up the volume to giant sizes at constant particle content effectively suppresses finite-range effects, although at dramatically larger numerical cost [107].

Finally, let us comment on the possibilities to study the phase-structure in the zero-temperature limit via MC approaches. As remarked above, several MC studies have been performed in the unpolarized limit at $p = 0$, which is known to feature a BCS-superfluid [12]. At large polarizations, where the nodal structure of the wavefunction appears to be quite similar to the one of a noninteracting Fermi gas, FN-DMC studies showed that the UFG is described well by a Fermi-polaron picture, i.e., a Fermi liquid of quasiparticles [39] which is also supported by experimental measurements [36, 43]. At intermediate polarizations, however, the possible existence of exotic superfluid phases renders the nodal structure of the wavefunction essentially unknown. An assumed nodal structure, which is necessary to avoid the sign-problem in DMC simulations, therefore introduces an uncontrolled approximation and prohibits a straightforward FN-DMC investigation in this parameter range.

The CL approach, on the other hand, does not suffer from such a limitation and potentially is suitable to study the properties of the ground state for intermediate polarizations in *ab initio* manner. To reliably analyze the structure of the ground state, for instance through the evaluation of suitable two-body correlation functions, however, it is first necessary to accurately reproduce the known results for the energy EOS, in order to ensure the validity of the CL approach in this regime.

6.5   Recap & future directions

The results discussed in this chapter represent the first systematic study of the thermodynamics of the spin-imbalanced UFG based on *ab initio* methods. Our analysis rests on the precise determination of the spin densities of both flavors in dependence of $\beta\mu$. After a thorough investigation of systematic errors associated with the CL treatment, we have obtained an extrapolated EOS free of discretization artifacts. The resulting density EOS shows excellent agreement with state-of-the-art experimental and theoretical values for the normal phase of the balanced UFG. At finite spin imbalance, which is accessible within the same numerical effort, our values mark predictions whose experimental investigation is expected in the near future.

From the precise density EOS we obtained a variety of other quantities through suitable thermodynamic relations. Via integrating the Gibbs-Duhem relation, we were able to compute pressure and energy equations of state, which were also observed to be in remarkable agreement with experiment at temperatures $T/T_{\mathrm{F}} \gtrsim 0.25$. By differentiation, we extracted several thermodynamic response functions, namely the isothermal compressibility and the specific heat per

particle. These quantities display quantitative agreement with experiment and other theoretical determinations across essentially all of the normal phase. In the critical region, however, the remnants of the expected divergence are only resolved in a qualitative manner as a consequence of the finite system sizes under study. A proper finite-size scaling procedure, including larger lattice sizes, will improve this instance in future investigations.

One of the main results of our investigation is the determination of the magnetic susceptibility, not only in the balanced case, but also at finite values of the Zeeman field h. To the best of our knowledge, the quantity has neither been measured nor treated theoretically in this regime. Our analysis reveals that the functional form of the spin susceptibility resembles the Pauli susceptibility of the free gas, however, rescaled by a temperature dependent factor. In the balanced case, we compare this quantity to a variety of other determinations and find excellent agreement with LW [24] and AFQMC [293] computations. This verifies the accuracy of our approach for this quantity and suggests the validity of our prediction for the spin-imbalanced gas.

Quantitative benchmark data for the UFG is essentially only existent for the balanced gas. A recent study based on LW theory [38] marks the notable exception. Up to intermediate values of $\beta\mu \lesssim 0.5$, we observe excellent agreement for the pressure scaling function, however, above this value the methods start to slightly disagree. Since our CL approach better reproduces the balanced experimental values, it is likely that the LW method overestimates the density in this system.

6.5.1 Implications for the phase diagram

The phase diagram of the spin-imbalanced UFG has been investigated via several methods before, however, its precise structure is not yet fully understood beyond the mean-field level which, at best, yields a qualitative picture at strong interactions [57–59]. To set our findings in relation to what is already known, Fig. 6.20 summarizes the current knowledge on the subject beyond simple mean-field predictions. For completeness, we summarize selected results for critical quantities in Tab. 6.1.

In the left panel of Fig. 6.20, which reflects the system in the "grand-canonical plane" $1/(\beta\mu)$ versus h/μ, a recent phase diagram obtained via the functional renormalization group (fRG) [37] is shown. In the balanced limit, the study agrees well with two experimental determinations of $(\beta\mu)_c$ [43, 271] as well as with a recent result obtained via LW theory [38]. While the critical temperature in the balanced case is well understood, much less is known about the critical field strength above which superfluidity gives way to the normal phase via a first-order transition. There, determinations from fRG, experiment [43] and FN-DMC [39] are in proximity, however, disagree with the LW approach (beyond the plot range) and a result from the ϵ-expansion [314].

As remarked earlier, our results do not allow a quantitative prediction of the critical values. The inspection of the magnetization EOS as well as the thermodynamic response, however, indicates that the curvature of the phase boundary near the balanced limit is small, in line with the present knowledge in this regime.

In the right panel of Fig. 6.20, an experimental determination of the "canonical" phase diagram $T/T_{F,\uparrow}$ versus relative polarization is shown [312] (symbols reflect experimental measurements, the phase boundaries are linear fits). Additionally, the recent critical line from LW theory [38] is shown for comparison. The agreement for the critical temperature carries over
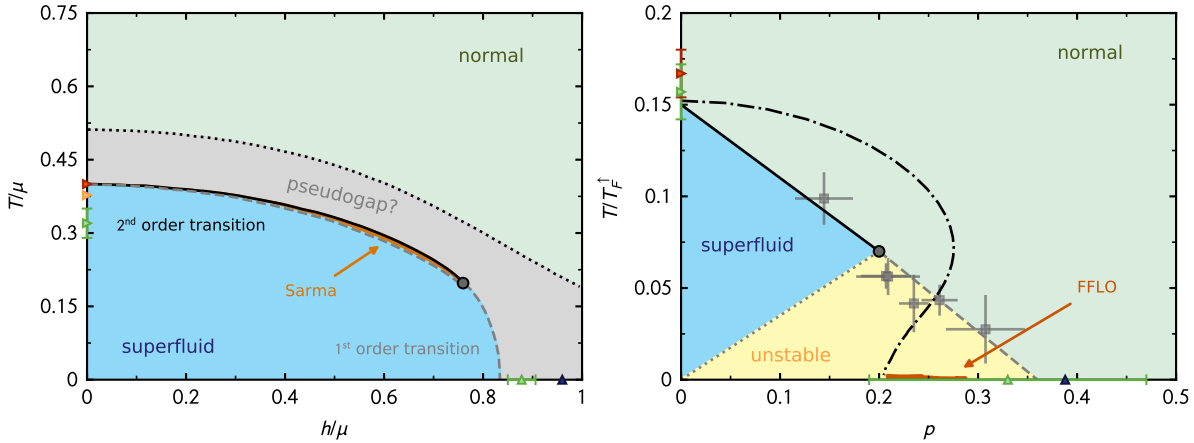
Figure 6.20: Phase diagrams of the spin-polarized UFG. (Left) Grand-canonical phase diagram $(\beta\mu)^{-1}$ vs. h/μ as obtained via fRG [37] (Right) $T/T_{\mathrm{F},\uparrow}$ vs. polarization phase diagram as measured in experiment [312] (gray error crosses) and compared to a recent determination via LW theory [38] (dot-dashed lines). Critical values in both panels correspond to experimental values from the MIT group [271] (red triangles) and ENS group [36, 43] (green triangles), LW results [38] (orange triangle) and FN-DMC calculations [39] (dark triangles).

from the discussion in the grand-canonical plane.[18] The critical polarization is again much more the center of debate. The experimental measurement by the ENS group shows a large uncertainty [43] such that other results lie easily within their errorbar.

For completeness, we note determinations of the second-order transition line based on NSR [299] and ETMA [316], both of which predict a transition temperature for the balanced gas well above $T/T_{\mathrm{F},\uparrow} = 0.2$. This overestimation continues to the spin-polarized case until eventually unphysical re-entrant behavior is reported, similar to the LW curve. Additionally, a RG study reports quantitative agreement to the experimental measurement as well as the tri-critical point [59], however, contains some arbitrary choice in the considered couplings, as remarked already in [13]. Finally, let us return to the left panel of Fig. 6.20, where also a pseudogap region is featured. Our results at finite lattice sizes suggest the tentative conclusion that this region is small, if present at all. However, an exact prediction is challenging at this point and requires the calculation of more suitable quantities such as the density of states which is expected to show a pronounced dip in the case of a pseudogap. Alternatively, a precise determination of the spectral function could clarify the issue. From a stochastic perspective, this is troublesome because the computation of these quantities involves an analytic continuation from imaginary to real frequencies. Although this procedure is performed frequently, it demands exquisite precision of the numerical data in order to yield reliable numbers. Generally, little is known about the pseudogap regime at finite polarization, which makes an experimental comparison all the more desirable.

This concludes our discussion on the phase diagram of the spin-polarized UFG. A quantitative determination of the full phase diagram from first principles is a challenging task and still absent from the literature. The present investigation is not able to remedy this instance, however, marks an important step towards the characterization of the phase diagram via *ab initio* methods.

---

[18]No determinations of the critical temperature from MC in the balanced case are shown in the above summary. Several values have been computed before, which, if properly scaled to the continuum limit, show good agreement to the values shown here [276, 277, 315].

study	year	$T_c/T_{\mathrm{F},\uparrow}$	p_c	$(\beta\mu)_c$	$(\frac{h}{\mu})_c$
MIT experiment I [312]	2008	~ 0.15	~ 0.36	—	~ 0.95
ENS experiment [36, 43]	2010	0.157(15)	0.33(14)	3.13(29)	0.878(28)
MIT experiment II [271]	2012	0.167(13)	—	~ 2.5	—
FN-DMC [39]	2006	—	0.388	—	0.96
ϵ-expansion [314]	2007	—	—	—	1.15
fRG [37]	2015	—	—	2.5	0.83
LW [38]	2018	0.152	—	2.65	1.09(5)

Table 6.1:   Various determinations for the critical quantities in the grand-canonical and canonical ensembles.

6.5.2   CL & the future of the spin-polarized UFG

The above summary highlights the amount of knowledge on strongly-correlated Fermi gases accumulated over the years. Many things, however, are left to be understood. Regarding the future of CL in this endeavor, besides technical improvements that will be addressed further below, it is certainly important to study pair correlation functions. From these, more revealing quantities, such as the pairing gap and the condensate fraction, may be extracted. Additionally, as our analysis for one-dimensional systems showed, it would be of interest to study so-called shot-noise correlations for three-dimensional systems in order to properly resolve the exact nature of pairing in the presence of mismatched Fermi surfaces.

With these advances, it might be possible to conclusively investigate the nature of the intermediate polarized superfluid phases. As already remarked earlier, several mechanisms have been proposed in the literature [48–53] but, to date, no experimental measurement has confirmed either of them. Amongst the proposed variants, the FFLO mechanism has received most theoretical attention [54] and constitutes the perhaps most interesting phase as it features a spatially varying order parameter. It is expected to be stable only at very low temperatures. The access to low temperatures, however, is challenging in both experimental and theoretical efforts. In the latter, searching for this elusive state of matter may therefore be best done in the ground state. So far, MC studies in this regime have relied on the fixed-node approximation which introduces a possibly severe systematic bias. The CL approach may help to circumvent this limitation and first steps in this direction have been taken, as discussed in this chapter.

Experimentally, the challenge of addressing inhomogeneous pairing was for the longest time limited by the position-dependent harmonic trapping potential. In these setups, the superfluid phase is only present in a small fraction of the entire sample which renders measurements on the spatial-dependence of the order parameter impossible. Recently, however, flat trap geometries have been implemented to study ultracold Fermi gases [317, 318]. Although at the present moment it is unclear how this broken translational and rotational invariance will be accessed in experiment, it is conceivable that these sophisticated trapping techniques are capable of shedding light onto this topic.

A complementary route towards the detection of inhomogeneous phases may be the study of mixtures of different atom species. The mass ratio between the particles may be exploited to realize mismatched Fermi surfaces which in turn influences the pairing behavior. A potential roadblock, however, could be unfavorable scattering properties which are challenging to predict for general atom mixtures and rendered studies on systems with ^{6}Li-^{40}K too short lived. A promising candidate is a mixed system of ^{161}Dy-^{40}K for which stable realizations have been reported recently [248].

The experimental advances in trapping and setting up ever more elaborate systems yields an optimistic outlook on the near term detection of the exact phase structure of spin-imbalanced Fermi gases. Also on the theory side, interest is again picking up speed. It seems that the hunt for a clear observation of inhomogeneous paring is on.

7 | Summary & final remarks

"There's always a bigger fish."

Qui-Gon Jinn

The central theme of this thesis is the study of strongly-interacting imbalanced Fermi gases. The past two decades have seen remarkable and exciting advances, in both experiment as well as theory, which have revealed the rich physical content of these systems. On the theory side, however, the strong correlation between the particles causes serious problems in their quantitative description and calls for reliable and systematic nonperturbative methods. Another major topic of this work is to further push the development of efficient stochastic lattice approaches in the context of nonrelativistic Fermi gases. To conclude, these two parts are briefly recapitulated, and the current state of development is summarized. Finally, a brief perspective on possible extensions of these advances is given.

7.1 Part I: methodological advances

As a first step towards a precise treatment of fermionic many-body systems, a suitable method was needed. Our investigations relied on a fairly standard auxiliary field representation, albeit in a somewhat specific incarnation regarding the exact nature of the auxiliary fields. The cornerstone of such an approach is a decoupling of the interaction which ultimately results in a highly nontrivial path integral. While this is the basis of a range of powerful Monte Carlo methods, a nagging issue persists (and also plagues all other incarnations of Monte Carlo sampling) in the case of fermionic systems: the infamous sign problem. It prohibits straightforward evaluation of these high-dimensional integrals via importance sampling and ultimately leads to a severe signal-to-noise issue. This essentially implied a roadblock in the study of nonrelativistic Fermi gases of interest in this work.

The common theme of all approaches applied in this thesis is the use of continuous auxiliary fields in a lattice representation of the physical model. This allows for the application of highly efficient global update algorithms, similar to the ones often used to study lattice field theories in the context of high-energy physics. First, the paradigmatic Metropolis-based hybrid Monte Carlo method was introduced and subsequently extended to surmount a sign-problem in mass-imbalanced systems through an escape to imaginary asymmetries. These methods have proven suitable in the study of a variety of problems in the past, including several systems of interest in this thesis.

The main workhorse of the present work, however, is based on stochastic quantization which was found to be an exceptionally well suited tool to investigate ultracold Fermi gases. In particular,

its extension to complex random walks, i.e. the CL method, turned out to be a "magic" approach in this context, allowing us to access previously prohibitive problems with modest computational effort. As the method has presently still some limitations regarding its mathematical justification, progress has been slower than one would expect for a possible way around the notoriously challenging sign problem. Hence, this thesis represents one of the first extensive studies of asymmetric Fermi gases relying on this technique. Consequently, the technical part of this thesis dealt with introducing the full formalism of this powerful approach in detail, as well as with the discussion of possible shortcomings. Special emphasis was given to an intuitive presentation of the concepts, which involved several toy problems to complement the methodological survey. Moreover, the similar nature of all the mentioned heavy-duty numerical methods renders it possible to generalize their implementation structure efficiently. As part of this thesis, the `gMacs` package was developed with the purpose to simplify problem-specific implementations in future applications.

7.2 Part II: the CL machinery at work

In the second part of the present work, these numerical techniques were put to use in order to address the physical questions posed in the introduction. First, an extensive benchmark of the lattice treatment with the HMC method was performed in the crossover from few- to many-body systems in a one-dimensional geometry. This is a natural stepping stone towards higher dimensional systems, as the reduced dimensionality eases the computational burden considerably. However, since the impact of fluctuations is dramatically enhanced in lower dimensions, these systems are intrinsically strongly interacting and therefore nontrivial to address numerically.

The insights on the quantities as well as on the numerical behavior of the approach laid the foundation to later tackle the challenging problem of mass-imbalanced fermionic systems. Note that the reduced symmetry puts these systems beyond the reach of analytic studies based on the celebrated Bethe ansatz. An extension of the HMC method to imaginary asymmetries, dubbed iHMC, was successfully applied to obtain results up to intermediate mass-imbalances. As a consequence of the involved analytic continuation from imaginary asymmetries to real mass-imbalances, the associated statistical error blows up towards large mass asymmetries such that the approach is of limited use in this regime.

To mitigate this issue, the system was subsequently approached via the main method of interest in this thesis, namely the CL approach. To the best of our knowledge, this marked the first usage of this technique for the ground state of nonrelativistic fermionic systems. The success of this initial study is backed up by cross-checks with the iHMC method which yielded an excellent match in the applicable parameter ranges and continued to be smooth beyond the reach of the iHMC method. The main result of this study was the determination of the energy dependence on the coupling strength for a variety of mass imbalances.

Despite excellent agreement among several methods for attractive interactions, the method displayed problematic behavior at repulsive interactions. A later study based on the worldline algorithm [122, 123] revealed that the CL method indeed yielded faulty values at large repulsions, as conjectured already from the broad observable distributions. At this point, this marks a limitation of our present implementation of the CL method and certainly calls for an in depth investigation of the issue in the future.

For attractive interactions, however, no problems were detected which allowed the study of

pairing in the form of two-body correlation functions. The central quantity under investigation was given by the density-density correlation function in momentum space, which displays clear signals of fermion pairing. While FFLO-type ordering was expected for the mass-balanced but spin-imbalanced case, it was unclear how the pairing correlations would evolve in the presence of finite mass asymmetry. As it turned out, the pairing still happens at finite center-of-mass momentum, however, with shifted peaks in momentum space. To the best of our knowledge, this was the first observation of this effect. Since shot-noise correlations are often measured in experiment, it is conceivable that this prediction might be checked in the near future.

Perhaps the most extensive study in this thesis was undertaken for the spin-imbalanced unitary Fermi gas. The main quantity of interest was the density equation of state, which was computed to excellent precision across a wide parameter window. Thermodynamic relations allowed for the determination of a range of other quantities and comparisons to a broad range of experimental and theoretical results in the balanced limit revealed the excellent accuracy of our results.

Most of our investigation took place in the normal phase above the superfluid phase transition. This is, in part, caused by the occurrence of some subtle technical reasons but also a consequence of the employed lattices sizes in our CL studies, which, to some extent, obfuscate the study of critical phenomena. Both of these shortcomings, however, may be systematically cured and are not principal roadblocks towards the full characterizations of these systems also in the superfluid phase.

As a first extension towards the investigation of possible FFLO-type ground states in three-dimensional Fermi gases, projective calculations at $T = 0$ have been presented. While the presented numerical results must still be considered at a preliminary level with respect to the numerical control of several factors, the study yields an optimistic outlook for the future study of pairing correlations in this regime.

The large range of computed thermodynamic quantities enabled us to draw conclusions about the phase diagram in the temperature versus polarization plane. First, we found indications for a flat phase boundary near the balanced case, in line with previous arguments in the literature. Additionally, we argued against the existence of an extensive pseudogap regime above the critical temperature based on the absence of a suppressed magnetic response of the system. Moreover, we have predicted a variety of thermodynamic properties for spin-imbalanced systems which, to the best of our knowledge, have been computed for the first time at a quantitative level. Hence, it will be interesting to see whether these predictions stand the test of time with respect to further theoretical developments and possible experimental measurements.

7.3 What the future may hold

This thesis constitutes an early stage in the development of the CL method for nonrelativistic systems. While solid results have been achieved so far, several technical improvements will help to cure some of the childhood sicknesses and to further establish the CL method as a valuable member of the numerical toolbox.

Some of the proposed technical improvements suitable for the CL method include:

Numerical stabilization The repeated matrix multiplication of the transfer matrix during the imaginary-time propagation causes the spread of the eigenvalues to grow exponentially. Ultimately, floating point arithmetic will not be able to resolve this spread and the lowest

lying eigenstates will be washed out, resulting in an ill-conditioned matrix. This issue may be mitigated via suitable matrix decompositions which yields a stabilized numerical propagation in imaginary time. While it was found to be omissible for the HS transformation and system sizes in this work, such a stabilization scheme will allow for the study of larger systems at larger imaginary times in three spatial dimensions.

Improved operators A route towards better reproducing the continuum physics without resorting to possibly prohibitive lattice size are improved operators. The idea is to better match the low-energy scattering properties on the lattice such that an arising finite range effect is suppressed. Initial studies in the ground state have been conducted [91]. However, no implementation at finite temperatures is on the market as of yet.

Alternate HS transformations Inspired by the success of bounded HS transformations in our HMC calculations, the specific form carried over to the CL method. The complex field, however, causes an unbounded imaginary direction which must be counteracted with a suitable mass-like regulator term. Conveniently, it is possible to construct a variety of HS transformations due to the idempotency of the fermionic density operators. This could allow for "self-regulated" versions of the transformation, which circumvents the need for the regulator. A possible version, for instance, is the decomposition in the pairing channel rather than the density channel, which is routinely carried out in analytic studies and could provide a viable option for an optimized CL implementation. Possible bottlenecks in this regard include the larger Fermi matrices, which would at least have to be $2V \times 2V$ and the possible need to resort to a conjugent gradient type inversion of these large matrices.

Optimized trial wavefunctions For the projective formulations, a more favorable choice of trial wavefuctions beyond simple Slater determinants may help to confine overly broad distributions of observables and thus considerable improve the statistics and range of accessible couplings. The obvious example is given by the BCS-type wavefunction, which already favors pairing and has been shown to be efficient for the three-dimensional balanced UFG [107].

Particle projection In light of possible finite-size scaling it may be beneficial to project to a fixed particle number at finite temperature, i.e., the canonical ensemble. Recent advances have been made with this approach in light of the UFG [275]. Further, it was recently shown that discarding all but the lowest lying singular values helps to reduce the computational cost of finite-temperature calculations [282, 319], which could also be an interesting avenue to explore with the CL approach.

Once these technical refinements are addressed, exciting physical systems await to be investigated with the lattice approaches developed in this thesis. Examples include recent reports on the realization of stable Fermi-Fermi mixtures with ^{161}Dy-^{40}K by the Innsbruck group [248]. A precise measurement of the equation of state for these mass-imbalanced systems at finite temperatures is absent from the literature and would be a natural extension of the present thesis. Another exciting possibility in this regard is highlighted by our results for one-dimensional systems, which reveal the great potential of shot-noise correlations to investigate subtle effects arising from mass asymmetry. It will be interesting to study this quantity in higher dimensional counterpart, in

particular for the unitary Fermi gas, which could provide the key step in the search for the elusive FFLO phase conjectured to be present at unitarity (see, e.g., [56]).

Moreover, the advent of quantum gas microscopes allows for the precise measurement of correlations in two-dimensional systems. Recent experiments even considered mixed-dimensional atomic gases in the crossover from one to two spatial dimensions [320]. Experimentally, this was realized via a direction-dependent hopping term in an optical lattice. Naturally, this reduces the symmetry of the underlying Hamiltonian and introduces a severe sign problem in conventional Monte Carlo approaches. In this context, a particular interesting topic concerns the evolution of pairing correlations in imbalanced gases: On the one hand, it is known that correlations of the FFLO type are the leading instability in one-dimensional lattice systems across most of the physical parameter space. On the other hand, little is known on the nature of the FFLO in two-dimensional systems. It will be interesting to see whether the CL approach is able to address this dimensional crossover reasonably well.

Finally, it is conceivable that the CL method could spread into the toolbox of condensed matter physics, where auxiliary field methods are routinely applied. A paradigmatic field of interest is of course the repulsive Hubbard model away from half filling, which is a model candidate brought in connection to high-T_c superconductors, but features a severe sign problem. The difficulty here lies in the solution of the problems observed in ground-state calculations of dilute repulsive Fermi gases. At this point it is unclear whether the failure is caused by numerical shortcomings (such as an overlap problem) or by a fundamental flaw of the CL approach itself. A resolution of the issue, however, would pave the way towards the study of this long-standing problem.

It is important to note that, despite the various success stories, the CL approach remains a method under construction. Our understanding of its shortcomings has come a long way ever since the initial proposal of this approach in the early eighties, but we are still lacking *a priori* insights on its applicability without performing actual simulations.

At the end of the day, there is no "silver bullet" that will solve all our sign problems. The complex Langevin method is no exception and there will always be theories for which the approach fails to deliver reliable numbers. In the context of nonrelativistic Fermi gases, however, this thesis presents stable and physically sound results for otherwise intractable problems. The method therefore constitutes a step forward towards a better understanding of the challenging and fascinating world of asymmetric quantum matter.

Appendices

A │ Many-body derivations

In this appendix, we detail some derivations in the context of the auxiliary field framework. An educational overview on the finite-temperature as well as the ground-state formalism can be found in [100, 102, 321], where also derivations beyond the scope of this work are presented.

A.1 Bounded & continuous auxiliary field transformations

The particular auxiliary-field transformation used in this work is given by Eq. (2.4.2a). To derive this expression we start with an expansion of the two-body term

$$\mathrm{e}^{-g\Delta\tau\hat{\rho}_\uparrow\hat{\rho}_\downarrow} = \sum_{n=0}^{\infty} \frac{(-\Delta\tau g)^k}{k!}(\hat{\rho}_\uparrow\hat{\rho}_\downarrow)^k \tag{A.1.1a}$$

$$= 1 + \hat{\rho}_\uparrow\hat{\rho}_\downarrow \sum_{n=1}^{\infty} \frac{(-\Delta\tau g)^k}{k!} \tag{A.1.1b}$$

$$= 1 + \hat{\rho}_\uparrow\hat{\rho}_\downarrow \left(\mathrm{e}^{-\Delta\tau g} - 1\right) \tag{A.1.1c}$$

$$\equiv 1 + \hat{\rho}_\uparrow\hat{\rho}_\downarrow B \tag{A.1.1d}$$

where the second equality is due to the fact that $\hat{\rho}_\sigma$ is a fermionic density operator. The decomposition in Eq. (2.4.2a) is given by

$$\mathrm{e}^{-g\Delta\tau\hat{\rho}_\uparrow\hat{\rho}_\downarrow} = \int_{-\pi}^{\pi} \frac{\mathrm{d}\phi}{2\pi} \left[1 + \hat{\rho}_\uparrow A\sin\phi\right]\left[1 + \hat{\rho}_\downarrow A\sin\phi\right] \tag{A.1.2}$$

which can be shown to be equivalent by noting that

$$\frac{1}{2\pi} \int_{-\pi}^{\pi} \mathrm{d}\phi = 1 \tag{A.1.3a}$$

$$\frac{1}{2\pi} \int_{-\pi}^{\pi} \mathrm{d}\phi \; \hat{\rho}_\sigma \sin\phi = 0 \tag{A.1.3b}$$

$$\frac{1}{2\pi} \int_{-\pi}^{\pi} \mathrm{d}\phi \; A^2\hat{\rho}_\uparrow\hat{\rho}_\downarrow \sin^2\phi = \frac{A^2}{2}\hat{\rho}_\uparrow\hat{\rho}_\downarrow \tag{A.1.3c}$$

which leads to the equation

$$1 + \frac{A^2}{2}\hat{\rho}_\uparrow\hat{\rho}_\downarrow = 1 + \hat{\rho}_\uparrow\hat{\rho}_\downarrow B \tag{A.1.4}$$

and thus sets the coefficient

$$A = \sqrt{2B} = \sqrt{2\left(e^{-\Delta\tau g} - 1\right)}. \tag{A.1.5}$$

For repulsive interactions, i.e. $g > 0$, the coefficient A is imaginary which leads to a complex action and thus a phase-problem.

A.2   Trace over Fock space

In this appendix, we want to derive the relation

$$\mathrm{Tr}\left[\prod_k e^{\sum_{ij} \hat{\psi}_i^\dagger [A_k]_{ij} \hat{\psi}_j}\right] = \det\left[\mathbb{1} + \prod_k e^{A_k}\right]. \tag{A.2.1}$$

As a first step, we consider the case of only one factor in the product, i.e. the trace over a single one-body operator. Assuming the matrix A is diagonalizable throuh a unitary transformation (as is the case for hermitian matrices) we can always find a suitable diagonal representation:

$$\mathrm{Tr}\left[e^{\sum_{ij} \hat{\psi}_i^\dagger A_{ij} \hat{\psi}_j}\right] = \mathrm{Tr}\left[e^{\sum_{ijkl} \hat{\psi}_i^\dagger U_{ik}^\dagger D_{kl} U_{lj} \hat{\psi}_j}\right] \tag{A.2.2a}$$

$$\equiv \mathrm{Tr}\left[e^{\sum_{kl} \hat{\chi}_k^\dagger D_{kl} \hat{\chi}_l}\right] \tag{A.2.2b}$$

$$= \mathrm{Tr}\left[e^{\sum_k \lambda_{(k)} \hat{\chi}_k^\dagger \hat{\chi}_k}\right]. \tag{A.2.2c}$$

where $\lambda_{(k)}$ are the eigenvalues of A. Note that the transformed creation and anihilation operators $\hat{\chi}_k^\dagger$ and $\hat{\chi}_k$ have only been rotated by a unitary transformation and therefore still obey the fermionic anticommutator rules. We can now evaluate the trace over the corresponding Fock space:

$$\mathrm{Tr}\left[e^{\sum_k \lambda_{(k)} \hat{\chi}_k^\dagger \hat{\chi}_k}\right] = \sum_n \langle n | e^{\sum_k \lambda_{(k)} \hat{\chi}_k^\dagger \hat{\chi}_k} | n \rangle \tag{A.2.3a}$$

$$= \sum_n \langle n | \prod_k e^{\lambda_{(k)} \hat{\chi}_k^\dagger \hat{\chi}_k} | n \rangle \tag{A.2.3b}$$

$$= \sum_n \langle n | \prod_k \left[1 + (e^{\lambda_{(k)}} - 1)\hat{\chi}_k^\dagger \hat{\chi}_k\right] | n \rangle \tag{A.2.3c}$$

$$= \prod_k \left(1 + e^{\lambda_{(k)}}\right) \tag{A.2.3d}$$

$$= \det\left[\mathbb{1} + e^A\right]. \tag{A.2.3e}$$

For multiple factors in Eq. (A.2.1), however, the simple diagonalization strategy is not applicable. The result holds nevertheless, as can be shown by considering the relation for two factors

$$\mathrm{Tr}\left[e^{\sum_{ij} \hat{\psi}_i^\dagger A_{ij} \hat{\psi}_j} e^{\sum_{ij} \hat{\psi}_i^\dagger B_{ij} \hat{\psi}_j}\right] = \det\left[\mathbb{1} + e^A e^B\right]. \tag{A.2.4}$$

The key step is to consider the Baker-Campbell-Hausdorff (BCH) formula which gives a formal

solution Z for the problem

$$e^Z = e^X e^Y \tag{A.2.5}$$

for generally non-commuting matrices X and Y. The result may be written as an infinite series of nested commutators whose first few terms read

$$Z = X + Y + \frac{1}{2}[X,Y] + \frac{1}{12}[X,[X,Y]] - \frac{1}{12}[Y,[X,Y]] + \cdots \tag{A.2.6}$$

In order to treat this infinite sum we consider the commutator of the exponentiated single-particle operators (to simplify the notation, we assume sums over doubly occurring indicies):

$$\left[\hat{\psi}_i^\dagger A_{ij}\hat{\psi}_j, \hat{\psi}_i^\dagger B_{ij}\hat{\psi}_j\right] = \hat{\psi}_i^\dagger A_{ij}\hat{\psi}_j\hat{\psi}_k^\dagger B_{km}\hat{\psi}_m - \hat{\psi}_k^\dagger B_{km}\hat{\psi}_m\hat{\psi}_i^\dagger A_{ij}\hat{\psi}_j \tag{A.2.7a}$$

$$= A_{ij}B_{km}\left[\hat{\psi}_i^\dagger\hat{\psi}_j\hat{\psi}_k^\dagger\hat{\psi}_m - \hat{\psi}_k^\dagger\hat{\psi}_m\hat{\psi}_i^\dagger\hat{\psi}_j\right] \tag{A.2.7b}$$

$$= A_{ij}B_{km}\left[\hat{\psi}_i^\dagger(\delta_{jk} - \hat{\psi}_k^\dagger\hat{\psi}_j)\hat{\psi}_m - \hat{\psi}_k^\dagger\hat{\psi}_m\hat{\psi}_i^\dagger\hat{\psi}_j\right] \tag{A.2.7c}$$

$$= A_{ik}B_{km}\hat{\psi}_i^\dagger\hat{\psi}_m - A_{ij}B_{km}\left[\hat{\psi}_k^\dagger\hat{\psi}_i^\dagger\hat{\psi}_m\hat{\psi}_j + \hat{\psi}_k^\dagger\hat{\psi}_m\hat{\psi}_i^\dagger\hat{\psi}_j\right] \tag{A.2.7d}$$

$$= A_{ik}B_{km}\hat{\psi}_i^\dagger\hat{\psi}_m - A_{ij}B_{km}\left[\hat{\psi}_k^\dagger(\delta_{im} - \hat{\psi}_m\hat{\psi}_i^\dagger)\hat{\psi}_j + \hat{\psi}_k^\dagger\hat{\psi}_m\hat{\psi}_i^\dagger\hat{\psi}_j\right] \tag{A.2.7e}$$

$$= A_{ik}B_{km}\hat{\psi}_i^\dagger\hat{\psi}_m - A_{mj}B_{km}\hat{\psi}_k^\dagger\hat{\psi}_j \tag{A.2.7f}$$

$$= A_{ik}B_{kj}\hat{\psi}_i^\dagger\hat{\psi}_j - B_{ik}A_{kj}\hat{\psi}_i^\dagger\hat{\psi}_j \tag{A.2.7g}$$

$$= \hat{\psi}_i^\dagger[A,B]_{ij}\hat{\psi}_j \tag{A.2.7h}$$

where we used the fermionic anticommutator rules. For all higher terms it is now possible to repreatedly subsitute the commutator involving fermion operators with a matrix that is sandwiched by the creation and anihilation opertators. Ultimately, this allows to write

$$\hat{\psi}_i^\dagger A_{ij}\hat{\psi}_j, \hat{\psi}_i^\dagger B_{ij}\hat{\psi}_j = \hat{\psi}_i^\dagger\left\{A + B + \frac{1}{2}[A,B] + \frac{1}{12}[A,[A,B]] + \cdots\right\}_{ij}\hat{\psi}_j \equiv \hat{\psi}_i^\dagger M_{ij}\hat{\psi}_j, \tag{A.2.8}$$

where M is the formal solution of

$$M = \ln\left[e^A e^B\right]. \tag{A.2.9}$$

We have arrived at a single operator in the product, for which the relation was shown above. Thus, we may write

$$\text{Tr}\left[e^{\hat{\psi}_i^\dagger M_{ij}\hat{\psi}_j}\right] = \det\left[\mathbb{1} + e^M\right] = \det\left[\mathbb{1} + e^A e^B\right] \tag{A.2.10}$$

which proves Eq. (A.2.4). For more than two operators in the product we may simply repeat this reduction arbitrarily many times.

For completeness it is noted that an alternative proof may be found in the appendix of Ref. [100]. Even beyond that, the above relations may be proven by means of Grassmann numbers.

A.3 Observables with auxiliary fields

Our aim is to derive the expression for the observables given in Eq. (2.6.3c). We start by taking the derivative with respect to the source term

$$\langle \hat{O} \rangle = \frac{1}{\mathcal{Z}} \frac{\partial \mathcal{Z}[J]}{\partial J}\bigg|_{J=0} \tag{A.3.1a}$$

$$= \frac{1}{\mathcal{Z}} \int \mathcal{D}\phi \, \frac{\partial}{\partial J} \text{Tr} \left[\hat{T}_\phi(\beta, \theta) \, \text{e}^{J\hat{O}} \, \hat{T}_\phi(\theta, 0) \right]\bigg|_{J=0}. \tag{A.3.1b}$$

Assuming $\hat{O}$ represents a single-particle operator in the appropriate basis we may convert the trace in the expression to a determinant by using the identity

$$\text{Tr}[\hat{A}] = \det[\mathbb{1} + A] \tag{A.3.2}$$

which holds for single-particle operators, or products thereof. Thus we may write

$$\langle \hat{O} \rangle = \frac{1}{\mathcal{Z}} \int \mathcal{D}\phi \, \frac{\partial}{\partial J} \det \left[\mathbb{1} + \hat{T}_\phi(\beta, \theta) \, \text{e}^{JO} \, \hat{T}_\phi(\theta, 0) \right]\bigg|_{J=0} \tag{A.3.3a}$$

$$= \frac{1}{\mathcal{Z}} \int \mathcal{D}\phi \, \frac{\partial}{\partial J} \text{e}^{\ln \det \left[\mathbb{1} + \hat{T}_\phi(\beta, \theta) \, \text{e}^{JO} \, \hat{T}_\phi(\theta, 0)\right]}\bigg|_{J=0} \tag{A.3.3b}$$

$$= \frac{1}{\mathcal{Z}} \int \mathcal{D}\phi \, \det M_\phi \, \frac{\partial}{\partial J} \ln \det \left[\mathbb{1} + \hat{T}_\phi(\beta, \theta) \, \text{e}^{JO} \, \hat{T}_\phi(\theta, 0) \right]\bigg|_{J=0} \tag{A.3.3c}$$

where for the third equality we have used the fact that

$$\det \left[\mathbb{1} + \hat{T}_\phi(\beta, \theta) \, \text{e}^{JO} \, \hat{T}_\phi(\theta, 0) \right]\bigg|_{J=0} = \det M_\phi. \tag{A.3.4}$$

By exploiting the relation $\text{Tr} \ln A = \ln \det A$ we write

$$\langle \hat{O} \rangle = \frac{1}{\mathcal{Z}} \int \mathcal{D}\phi \, \det M_\phi \, \frac{\partial}{\partial J} \text{Tr} \ln \left[\mathbb{1} + \hat{T}_\phi(\beta, \theta) \, \text{e}^{JO} \, \hat{T}_\phi(\theta, 0) \right]\bigg|_{J=0} \tag{A.3.5a}$$

$$= \frac{1}{\mathcal{Z}} \int \mathcal{D}\phi \, \det M_\phi \, \text{Tr} \left\{ M_\phi^{-1} \frac{\partial}{\partial J} \left[\mathbb{1} + \hat{T}_\phi(\beta, \theta) \, \text{e}^{JO} \, \hat{T}_\phi(\theta, 0) \right]\bigg|_{J=0} \right\} \tag{A.3.5b}$$

$$= \frac{1}{\mathcal{Z}} \int \mathcal{D}\phi \, \det M_\phi \, \text{Tr} \left[\hat{T}_\phi(\theta, 0) \, M_\phi^{-1} \hat{T}_\phi(\beta, \theta) \, O \right] \tag{A.3.5c}$$

which is our final expression for the expectation values of arbitrary observables.

A.3.1 One-body density matrix

An important observable is the to one-body density matrix which is given by

$$\rho_{ij}^\sigma(\phi) = \langle \hat{\psi}_{\sigma i}^\dagger \hat{\psi}_{\sigma j} \rangle_\phi. \tag{A.3.6}$$

As remarked in the main text, in this thesis we consider the case $\theta = 0$ such that Eq. (A.3.5) reads

$$\langle \hat{\psi}_{\sigma i}^\dagger \hat{\psi}_{\sigma j} \rangle_\phi = \frac{1}{\mathcal{Z}} \int \mathcal{D}\phi \ \det M_\phi \ \mathrm{Tr} \left[M_\phi^{-1} \hat{T}_\phi(\beta, 0) \, \hat{\psi}_{\sigma i}^\dagger \hat{\psi}_{\sigma j} \right] \tag{A.3.7a}$$

$$= \frac{1}{\mathcal{Z}} \int \mathcal{D}\phi \ \det M_\phi \ \mathrm{Tr} \left[(\mathbb{1} + \hat{T}_\phi(\beta, 0))^{-1} \hat{T}_\phi(\beta, 0) \, \hat{\psi}_{\sigma i}^\dagger \hat{\psi}_{\sigma j} \right] . \tag{A.3.7b}$$

where the second equality was obtainted by inserting the definition of the Fermi matrix

$$M_\phi = \mathbb{1} + \hat{T}_\phi(\beta, 0). \tag{A.3.8}$$

By using the matrix relation

$$\mathbb{1} - (\mathbb{1} + A)^{-1} = (\mathbb{1} + A)^{-1} A \tag{A.3.9}$$

we may write

$$\langle \hat{\psi}_{\sigma i}^\dagger \hat{\psi}_{\sigma j} \rangle_\phi = \frac{1}{\mathcal{Z}} \int \mathcal{D}\phi \ \det M_\phi \ \mathrm{Tr} \left\{ [\mathbb{1} - (\mathbb{1} + \hat{T}_\phi(\beta, 0))^{-1}] \, \hat{\psi}_{\sigma i}^\dagger \hat{\psi}_{\sigma j} \right\} \tag{A.3.10a}$$

$$= \frac{1}{\mathcal{Z}} \int \mathcal{D}\phi \ \det M_\phi \ \mathrm{Tr} \left[(\mathbb{1} - M_\phi^{-1}) \, \hat{\psi}_{\sigma i}^\dagger \hat{\psi}_{\sigma j} \right] . \tag{A.3.10b}$$

Furhter we may write the trace over the orthonormal coordinate-space basis $\{|y\rangle\}$ with

$$|y\rangle = \hat{\psi}_{\sigma y}^\dagger |0\rangle \tag{A.3.11}$$

and such that

$$\mathrm{Tr} \left[(\mathbb{1} - M_\phi^{-1}) \, \hat{\psi}_{\sigma i}^\dagger \hat{\psi}_{\sigma j} \right] = \mathrm{Tr} \left[\mathbb{1} \, \hat{\psi}_{\sigma i}^\dagger \hat{\psi}_{\sigma j} \right] - \mathrm{Tr} \left[M_\phi^{-1} \, \hat{\psi}_{\sigma i}^\dagger \hat{\psi}_{\sigma j} \right] \tag{A.3.12a}$$

$$= \sum_y \langle y | \hat{\psi}_{\sigma i}^\dagger \hat{\psi}_{\sigma j} | y \rangle - \sum_y \langle y | M_\phi^{-1} \, \hat{\psi}_{\sigma i}^\dagger \hat{\psi}_{\sigma j} | y \rangle . \tag{A.3.12b}$$

With

$$\hat{\psi}_{\sigma i}^\dagger \hat{\psi}_{\sigma j} | y \rangle = | i \rangle \delta_{jy} \tag{A.3.13}$$

it follows that

$$\mathrm{Tr} \left[(\mathbb{1} - M_\phi^{-1}) \, \hat{\psi}_{\sigma i}^\dagger \hat{\psi}_{\sigma j} \right] = \delta_{ij} - \langle j | (M_\phi^\sigma)^{-1} | i \rangle \tag{A.3.14}$$

such that the one-body density-matrix is really just the coordinate space representation of the inverse Fermi matrix. In exactly the same fashion, we could have computed momentum-space quantities with the only change being the usage of the momentum-space single-particle basis.

B | Error estimation of correlated random samples

In this appendix, we briefly detail useful derivations and techniques necessary for the unbiased estimation of statistical errors of correlated random samples. We begin by deriving the general expression Eq. (3.2.9). Further we define the autocorrelation function along with some of its properties as well as the integrated autocorrelation time. Subsequently, we provide a brief overview on standard techniques to estimate the unbiased error. More extensive derivations can be found, e.g., in [114, 322].

B.1 Autocorrelation function & integrated autocorrelation time

Random samples generated by MCMC algorithms are generally correlated. To correctly estimate the statistical error we have to consider the variance of the mean, given by the quadratic fluctuations around the mean value:

$$\mathrm{Var}[\bar{O}] = \left\langle \left(\bar{O} - \langle\bar{O}\rangle\right)^2 \right\rangle \tag{B.1.1a}$$

$$= \left\langle \left(\frac{1}{N}\sum_i O_i - \langle\bar{O}\rangle\right)^2 \right\rangle \tag{B.1.1b}$$

$$= \frac{1}{N^2}\sum_{ij} \langle O_i O_j\rangle - \langle O\rangle^2 \tag{B.1.1c}$$

$$\equiv \frac{1}{N^2}\sum_{ij} C(i-j). \tag{B.1.1d}$$

Here, we have used the linearity of the expectation value and the relation

$$\langle\bar{O}\rangle = \left\langle \frac{1}{N}\sum_i O_i \right\rangle = \frac{1}{N}\sum_i \langle O_i\rangle = \langle O\rangle. \tag{B.1.2}$$

Further, we assume the samples to be taken from the equilibrium distribution of the Markov process, that is, after some warmup time to avoid initialization bias. The last line of Eq. (B.1.1) implicitly defines the autocovariance function $C(r)$ which only depends on the sample lag (i.e. the lag in Markov time) as a consequence of the equilibrium. This allows us to rewrite the double

sum as a single sum with an appropriate weighting function:

$$\text{Var}[\bar{O}] = \frac{1}{N^2} \sum_{r=-N+1}^{N-1} (N - |r|) \, C(r) \tag{B.1.3a}$$

$$= \frac{1}{N} \sum_{r=-N+1}^{N-1} \left(1 - \frac{|r|}{N}\right) C(r) \tag{B.1.3b}$$

$$= \frac{C(0)}{N} \left[1 + 2 \sum_{r=1}^{N-1} \left(1 - \frac{|r|}{N}\right) \Gamma_O(r)\right] \tag{B.1.3c}$$

$$= \frac{\text{Var}[O]}{N} \left(1 + 2\tau_{\text{int}}\right). \tag{B.1.3d}$$

Here we used the fact that $C(0) = \text{Var}[O]$ and defined the autocorrelation function

$$\Gamma_O(r) \equiv \frac{C(r)}{C(0)} = \frac{\langle O_{i+r} O_i \rangle - \langle O_{i+r} \rangle \langle O_i \rangle}{\text{Var}[O]} = \frac{\langle O_{1+r} O_1 \rangle - \langle O \rangle^2}{\text{Var}[O]}, \tag{B.1.4}$$

where r denotes the "sample lag" (in continuous signal processing this corresponds to the time lag). The last equality only holds once the equilibrium distribution is reached, since then the linear expectation values are independent of i. It follows, that in this limit $\Gamma(0) = 1$ and $|\Gamma(r > 0)| < 1$. Furthermore, the quantity eventually decays exponentially in the limit of large r.

The last line of Eq. (B.1.3) defines[1] the so-called integrated autocorrelation time as

$$\tau_{\text{int}} = \sum_{r=1}^{N-1} \left(1 - \frac{|r|}{N}\right) \Gamma_O(r) \overset{N \to \infty}{=} \sum_{r=1}^{N-1} \Gamma_O(r). \tag{B.1.5}$$

To determine τ_{int}, however, the above formula may be problematic. In fact, the variance of τ_{int} diverges in the limit of $N \to \infty$ as the actual signal of the autocorrelation dies off exponentially and every term in the sum then adds some amount of noise (which has approximately constant amplitude). In practice it is therefore useful to compute τ_{int} as a function of the considered samples. Once a window of (approximately) constant τ_{int} is identified, the value of the plateau can be considered a faithful estimate.

Finally it is mentioned that a straightforward calculation of $\Gamma_O(r)$ with Eq. (B.1.4) is cumbersome and numerically expensive for a large number of samples. However, by realizing that Eq. (B.1.4) is nothing but a convolution of the signal with itself, we may exploit the convolution theorem to efficiently calculate the autocorrelation function using fast Fourier transforms (FFT).

B.2 Resampling techniques

Besides the direct calculation of the autocorrelation function and the extraction of the integrated autocorrelation time, there are other methods to estimate the statistical error of the mean in an unbiased way. Here, we outline some of the most commonly used approaches and also perform a comparison on a production dataset.

Moreover, it is possible to infer the integrated autocorrelation time from a correctly estimated

---

[1]Note that there exist slightly different definitions in the literature.

uncertainty $\sigma_{\bar{O}}$ by rewriting Eq. (B.1.3d):

$$\tau_{\text{int}} = \frac{1}{2}\left(\frac{\text{Var}[\bar{O}]}{\text{Var}[O]} - 1\right) = \frac{1}{2}\left(\sqrt{\frac{\sigma_{\bar{O}}}{\sigma_O}} - 1\right). \tag{B.2.1}$$

Again, σ_O denotes the naive, i.e. uncorrelated, estimate of the uncertainty.

B.2.1 Binning

The idea of binning is to create a new sequence of random samples by combining (hence binning) subsequent samples into an average sample:

$$O_i^{(1)} = \frac{O_{2i}^{(0)} + O_{2i+1}^{(0)}}{2}, \tag{B.2.2}$$

where $O_i^{(0)}$ denotes samples of the 0th binning level, i.e., the original series. The resulting sequence is only half as long as the original sequence, however, less correlated. This can be considered the first binning level. The naive error estimate for this sequence then gives a better estimate of the true error due to the lower correlation between the new samples $O_i^{(1)}$.

Repeating this procedure yields a sequence of error estimates $\left\{\sigma_{\bar{O}}^{(l)}\right\}$ as a function of the binning level l. Once a plateau is reached, the value of the plateau can be considered an unbiased estimate of the true error (to show this, the central limit theorem may be used). Eventually, though, the binning level becomes too large, which results in a very short sequence of samples (the length decreases exponentially fast) and the plateau will either break down or be nonexistent. In the former case, the procedure simply has to be cut off earlier. The latter case is more problematic and highlights that the autocorrelation is much larger than the amount of samples in the simulation. In such a case, much more simulation time is needed for a correct uncertainty estimate. An exemplifying binning analysis is shown in the top left panel of Fig. B.1.

A major benefit over other error estimation methods is the possibility of online binning, that is, during the sampling process (see, e.g., [323] for a recent proposal). For correlation functions, which come in the form of large arrays, binning is often the only efficient option since storage of the full Markov chain of such a quantity is highly disk-space intensive. Moreover, binning is also relatively cheap in the post-processing and is therefore often the method of choice.

B.2.2 Jackknife

Jackknife resampling is a relatively cheap, yet accurate, tool and is most commonly used in the post-processing of MCMC data [115, 324]. The idea is to produce a sequence of averages $\{\bar{O}_n\}$ where the n-th sample is deleted from the original sequence:

$$\bar{O}_n = \frac{N\bar{O} - O_n}{N - 1}. \tag{B.2.3}$$

N denotes the total number of samples. The variance of this new sequence is the same as the sample variance of the original values [115]. So far, however, the estimate is still biased in the same way the naive guess for the error is. To account for correlation, the strategy is similar to binning: instead of deleting single entries in the sequence, we group subsequent samples into blocks of length M. This results in a series of N_B blocks which we now repeatedly delete according

to the above prescription to obtain averages. With increasing block length, the estimated error converges to the true error.[2] An example of jackknife resampling is shown in the lower left panel of Fig. B.1.

A major benefit of jackknife resampling is that it generalizes to estimators other than the sample mean. Specifically, we may compute a new dataset as a function of the sampled Markov chain via $M_n = f(\{O_{i \neq n}\})$ and subsequently perform the same procedure as for the original series. In this way we do not have to bother with error propagation, which is often challenging in practice. Moreover, this procedure respects non-linear effects whereas plain error propagation is based on linearization.

B.2.3   Bootstrap

The strategy of bootstrap is to resample an existing Markov chain $\{O_i\}$ to obtain a new sequence $\{Q_i\}$ of equal length. This is done by randomly drawing N times out of the N original samples *with* repetition and subsequently taking the average. Repeating this sequence for L times yields a distribution of the L averages that, according to the central limit theorem, is normally distributed around the true mean. The corresponding standard deviation is the unbiased estimation of the variance of the mean. Note that such a procedure produces (slightly) different results for every run as it involves random resampling of the original dataset. Therefore, especially in the statistical literature, bootstrap is sometimes referred to as a special kind of Monte Carlo method to estimate the error. The behavior as a function of the iteration number L is shown in the lower right panel of Fig. B.1.

The method has a similar origin as the jackknife method and like before, we have to extend this procedure to blocks in order to account for correlation. So, rather than resampling single measurements, the series is again partitioned into blocks and entire blocks are resampled with repetition. The results of this procedure are shown in the lower left panel of Fig. B.1.

Like jackknife, the bootstrap method allows for the generalization to arbitrary functions of the original samples. Generally, bootstrap performs slightly better than jackknife, however, it comes at a larger numerical price due to multiple iterations [115]. Especially for a large number of samples, jackknife is therefore the method of choice.

B.2.4   Comparison of methods

To benchmark these methods versus each other, we apply the techniques discussed above to a production dataset of 10^6 correlated samples for a 1D balanced Fermi gas (although the physical parameters do not matter for the conclusions of this section). The results are summarized in Fig. B.1.

In Tab. B.1 we compare numerical values for the integrated autocorrelation time and the standard error of the mean. A comparison to the naive estimate reveals that neglecting the correlations between the samples underestimates the statistical error by a factor of ~ 20. For this dataset, all methods yield consistent results for both quantities, albeit, at varying effort.

The practical conclusion of this analysis is: in post-processing, use jackknife. If online binning is required, use binning. However, any method will do.

---

[2]In fact, it may be shown that this is a conservative estimator, that is, the computed variance is greater or equal to the true variance. For a proof see, e.g., [325].
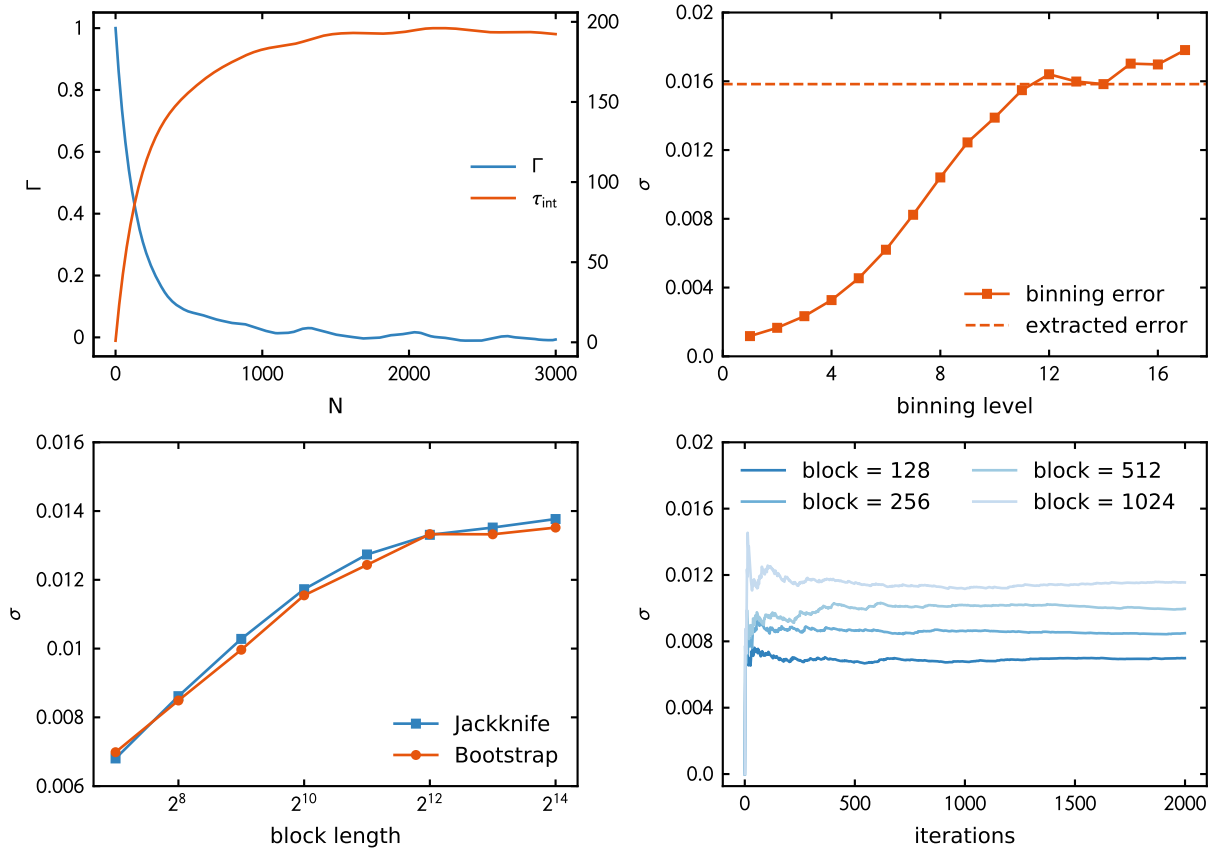
Figure B.1: Comparison of various error estimation methods. (Top left) Autocorrelation function Γ as function of sample lag N. Additionally, the integrated autocorrelation is shown as a function of the sample lag. (Top right) Estimated uncertainty versus binning level. The dashed horizontal line shows the estimated overall error. (Bottom left) Uncertainty estimates from Jackknife (blue squares) and Bootstrap (orange dots) as function of the block size on a semi log scale. (Bottom right) Uncertainty estimates from Bootstrap versus iteration number.

	integrated autocorrelation time τ_{int}	standard error of the mean $\sigma_{\bar{O}}$
naive estimate	—	0.000690
direct evaluation	192.36	0.013543
Binning	263.13	0.015834
Jackknife	198.81	0.013768
Bootstrap	191.67	0.013519

Table B.1: Comparison of autocorrelation time (in units of samples) and standard error of the mean from various methods.

C | Scales & relations for the ideal Fermi gas

When studying interacting Fermi gases it is instructive to consider the noninteracting Fermi gas as a first reference. Furthermore, the corresponding noninteracting quantities are often used as dimensionful scales to normalize numerical results. In this appendix we briefly introduce important relations and derive the scales necessary for the main text. An excellent and detailed description far beyond this appendix may be found in [298].

C.1 Fermi-Dirac distribution

The energy distribution function of an ideal Fermi gas at given temperature $T = \beta^{-1}$ and chemical potential μ is given by the Fermi-Dirac distribution

$$n(\varepsilon) = \frac{1}{1 + e^{\beta(\varepsilon - \mu)}}, \tag{C.1.1}$$

where ε denotes the energy. Accordingly, thermodynamic quantities may be obtained by the weighted integral

$$\langle O \rangle = \int d\varepsilon \, O(\varepsilon) n(\varepsilon). \tag{C.1.2}$$

Generally, these expectation values can only be obtained by numeric integration, although several recursive relations of these so-called Fermi-Dirac Integrals exist (see, e.g., [298]). At high temperatures (and/or low densities) the gas becomes classical and well-known relations from classical thermodynamics apply. In the zero-temperature limit, where $\beta \to \infty$, energies are only occupied up to the Fermi energy ε_F and $n(\varepsilon)$ becomes a step function as shown in Fig. C.1. In this case, many properties are easy to evaluate, as shown below. Beyond the exact $T = 0$ limit, it is possible to perform a Sommerfeld expansion to obtain the temperature dependence to low orders of T.

The above expressions are valid for the continuum. To properly normalize numerical results from lattice calculations, however, we need the corresponding lattice expressions. Therefore, we rewrite Eq. (C.1.2) as a sum over all possible momentum states on the lattice:

$$\langle O \rangle_{\text{lat}} = \sum_{\vec{k}} n(\varepsilon_{\vec{k}}) O(\vec{k}), \tag{C.1.3}$$
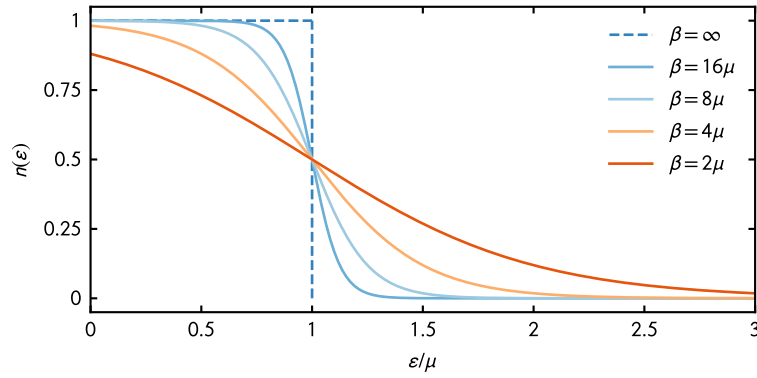
Figure C.1: Fermi-Dirac distribution at various temperatures.

where $\varepsilon_{\vec{k}}$ denotes the energy for the momentum $\vec{k}$ and is given by the dispersion relation

$$\varepsilon_{\vec{k}} = \frac{\vec{k}^2}{2m}. \tag{C.1.4}$$

Finally, the one-body partition function is given by

$$Q_{1,\sigma} = \sum_{\vec{k}} e^{-\beta \frac{\vec{k}^2}{2m_\sigma}}, \tag{C.1.5}$$

which is valid for a single particle of a single species σ. For a spin-$\frac{1}{2}$ system with species $\sigma \in \{\uparrow, \downarrow\}$, we write

$$Q_1 = Q_{1,\uparrow} + Q_{1,\downarrow}, \tag{C.1.6}$$

which is used as a prefactor in the virial expansion (see Eq. (D.1.3)).

A straightforward evaluation of both the lattice and continuum quantities is possible with standard integration routines. However, for some unfavorable combinations of β and μ, cancellations and subtle numerical effects could lead to unphysical values due to failure of floating-point arithmetic.

C.2 Noninteracting quantities at zero temperature

The full particle number is given by integrating the Fermi-Dirac distribution over all possible states while considering the multiplicities of the states. This is most conveniently carried out in momentum space:

$$\langle N_\sigma \rangle = V \int \frac{\mathrm{d}^d k}{(2\pi)^d} \frac{1}{1 + e^{\beta(\varepsilon_{\vec{k},\sigma} - \mu_\sigma)}}, \tag{C.2.1}$$

where $V = L^d$ is the spatial volume of our system. Again, this integral cannot be performed analytically for arbitrary T. At zero temperature, the integral simplifies to an integration over a

Quantity		1D	3D
Fermi momentum	$k_{\mathrm{F},\sigma}$	πn_σ	$(6\pi^2 n_\sigma)^{\frac{1}{3}}$
Fermi energy	$\varepsilon_{\mathrm{F},\sigma} = \frac{k_{\mathrm{F},\sigma}}{2m_\sigma}$	$\frac{1}{2m_\sigma}\pi^2 n_\sigma^2$	$\frac{1}{2m_\sigma}(6\pi^2 n_\sigma)^{\frac{2}{3}}$
density	n_σ	$\frac{k_{\mathrm{F},\sigma}}{\pi}$	$6\pi^2 k_{\mathrm{F},\sigma}^3$
energy	E_{FG}	$\frac{1}{3}N\varepsilon_{\mathrm{F}}$	$\frac{3}{5}N\varepsilon_{\mathrm{F}}$
pressure	$P_{\mathrm{FG}} = \left(\frac{\partial E}{\partial V}\right)_{N,T}$	$\frac{2}{V}E = \frac{2}{3}n\varepsilon_{\mathrm{F}}$	$\frac{2}{3V}E = \frac{2}{5}n\varepsilon_{\mathrm{F}}$
compressibility	$\kappa_{\mathrm{FG}} = \frac{1}{n}\left(\frac{\partial n}{\partial P}\right)_{T,V}$	$\frac{1}{2}\frac{1}{n\varepsilon_{\mathrm{F}}}$	$\frac{3}{2}\frac{1}{n\varepsilon_{\mathrm{F}}}$
spin susceptibility	$\chi_{\mathrm{P}} = \left(\frac{\partial M}{\partial h}\right)_{T,V}$	$\frac{1}{2}\frac{n}{\varepsilon_{\mathrm{F}}}$	$\frac{3}{2}\frac{n}{\varepsilon_{\mathrm{F}}}$
specific heat	$C_V/N = \frac{1}{N}\left(\frac{\partial E}{\partial T}\right)_{V,N}$	0	0

Table C.1: Quantities for the ideal Fermi gas at zero temperature in dependence of the Fermi energy. Note that the top three quantities are given *per spin species* whereas other quantities are for total thermodynamic properties of a spin-$\frac{1}{2}$ system.

d-dimensional sphere whose radius is given by the Fermi momentum:

$$\langle N_\sigma \rangle = N_\sigma = V \int_{|k| \leq |k_{\mathrm{F},\sigma}|} \frac{\mathrm{d}^d k}{(2\pi)^d}. \tag{C.2.2}$$

The above expression is readily evaluated by using the d-dimensional solid angle

$$\int \mathrm{d}^d k = \frac{2\pi^{\frac{d}{2}}}{\Gamma(\frac{d}{2})} \int_0^\infty \mathrm{d}k\ k^{d-1}. \tag{C.2.3}$$

We may rearrange and obtain an expression for the Fermi momentum of a single spin species in arbitrary dimension

$$k_{\mathrm{F},\sigma}^{(d)} = \left[2^{d-1}\pi^{\frac{d}{2}} d\, \Gamma\left(\frac{d}{2}\right) n_\sigma \right]^{\frac{1}{d}}. \tag{C.2.4}$$

For $d = 1,2,3$ the values of the gamma function are given by $\Gamma(\frac{1}{2}) = \pi^{\frac{1}{2}}$, $\Gamma(1) = 1$ and $\Gamma(\frac{3}{2}) = \frac{1}{2}\pi^{\frac{1}{2}}$, respectively.

The Fermi momentum and Fermi energy define the physical scales in any fermionic system and are regularly used to normalize other thermodynamic quantities. In Tab. D.1 all relevant quantities for this work are summarized and given in terms of k_{F} and ε_{F}.

D | The virial expansion

The virial expansion (VE) is an important tool to learn about high-temperature properties of a given system. In this appendix we give a brief overview of its general framework, summarize the relevant virial coefficients for balanced as well as polarized systems and derive expressions for the thermodynamic quantities of interest in this thesis. A recent and extensive overview may be found in [326].

D.1   General framework & balanced scenario

At large temperatures, i.e. small values of β, the thermal wavelength λ_T is much smaller than the interparticle spacing, and with it, the scattering cross-section, which is proportional to λ_T^2, decreases. As a consequence, only few-body correlations dictate the physics in this regime. This motivates rewriting the partition function in terms of the N-body partition functions Q_N:

$$\mathcal{Z} = \mathrm{Tr}\left[\mathrm{e}^{-\beta(\hat{H}-\mu\hat{N})}\right] \tag{D.1.1a}$$

$$= \sum_{N=0}^{\infty} \mathrm{Tr}_N\left[\mathrm{e}^{-\beta\hat{H}}\right]\mathrm{e}^{\beta\mu N} \tag{D.1.1b}$$

$$= \sum_{N=0}^{\infty} Q_N z^N. \tag{D.1.1c}$$

where Tr_N denotes the trace over all N-body states. The last line implicitly defines the fugacity

$$z = \mathrm{e}^{\beta\mu}, \tag{D.1.2}$$

which is a small quantity if $\beta\mu$ is large and negative. In this case, we may expand the grand potential $\Omega = -\beta^{-1}\ln\mathcal{Z}$ in terms of z. After some arithmetic, one arrives at the usual form of the virial expansion for the balanced gas

$$\Omega = -\beta^{-1}Q_1\sum_{n=1} z^n b_n. \tag{D.1.3}$$

where Q_1 denotes the single-particle partition function defined in Eq. (C.1.6). The coefficients b_n are called virial coefficients and are generally unknown. To obtain the n-th order coefficient, however, it is "only" necessary to solve the n-body problem, which becomes a challenging task with increasing particle number. For the UFG, only the first few virial coefficients are known to sufficient precision (see below).

In practice it is useful to single out the interaction effects such that the expansion reads

$$\Omega = \Omega^{(0)} + \Delta\Omega = \Omega^{(0)} + \beta^{-1}Q_1 \sum_{n=1} z^n \Delta b_n. \tag{D.1.4}$$

with the noninteracting contribution $\Omega^{(0)}$ and

$$\Delta b_n = b_n - b_n^{(0)} \tag{D.1.5}$$

where $b_n^{(0)}$ are the noninteracting virial coefficients given by

$$\text{``}b_n^{(0)} = (-1)^{n+1} n^{-\frac{5}{2}}. \tag{D.1.6}$$

The values for the first few coefficients of the UFG are

$$\Delta b_1 = 0 \tag{D.1.7a}$$

$$\Delta b_2 = \frac{1}{\sqrt{2}} \tag{D.1.7b}$$

$$\Delta b_3 = \Delta b_{21} + \Delta b_{12} \approx -0.3551030264897 \tag{D.1.7c}$$

$$\Delta b_4 = \frac{\Delta b_{31} + \Delta b_{13} + \Delta b_{22}}{2} \approx 0.078(18) \tag{D.1.7d}$$

where Δb_2 is known exactly through the Beth-Uhlenbeck formula [327] and Δb_3 may be obtained numerically up to high precision [328]. There exist several determinations for the coefficient Δb_4, however, with some deviations among the various methods and experiment. The above fourth-order coefficient is taken from a recent MC determination [329], where a comparison to other determinations may also be found.

In the literature, the values for the virial coefficients are often provided for harmonically trapped systems. The values may be translated to the homogeneous case considered here via

$$b_n^{\mathrm{T}} = b_n \, n^{-\frac{3}{2}} \tag{D.1.8}$$

where b_n^{T} are the coefficients for the trapped system.

D.2   Virial expansion for population imbalance

To consider the effects of spin imbalance in a two-component system, we must write the above expansion in the fugacities per spin species:

$$\Omega = -\beta^{-1}Q_1 \sum_{n,m=0} z_\uparrow^n z_\downarrow^m b_{nm}. \tag{D.2.1}$$

with $z_\sigma = e^{\beta\mu_\sigma}$ and $Q_1 = Q_{10} + Q_{01}$ as in Eq. (C.1.5). Analogously to the balanced case, we may write

$$\Omega = \Omega^{(0)} + \beta^{-1}Q_1 \sum_{n,m=0} z_\uparrow^n z_\downarrow^m \Delta b_{nm}. \tag{D.2.2}$$

$b_{00}^{(0)} = 0$	$b_{01}^{(0)} = \frac{1}{2}b_1^{(0)} = \frac{1}{2}$	$b_{02}^{(0)} = \frac{1}{2}b_2^{(0)} = -2^{-\frac{7}{2}}$	$b_{03}^{(0)} = \frac{1}{2}b_3^{(0)} = \frac{1}{2}3^{-\frac{5}{2}}$
$b_{00} = 0$	$b_{01} = \frac{1}{2}$	$b_{02} = b_{02}^{(0)}$	$b_{03} = b_{03}^{(0)}$
$\Delta b_{00} = 0$	$\Delta b_{01} = 0$	$\Delta b_{02} = 0$	$\Delta b_{03} = 0$
$b_{10}^{(0)} = \frac{1}{2}b_1^{(0)} = \frac{1}{2}$	$b_{11}^{(0)} = 0$	$b_{12}^{(0)} = 0$	$b_{13}^{(0)} = 0$
$b_{10} = \frac{1}{2}$	$b_{11} = \Delta b_{11}$	$b_{12} = \Delta b_{12} = \frac{1}{2}\Delta b_3$	$b_{13} = \Delta b_{13}$
$\Delta b_{10} = 0$	$\Delta b_{11} = \Delta b_2 = \frac{1}{\sqrt{2}}$	$\Delta b_{12} = -0.17755\ldots$	$\Delta b_{13} = 0.1696(64)$
$b_{20}^{(0)} = \frac{1}{2}b_2^{(0)} = -2^{-\frac{7}{2}}$	$b_{21}^{(0)} = 0$	$b_{22}^{(0)} = 0$	
$b_{20} = b_{20}^{(0)}$	$b_{21} = \Delta b_{21} = \frac{1}{2}\Delta b_3$	$b_{22} = \Delta b_{22}$	?
$\Delta b_{20} = 0$	$\Delta b_{21} = -0.17755\ldots$	$\Delta b_{22} = -0.1840(128)$	
$b_{30}^{(0)} = \frac{1}{2}b_3^{(0)} = \frac{1}{2}3^{-\frac{5}{2}}$	$b_{31}^{(0)} = 0$		
$b_{30} = b_{30}^{(0)}$	$b_{31} = \Delta b_{31}$	?	?
$\Delta b_{30} = 0$	$\Delta b_{31} = 0.1696(64)$		

Table D.1: Virial coefficients for the noninteracting case ($b_{nm}^{(0)}$) and for the UFG in bare (b_{nm}) and differential (Δb_{nm}) form up to fourth order (taken from [329]). Coefficients are given for the polarized case and related to the corresponding expressions in the balanced case.

Again, the interaction effects are encoded in

$$\Delta b_{nm} = b_{nm} - b_{nm}^{(0)}, \tag{D.2.3}$$

and the noninteracting coefficients can be related to the balanced case via

$$b_{n0}^{(0)} = b_{0n}^{(0)} = \frac{1}{2}b_n^{(0)} \tag{D.2.4a}$$

$$b_{nm}^{(0)} = 0 \qquad \forall\, n \wedge m > 0. \tag{D.2.4b}$$

The values for Δb_{nm} may be related to the balanced case and are summarized up to fourth order in Tab. D.1. Note that at fourth order, two coefficients are necessary, stemming from clusters with $3+1$ and $2+2$ particles, respectively.

The relation to the harmonically trapped system generalizes to

$$b_{nm}^{\mathrm{T}} = b_{nm}\,(n+m)^{-\frac{3}{2}}, \tag{D.2.5}$$

where again b_{nm}^{T} denote the coefficients for the trapped UFG.

D.3 Expressions for thermodynamic quantities

Here, we provide some derivations for the virial expansion up to arbitrary order and provide explicit expressions for the central quantities up to third order.

We start by introducing the useful relations

$$\frac{\partial}{\partial\mu} = \frac{\partial}{\partial\mu_\uparrow}\frac{\partial\mu_\uparrow}{\partial\mu} + \frac{\partial}{\partial\mu_\downarrow}\frac{\partial\mu_\downarrow}{\partial\mu} = \frac{\partial}{\partial\mu_\uparrow} + \frac{\partial}{\partial\mu_\downarrow} \tag{D.3.1a}$$

$$\frac{\partial}{\partial h} = \frac{\partial}{\partial\mu_\uparrow}\frac{\partial\mu_\uparrow}{\partial h} + \frac{\partial}{\partial\mu_\downarrow}\frac{\partial\mu_\downarrow}{\partial h} = \frac{\partial}{\partial\mu_\uparrow} - \frac{\partial}{\partial\mu_\downarrow} \tag{D.3.1b}$$

as well as

$$\frac{\partial}{\partial\mu_\sigma} = \frac{\partial}{\partial z_\sigma}\frac{\partial z_\sigma}{\partial\mu_\sigma} = \beta z_\sigma\frac{\partial}{\partial z_\sigma}. \tag{D.3.2}$$

Thermodynamic quantities are obtained by appropriate derivatives of the partition function, which boils down to considering the general expression

$$\ln\mathcal{Z}^{(i,j)} \equiv \frac{\partial^{i+j}\ln\mathcal{Z}}{\partial(\beta\mu)^i\partial(\beta h)^j}. \tag{D.3.3}$$

To obtain an explicit expression, we consider Eq. (D.2.2) and start with the case $(i,j) = (1,0)$:

$$\frac{\partial\ln\mathcal{Z}}{\partial(\beta\mu)} = -\frac{1}{\beta}\frac{\partial\Omega}{\partial(\beta\mu)} = -\frac{1}{\beta}\frac{\partial}{\partial(\beta\mu)}\left(\Omega^{(0)} + \Delta\Omega\right) \tag{D.3.4}$$

For simplicity, we only treat the interacting part and add the non-interacting part at a later point:

$$-\frac{\partial\Delta\Omega}{\partial(\beta\mu)} = -\left[z_\uparrow\frac{\partial}{\partial z_\uparrow} + z_\downarrow\frac{\partial}{\partial z_\downarrow}\right]\Delta\Omega \tag{D.3.5a}$$

$$= \left[z_\uparrow\frac{\partial}{\partial z_\uparrow} + z_\downarrow\frac{\partial}{\partial z_\downarrow}\right]Q_1\sum_{n,m=0} z_\uparrow^n z_\downarrow^m \Delta b_{nm} \tag{D.3.5b}$$

$$= Q_1\sum_{n,m=0} z_\uparrow^n z_\downarrow^m (n+m)\Delta b_{nm}. \tag{D.3.5c}$$

An analogous treatment of the case $(i,j) = (0,1)$ yields

$$-\frac{\partial\Delta\Omega}{\partial(\beta\mu)} = -\left[z_\uparrow\frac{\partial}{\partial z_\uparrow} - z_\downarrow\frac{\partial}{\partial z_\downarrow}\right]\Delta\Omega \tag{D.3.6a}$$

$$= Q_1\sum_{n,m=0} z_\uparrow^n z_\downarrow^m (n-m)\Delta b_{nm}. \tag{D.3.6b}$$

It is straightforward to check that these expressions generalize to arbitrary values of (i,j) such that we may write

$$-\frac{\partial^{i+j}\Delta\Omega}{\partial(\beta\mu)^i\partial(\beta h)^j} = Q_1\sum_{n,m=0} z_\uparrow^n z_\downarrow^m (n+m)^i(n-m)^j\Delta b_{nm}, \tag{D.3.7}$$

which is the central ingredient for all observables to follow. The final expression for an observable given by

$$O = \frac{\partial^{i+j} \ln \mathcal{Z}}{\partial(\beta\mu)^i \partial(\beta h)^j} \tag{D.3.8}$$

may be written as

$$O = O^{(0)} + Q_1 \sum_{n,m=0} z_\uparrow^n z_\downarrow^m (n+m)^i (n-m)^j \Delta b_{nm} \tag{D.3.9}$$

with the exactly computable noninteracting part

$$O^{(0)} \equiv \frac{\partial^{i+j} \ln \mathcal{Z}^{(0)}}{\partial(\beta\mu)^i \partial(\beta h)^j}. \tag{D.3.10}$$

In the following we give explicit derivations for a few thermodynamic quantities up to third order.

D.3.1 Density

$$n_{\text{VE3}}(z_\uparrow, z_\downarrow) = \frac{\partial \ln \mathcal{Z}}{\partial(\beta\mu)} = n^{(0)}(z_\uparrow, z_\downarrow) + \frac{Q_1}{V} \sum_{n,m=0} z_\uparrow^n z_\downarrow^m (n+m) \Delta b_{nm} \tag{D.3.11a}$$

$$= n^{(0)}(z_\uparrow, z_\downarrow) + \frac{Q_1}{V} \left[2 z_\uparrow z_\downarrow \Delta b_{11} + 3(\Delta b_{12} z_\uparrow^2 z_\downarrow + \Delta b_{21} z_\uparrow z_\downarrow^2) \right] \tag{D.3.11b}$$

$$= n^{(0)}(z_\uparrow, z_\downarrow) + \frac{Q_1}{V} \left[2 z_\uparrow z_\downarrow \Delta b_2 + 3 \frac{\Delta b_3}{2} (z_\uparrow^2 z_\downarrow + z_\uparrow z_\downarrow^2) \right] \tag{D.3.11c}$$

D.3.2 Magnetization

$$m_{\text{VE3}}(z_\uparrow, z_\downarrow) = \frac{\partial \ln \mathcal{Z}}{\partial(\beta h)} = m^{(0)}(z_\uparrow, z_\downarrow) + \frac{Q_1}{V} \sum_{n,m=0} z_\uparrow^n z_\downarrow^m (n-m) \Delta b_{nm} \tag{D.3.12a}$$

$$= m^{(0)}(z_\uparrow, z_\downarrow) + \frac{Q_1}{V} \left(\Delta b_{12} z_\uparrow^2 z_\downarrow - \Delta b_{21} z_\uparrow z_\downarrow^2 \right) \tag{D.3.12b}$$

$$= m^{(0)}(z_\uparrow, z_\downarrow) + \frac{Q_1}{V} \frac{\Delta b_3}{2} \left(z_\uparrow^2 z_\downarrow - z_\uparrow z_\downarrow^2 \right) \tag{D.3.12c}$$

E | Derivations of thermodynamic relations

In this appendix, we show derivations of some thermodynamic relations as used in the main text. Before jumping to the actual derivation, we note a few useful relations.

Firstly, the temperature derivative is best expressed in terms of the inverse temperature:

$$\frac{\partial}{\partial T} = \frac{\partial \beta}{\partial T}\frac{\partial}{\partial \beta} = -\beta^2 \frac{\partial}{\partial \beta}. \tag{E.0.1a}$$

Furthermore, we write thermodynamic expectation values corresponding to the partition function

$$\mathcal{Z} = \mathrm{Tr}\left[e^{-\beta(\hat{H}-\eta\hat{O})} \right] \tag{E.0.2}$$

as the derivative with respect to the appropriate coupling:

$$\langle O \rangle = \frac{1}{\beta}\left(\frac{\partial \ln \mathcal{Z}}{\partial \eta} \right)_\beta = \frac{1}{\mathcal{Z}}\left(\frac{\partial \mathcal{Z}}{\partial (\beta\eta)} \right)_\beta \tag{E.0.3a}$$

$$= \mathrm{Tr}\left[e^{-\beta(\hat{H}-\eta\hat{O})}\, \hat{O} \right]. \tag{E.0.3b}$$

E.1 Compressibility

The isothermal compressibility is defined as

$$\kappa_{\mathrm{T}} = \frac{1}{n}\left(\frac{\partial n}{\partial P} \right)_{T,V} = \frac{\beta}{n^2}\left(\frac{\partial n}{\partial (\beta\mu)} \right)_{T,V}. \tag{E.1.1}$$

which we can rewrite as the expectation value of the density fluctuations. Writing for the second derivative

$$\left(\frac{\partial n}{\partial (\beta\mu)} \right)_{T,V} = \frac{1}{V}\frac{\partial}{\partial (\beta\mu)}\left(\frac{1}{\mathcal{Z}}\frac{\partial \mathcal{Z}}{\partial (\beta\mu)} \right) \tag{E.1.2a}$$

$$= \frac{1}{V}\left(-\frac{1}{\mathcal{Z}^2}\frac{\partial \mathcal{Z}}{\partial (\beta\mu)}\frac{\partial \mathcal{Z}}{\partial (\beta\mu)} + \frac{1}{\mathcal{Z}}\frac{\partial^2 \mathcal{Z}}{\partial (\beta\mu)^2} \right) \tag{E.1.2b}$$

$$= \frac{1}{V}\left(\langle N^2 \rangle - \langle N \rangle^2 \right) \tag{E.1.2c}$$

leads to

$$\kappa_{\mathrm{T}} = \frac{\beta}{V} \frac{1}{n^2} \left(\langle N^2 \rangle - \langle N \rangle^2 \right) = \frac{V\beta}{n^2} \left(\langle n^2 \rangle - \langle n \rangle^2 \right). \tag{E.1.3}$$

E.2 Magnetic susceptibility

The magnetic susceptibility, defined as

$$\chi_{\mathrm{M}} = \left(\frac{\partial M}{\partial h} \right)_{T,V}, \tag{E.2.1}$$

may be rewritten as the fluctuations of the magnetization:

$$\kappa_{\mathrm{T}} = \frac{\partial M}{\partial h} = \beta \frac{\partial M}{\partial(\beta h)} = \beta \frac{\partial}{\partial(\beta h)} \left(\frac{1}{\mathcal{Z}} \frac{\partial \mathcal{Z}}{\partial(\beta h)} \right) \tag{E.2.2a}$$

$$= \beta \left(-\frac{1}{\mathcal{Z}^2} \frac{\partial \mathcal{Z}}{\partial(\beta h)} \frac{\partial \mathcal{Z}}{\partial(\beta h)} + \frac{1}{\mathcal{Z}} \frac{\partial^2 \mathcal{Z}}{\partial(\beta h)^2} \right) \tag{E.2.2b}$$

$$= \beta \left(\langle M^2 \rangle - \langle M \rangle^2 \right) = V^2 \beta \left(\langle m^2 \rangle - \langle m \rangle^2 \right). \tag{E.2.2c}$$

E.3 Specific heat

The specific heat at constant volume is defined as

$$\frac{C_V}{k_B N} \equiv c_V = \frac{1}{k_B N} \left(\frac{\partial E}{\partial T} \right)_{N,V}. \tag{E.3.1}$$

E.3.1 General expression

For general Fermi gases with arbitrary interaction, we can rewrite c_V as the expectation of the energy fluctuations. First we consider the second derivative

$$\frac{\partial E}{\partial T} = \frac{\partial}{\partial T} \left(-\frac{1}{\mathcal{Z}} \frac{\partial \mathcal{Z}}{\partial \beta} \right) \tag{E.3.2a}$$

$$= \beta^2 \frac{\partial}{\partial \beta} \left(\frac{1}{\mathcal{Z}} \frac{\partial \mathcal{Z}}{\partial \beta} \right) \tag{E.3.2b}$$

$$= \beta^2 \left(-\frac{1}{\mathcal{Z}^2} \frac{\partial \mathcal{Z}}{\partial \beta} \frac{\partial \mathcal{Z}}{\partial \beta} + \frac{1}{\mathcal{Z}} \frac{\partial^2 \mathcal{Z}}{\partial \beta^2} \right) \tag{E.3.2c}$$

$$= \beta^2 \left(\langle E^2 \rangle - \langle E \rangle^2 \right) \tag{E.3.2d}$$

to arrive at

$$c_V = \frac{\beta^2}{k_B N} \left(\langle E^2 \rangle - \langle E \rangle^2 \right). \tag{E.3.3}$$

E.3.2 Expression for the UFG

Alternatively, we derive an expression for the specific heat that holds at the unitary point. Our goal is to derive an expression for the *specific heat* per particle c_V as defined above. In the following we set $k_B = 1$ and thus make the above expression *dimensionless* (in our units).

$$\left(\frac{\partial E}{\partial T}\right)_{N,V} = \left(\frac{\partial E}{\partial T}\right)_{\mu,V} + \left(\frac{\partial E}{\partial \mu}\right)_{T,V}\left(\frac{\partial \mu}{\partial T}\right)_{N,V}. \tag{E.3.4}$$

By using the pressure-energy relation that holds for the UFG

$$\frac{3}{2}PV = E \tag{E.3.5}$$

and

$$\left(\frac{\partial P}{\partial \mu}\right)_{T,V} = n = \frac{N}{V} \tag{E.3.6}$$

we can immediately evaluate

$$\left(\frac{\partial E}{\partial \mu}\right)_{T,V} = \frac{3}{2}V\left(\frac{\partial P}{\partial \mu}\right)_{T,V} = \frac{3}{2}N. \tag{E.3.7}$$

Additionally, we can use the fact that the particle number $N(\mu, T, V)$ is constant:

$$dN = 0 = \left(\frac{\partial N}{\partial \mu}\right)_{T,V} d\mu + \left(\frac{\partial N}{\partial T}\right)_{\mu,V} dT + \left(\frac{\partial N}{\partial V}\right)_{T,\mu} dV. \tag{E.3.8}$$

With this, and the fact that $dV = 0$, follows:

$$\left(\frac{\partial \mu}{\partial T}\right)_{N,V} = -\left(\frac{\partial N}{\partial T}\right)_{\mu,V}\left(\frac{\partial \mu}{\partial N}\right)_{T,V} \tag{E.3.9}$$

Furthermore, we can write

$$\left(\frac{\partial \mu}{\partial N}\right)_{T,V} = \left(\frac{\partial \mu}{\partial P}\right)_{T,V}\left(\frac{\partial P}{\partial N}\right)_{T,V} = \frac{V}{N}\left(\frac{\partial P}{\partial N}\right)_{T,V} = \frac{V}{N^2}\frac{1}{\kappa_T} \tag{E.3.10}$$

where we again used Eq. (E.3.6) as well as the definition of the *isothermal compressibility*

$$\kappa_T = \frac{1}{N}\left(\frac{\partial N}{\partial P}\right)_{T,V} = \frac{1}{n}\left(\frac{\partial n}{\partial P}\right)_{T,V}. \tag{E.3.11}$$

As an intermediate result, we have the expression

$$c_V = \left(\frac{\partial E}{\partial T}\right)_{\mu,V} - \frac{3}{2n}\frac{1}{\kappa_T}\left(\frac{\partial N}{\partial T}\right)_{\mu,V} \tag{E.3.12}$$

For the remaining two partial derivatives, we use the *universal scaling* valid at unitarity, i.e. we can write any thermodynamic quantity as a dimensionful scale and a dimensionless *scaling*

function. Thus, we write for the pressure

$$P = \beta^\alpha f(x) \tag{E.3.13}$$

where we introduced $x = \beta\mu$ and $f(x)$ as our scaling function. By dimensional analysis, one finds $\alpha = -\frac{5}{2}$. We perform the partial derivatives:

$$N = V\left(\frac{\partial P}{\partial \mu}\right)_{T,V} = V\beta^\alpha \frac{\partial f(x)}{\partial \mu} = V\beta^\alpha \frac{\partial f(x)}{\partial x}\frac{\partial x}{\partial \mu} = V\beta^{\alpha+1}\frac{\partial f(x)}{\partial x} \tag{E.3.14}$$

$$\left(\frac{\partial N}{\partial \mu}\right)_{T,V} = V\beta^{\alpha+1}\frac{\partial}{\partial \mu}\left(\frac{\partial f(x)}{\partial x}\right) = V\beta^{\alpha+2}\frac{\partial^2 f(x)}{\partial x^2} \tag{E.3.15}$$

Going back to Eq. (E.3.12), we can now evaluate the remaining partial derivatives by using Eq. (E.0.1):

$$\begin{aligned}
\left(\frac{\partial P}{\partial T}\right)_{\mu,V} &= -\beta^2 \frac{\partial}{\partial \beta}(\beta^\alpha f(x)) \\
&= -\beta^2\left[\alpha\beta^{\alpha-1}f(x) + \beta^\alpha\frac{\partial f(x)}{\partial \beta}\right] \\
&= -\alpha\beta^{\alpha+1}f(x) - \beta^{\alpha+2}\mu\frac{\partial f(x)}{\partial x} \\
&= -\alpha\beta[\beta^\alpha f(x)] - \frac{\beta\mu}{V}\left[V\beta^{\alpha+1}\frac{\partial f(x)}{\partial x}\right] \\
&= -\alpha\beta P - \frac{\beta\mu}{V}N
\end{aligned} \tag{E.3.16}$$

which then allows us to write

$$\left(\frac{\partial E}{\partial T}\right)_{\mu,V} = \frac{3}{2}V\left(\frac{\partial P}{\partial T}\right)_{\mu,V} = -\frac{3}{2}\left[\alpha\beta PV + \beta\mu N\right] \tag{E.3.17}$$

by again using Eq. (E.3.5). For the last remaining partial derivative we use Eq. (E.3.14) and write

$$\left(\frac{\partial N}{\partial T}\right)_{\mu,V} = -\beta^2\frac{\partial}{\partial \beta}\left[\beta^{V\alpha+1}\frac{\partial f(x)}{\partial x}\right] \tag{E.3.18a}$$

$$= -\beta^2 V\left[(\alpha+1)\beta^\alpha\frac{\partial f(x)}{\partial x} + \beta^{\alpha+1}\frac{\partial^2 f(x)}{\partial x^2}\frac{\partial x}{\partial \beta}\right] \tag{E.3.18b}$$

$$= -V(\alpha+1)\beta^{\alpha+2}\frac{\partial f(x)}{\partial x} - V\beta^{\alpha+3}\mu\frac{\partial^2 f(x)}{\partial x^2} \tag{E.3.18c}$$

$$= -V(\alpha+1)\beta^{\alpha+2}\frac{\partial f(x)}{\partial x} - \beta\mu\left(\frac{\partial N}{\partial \mu}\right)_{T,V} \tag{E.3.18d}$$

$$= -V(\alpha+1)\beta^{\alpha+2}\frac{\partial f(x)}{\partial x} - \beta\mu\left(\frac{\partial N}{\partial P}\right)_{T,V}\left(\frac{\partial P}{\partial \mu}\right)_{T,V} \tag{E.3.18e}$$

$$= -(\alpha + 1)\beta N - \beta\mu\frac{\kappa_T N^2}{V} \tag{E.3.18f}$$

Again, we used the definition of the compressibility here. This takes out any partial derivatives and we can collect all expressions to write for the specific heat

$$
\begin{aligned}
c_V &= -\frac{3}{2}\frac{V}{N}\alpha\beta P - \frac{3}{2}\beta\mu + \frac{3V}{2N^2}\frac{1}{\kappa_T}\left[(\alpha + 1)\beta N + \beta\mu\frac{\kappa_T N^2}{V}\right] \\
&= \frac{3}{2}\frac{\beta}{n}\left(\frac{\alpha + 1}{\kappa_T} - \alpha P\right)
\end{aligned}
\tag{E.3.19}
$$

With $\alpha = -\frac{5}{2}$, as well as $\kappa_{\mathrm{FG}} = \frac{3}{2}\frac{1}{n\varepsilon_{\mathrm{F}}}$ and $P_{\mathrm{FG}} = \frac{5}{2}n\varepsilon_{\mathrm{F}}$, we can finally write the specific heat per particle in dimensionless form:

$$c_V = \frac{3}{2}\left(\frac{T}{T_F}\right)^{-1}\left[\frac{P}{P_{\mathrm{FG}}} - \frac{\kappa_{\mathrm{FG}}}{\kappa_T}\right]. \tag{E.3.20}$$

F | `gMacs`

A large number of MCMC implementations follow the simple pattern discussed in Section 3.2.2. Often, these implementations involve a large number of generic tasks such as the setup of a data persistence module or statistical evaluation of transient simulation data. It is common practice to copy existing code into similar implementations for new algorithms. This often results in legacy code that is hard to maintain and challenging to track (due to its many copies). `gMacs` tries to mitigate these issues by providing a framework for heavy-duty MCMC simulations. Its two main motivations can be summarized as follows:

Reduction of overhead coding: The list of repetitive tasks for different (yet similar) MCMC implementations is long and ranges from data persistence via proper initialization to cluster usage of simulation codes. `gMacs` provides pre-defined data structures that already come with a lot of functionality, mainly for the handling of data through the pipeline from calculation to storage. The package is set up in an easily extendible way, should further functionality be required.

Consistent format for simulation data: Data is the reason for performing numerical calculations in the first place. Often, however, its proper handling receives less attention than it should and quick-and-dirty data dumps to text files without sufficient labeling is a common sight. This is not only inefficient usage of disk space but also leads to a lack meta-information on the origin of the data and thus hinders reproducibility. `gMacs` provides a standard data format based on the binary HDF5 protocol that automatically stores all relevant meta data along with the actual numerical results.

The package is written in Python3 and relies heavily on `numpy`, `pandas` and the HDF5 wrapper `h5py`. Special emphasis was given to a lightweight implementation as well as to usability, reproducibility and extensive documentation. From a computational standpoint, the generic structure introduces a slight time penalty (mostly stemming from file I/O operations). This is especially apparent in very cheap simple examples. For heavy-duty computations, as applied in this thesis for instance, the introduced overhead is negligible and far below the statistical fluctuations of CPU time between runs. In the following we highlight the main pieces of the package and provide a minimal example of a Langevin methods for simple integrals.

F.1   Core concepts

At the core of `gMacs` are two main ingredients, which we introduce in this section: the base class `MarkovChainSampler` and data capsules.
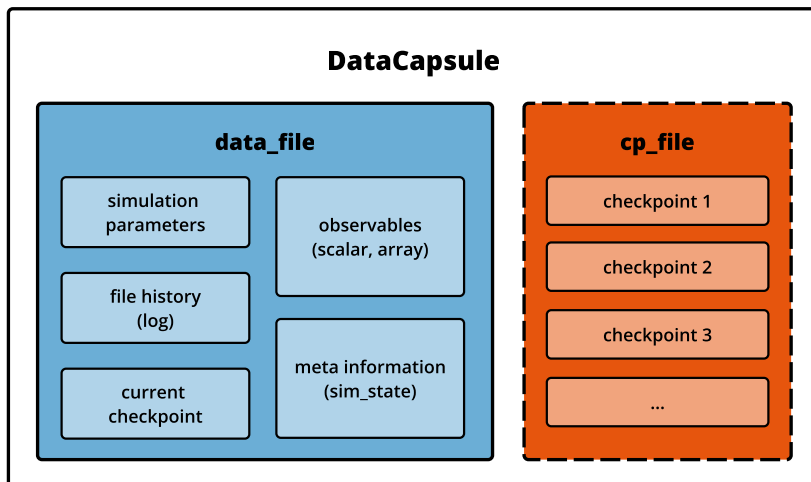
Figure F.1: Schematic structure of a DataCapsule. Along with the wrapper to access these HDF5 files, this constitutes one of the two main functions of `gMacs` .

MarkovChainSampler   The class `MarkovChainSampler` is the workhorse of `gMacs` . If utilized correctly, it takes care of everything concerning the data flow of the simulation as well as sampling itself. It represents our Simulation object that holds all information and functionality for producing a random sequence of samples.

For a functioning implementation of a given MCMC algorithm, we just have to extend the class `MarkovChainSampler` and provide implementations the functions `random_sample()` and `next_sample()` in the child class. These functions determine the initial value as well as the jump to the next state in the Markov chain, respectively. That's all - everything else needed to actually produce the random process is already included in the base class.

To actually compute observables, however, it is necessary to tell `gMacs` how to convert any given configuration (also called sample or state) into a measurement of an observable. This is done by providing Python callables (names of implemented functions). Note that the class `MarkovChainSampler` can not be instantiated directly as this is realized as an abstract class, i.e., it does not possess the required functionality itself. To use the class, we need to extend it.

Data capsules   Data capsules represent the data structure in which `gMacs` stores all relevant information in a self-descriptive manner. In the backend, this is realized as HDF5 files which we wrap with the so-called `DataCapsuleReader` to efficiently read out the information in the form of `pandas.DataFrame` . The structure is depicted in Fig. F.1. For technical reasons, there are actually two separate files - `data_file` and the `cp_file` although the latter is optional. There are various things bundled up in this structure:

simulation parameters: These are stored as attributes of the base group of the `data_file` and are essentially the parameters given to the simulation object. Their values may be retrieved via `DataCapsuleReader.get_attrs()` .

file history: Holds information on any writing access to the data capsule along with meta data such as username, system and timestamps.

current checkpoint: Holds the current state of the Markov chain along with the necessary information to seamlessly pick up from this point. Should not be touched by the user.

observables: This is where the results of measurements are stored. For technical reasons, there are two types of observables: `scalar` and `array` which needs to be specified when we register observables in the `available_observables` dictionary. Any function that delivers a single number (or a dictionary with key : number pairs) of any datatype qualifies as scalar type. Anything that yields an array should be marked as such. The methods to retrieve the data are type-independent and mainly given by `DataCapsuleReader.get_average()` and `DataCapsuleReader.get_series()`.

simulation state: Holds meta information on the simulation, for instance the sample number in the sequence or the elapsed Markov time. Technically, this works in the same way as observables except that no averages are computed for it - but otherwise information may be added in the same way.

Checkpoints `gMacs` works with checkpoints (CP) as its 'unit of measure'. When we specify a run length, for instance, we want to set the option `'n_cp'`. A CP is the same as any other configuration, however, it represents a special point in the chain at which the current status of the simulation is dumped to the data capsule. By default, observables are only computed at checkpoints (but this can be toggled). This notion originates from the need of producing decorrelated samples - CPs therefore are typically separated by an autocorrelation length (that needs to be pre-determined or just crudely estimated somehow).

F.2   Hello World - Langevin style

As per usual, numerical packages ship with a "Hello World!" application. Here we provide a fully working minimal example of a Langevin example of simple integrals.[1] The integral we want to sample is given by

$$\mathcal{Z} = \int_{-\infty}^{\infty} d\phi \ e^{-(\frac{\mu}{2}\phi^2 + \frac{\lambda}{24}\phi^4)} \equiv \int_{-\infty}^{\infty} d\phi \ e^{-S(\phi)}, \qquad (F.2.1)$$

where we can consider $S(x)$ the "action" of our $0 + 0$ dimensional field theory. According to stochastic quantization, the next step in the random process is given by

$$\phi_{n+1} = \phi_n - \left(\mu\phi_n + \frac{\lambda}{6}\phi_n^3\right)\Delta t \ + \ \sqrt{2\Delta t}\,\eta. \qquad (F.2.2)$$

Phase 1: Setting up the sampler class Our main task is to suitably construct a sampler object such that it performs the above random process. A few steps are necessary to achieve this:

1. First of all, we need to define an object that extends the base class `MarkovChainSampler`. In the present example we called it `ScalarLangevinSampler`. It is recommended to call the constructor of the base class with `super()`.

---

[1]This is in fact the same implementation that has been used to obtain the data for the $0 + 0$-dimensional examples in Section 4.4.

```python
class ScalarLangevinSampler(MarkovChainSampler):

    def __init__(self, *args, **kwargs):
        super().__init__(*args, **kwargs)

        # initialize the Langevin time measurement
        self.sim_state.update({
            'elapsed_cl_time': 0.,
            'dtcl_cp': 0.
        })

        # lists all observables with their corresponding returning functions
        self.available_observables = {
            'phi_square': {'func'  : self.phi_square,
                           'type'  : 'scalar',
                           'dtype' : np.float}
        }

        # initialize the noise amplitude
        self.sig = np.sqrt(2 * self.param['cl_time_step'])

        # extract the parameters for the action.
        self.mu, self.lam = self.param['args']

    def random_sample(self):
        """Create the initial sample of the Markov chain"""
        self.sample = np.random.normal(0, self.sig)


    def next_sample(self):
        """Create the next sample of the Markov chain"""

        # add the drift
        self.sample -= (self.mu*self.sample + self.lam/6*self.sample**3
                        * self.param['cl_time_step'])

        # add noise
        self.sample += np.random.normal(0, self.sig)

        # update the progress of the simulation
        self.sim_state['elapsed_cl_time'] += self.param['cl_time_step']

        # manage checkpointing
        if self.checkpoint:
            self.sim_state['dtcl_cp'] = self.param['cl_time_step']
        else:
            self.sim_state['dtcl_cp'] += self.param['cl_time_step']
        self.checkpoint = self.sim_state['dtcl_cp'] >= self.param['cl_time_per_checkpoint']

    @staticmethod
    def phi_square(sample):
        return np.dot(sample, sample)
```

Listing F.1: Definition of the `ScalarLangevinSampler`

2. A starting point for the random process has to be defined, which is done by implementing the function `random_sample()`. In this simple case, this is nothing but a random number.

3. The central piece of the implementation is the method `next_sample()`. This function is called to move from the current sample to the next state in the Markov chain, so this is where the update of Eq. (F.2.2) is implemented.

   Furthermore, we need to decide whether a checkpoint is reached or not. In our example this is the case after a certain amount of Langevin time has passed. We set this time span by providing a value for the key `'cl_time_per_checkpoint'` in the `parameters` dictionary. Finally, the elapsed Langevin time has to be tracked which can conveniently done via an entry in the dictionary `sim_state` (this should be initialized in the `__init()__` method).

So far so good - this is all that needs to be done to step through the Markov chain. However, we did not tell `gMacs` to compute any observables yet. To do this, we need to specify functions that map a sample value to an observable value. In our example the observable will be the square of the field value ϕ and it is implemented in the static function `phi_square(sample)` (the function does not have to be static nor does it necessarily have to be a class member). Finally we "register" this newly available observable in the dictionary `available_observables`. That's it - everything else is already taken care of. Lst. F.1 contains the full definition of our `ScalarLangevinSampler`.

Phase 2: Running the simulation Having set up the sampler class, we now are in a position to perform the actual simulation. All we have to do is to specify a dictionary that holds our parameters, create an object of `ScalarLangevinSampler` and finally start the simulation by calling the object. A Python script that does the job could look like the following listing.

```python
parameters = {
    'seed': 123,                          # Define the initial state of the
                                          # random number generator.
    'data_file': 'scalar_langevin.hdf5', # Filename for the DataCapsule.
    'file_access_mode': 'replace',        # Create a file or replace an existing one.
    'n_cp': 10,                           # Number of checkpoints to calculate
                                          # before terminating the run.
    'observables': ['phi_square'],        # Observables to calculate and save at
                                          # every checkpoint (needs to be a subset of
                                          # the `available_observables`).
    'cl_time_step': 0.05,                 # Time step in the Langevin equation.
    'cl_time_per_checkpoint': 10,         # Langevin time between checkpoints.
    'args': [-0.5, 1]                     # Arguments for the action.
}


# Create a sampler with parameters and action and run the simulation.
sim = ScalarLangevinSampler(param=parameters)
sim()
```

A few remarks on the parameters are in order:

■ Some of the parameters (`'args'`, `'cl_time_step'`, `'cl_time_per_checkpoint'`) we have used in our sampler class and thus they need to be in the dictionary for the simulation to run. Otherwise a `KeyError` will be thrown.

- The only parameter required by `gMacs` itself is `'n_cp'`. It sets the length of the simulation by specifying how many checkpoints are sampled.

- Optional parameters are:

    - `'data_file'`: Output file name of the data capsule. Defaults to `'results.hdf5'`.
    - `'file_access_mode'`: Determines whether files are overridden (`'replace'`) or protected (`'create'`). The possibilities to append data (via the modes `'append'` or `'observables'`) are discussed in the documentation.
    - `'seed'`: Sets the random number seed. It is highly recommended to set a value for debugging purposes.

- The parameter `'observables'` determines which observables are computed at the checkpoints. Names specified must be present in the dictionary `'available_operators'`, otherwise a `KeyError` will be thrown. Note, that we could have specified many more available observables - only the ones specified here will actually be computed in this run.

Now that was it - the simulation executed and everything is neatly stored in a data capsule at the specified file. Note that nothing seems to have happened - `gMacs` does not print things by default (although this could be implemented, if desired).

Post processing: retrieving the data   The simulation is done and our data is stored safely. To access the data we simply import `DataCapsuleReader` and create an object with the corresponding file name. The object then holds all simulation data.

In the example below, we access the full series of samples by calling `get_series()`. This returns a `pandas.DataFrame` from which we can easily obtain average and standard deviation of the observable `'phi_square'`.

```python
from gmacs import DataCapsuleReader
import numpy as np

# Produce the object and read its contents.
dcr = DataCapsuleReader('scalar_langevin.hdf5')
df = dcr.get_series()

# Check the average value.
avg = np.mean(df['phi_square'])
sig = np.std(df['phi_square']) / np.sqrt(len(df['phi_square']))
print('Average square of the field: {:.6f} +- {:.6f}'.format(avg, sig))
```

This is by far not all that can be done with the `DataCapsuleReader`. For instance, we may be interested in the history of the data. We may simply run the following script to obtain a dump of everything that has ever been written to the present data capsule.

```python
log = dcr.get_file_history()
for line in log:
    print(line)
```

This concludes this brief glimpse in the functionality of `gMacs`. The documentation comes with an extensive overview an further features and has more examples and use cases.

F.3   Outlook: the future of `gMacs`

Currently `gMacs_v0.1.0` is available, which essentially includes the basic usage as shown above and a bunch of additional features. The package is, however, still under construction. Plans for new features include:

– Extended capabilities for statistical evaluation (Jackknife, Bootstrap, Binning).

– Online binning (see, e.g., [323]).

– Concurrent execution of file I/O operations.

– Generalized sample structure.

– Hot start from a provided sample.

– Utilities for the batching of multiple jobs on clusters.

– An assortment of various implemented algorithms (CL, HMC, etc.).

Eventually `gMacs` will be released as open source package. Stay tuned.

Bibliography

[1] P. A. M. Dirac and R. H. Fowler. *"Quantum mechanics of many-electron systems"*. Proc. Royal Soc. A **123**, 714-733 (1929)

[2] M. Troyer and U.-J. Wiese. *"Computational Complexity and Fundamental Limitations to Fermionic Quantum Monte Carlo Simulations"*. Phys. Rev. Lett. **94**(17), 170201 (2005)

[3] R. P. Feynman. *"Simulating physics with computers"*. Int. J. Theor. Phys. **21**, 467-488 (1982)

[4] K. Davis, M.-O. Mewes, M. Andrews, N. van Druten, D. Durfee, D. Kurn, and W. Ketterle. *"Bose-Einstein Condensation in a Gas of Sodium Atoms"*. Phys. Rev. Lett. **75**(22), 3969-3973 (1995)

[5] M. H. Anderson, J. R. Ensher, M. R. Matthews, C. E. Wieman, and E. A. Cornell. *"Observation of Bose-Einstein Condensation in a Dilute Atomic Vapor"*. Science **269**, 198-201 (1995)

[6] B. DeMarco and D. S. Jin. *"Onset of Fermi Degeneracy in a Trapped Atomic Gas"*. Science **285**, 1703-1706 (1999)

[7] L. N. Cooper. *"Bound Electron Pairs in a Degenerate Fermi Gas"*. Phys. Rev. **104**(4), 1189-1190 (1956)

[8] J. Bardeen, L. N. Cooper, and J. R. Schrieffer. *"Theory of Superconductivity"*. Phys. Rev. **108**(5), 1175-1204 (1957)

[9] D. M. Eagles. *"Possible Pairing without Superconductivity at Low Carrier Concentrations in Bulk and Thin-Film Superconducting Semiconductors"*. Phys. Rev. **186**(2), 456-463 (1969)

[10] A. J. Leggett. *"Diatomic molecules and cooper pairs"*. In: *"Modern Trends in the Theory of Condensed Matter"* edited by: A. Pękalski and J. A. Przystawa. Berlin, Heidelberg: Springer Berlin Heidelberg (1980)

[11] P. Nozières and S. Schmitt-Rink. *"Bose condensation in an attractive fermion gas: From weak to strong coupling superconductivity"*. J. Low. Temp. Phys. **59**, 195-211 (1985)

[12] S. Giorgini, L. P. Pitaevskii, and S. Stringari. *"Theory of ultracold atomic Fermi gases"*. Rev. Mod. Phys. **80**(4), 1215-1274 (2008)

[13] G. C. Strinati, P. Pieri, G. Röpke, P. Schuck, and M. Urban. *"The BCS–BEC crossover: From ultra-cold Fermi gases to nuclear systems"*. Phys. Rep. **738**, 1-76 (2018)

[14] H. Feshbach. *"Unified theory of nuclear reactions"*. Ann. Phys. **5**, 357-390 (1958)

[15] U. Fano. *"Effects of Configuration Interaction on Intensities and Phase Shifts"*. Phys. Rev. **124**(6), 1866-1878 (1961)

[16] H. Feshbach. *"A unified theory of nuclear reactions. II"*. Ann. Phys. **19**, 287-313 (1962)

[17] C. Chin, R. Grimm, P. Julienne, and E. Tiesinga. *"Feshbach resonances in ultracold gases"*. Rev. Mod. Phys. **82**(2), 1225-1286 (2010)

[18] J. Taron. *"Feshbach resonance: A one dimensional example"*. Am. J. Phys. **81**, 603-609 (2013)

[19] J. Taylor. *"Scattering Theory"*. New York: Wiley (1972)

[20] W. Zwerger (Ed.) *"The BCS-BEC Crossover and the Unitary Fermi Gas"*. Berlin Heidelberg: Springer-Verlag (2012)

[21] T. Mehen, I. W. Stewart, and M. B. Wise. *"Conformal invariance for non-relativistic field theory"*. Phys. Lett. B **474**, 145-152 (2000)

[22] Y. Nishida and D. T. Son. *"Nonrelativistic conformal field theories"*. Phys. Rev. D **76**(8), 086004 (2007)

[23] X. Bekaert, E. Meunier, and S. Moroz. *"Towards a gravity dual of the unitary Fermi gas"*. Phys. Rev. D **85**(10), 106001 (2012)

[24] T. Enss. *"Quantum critical transport in the unitary Fermi gas"*. Phys. Rev. A **86**(1), 013616 (2012)

[25] A. Schnell, G. Röpke, and P. Schuck. *"Precritical Pair Fluctuations and Formation of a Pseudogap in Low-Density Nuclear Matter"*. Phys. Rev. Lett. **83**(10), 1926-1929 (1999)

[26] A. Schwenk and C. J. Pethick. *"Resonant Fermi Gases with a Large Effective Range"*. Phys. Rev. Lett. **95**(16), 160401 (2005)

[27] I. Tews, J. M. Lattimer, A. Ohnishi, and E. E. Kolomeitsev. *"Symmetry Parameter Constraints from a Lower Bound on Neutron-matter Energy"*. Astrophys. J. **848**, 105 (2017)

[28] S. Jensen, C. N. Gilbreth, and Y. Alhassid. *"The pseudogap regime in the unitary Fermi gas"*. EPJ ST **227**, 2241-2261 (2019)

[29] A. M. Clogston. *"Upper Limit for the Critical Field in Hard Superconductors"*. Phys. Rev. Lett. **9**(6), 266-267 (1962)

[30] B. S. Chandrasekhar. *"A note on the maximum critial field of high-field superconductors"*. Appl. Phys. Lett. **1**, 7-8 (1962)

[31] M. W. Zwierlein, A. Schirotzek, C. H. Schunck, and W. Ketterle. *"Fermionic Superfluidity with Imbalanced Spin Populations"*. Science **311**, 492-496 (2006)

[32] M. W. Zwierlein, C. H. Schunck, A. Schirotzek, and W. Ketterle. *"Direct observation of the superfluid phase transition in ultracold Fermi gases"*. Nature **442**, 54-58 (2006)

[33] G. B. Partridge, W. Li, R. I. Kamar, Y.-a. Liao, and R. G. Hulet. *"Pairing and Phase Separation in a Polarized Fermi Gas"*. Science **311**, 503-505 (2006)

[34] G. B. Partridge, W. Li, Y. A. Liao, R. G. Hulet, M. Haque, and H. T. C. Stoof. *"Deformation of a Trapped Fermi Gas with Unequal Spin Populations"*. Phys. Rev. Lett. **97**(19), 190407 (2006)

[35] W. Ketterle and M. W. Zwierlein. *"Making, probing and understanding ultracold Fermi gases"*. In: *"Ultra-Cold Fermi Gases (Proceedings of the International Schoolof Physics "Enrico Fermi", Course CLXIV)"* edited by: M. Inguscio, W. Ketterle, and C. Salomon. Amsterdam: IOS Press (2008)

[36] S. Nascimbène, N. Navon, S. Pilati, F. Chevy, S. Giorgini, A. Georges, and C. Salomon. *"Fermi-Liquid Behavior of the Normal Phase of a Strongly Interacting Gas of Cold Atoms"*. Phys. Rev. Lett. 106(21), 215303 (2011)

[37] I. Boettcher, J. Braun, T. K. Herbst, J. M. Pawlowski, D. Roscher, and C. Wetterich. *"Phase structure of spin-imbalanced unitary Fermi gases"*. Phys. Rev. A 91(1), 013610 (2015)

[38] B. Frank, J. Lang, and W. Zwerger. *"Universal Phase Diagram and Scaling Functions of Imbalanced Fermi Gases"*. JETP 127, 812-825 (2018)

[39] C. Lobo, A. Recati, S. Giorgini, and S. Stringari. *"Normal State of a Polarized Fermi Gas at Unitarity"*. Phys. Rev. Lett. 97(20), 200403 (2006)

[40] R. Combescot, A. Recati, C. Lobo, and F. Chevy. *"Normal State of Highly Polarized Fermi Gases: Simple Many-Body Approaches"*. Phys. Rev. Lett. 98(18), 180402 (2007)

[41] Z. Yan, P. B. Patel, B. Mukherjee, R. J. Fletcher, J. Struck, and M. W. Zwierlein. *"Boiling a Unitary Fermi Liquid"*. Phys. Rev. Lett. 122(9), 093401 (2019)

[42] A. Schirotzek, C.-H. Wu, A. Sommer, and M. W. Zwierlein. *"Observation of Fermi Polarons in a Tunable Fermi Liquid of Ultracold Atoms"*. Phys. Rev. Lett. 102(23), 230402 (2009)

[43] S. Nascimbène, N. Navon, K. J. Jiang, F. Chevy, and C. Salomon. *"Exploring the thermodynamics of a universal Fermi gas"*. Nature 463, 1057 (2010)

[44] N. Navon, S. Nascimbène, F. Chevy, and C. Salomon. *"The Equation of State of a Low-Temperature Fermi Gas with Tunable Interactions"*. Science 328, 729-732 (2010)

[45] S. Stringari. *"Density and Spin Response Function of a Normal Fermi Gas at Unitarity"*. Phys. Rev. Lett. 102(11), 110406 (2009)

[46] S. Pilati and S. Giorgini. *"Phase Separation in a Polarized Fermi Gas at Zero Temperature"*. Phys. Rev. Lett. 100(3), 030401 (2008)

[47] P. F. Bedaque, H. Caldas, and G. Rupak. *"Phase Separation in Asymmetrical Fermion Superfluids"*. Phys. Rev. Lett. 91(24), 247002 (2003)

[48] A. Sedrakian, J. Mur-Petit, A. Polls, and H. Müther. *"Pairing in a two-component ultracold Fermi gas: Phases with broken-space symmetries"*. Phys. Rev. A 72(1), 013613 (2005)

[49] G. Sarma. *"On the influence of a uniform exchange field acting on the spins of the conduction electrons in a superconductor"*. J. Phys. Chem. Solids 24, 1029-1032 (1963)

[50] W. V. Liu and F. Wilczek. *"Interior Gap Superfluidity"*. Phys. Rev. Lett. 90(4), 047002 (2003)

[51] A. Bulgac, M. M. Forbes, and A. Schwenk. *"Induced P-Wave Superfluidity in Asymmetric Fermi Gases"*. Phys. Rev. Lett. 97(2), 020402 (2006)

[52] P. Fulde and R. A. Ferrell. *"Superconductivity in a Strong Spin-Exchange Field"*. Phys. Rev. 135(3A), A550-A563 (1964)

[53] A. Larkin and Y. Ovchinnikov. *"Inhomogeneous State of Superconductors"*. Sov. Phys. JETP 20, 762 (1965)

[54] J. J. Kinnunen, J. E. Baarsma, J.-P. Martikainen, and P. Törmä. *"The Fulde–Ferrell–Larkin–Ovchinnikov state for ultracold fermions in lattice and harmonic potentials: a review"*. Rep. Prog. Phys. 81, 046401 (2018)

[55] B. Mukherjee, P. B. Patel, Z. Yan, R. J. Fletcher, J. Struck, and M. W. Zwierlein. *"Spectral Response and Contact of the Unitary Fermi Gas"*. Phys. Rev. Lett. 122(20), 203402 (2019)

[56] D. T. Son and M. A. Stephanov. *"Phase diagram of a cold polarized Fermi gas"*. Phys. Rev. A 74(1), 013614 (2006)

[57] L. Radzihovsky and D. E. Sheehy. *"Imbalanced Feshbach-resonant Fermi gases"*. Rep. Prog. Phys. 73, 076501 (2010)

[58] F. Chevy and C. Mora. *"Ultra-cold polarized Fermi gases"*. Rep. Prog. Phys. 73, 112401 (2010)

[59] K. Gubbels and H. Stoof. *"Imbalanced Fermi gases at unitarity"*. Phys. Rep. 525, 255–313 (2013)

[60] G. Jotzu, M. Messer, F. Görg, D. Greif, R. Desbuquois, and T. Esslinger. *"Creating State-Dependent Lattices for Ultracold Fermions by Magnetic Gradient Modulation"*. Phys. Rev. Lett. 115(7), 073002 (2015)

[61] J. Wang, Y. Che, L. Zhang, and Q. Chen. *"Enhancement effect of mass imbalance on Fulde-Ferrell-Larkin-Ovchinnikov type of pairing in Fermi-Fermi mixtures of ultracold quantum gases"*. Sci. Rep. 7, 39783 (2017)

[62] D. Roscher, J. Braun, and J. E. Drut. *"Phase structure of mass- and spin-imbalanced unitary Fermi gases"*. Phys. Rev. A 91(5), 053611 (2015)

[63] J. Braun, J. E. Drut, and D. Roscher. *"Zero-Temperature Equation of State of Mass-Imbalanced Resonant Fermi Gases"*. Phys. Rev. Lett. 114(5), 050404 (2015)

[64] J. von Stecher, C. H. Greene, and D. Blume. *"BEC-BCS crossover of a trapped two-component Fermi gas with unequal masses"*. Phys. Rev. A 76(5), 053613 (2007)

[65] A. Gezerlis, S. Gandolfi, K. E. Schmidt, and J. Carlson. *"Heavy-Light Fermion Mixtures at Unitarity"*. Phys. Rev. Lett. 103(6), 060403 (2009)

[66] G. E. Astrakharchik, S. Giorgini, and J. Boronat. *"Stability of resonantly interacting heavy-light Fermi mixtures"*. Phys. Rev. B 86(17), 174518 (2012)

[67] C. N. Yang. *"Some Exact Results for the Many-Body Problem in one Dimension with Repulsive Delta-Function Interaction"*. Phys. Rev. Lett. 19(23), 1312–1315 (1967)

[68] M. Gaudin. *"Un systeme a une dimension de fermions en interaction"*. Phys. Lett. A 24, 55–56 (1967)

[69] E. H. Lieb and F. Y. Wu. *"Absence of Mott Transition in an Exact Solution of the Short-Range, One-Band Model in One Dimension"*. Phys. Rev. Lett. 20(25), 1445–1448 (1968)

[70] H. Bethe. *"Zur Theorie der Metalle"*. Z. Phys. 71, 205–226 (1931)

[71] X.-W. Guan, M. T. Batchelor, and C. Lee. *"Fermi gases in one dimension: From Bethe ansatz to experiments"*. Rev. Mod. Phys. 85(4), 1633–1691 (2013)

[72] T. Giamarchi. *"Quantum Physics in One Dimension"*. Oxford: Oxford University Press (2003)

[73] F. H. L. Essler, H. Frahm, F. Göhmann, A. Klümper, and V. E. Korepin. *"The One-Dimensional Hubbard Model"*. Cambridge: Cambridge University Press (2005)

[74] S.-i. Tomonaga. *"Remarks on Bloch's Method of Sound Waves applied to Many-Fermion Problems"*. Prog. Theor. Phys. **5**, 544-569 (1950)

[75] J. M. Luttinger. *"An Exactly Soluble Model of a Many-Fermion System"*. J. Math. Phys. **4**, 1154-1162 (1963)

[76] I. Bloch. *"Ultracold quantum gases in optical lattices"*. Nat. Phys. **1**, 23-30 (2005)

[77] J. Fortágh and C. Zimmermann. *"Magnetic microtraps for ultracold atoms"*. Rev. Mod. Phys. **79**(1), 235-289 (2007)

[78] L. Rammelmüller, W. J. Porter, J. Braun, and J. E. Drut. *"Evolution from few- to many-body physics in one-dimensional Fermi systems: One- and two-body density matrices and particle-partition entanglement"*. Phys. Rev. A **96**(3), 033635 (2017)

[79] L. Rammelmüller, W. J. Porter, J. E. Drut, and J. Braun. *"Surmounting the sign problem in nonrelativistic calculations: A case study with mass-imbalanced fermions"*. Phys. Rev. D **96**(9), 094506 (2017)

[80] L. Rammelmüller, J. E. Drut, and J. Braun. *"A complex Langevin approach to ultracold fermions"*. J. Phys. Conf. Ser. **1041**, 012006 (2018)

[81] L. Rammelmüller, A. C. Loheac, J. E. Drut, and J. Braun. *"Finite-Temperature Equation of State of Polarized Fermions at Unitarity"*. Phys. Rev. Lett. **121**(17), 173001 (2018)

[82] C. E. Berger, L. Rammelmüller, A. C. Loheac, F. Ehmann, J. Braun, and J. E. Drut. *"Complex Langevin and other approaches to the sign problem in quantum many-body physics"*. arXiv:1907.10183

[83] K. G. Wilson. *"Confinement of quarks"*. Phys. Rev. D **10**(8), 2445-2459 (1974)

[84] H. J. Rothe. *"Lattice Gauge Theories"*. World Scientific (2012)

[85] D. Lee. *"Lattice Methods and the Nuclear Few- and Many-Body Problem"*. In: *""An Advanced Course in Computational Nuclear Physics: Bridging the Scales from Quarks to Neutron Stars""* edited by: M. Hjorth-Jensen, M. P. Lombardo, and U. van Kolck. Cham: Springer International Publishing (2017)

[86] J. E. Drut and A. N. Nicholson. *"Lattice methods for strongly interacting many-body systems"*. J. Phys. G **40**, 043101 (2013)

[87] R. Shankar. *"Quantum Field Theory and Condensed Matter: An Introduction"*. Cambridge: Cambridge University Press (2017)

[88] N. Hatano and M. Suzuki. *"Finding Exponential Product Formulas of Higher Orders"*. In: *"Quantum Annealing and Other Optimization Methods"* edited by: A. Das and B. K. Chakrabarti. Berlin, Heidelberg: Springer Berlin Heidelberg (2005)

[89] M. Lüscher. *"Volume dependence of the energy spectrum in massive quantum field theories. I. Stable particle states"*. Comm. Math. Phys. **104**, 177-206 (1986)

[90] M. Lüscher. *"Volume dependence of the energy spectrum in massive quantum field theories. II. Scattering states"*. Comm. Math. Phys. **105**, 153-188 (1986)

[91] J. E. Drut. *"Improved lattice operators for nonrelativistic fermions"*. Phys. Rev. A **86**(1), 013604 (2012)

[92] Y. Castin and F. Werner. *"The Unitary Gas and its Symmetry Properties"*. In: *"The BCS-BEC Crossover and the Unitary Fermi Gas"* edited by: W. Zwerger. Berlin, Heidelberg: Springer Berlin Heidelberg (2012)

[93] M. G. Endres, D. B. Kaplan, J.-W. Lee, and A. N. Nicholson. *"Lattice Monte Carlo calculations for unitary fermions in a finite box"*. Phys. Rev. A **87**(2), 023615 (2013)

[94] M. Valiente and N. T. Zinner. *"Unitary fermions and Lüscher's formula on a crystal"*. Sci. China Phys. Mech. **59**, 114211 (2016)

[95] N. Klein, D. Lee, and U. G. Meißner. *"Lattice improvement in lattice effective field theory"*. Eur. Phys. J. A **54**(12), 233 (2018)

[96] R. L. Stratonovich. *"On a Method of Calculating Quantum Distribution Functions"*. Sov. Phys. Dokl. **2**, 416 (1957)

[97] J. Hubbard. *"Calculation of Partition Functions"*. Phys. Rev. Lett. **3**(2), 77-78 (1959)

[98] D. Lee. *"Ground state energy at unitarity"*. Phys. Rev. C **78**(2), 024001 (2008)

[99] J. E. Hirsch. *"Discrete Hubbard-Stratonovich transformation for fermion lattice models"*. Phys. Rev. B **28**(7), 4059-4061 (1983)

[100] F. Assaad and H. Evertz. *"World-line and Determinantal Quantum Monte Carlo Methods for Spins, Phonons and Electrons"*. In: *"Computational Many-Particle Physics"* edited by: H. Fehske, R. Schneider, and A. Weiße. Berlin, Heidelberg: Springer Berlin Heidelberg (2008)

[101] A. Bulgac, J. E. Drut, and P. Magierski. *"Quantum Monte Carlo simulations of the BCS-BEC crossover at finite temperature"*. Phys. Rev. A **78**(2), 023625 (2008)

[102] D. Lee. *"Lattice simulations for few- and many-body systems"*. Prog. Part. Nucl. Phys. **63**, 117-154 (2009)

[103] R. Blankenbecler, D. J. Scalapino, and R. L. Sugar. *"Monte Carlo calculations of coupled boson-fermion systems. I"*. Phys. Rev. D **24**(8), 2278-2286 (1981)

[104] J. E. Drut, J. R. McKenney, W. S. Daza, C. L. Lin, and C. R. Ordóñez. *"Quantum Anomaly and Thermodynamics of One-Dimensional Fermions with Three-Body Interactions"*. Phys. Rev. Lett. **120**(24), 243002 (2018)

[105] J. R. McKenney and J. E. Drut. *"Fermi-Fermi crossover in the ground state of one-dimensional few-body systems with anomalous three-body interactions"*. Phys. Rev. A **99**(1), 013615 (2019)

[106] D. Thouless. *"Stability conditions and nuclear rotations in the Hartree-Fock theory"*. Nucl. Phys. **21**, 225-232 (1960)

[107] J. Carlson, S. Gandolfi, K. E. Schmidt, and S. Zhang. *"Auxiliary-field quantum Monte Carlo method for strongly paired fermions"*. Phys. Rev. A **84**(6), 061602 (2011)

[108] H. Shi and S. Zhang. *"Many-body computations by stochastic sampling in Hartree-Fock-Bogoliubov space"*. Phys. Rev. B **95**(4), 045144 (2017)

[109] E. Vitali, P. Rosenberg, and S. Zhang. *"Calculating ground state properties of correlated fermionic systems with BCS trial wave functions in Slater determinant path-integral approaches"*. arXiv:1905.05012

[110] R. Eckhardt. *"Stan Ulam, John von Neumann, and the Monte Carlo method"*. Los Alamos Science **15**, 131-136 (1987)

[111] V. Ambegaokar and M. Troyer. *"Estimating errors reliably in Monte Carlo simulations of the Ehrenfest model"*. `Am. J. Phys. 78(2), 150-157 (2010)`

[112] J. Sherman and W. J. Morrison. *"Adjustment of an Inverse Matrix Corresponding to a Change in One Element of a Given Matrix"*. `Ann. Math. Statist. 21(1), 124-127 (1950)`

[113] T. W. Anderson. *"The Statistical Analysis of Time Series"*. John Wiley & Sons, Ltd (1994)

[114] A. Sokal. *"Monte Carlo Methods in Statistical Mechanics: Foundations and New Algorithms"*. In: *"Functional Integration: Basics and Applications"* edited by: C. DeWitt-Morette, P. Cartier, and A. Folacci. Boston, MA: Springer US (1997)

[115] B. Efron and G. Gong. *"A Leisurely Look at the Bootstrap, the Jackknife, and Cross-Validation"*. `Am. Stat. 37, 36-48 (1983)`

[116] E. Y. Loh, J. E. Gubernatis, R. T. Scalettar, S. R. White, D. J. Scalapino, and R. L. Sugar. *"Sign problem in the numerical simulation of many-electron systems"*. `Phys. Rev. B 41(13), 9301-9307 (1990)`

[117] R. Levy and B. K. Clark. *"Mitigating the Sign Problem Through Basis Rotations"*. `arXiv:1907.02076`

[118] L. Wang, Y.-H. Liu, M. Iazzi, M. Troyer, and G. Harcos. *"Split Orthogonal Group: A Guiding Principle for Sign-Problem-Free Fermionic Simulations"*. `Phys. Rev. Lett. 115(25), 250601 (2015)`

[119] Z. C. Wei, C. Wu, Y. Li, S. Zhang, and T. Xiang. *"Majorana Positivity and the Fermion Sign Problem of Quantum Monte Carlo Simulations"*. `Phys. Rev. Lett. 116(25), 250601 (2016)`

[120] Z.-C. Wei. *"Semigroup Approach to the Sign Problem in Quantum Monte Carlo Simultions"*. `arXiv:1712.09412`

[121] U.-J. Wiese. *"Bosonization and cluster updating of lattice fermions"*. `Phys. Lett. B 311, 235-240 (1993)`

[122] H. Singh and S. Chandrasekharan. *"Few-body physics on a spacetime lattice in the worldline approach"*. `Phys. Rev. D 99(7), 074511 (2019)`

[123] H. Singh. *"Worldline approach to few-body physics on the lattice"*. `arXiv:1812.02364`

[124] S. Chandrasekharan and U.-J. Wiese. *"Meron-Cluster Solution of Fermion Sign Problems"*. `Phys. Rev. Lett. 83(16), 3116-3119 (1999)`

[125] S. Chandrasekharan. *"Fermion bag approach to lattice field theories"*. `Phys. Rev. D 82(2), 025007 (2010)`

[126] S. Chandrasekharan. *"Fermion bag approach to fermion sign problems"*. `Eur. Phys. J. A 49, 90 (2013)`

[127] E. Huffman and S. Chandrasekharan. *"Fermion bag approach to Hamiltonian lattice field theories in continuous time"*. `Phys. Rev. D 96(11), 114502 (2017)`

[128] G. Aarts. *"Lefschetz thimbles and stochastic quantization: Complex actions in the complex plane"*. `Phys. Rev. D 88(9), 094501 (2013)`

[129] N. Rom, E. Fattal, A. K. Gupta, E. A. Carter, and D. Neuhauser. *"Shifted-contour auxiliary-field Monte Carlo for molecular electronic structure"*. `J. Chem. Phys. 109, 8241-8248 (1998)`

[130] M. Cristoforetti, F. Di Renzo, and L. Scorzato. *"New approach to the sign problem in quantum field theories: High density QCD on a Lefschetz thimble"*. Phys. Rev. D **86**(7), 074506 (2012)

[131] M. V. Ulybyshev and S. N. Valgushev. *"Path integral representation for the Hubbard model with reduced number of Lefschetz thimbles"*. arXiv:1712.02188

[132] P. Broecker, J. Carrasquilla, R. G. Melko, and S. Trebst. *"Machine learning quantum phases of matter beyond the fermion sign problem"*. Sci. Rep. **7**(1), 2045-2322 (2017)

[133] C. Gattringer and K. Langfeld. *"Approaches to the sign problem in lattice field theory"*. Int. J. Mod. Phys. A **31**, 1643007 (2016)

[134] Z.-X. Li and H. Yao. *"Sign-Problem-Free Fermionic Quantum Monte Carlo: Developments and Applications"*. Annu. Rev. Condens. Matter Phys. **10**, 337-356 (2019)

[135] N. Metropolis, A. W. Rosenbluth, M. N. Rosenbluth, A. H. Teller, and E. Teller. *"Equation of State Calculations by Fast Computing Machines"*. J. Chem. Phys. **21**, 1087-1092 (1953)

[136] S. Duane, A. Kennedy, B. J. Pendleton, and D. Roweth. *"Hybrid Monte Carlo"*. Phys. Lett. B **195**, 216-222 (1987)

[137] G. Parisi and Y.-s. Wu. *"Perturbation Theory Without Gauge Fixing"*. Sci. Sin. **24**, 483 (1981)

[138] G. Parisi. *"On complex probabilities"*. Phys. Lett. B **131**, 393-395 (1983)

[139] G. Aarts. *"Can Stochastic Quantization Evade the Sign Problem? The Relativistic Bose Gas at Finite Chemical Potential"*. Phys. Rev. Lett. **102**(13), 131601 (2009)

[140] C. Adami and S. E. Koonin. *"Complex Langevin equation and the many-fermion problem"*. Phys. Rev. C **63**(3), 034319 (2001)

[141] R. H. Swendsen and J.-S. Wang. *"Nonuniversal critical dynamics in Monte Carlo simulations"*. Phys. Rev. Lett. **58**(2), 86-88 (1987)

[142] U. Wolff. *"Collective Monte Carlo Updating for Spin Systems"*. Phys. Rev. Lett. **62**(4), 361-364 (1989)

[143] G. G. Batrouni, G. R. Katz, A. S. Kronfeld, G. P. Lepage, B. Svetitsky, and K. G. Wilson. *"Langevin simulations of lattice field theories"*. Phys. Rev. D **32**(10), 2736-2747 (1985)

[144] M. Bercx, F. Goth, J. S. Hofmann, and F. F. Assaad. *"The ALF (Algorithms for Lattice Fermions) project release 1.0. Documentation for the auxiliary field quantum Monte Carlo code"*. SciPost Phys. **3**(2), 013 (2017)

[145] W. K. Hastings. *"Monte Carlo sampling methods using Markov chains and their applications"*. Biometrika **57**, 97-109 (1970)

[146] J. Dongarra and F. Sullivan. *"Guest Editors' Introduction: The Top 10 Algorithms"*. Comput. Sci. Eng. **2**(1), 22-23 (2000)

[147] S. Chib and E. Greenberg. *"Understanding the Metropolis-Hastings Algorithm"*. Am. Stat. **49**, 327-335 (1995)

[148] R. T. Scalettar, D. J. Scalapino, R. L. Sugar, and D. Toussaint. *"Hybrid molecular-dynamics algorithm for the numerical simulation of many-electron systems"*. Phys. Rev. B **36**(16), 8632-8641 (1987)

[149] S. Beyl, F. Goth, and F. F. Assaad. *"Revisiting the hybrid quantum Monte Carlo method for Hubbard and electron-phonon models".* Phys. Rev. B **97**(8), 085144 (2018)

[150] M. R. Hestenes and E. Stiefel. *"Methods of Conjugate Gradients for Solving Linear Systems".* J. Res. Natl. Bur. Stand. **49**(6), 409 (1952)

[151] J. E. Drut, T. A. Lähde, and T. Ten. *"Momentum Distribution and Contact of the Unitary Fermi Gas".* Phys. Rev. Lett. **106**(20), 205302 (2011)

[152] J. E. Drut, T. A. Lähde, G. Wlazłowski, and P. Magierski. *"Equation of state of the unitary Fermi gas: An update on lattice calculations".* Phys. Rev. A **85**(5), 051601 (2012)

[153] E. R. Anderson and J. E. Drut. *"Pressure, Compressibility, and Contact of the Two-Dimensional Attractive Fermi Gas".* Phys. Rev. Lett. **115**(11), 115301 (2015)

[154] L. Rammelmüller, W. J. Porter, and J. E. Drut. *"Ground state of the two-dimensional attractive Fermi gas: Essential properties from few to many body".* Phys. Rev. A **93**(3), 033639 (2016)

[155] L. Rammelmüller, W. J. Porter, A. C. Loheac, and J. E. Drut. *"Few-fermion systems in one dimension: Ground- and excited-state energies and contacts".* Phys. Rev. A **92**(1), 013631 (2015)

[156] M. D. Hoffman, P. D. Javernick, A. C. Loheac, W. J. Porter, E. R. Anderson, and J. E. Drut. *"Universality in one-dimensional fermions at finite temperature: Density, pressure, compressibility, and contact".* Phys. Rev. A **91**(3), 033618 (2015)

[157] C. E. Berger, E. R. Anderson, and J. E. Drut. *"Energy, contact, and density profiles of one-dimensional fermions in a harmonic trap via nonuniform-lattice Monte Carlo calculations".* Phys. Rev. A **91**(5), 053618 (2015)

[158] J. R. McKenney, C. R. Shill, W. J. Porter, and J. E. Drut. *"Ground-state energy, density profiles, and momentum distribution of attractively interacting 1D Fermi gases with hard-wall boundaries: a Monte Carlo study".* J. Phys. B **49**, 225001 (2016)

[159] J. E. Drut and W. J. Porter. *"Hybrid Monte Carlo approach to the entanglement entropy of interacting fermions".* Phys. Rev. B **92**(12), 125126 (2015)

[160] W. J. Porter and J. E. Drut. *"Entanglement spectrum and Rényi entropies of nonrelativistic conformal fermions".* Phys. Rev. B **94**(16), 165112 (2016)

[161] J. E. Drut and T. A. Lähde. *"Is Graphene in Vacuum an Insulator?".* Phys. Rev. Lett. **102**(2), 026802 (2009)

[162] J. E. Drut and T. A. Lähde. *"Lattice field theory simulations of graphene".* Phys. Rev. B **79**(16), 165425 (2009)

[163] J. E. Drut and T. A. Lähde. *"Critical exponents of the semimetal-insulator transition in graphene: A Monte Carlo study".* Phys. Rev. B **79**(24), 241405 (2009)

[164] M. V. Ulybyshev, P. V. Buividovich, M. I. Katsnelson, and M. I. Polikarpov. *"Monte Carlo Study of the Semimetal-Insulator Phase Transition in Monolayer Graphene with a Realistic Interelectron Interaction Potential".* Phys. Rev. Lett. **111**(5), 056801 (2013)

[165] S. Hands and C. Strouthos. *"Quantum critical behavior in a graphenelike model".* Phys. Rev. B **78**(16), 165423 (2008)

[166] P. V. Buividovich and M. I. Polikarpov. *"Monte Carlo study of the electron transport properties of monolayer graphene within the tight-binding model".* Phys. Rev. B **86**(24), 245117 (2012)

[167] D. Smith and L. von Smekal. *"Monte Carlo simulation of the tight-binding model of graphene with partially screened Coulomb interactions"*. `Phys. Rev. B 89(19), 195429 (2014)`

[168] R. Brower, C. Rebbi, and D. Schaich. *"Hybrid Monte Carlo simulation on the graphene hexagonal lattice"*. `arXiv:1204.5424`

[169] T. Luu and T. A. Lähde. *"Quantum Monte Carlo calculations for carbon nanotubes"*. `Phys. Rev. B 93(15), 155106 (2016)`

[170] J.-L. Wynen, E. Berkowitz, C. Körber, T. A. Lähde, and T. Luu. *"Avoiding Ergodicity Problems in Lattice Discretizations of the Hubbard Model"*. `arXiv:1812.09268`

[171] S. Krieg, T. Luu, J. Ostmeyer, P. Papaphilippou, and C. Urbach. *"Accelerating Hybrid Monte Carlo simulations of the Hubbard model on the hexagonal lattice"*. `Comput. Phys. Commun. 236, 15-25 (2019)`

[172] J. Braun, J.-W. Chen, J. Deng, J. E. Drut, B. Friman, C.-T. Ma, and Y.-D. Tsai. *"Imaginary Polarization as a Way to Surmount the Sign Problem in Ab Initio Calculations of Spin-Imbalanced Fermi Gases"*. `Phys. Rev. Lett. 110(13), 130404 (2013)`

[173] D. Roscher, J. Braun, J.-W. Chen, and J. E. Drut. *"Fermi gases with imaginary mass imbalance and the sign problem in Monte-Carlo calculations"*. `J. Phys. G 41, 055110 (2014)`

[174] E. Dagotto, A. Moreo, R. L. Sugar, and D. Toussaint. *"Binding of holes in the Hubbard model"*. `Phys. Rev. B 41(1), 811-814 (1990)`

[175] P. de Forcrand and O. Philipsen. *"The QCD phase diagram for small densities from imaginary chemical potential"*. `Nucl. Phys. B 642, 290-306 (2002)`

[176] P. de Forcrand and O. Philipsen. *"The QCD phase diagram for three degenerate flavors and small baryon density"*. `Nucl. Phys. B 673, 170-186 (2003)`

[177] A. C. Loheac, J. Braun, J. E. Drut, and D. Roscher. *"Thermal equation of state of polarized fermions in one dimension via complex chemical potentials"*. `Phys. Rev. A 92(6), 063609 (2015)`

[178] J. Berges and I.-O. Stamatescu. *"Simulating Nonequilibrium Quantum Fields with Stochastic Quantization Techniques"*. `Phys. Rev. Lett. 95(20), 202003 (2005)`

[179] J. Berges, S. Borsányi, D. Sexty, and I.-O. Stamatescu. *"Lattice simulations of real-time quantum fields"*. `Phys. Rev. D 75(4), 045007 (2007)`

[180] P. H. Damgaard and H. Hüffel. *"Stochastic quantization"*. `Phys. Rep. 152, 227-398 (1987)`

[181] K. Okano, L. Schülke, and B. Zheng. *"Complex Langevin Simulation"*. `Prog, Theor. Phys. Supp. 111, 313-347 (1993)`

[182] G. Jona-Lasinio and P. K. Mitter. *"On the stochastic quantization of field theory"*. `Comm. Math. Phys. 101, 409-436 (1985)`

[183] G. Maruyama. *"Continuous Markov processes and stochastic equations"*. `Rend. Circ. Mat. Palermo 4, 48 (1955)`

[184] C. Chang. *"Numerical solution of stochastic differential equations with constant diffusion coefficients"*. `Math. Comp. 49, 523-542 (1987)`

[185] G. Aarts and F. A. James. *"Complex Langevin dynamics in the SU(3) spin model at nonzero chemical potential revisited"*. `JHEP 2012, 118 (2012)`

[186] I. Drummond, S. Duane, and R. Horgan. *"The stochastic method for numerical simulations:: Higher order corrections"*. `Nucl. Phys. B 220, 119-136 (1983)`

[187] A. M. Horowitz. *"The second order Langevin equation and numerical simulations"*. `Nucl. Phys. B 280, 510-522 (1987)`

[188] S. Catterall, I. Drummond, and R. Horgan. *"Langevin algorithms for spin models"*. `Phys. Lett. B 254, 177-184 (1991)`

[189] G. Aarts, E. Seiler, and I.-O. Stamatescu. *"Complex Langevin method: When can it be trusted?"*. `Phys. Rev. D 81(5), 054508 (2010)`

[190] G. Aarts, E. Seiler, D. Sexty, and I.-O. Stamatescu. *"Complex Langevin dynamics and zeroes of the fermion determinant"*. `JHEP 2017, 44 (2017)`

[191] E. Seiler. *"Status of Complex Langevin"*. `EPJ Web Conf. 175, 01019 (2018)`

[192] G. Aarts, F. A. James, E. Seiler, and I.-O. Stamatescu. *"Complex Langevin: etiology and diagnostics of its main problem"*. `Eur. Phys. J. C 71, 1756 (2011)`

[193] M. Scherzer, E. Seiler, D. Sexty, and I.-O. Stamatescu. *"Complex Langevin: Boundary terms and application to QCD"*. `arXiv:1810.09713`

[194] M. Scherzer, E. Seiler, D. Sexty, and I.-O. Stamatescu. *"Complex Langevin and boundary terms"*. `Phys. Rev. D 99(1), 014512 (2019)`

[195] K. Nagata, J. Nishimura, and S. Shimasaki. *"Argument for justification of the complex Langevin method and the condition for correct convergence"*. `Phys. Rev. D 94(11), 114515 (2016)`

[196] A. Mollgaard and K. Splittorff. *"Complex Langevin dynamics for chiral random matrix theory"*. `Phys. Rev. D 88(11), 116007 (2013)`

[197] G. Aarts, F. A. James, E. Seiler, and I.-O. Stamatescu. *"Adaptive stepsize and instabilities in complex Langevin dynamics"*. `Phys. Lett. B 687, 154-159 (2010)`

[198] A. C. Loheac and J. E. Drut. *"Third-order perturbative lattice and complex Langevin analyses of the finite-temperature equation of state of nonrelativistic fermions in one dimension"*. `Phys. Rev. D 95(9), 094502 (2017)`

[199] E. Seiler, D. Sexty, and I.-O. Stamatescu. *"Gauge cooling in complex Langevin for lattice QCD with heavy quarks"*. `Phys. Lett. B 723, 213-216 (2013)`

[200] L. Bongiovanni, G. Aarts, E. Seiler, D. Sexty, and I.-O. Stamatescu. *"Adaptive gauge cooling for complex Langevin dynamics"*. `arXiv:1311.1056`

[201] K. Nagata, J. Nishimura, and S. Shimasaki. *"Justification of the complex Langevin method with the gauge cooling procedure"*. `Prog. Theor. Exp. Phys. 2016, (2016)`

[202] K. Nagata, J. Nishimura, and S. Shimasaki. *"Gauge cooling for the singular-drift problem in the complex Langevin method — a test in Random Matrix Theory for finite density QCD"*. `JHEP 2016, 73 (2016)`

[203] G. Aarts, F. Attanasio, B. Jäger, and D. Sexty. *"Complex Langevin in Lattice QCD: dynamic stabilisation and the phase diagram"*. `arXiv:1607.05642`

[204] Attanasio, Felipe and Jäger, Benjamin. *"Improved convergence of Complex Langevin simulations"*. `EPJ Web Conf. 175, 07039 (2018)`

[205] F. Attanasio and B. Jäger. *"Dynamical stabilisation of complex Langevin simulations of QCD"*. `Eur. Phys. J. C 79, 16 (2019)`

[206] M. Olshanii and S. G. Jackson. *"An exactly solvable quantum four-body problem associated with the symmetries of an octacube".* New J. Phys. **17**, 105005 (2015)

[207] A. S. Dehkharghani, A. G. Volosniev, and N. T. Zinner. *"Impenetrable mass-imbalanced particles in one-dimensional harmonic traps".* J. Phys. B **49**, 085301 (2016)

[208] N. L. Harshman, M. Olshanii, A. S. Dehkharghani, A. G. Volosniev, S. G. Jackson, and N. T. Zinner. *"Integrable Families of Hard-Core Particles with Unequal Masses in a One-Dimensional Harmonic Trap".* Phys. Rev. X **7**(4), 041001 (2017)

[209] S. R. White. *"Density matrix formulation for quantum renormalization groups".* Phys. Rev. Lett. **69**(19), 2863-2866 (1992)

[210] U. Schollwöck. *"The density-matrix renormalization group in the age of matrix product states".* Ann. Phys. **326**, 96-192 (2011)

[211] R. Orús. *"A practical introduction to tensor networks: Matrix product states and projected entangled pair states".* Ann. Phys. **349**, 117-158 (2014)

[212] M. Motta, D. M. Ceperley, G. K.-L. Chan, J. A. Gomez, E. Gull, S. Guo, C. A. Jiménez-Hoyos, T. N. Lan, J. Li, F. Ma, A. J. Millis, N. V. Prokof'ev, U. Ray, G. E. Scuseria, S. Sorella, E. M. Stoudenmire, Q. Sun, I. S. Tupitsyn, S. R. White, D. Zgid, and S. Zhang. *"Towards the Solution of the Many-Electron Problem in Real Materials: Equation of State of the Hydrogen Chain with State-of-the-Art Many-Body Methods".* Phys. Rev. X **7**(3), 031059 (2017)

[213] N. D. Mermin and H. Wagner. *"Absence of Ferromagnetism or Antiferromagnetism in One- or Two-Dimensional Isotropic Heisenberg Models".* Phys. Rev. Lett. **17**(22), 1133-1136 (1966)

[214] E. Altman, E. Demler, and M. D. Lukin. *"Probing many-body states of ultracold atoms via noise correlations".* Phys. Rev. A **70**(1), 013603 (2004)

[215] G. Zürn, F. Serwane, T. Lompe, A. N. Wenz, M. G. Ries, J. E. Bohn, and S. Jochim. *"Fermionization of Two Distinguishable Fermions".* Phys. Rev. Lett. **108**(7), 075303 (2012)

[216] A. N. Wenz, G. Zürn, S. Murmann, I. Brouzos, T. Lompe, and S. Jochim. *"From Few to Many: Observing the Formation of a Fermi Sea One Atom at a Time".* Science **342**, 457-460 (2013)

[217] M. Wadati and T. Iida. *"BCS-BEC crossover in one-dimensional integrable model".* Phys. Lett. A **360**, 423-428 (2007)

[218] C. A. Tracy and H. Widom. *"On the ground state energy of the delta-function Fermi gas".* J. Math. Phys. **57**, 103301 (2016)

[219] M. Girardeau. *"Relationship between Systems of Impenetrable Bosons and Fermions in One Dimension".* J. Math. Phys. **1**, 516-523 (1960)

[220] E. H. Lieb and W. Liniger. *"Exact Analysis of an Interacting Bose Gas. I. The General Solution and the Ground State".* Phys. Rev. **130**(4), 1605-1616 (1963)

[221] E. H. Lieb. *"Exact Analysis of an Interacting Bose Gas. II. The Excitation Spectrum".* Phys. Rev. **130**(4), 1616-1624 (1963)

[222] V. Krivnov and A. Ovchinnikov. *"One-dimensional Fermi gas with attraction between the electrons".* Sov. Phys. JETP **40**, 781 (1965)

[223] J. N. Fuchs, A. Recati, and W. Zwerger. *"Exactly Solvable Model of the BCS-BEC Crossover".* Phys. Rev. Lett. **93**(9), 090408 (2004)

[224] D. J. Griffiths. *"Introduction to Quantum Mechanics"*. Cambridge: Cambridge University Press (2004)

[225] S. Kemler, M. Pospiech, and J. Braun. *"Formation of selfbound states in a one-dimensional nuclear model—a renormalization group based density functional study"*. `J. Phys. G 44, 015101 (2016)`

[226] A. Luther and I. Peschel. *"Single-particle states, Kohn anomaly, and pairing fluctuations in one dimension"*. `Phys. Rev. B 9(7), 2911-2919 (1974)`

[227] F. D. M. Haldane. *"Effective Harmonic-Fluid Approach to Low-Energy Properties of One-Dimensional Quantum Fluids"*. `Phys. Rev. Lett. 47(25), 1840-1843 (1981)`

[228] S. Tan. *"Large momentum part of a strongly correlated Fermi gas"*. `Ann. Phys. 323, 2971-2986 (2008)`

[229] S. Tan. *"Energetics of a strongly correlated Fermi gas"*. `Ann. Phys. 323, 2952-2970 (2008)`

[230] S. Tan. *"Generalized virial theorem and pressure relation for a strongly correlated Fermi gas"*. `Ann. Phys. 323, 2987-2990 (2008)`

[231] M. Barth and W. Zwerger. *"Tan relations in one dimension"*. `Ann. Phys. 326, 2544-2565 (2011)`

[232] M. Casula, D. M. Ceperley, and E. J. Mueller. *"Quantum Monte Carlo study of one-dimensional trapped fermions with attractive contact interactions"*. `Phys. Rev. A 78(3), 033607 (2008)`

[233] J. Lee and X. Guan. *"Asymptotic correlation functions and FFLO signature for the one-dimensional attractive spin-1/2 Fermi gas"*. `Nucl. Phys. B 853, 125-138 (2011)`

[234] D. Roscher and J. Braun. *"In-medium bound-state formation and inhomogeneous condensation in Fermi gases in a hard-wall box"*. `J. Phys. B 50, 205301 (2017)`

[235] A. G. Volosniev. *"Strongly Interacting One-dimensional Systems with Small Mass Imbalance"*. `Few-Body Syst. 58, 54 (2017)`

[236] Y.-H. Liu and L. Wang. *"Quantum Monte Carlo study of mass-imbalanced Hubbard models"*. `Phys. Rev. B 92(23), 235129 (2015)`

[237] M.-T. Philipp, M. Wallerberger, P. Gunacker, and K. Held. *"Mott-Hubbard transition in the mass-imbalanced Hubbard model"*. `Eur. Phys. J. B 90, 114 (2017)`

[238] G. G. Batrouni, M. J. Wolak, F. Hébert, and V. G. Rousseau. *"Pair formation and collapse in imbalanced fermion populations with unequal masses"*. `EPL 86, 47006 (2009)`

[239] P. Farkašovský. *"Ground-state properties of fermionic mixtures with mass imbalance in optical lattices"*. `EPL 84, 37010 (2008)`

[240] D. Pecak, M. Gajda, and T. Sowiński. *"Two-flavour mixture of a few fermions of different mass in a one-dimensional harmonic trap"*. `New J. Phys. 18, 013030 (2016)`

[241] D. Pęcak, M. Gajda, and T. Sowiński. *"Experimentally Accessible Invariants Encoded in Interparticle Correlations of Harmonically Trapped Ultra-cold Few-Fermion Mixtures"*. `Few-Body Syst. 58, 159 (2017)`

[242] T. Sowiński and M. Á. García-March. *"One-dimensional mixtures of several ultracold atoms: a review"*. `Rep. Prog. Phys. 82, 104401 (2019)`

[243] S. Kemler. *"From Microscopic Interactions to Density Functionals"* (Dissertation). TU Darmstadt (2017)

[244] J. Polonyi and K. Sailer. *"Effective action and density-functional theory"*. Phys. Rev. B **66**(15), 155113 (2002)

[245] A. Schwenk and J. Polonyi. *"Towards density functional calculations from nuclear forces"*. In: *32nd International Workshop on Gross Properties of Nuclei and Nuclear Excitation: Probing Nuclei and Nucleons with Electrons and Photons (Hirschegg 2004) Hirschegg, Austria, January 11-17, 2004.*

[246] S. Kemler and J. Braun. *"Towards a renormalization group approach to density functional theory—general formalism and case studies"*. J. Phys. G **40**, 085105 (2013)

[247] S. Kemler, M. Pospiech, and J. Braun. *"Formation of selfbound states in a one-dimensional nuclear model: a renormalization group based density functional study"*. J. Phys. G **44**, 015101 (2017)

[248] C. Ravensbergen, E. Soave, V. Corre, M. Kreyer, B. Huang, E. Kirilov, and R. Grimm. *"Strongly Interacting Fermi-Fermi Mixture of 161Dy and 40K"*. arXiv:1909.03424

[249] M. Lu, N. Q. Burdick, and B. L. Lev. *"Quantum Degenerate Dipolar Fermi Gas"*. Phys. Rev. Lett. **108**(21), 215301 (2012)

[250] A. Frisch, K. Aikawa, M. Mark, F. Ferlaino, E. Berseneva, and S. Kotochigova. *"Hyperfine structure of laser-cooling transitions in fermionic erbium-167"*. Phys. Rev. A **88**(3), 032508 (2013)

[251] D. S. Petrov, G. V. Shlyapnikov, and J. T. M. Walraven. *"Regimes of Quantum Degeneracy in Trapped 1D Gases"*. Phys. Rev. Lett. **85**(18), 3745-3749 (2000)

[252] M. D. Girardeau. *"Two super-Tonks-Girardeau states of a trapped one-dimensional spinor Fermi gas"*. Phys. Rev. A **82**(1), 011607 (2010)

[253] T. Kinoshita, T. Wenger, and D. S. Weiss. *"Observation of a one-dimensional Tonks-Girardeau gas"*. Science **305**, 1125-1128 (2004)

[254] T. Kinoshita, T. Wenger, and D. S. Weiss. *"Local Pair Correlations in One-Dimensional Bose Gases"*. Phys. Rev. Lett. **95**(19), 190406 (2005)

[255] E. Haller, M. Gustavsson, M. J. Mark, J. G. Danzl, R. Hart, G. Pupillo, and H.-C. Nägerl. *"Realization of an Excited, Strongly Correlated Quantum Gas Phase"*. Science **325**, 1224-1227 (2009)

[256] G. Orso. *"Attractive Fermi Gases with Unequal Spin Populations in Highly Elongated Traps"*. Phys. Rev. Lett. **98**(7), 070402 (2007)

[257] H. Hu, X.-J. Liu, and P. D. Drummond. *"Phase Diagram of a Strongly Interacting Polarized Fermi Gas in One Dimension"*. Phys. Rev. Lett. **98**(7), 070403 (2007)

[258] A. E. Feiguin and F. Heidrich-Meisner. *"Pairing states of a polarized Fermi gas trapped in a one-dimensional optical lattice"*. Phys. Rev. B **76**(22), 220508 (2007)

[259] A. Lüscher, A. M. Läuchli, and R. M. Noack. *"Spatial noise correlations of a chain of ultracold fermions: A numerical study"*. Phys. Rev. A **76**(4), 043614 (2007)

[260] A. Lüscher, R. M. Noack, and A. M. Läuchli. *"Fulde-Ferrell-Larkin-Ovchinnikov state in the one-dimensional attractive Hubbard model and its fingerprint in spatial noise correlations"*. Phys. Rev. A **78**(1), 013637 (2008)

[261] M. Rizzi, M. Polini, M. A. Cazalilla, M. R. Bakhtiari, M. P. Tosi, and R. Fazio. *"Fulde-Ferrell-Larkin-Ovchinnikov pairing in one-dimensional optical lattices"*. Phys. Rev. B **77**(24), 245105 (2008)

[262] G. G. Batrouni, M. H. Huntley, V. G. Rousseau, and R. T. Scalettar. *"Exact Numerical Study of Pair Formation with Imbalanced Fermion Populations"*. Phys. Rev. Lett. 100(11), 116405 (2008)

[263] T. Iida and M. Wadati. *"Exact analysis of a delta-function spin-1/2 attractive Fermi gas with arbitrary polarization"*. J. Stat. Mech. , P06011 (2007)

[264] D. Huber and A. G. Volosniev. *Unpublished.*

[265] A. E. Feiguin, F. Heidrich-Meisner, G. Orso, and W. Zwerger. *"BCS–BEC Crossover and Unconventional Superfluid Order in One Dimension"*. In: *"The BCS-BEC Crossover and the Unitary Fermi Gas"* edited by: W. Zwerger. Berlin, Heidelberg: Springer Berlin Heidelberg (2012)

[266] M. A. Cazalilla, A. F. Ho, and T. Giamarchi. *"Two-Component Fermi Gas on Internal-State-Dependent Optical Lattices"*. Phys. Rev. Lett. 95(22), 226402 (2005)

[267] L. Barbiero, M. Casadei, M. Dalmonte, C. Degli Esposti Boschi, E. Ercolessi, and F. Ortolani. *"Phase separation and pairing regimes in the one-dimensional asymmetric Hubbard model"*. Phys. Rev. B 81(22), 224512 (2010)

[268] L. Mathey. *"Commensurate mixtures of ultracold atoms in one dimension"*. Phys. Rev. B 75(14), 144510 (2007)

[269] B. Wang, H.-D. Chen, and S. Das Sarma. *"Quantum phase diagram of fermion mixtures with population imbalance in one-dimensional optical lattices"*. Phys. Rev. A 79(5), 051604 (2009)

[270] T.-L. Ho. *"Universal Thermodynamics of Degenerate Quantum Gases in the Unitarity Limit"*. Phys. Rev. Lett. 92(9), 090402 (2004)

[271] M. J. H. Ku, A. T. Sommer, L. W. Cheuk, and M. W. Zwierlein. *"Revealing the Superfluid Lambda Transition in the Universal Thermodynamics of a Unitary Fermi Gas"*. Science 335, 563–567 (2012)

[272] K. Van Houcke, F. Werner, E. Kozik, N. Prokof'ev, B. Svistunov, M. J. H. Ku, A. T. Sommer, L. W. Cheuk, A. Schirotzek, and M. W. Zwierlein. *"Feynman diagrams versus Fermi-gas Feynman emulator"*. Nat. Phys. 8, 366 (2012)

[273] O. Goulko and M. Wingate. *"Numerical study of the unitary Fermi gas across the superfluid transition"*. Phys. Rev. A 93(5), 053604 (2016)

[274] R. Rossi, T. Ohgoe, K. Van Houcke, and F. Werner. *"Resummation of Diagrammatic Series with Zero Convergence Radius for Strongly Correlated Fermions"*. Phys. Rev. Lett. 121(13), 130405 (2018)

[275] S. Jensen, C. N. Gilbreth, and Y. Alhassid. *"Nature of pairing correlations in the homogeneous Fermi gas at unitarity"*. arXiv:1801.06163

[276] O. Goulko and M. Wingate. *"Thermodynamics of balanced and slightly spin-imbalanced Fermi gases at unitarity"*. Phys. Rev. A 82(5), 053621 (2010)

[277] O. Goulko and M. Wingate. *"The imbalanced Fermi gas at unitarity"*. arXiv:1011.0312

[278] J. D. Jackson and J. M. Blatt. *"The Interpretation of Low Energy Proton-Proton Scattering"*. Rev. Mod. Phys. 22(1), 77–118 (1950)

[279] D. Lee and T. Schäfer. *"Cold dilute neutron matter on the lattice. I. Lattice virial coefficients and large scattering lengths"*. Phys. Rev. C 73(1), 015201 (2006)

[280] W. E. Ormand, D. J. Dean, C. W. Johnson, G. H. Lang, and S. E. Koonin. *"Demonstration of the auxiliary-field Monte Carlo approach for sd-shell nuclei".* Phys. Rev. C **49(3)**, 1422-1427 (1994)

[281] Z. Wang, F. F. Assaad, and F. Parisen Toldin. *"Finite-size effects in canonical and grand-canonical quantum Monte Carlo simulations for fermions".* Phys. Rev. E **96(4)**, 042131 (2017)

[282] C. Gilbreth, S. Jensen, and Y. Alhassid. *"Reducing the complexity of finite-temperature auxiliary-field quantum Monte Carlo".* arXiv:1907.10596

[283] C. R. Shill and J. E. Drut. *"Particle Projection Using a Complex Langevin Method".* EPJ Web Conf. **175**, 03003 (2018)

[284] R. Rossi, T. Ohgoe, E. Kozik, N. Prokof'ev, B. Svistunov, K. Van Houcke, and F. Werner. *"Contact and Momentum Distribution of the Unitary Fermi Gas".* Phys. Rev. Lett. **121(13)**, 130406 (2018)

[285] B. Frank. *Private communication.*

[286] R. Haussmann, W. Rantner, S. Cerrito, and W. Zwerger. *"Thermodynamics of the BCS-BEC crossover".* Phys. Rev. A **75(2)**, 023610 (2007)

[287] K. B. Gubbels and H. T. C. Stoof. *"Renormalization Group Theory for the Imbalanced Fermi Gas".* Phys. Rev. Lett. **100(14)**, 140407 (2008)

[288] N. Trivedi and M. Randeria. *"Deviations from Fermi-Liquid Behavior above T_c in 2D Short Coherence Length Superconductors".* Phys. Rev. Lett. **75(2)**, 312-315 (1995)

[289] W. H. Press, S. A. Teukolsky, W. T. Vetterling, and B. P. Flannery. *"Numerical Recipes: The Art of Scientific Computing (3rd edition)".* New York, NY, USA: Cambridge University Press (2007)

[290] M. Horikoshi, S. Nakajima, M. Ueda, and T. Mukaiyama. *"Measurement of Universal Thermodynamic Functions for a Unitary Fermi Gas".* Science **327**, 442-445 (2010)

[291] T. Enss, R. Haussmann, and W. Zwerger. *"Viscosity and scale invariance in the unitary Fermi gas".* Ann. Phys. **326**, 770-796 (2011)

[292] H. Hu, X.-J. Liu, and P. D. Drummond. *"Universal contact of strongly interacting fermions at finite temperatures".* New J. Phys. **13**, 035007 (2011)

[293] S. Jensen, C. N. Gilbreth, and Y. Alhassid. *"The contact in the unitary Fermi gas across the superfluid phase transition".* arXiv:1906.10117

[294] C. Carcy, S. Hoinka, M. G. Lingham, P. Dyke, C. C. N. Kuhn, H. Hu, and C. J. Vale. *"Contact and Sum Rules in a Near-Uniform Fermi Gas at Unitarity".* Phys. Rev. Lett. **122(20)**, 203401 (2019)

[295] G. E. Astrakharchik, J. Boronat, J. Casulleras, Giorgini, and S. *"Equation of State of a Fermi Gas in the BEC-BCS Crossover: A Quantum Monte Carlo Study".* Phys. Rev. Lett. **93(20)**, 200404 (2004)

[296] L. Luo and J. E. Thomas. *"Thermodynamic Measurements in a Strongly Interacting Fermi Gas".* J. Low Temp. Phys. **154**, 1-29 (2009)

[297] R. He, N. Li, L. Bing-Nan, and D. Lee. *"Superfluid Condensate Fraction and Pairing Wave Function of the Unitary Fermi Gas".* arXiv:1910.01257

[298] R. Pathria and P. D. Beale. *"8 - Ideal Fermi Systems".* In: *"Statistical Mechanics (Third Edition)"* edited by: R. Pathria and P. D. Beale. Boston: Academic Press (2011)

[299] P.-A. Pantel, D. Davesne, and M. Urban. *"Polarized Fermi gases at finite temperature in the BCS-BEC crossover"*. Phys. Rev. A 90(5), 053629 (2014)

[300] T. Enss and R. Haussmann. *"Quantum Mechanical Limitations to Spin Diffusion in the Unitary Fermi Gas"*. Phys. Rev. Lett. 109(19), 195303 (2012)

[301] J. P. Gaebler, J. T. Stewart, T. E. Drake, D. S. Jin, A. Perali, P. Pieri, and G. C. Strinati. *"Observation of pseudogap behaviour in a strongly interacting Fermi gas"*. Nat. Phys. 6, 569–573 (2010)

[302] A. Sommer, M. Ku, G. Roati, and M. W. Zwierlein. *"Universal spin transport in a strongly interacting Fermi gas"*. Nature 472, 1476 (2011)

[303] Y. Sagi, T. E. Drake, R. Paudel, R. Chapurin, and D. S. Jin. *"Breakdown of the Fermi Liquid Description for Strongly Interacting Fermions"*. Phys. Rev. Lett. 114(7), 075301 (2015)

[304] E. J. Mueller. *"Review of pseudogaps in strongly interacting Fermi gases"*. Rep. Prog. Phys. 80, 104401 (2017)

[305] Q. Chen and J. Wang. *"Pseudogap phenomena in ultracold atomic Fermi gases"*. Front. Phys. 9, 539–570 (2014)

[306] F. Palestini, P. Pieri, and G. C. Strinati. *"Density and Spin Response of a Strongly Interacting Fermi Gas in the Attractive and Quasirepulsive Regime"*. Phys. Rev. Lett. 108(8), 080401 (2012)

[307] H. Tajima, T. Kashimura, R. Hanai, R. Watanabe, and Y. Ohashi. *"Uniform spin susceptibility and spin-gap phenomenon in the BCS-BEC-crossover regime of an ultracold Fermi gas"*. Phys. Rev. A 89(3), 033617 (2014)

[308] G. Wlazłowski, P. Magierski, J. E. Drut, A. Bulgac, and K. J. Roche. *"Cooper Pairing Above the Critical Temperature in a Unitary Fermi Gas"*. Phys. Rev. Lett. 110(9), 090401 (2013)

[309] M. Randeria, N. Trivedi, A. Moreo, and R. T. Scalettar. *"Pairing and spin gap in the normal state of short coherence length superconductors"*. Phys. Rev. Lett. 69(13), 2001–2004 (1992)

[310] M. M. Forbes, S. Gandolfi, and A. Gezerlis. *"Resonantly Interacting Fermions in a Box"*. Phys. Rev. Lett. 106(23), 235303 (2011)

[311] F. Ehmann. *"Ground-state equation of state of the spin-polarized unitary Fermi gas"* (Master thesis). TU Darmstadt (2019)

[312] Y.-i. Shin, C. H. Schunck, A. Schirotzek, and W. Ketterle. *"Phase diagram of a two-component Fermi gas with resonant interactions"*. Nature 451, 689–693 (2008)

[313] J. Carlson and S. Reddy. *"Asymmetric Two-Component Fermion Systems in Strong Coupling"*. Phys. Rev. Lett. 95(6), 060401 (2005)

[314] Y. Nishida and D. T. Son. *"Fermi gas near unitarity around four and two spatial dimensions"*. Phys. Rev. A 75(6), 063617 (2007)

[315] E. Burovski, N. Prokof'ev, B. Svistunov, and M. Troyer. *"The Fermi–Hubbard model at unitarity"*. New J. Phys. 8, 153–153 (2006)

[316] T. Kashimura, R. Watanabe, and Y. Ohashi. *"Spin susceptibility and fluctuation corrections in the BCS-BEC crossover regime of an ultracold Fermi gas"*. Phys. Rev. A 86(4), 043622 (2012)

[317] B. Mukherjee, Z. Yan, P. B. Patel, Z. Hadzibabic, T. Yefsah, J. Struck, and M. W. Zwierlein. *"Homogeneous Atomic Fermi Gases"*. `Phys. Rev. Lett.` **118**(12), 123401 (2017)

[318] K. Hueck, N. Luick, L. Sobirey, J. Siegl, T. Lompe, and H. Moritz. *"Two-Dimensional Homogeneous Fermi Gases"*. `Phys. Rev. Lett.` **120**(6), 060402 (2018)

[319] Y.-Y. He, H. Shi, and S. Zhang. *"Reaching the Continuum Limit in Finite-Temperature Ab Initio Field-Theory Computations in Many-Fermion Systems"*. `Phys. Rev. Lett.` **123**(13), 136402 (2019)

[320] G. Salomon, J. Koepsell, J. Vijayan, T. A. Hilker, J. Nespolo, L. Pollet, I. Bloch, and C. Gross. *"Direct observation of incommensurate magnetism in Hubbard chains"*. `Nature` **565**, 56-60 (2019)

[321] S. Zhang. *"Auxiliary-Field Quantum Monte Carlo for Correlated Electron Systems"*. In: *"Emergent Phenomena in Correlated Matter"* edited by: E. Pavarini, E. Koch, and U. Schollwöck. Forschungszentrum Jülich Zentralbibliothek: Verlag Jülich (2013)

[322] B. A. Berg. *"Introduction to Markov Chain Monte Carlo Simulations and their Statistical Analysis"*. `arXiv:cond-mat/0410490`

[323] M. Wallerberger. *"Efficient estimation of autocorrelation spectra"*. `arXiv:1810.05079`

[324] J. Tukey. *"Bias and Confidence in Not-Quite Large Sample"*. `Ann. Math. Statist.` **29**, 614-623 (1958)

[325] B. Efron and C. Stein. *"The Jackknife Estimate of Variance"*. `Ann. Statist.` **9**, 586-596 (1981)

[326] X.-J. Liu. *"Virial expansion for a strongly correlated Fermi system and its application to ultracold atomic Fermi gases"*. `Phys. Rep.` **524**, 37-83 (2013)

[327] G. E. Uhlenbeck and E. Beth. *"The quantum theory of the non-ideal gas I. Deviations from the classical theory"*. `Physica` **3**, 729-745 (1936)

[328] D. Rakshit, K. M. Daily, and D. Blume. *"Natural and unnatural parity states of small trapped equal-mass two-component Fermi gases at unitarity and fourth-order virial coefficient"*. `Phys. Rev. A` **85**(3), 033634 (2012)

[329] Y. Yan and D. Blume. *"Path-Integral Monte Carlo Determination of the Fourth-Order Virial Coefficient for a Unitary Two-Component Fermi Gas with Zero-Range Interactions"*. `Phys. Rev. Lett.` **116**(23), 230401 (2016)

Erklärung zur Dissertation

Hiermit versichere ich, dass ich die vorliegende Dissertation selbstständig angefertigt und keine anderen als die angegebenen Quellen und Hilfsmittel verwendet habe. Alle wörtlichen und paraphrasierten Zitate wurden angemessen kenntlich gemacht. Die Arbeit hat bisher noch nicht zu Prüfungszwecken gedient.

Darmstadt, den 28. Januar 2020

_____

(Lukas Rammelmüller)

Curriculum Vitae

——— ACADEMIC & PROFESSIONAL EXPERIENCE ———————————————————

January 2020 -
present

Postdoctoral Researcher
Faculty of Physics, Theoretical Nanophysics
Ludwig-Maximilians-Uiversität München, Germany

October 2016 -
December 2019

PhD Student
within the *HGS-HIRe for FAIR* programme
Institut für Kernphysik, Theoriezentrum
Technische Universität Darmstadt, Germany

Summer 2015,
Summer 2016
& Fall 2018

Visiting Researcher
Department of Physics and Astronomy
University of North Carolina, Chapel Hill, NC, USA

August 2014 -
December 2014

Exchange Student
Transatlantic Scientific Student Exchange Program (TASSEP)
University of North Carolina, Chapel Hill, NC, USA

——— EDUCATION ———————————————————————————————————

TU Darmstadt
2016 - 2019

PhD in physics (Dr. rer. nat.)
Thesis: *"Exploring imbalanced Fermi gases with stochastic quantization"*
Supervisor: Jens Braun

TU Wien
2014 - 2016

MSc in Physics
Thesis: *"Energetics and equal-time response of strongly correlated fermions in 1D and 2D"*
Supervisor: Joaquín Drut (UNC Chapel Hill) & Alessandro Toschi (TU Wien)

TU Wien
2010 - 2014

BSc in Physics
Thesis: *"Numerical solution of the radial Schrödinger equation with momentum dependent potential"*
Supervisor: Helmut Leeb

HTBLA Leonding
2004 - 2009

Matura
high school with focus on computer science & business administration